Experimental and Computational Mechanics for the Constitutive Modelling of Extrusion-based 3D Concrete Printing

by
Marchant van den Heever

Dissertation presented for the degree of
Doctor of Philosophy in Engineering in the
Faculty of Engineering at
Stellenbosch University

Supervisor: Prof Gideon van Zijl
Co-supervisor: Dr Jacques Kruger

December 2021

Declaration

By submitting this dissertation electronically, I declare that the entirety of the work contained therein is my own, original work, that I am the sole author thereof (save to the extent explicitly otherwise stated), that reproduction and publication thereof by Stellenbosch University will not infringe any third party rights and that I have not previously in its entirety or in part submitted it for obtaining any qualification.

December 2021

Abstract

The structural use of 3D concrete printing (3DCP) has globally gained traction owing to the host of benefits permitted by an industrialised manufacturing style approach to construction. However, due to the novelty of this technology, no standardised hardened-state mechanical characterisation or design specifications have been established. Moreover, limited research has been conducted on the non-linear hardened-state finite element (FE) analysis of 3DCP components. Therefore, this research proposes mechanical testing protocols, computational modelling strategies and advanced microstructural characterisation procedures to evaluate the fundamental failure mechanisms in 3D printed concrete (3DPC) to provide critical insights into the design and analysis of 3DCP components or structures.

Novel hardened-state material characterisation procedures are proposed, which elucidate the anisotropic strength and deformation attributes of 3DCP components and provide the necessary material and model parameters for FE simulation. An analogy between the well-established computational modelling strategies for masonry structures and 3DCP is drawn. Two anisotropic non-linear simulation strategies are adapted and introduced for application in the 3DCP design space. Both techniques are novel within the context of 3DCP and provide accurate results of the experimentally attained capacity and cracking patterns of the members. The constitutive models of the proposed simulation strategies are studied and found to overestimate the shear capacity of interfacial regions due to the assumption of a Mohr-Coulomb failure criterion. To further advance the current knowledge basis, the microstructural morphology is comprehensively characterised via X-ray computed tomography and deemed a potential contributor to the reduced strength and stiffness portrayed by 3DCP specimens. Subsequently, it is demonstrated how the microstructure and orientation of the axes of the composite material influence the direction of crack propagation, validating that porosity content and pore geometric attributes have distinct but complementary effects on the mechanical capacity of 3DPC. It is then revealed why anisotropy is so prevalent in 3DCP and why the shear strength of interfacial regions is overestimated. Thereafter, it is divulged how to improve predictions of the non-linear shear constitutive behaviour computationally through a novel modified Mohr-Griffith yield criterion. Solid theoretical descriptions relate the microstructural morphology to damage mechanisms and the resulting anisotropic shear strength in mould-cast and 3DCP elements. Employing the enriched understanding of the mechanical performance of 3DPC's, potential remedies to alleviate the anisotropic response in 3DCP components are proposed.

In essence, this research demonstrates how synergies between the experimental and computational mechanics and advanced microstructural characterisation techniques permit improved constitutive modelling for 3DCP. Finally, it is recommended how the knowledge gained from this dissertation can be utilised to take an incremental step towards the detailed design and analysis of 3DCP structures.

Opsomming

Die strukturele gebruik van 3D-gedrukte beton (3DGB) het wêreldwyd belangstelling verwerf as gevolg van die vele voordele wat 'n geïndustrialiseerde vervaardigingsstylbenadering tot konstruksie bied. As gevolg van die nuutheid van hierdie tegnologie, is daar egter geen gestandaardiseerde meganiese karakterisering of ontwerpspesifikasies vasgestel nie. Daar is boonop geringe navorsing gedoen oor die nie-lineêre ontleding deur eindige element (EE)-analise van 3DGB komponente. Dus, stel hierdie navorsing meganiese toetsprotokolle, modelleringstrategieë en gevorderde mikrostruktuur karakteriseringsprosedures voor om die fundamentele falingsmeganismes in 3DGB te evalueer en om kritiese insigte te bied vir die ontwerp en analise van 3DGB komponente of -strukture.

Nuwe prosedures vir die karakterisering van 3DGD komponente in die verharde toestand word voorgestel om die anisotropiese sterkte- en vervormingseienskappe van 3DGB toe te lig en om die nodige materiaal- en modelparameters vir EE-simulasie te bepaal. 'n Analogie tussen die gevestigde rekenaarmodelleringstrategieë vir messelwerk en 3DGB word getrek. Twee anisotropiese nie-lineêre simulasiestrategieë word aangepas en voorgestel vir toepassing in die 3DGB ontwerpruimte. Albei tegnieke is nuut binne die konteks van 3DGB en bied akkurate resultate van beide die komponente se kapasiteit en eksperimentele kraakpatrone. Die konstituerende modelle van die simulasiestrategieë is bestudeer en daar is bevind dat die aanname van 'n Mohr-Coulomb-falingskriterium die skuifweerstand van 3DGB se tussenlae oorskat. Om die huidige kennisbasis verder te bevorder, word die mikrostruktuur morfologie volledig gekarakteriseer deur middel van X-straaltomografie. Hiermee word daar bevestig dat die mikrostruktuur morfologie bydra tot die verminderde sterkte en styfheid tipies bevind in 3DGB. Daarbenewens word aangetoon hoe die mikrostruktuur en oriëntasie van die samestelling se material-asse die groeirigting van krake beïnvloed, wat bevestig dat die porositeit en porie-geometriese eienskappe unieke, maar aanvullende effekte op die meganiese gedrag van 3DGB het. Daarna word onthul waarom anisotropie so algemeen in 3DGB voorkom en waarom die skuifsterkte van 3DGB tussenlae oorskat word. Daarvolgens word voorgestel hoe om die nie-lineêre skuifkonstituerende gedrag berekeningsmatig beter te voorspel deur 'n nuwe, gewysigde Mohr-Griffith falingskriterium. Vaste teoretiese beskrywings verbind die mikrostrukturele morfologie aan die falingsmeganismes en gevolglike anisotropiese skuifsterkte in gegote en 3DGB elemente. Gebaseer op 'n fundamentele, dieper begrip van die meganiese optrede van 3DGB, word potensiële metodes om die anisotropiese gedrag in 3DGB komponente te verminder, voorgestel.

In essensie demonstreer hierdie navorsing hoe sinergieë tussen die eksperimentele- en berekeningsmeganika en gevorderde mikrostruktuur karakteriseringstegnieke verbeterde konstituerende modellering vir 3DGB moontlik maak. Ten slotte, word daar aangetoon hoe die kennis wat uit hierdie proefskrif verwerf is, gebruik kan word om 'n inkrementele stap te neem na die gedetailleerde ontwerp en analise van 3DGB strukture.

Acknowledgements

I want to extend my gratitude to the following individuals and Institutions for their respective contributions to the realisation of this dissertation.

- My supervisor, Prof Gideon van Zijl, for your guidance, mentorship, motivation, and wealth of knowledge that you so readily share with others. Thank you for helping me punch above my weight and achieve my greatest feat yet! One very seldom meets an individual with so many personal accolades that remains so humble – this has truly impacted my vision of success.

- My co-supervisor, Dr Jacques Kruger, for your guidance, example, motivation, and friendship. It has been my privilege embarking on this journey with you, and I can't wait to see what the future holds.

- My teammate, Mr Frederick Bester, for your support, motivation, friendship, and assistance with experimental work. Your determination and meticulous pursuit of excellence has driven me to become a better engineer and researcher. Thanks for challenging me but backing me up and embarking on this journey from undergraduate to doctoral study with me. It has been a privilege, and I can't wait to see what this next phase holds for us.

- The University of Stellenbosch, specifically the Structural Engineering Department, for the world-class facilities and personnel that it has granted me access to. Without these resources the research of such novel technologies would not be possible.

- The laboratory and workshop staff, for their assistance with experimental work and fantastic attitude making my time in the laboratory truly memorable.

- The Centre for the Development of Sustainable Infrastructure for its financial support during my postgraduate studies and the Concrete Society of Southern Africa for financing this research.

- My parents, Chani and Christo van den Heever thank you for affording me the incredible opportunity to pursue my passion. The determination, hunger for knowledge, and desire for excellence that you have engraved in me have allowed me to excel on a level that I had never

imagined possible. Thank you for always believing in me! Your unconditional love and support are truly appreciated.

- To my fiancé, Aniza Parsons, your love, support, motivation, interest, understanding and compassion has carried me to this significant milestone. Thanks for being my number one fan and sharing a passion for life and beautiful buildings with me. You inspire me to be the best version of myself. I love you!

- I praise the Lord for the talents and opportunities that I undeservingly receive by His grace. I pledge to apply the knowledge that I have gained to serve the Kingdom!

"In all that you do, strive to be Anything but Ordinary."

- M van den Heever

Contents

Table of Figures

Chapter 2:

Chapter 3:

Chapter 4:

Chapter 5:

Chapter 6:

List of Tables

List of Abbreviations and Acronyms

2D	Two-dimensional
3D	Three-dimensional
3DCP	3D concrete printing
3DPC	3D printed concrete
AM	Additive manufacturing
ANOVA	Analysis of variance
ASTM	American Society for Testing and Materials
BFGS	Broyden-Fletcher-Goldfarb-Shanno iterative solution procedure
BIM	Building information modelling
C1	Configuration 1
C2	Configuration 2
C3	Configuration 3
CAD	Computer-aided design
CCSC	Combined-cracking-shearing-crushing interface model
CDP	Concrete Damage Plasticity
CDSI	Centre for the development of sustainable infrastructure
CL12I	Quadratic line interface elements
CM	Continuum model
CMOD	Crack mouth opening displacement
CO_2	Carbon dioxide
CoV	Coefficient of Variation
CQ16M	Eight-node quadrilateral isoparametric plane stress elements
CT	Computed tomography
D1	Direction 1 - extrusion direction
D2	Direction 2 - transverse direction
D3	Direction 3 - vertical building direction
DFC	Digital fabrication of concrete
DIC	Digital image correlation
DOF	Degree of freedom
DST	Direct shear test
DTT	Direct tensile test
EN	European Norm
eTPB	Eccentric three-point bending
F-CMOD	Load crack mouth opening displacement
FE	Finite element

FEM	Finite element method
fib	The International Federation for Structural Concrete
FPB	Four-point bending
FPZ	Fracture process zone
FRC	Fibre-reinforced concrete
FRPC	Fibre-reinforced printable concrete
FvD	Force versus displacement
G-code	Machine readable language
HPC	High-performance concrete
HX24L	Linear 8-node brick isoparametric solid element
IBS	Interlayer bond strength
IFM	Interface-based model
IR	Interlayer region
ISO	International Standards Organisation
ITZ	Interfacial transition zone
JSCE	Japan Society of Civil Engineers
LBA	Lower bound analysis
LOA	Level of anisotropy
LOF	Lack-of-fusion
LVDT	Linear Variable Differential Transformer
MTM	Material testing machine
PP	Polypropylene
PS	Parameter study
Q24IF	4-by-4 node plane quadrilateral interface element
RC	Reinforced concrete
SEM	Scanning electron microscopy
SHCC	Strain-hardening cementitious composites
STL	Standard Tessellation Language
T18IF	3-by-3 node plane triangular interface element
TP18L	Linear 6-node wedge isoparametric solid element
TSC	Total strain-based cracking model
UCT	Uniaxial compressive test
VMA	Viscosity modifying agent
X-CT	X-ray computed tomography
XP	Experimental result

List of Symbols

Roman Symbols

A'	Adjusted cross-sectional area
A_m	Area of cementitious matrix
A_{rebar}	Rebar cross-sectional area
A_{thix}	Structuration rate
a_c	Half the critical crack length
b	Breadth
b_n	Notched specimen width
c	Cohesion
c_c	Cohesion
$c_{ss,j}$	Shear stress contribution to compressive failure in the interlayer
d	Width
E	Young's/ elastic modulus
E^*	Effective elastic modulus
E_{cm}	Concrete mean Young's modulus
E_{cmp}	Elastic modulus of cement paste
E_f	Young's modulus of fibre
E_{gel}	Elastic modulus of gel
E_{mod}	Young’s modulus
E_{mort}	Elastic modulus of mortar
f_c	Compressive strength
$f_{c,j}$	Interface compressive strength
f_{cm}	Concrete mean compressive strength
f_{ctm}	Concrete mean tensile strength
f_s	Shear strength
f_t	Tensile strength
$f_{t,i}$	Tensile strength in respective direction
$f_{t,j}$	Interface tensile strength
f_{ult}	Rebar ultimate stress
f_y	Rebar yield stress
G_{cc}	Interface compressive fracture energy
G_f	Fracture energy
$G_{fc,i}$	Compressive fracture energy in respective direction
$G_{ft,i}$	Tensile fracture energy in respective direction
$G^I_{f,j}$	Interface tensile fracture energy

G^{II}_{fc}	Interface shear fracture energy
GPa	Gigapascal
h	Element mesh size
h	Component height
Hz	Hertz
kg	kilogram
kN	kilonewton
k_{nc}	Elastic normal stiffness
k_{sc}	Elastic shear stiffness
kV	kilovolt
L	Length
l	Component length
$L_{colinear}$	Design specification for distance between collinear filaments
L_{FPZ}	Critical length of fracture process zone
L_h	Filament/layer height
$L_{internal}$	Design specification for distance between internal filaments
L_n	Notch depth
L_w	Filament/layer width
$L_{w,eff}$	Effective filament/layer width
m	Meter
m	Super-hyperbolic Rankine-Hill parameter
m	Degree of hydration
M	Material scaling factor for modified Mohr-Griffith failure criterion
min	Minutes
mm	millimeter
MPa	Megapascal
ms	milliseconds
N	Newton
n	Super-hyperbolic Rankine parameter
nm	nanometer
n_w	Nozzle width
P	Porosity percentage
Pa	Pascal
P_{cap}	Porosity percentage capillary pores
P_{gel}	Porosity percentage of gel pores
R^2	Root mean squared

R_{thix}	Reflocculation rate
s	Seconds
S1	Cauchy principal stress local x-direction
STS_x	Interface shear traction
STS_z	Interface normal traction
t	Plane stress thickness
t_{eff}	Effective plane stress thickness
V_{agg}	Fractional volume of aggregates
V_{gel}	Fractional volume of gel
w	Component width
w/c	Water-to-cement ratio

Greek Letters and Mathematical Symbols

%	Percent
ø	Diameter
Δ_{CF}	Interlayer contact factor
°	Degree
°C	Degree Celsius
µm	micrometer
α	Shear stress contribution to tensile failure Rankine Hill parameter
β	Biaxial compressive Rankine Hill parameter
γ	Shear stress contribution to compressive failure Rankine Hill parameter
Γ	Critically stressed sub-domain
$\delta_{f,i}$	Maximum crack mouth opening displacement in respective direction
$\delta_{peak,i}$	Peak displacement in respective direction
ε	Strain
ε_{su}	Ultimate strain in rebar
ζ	Sample domain
θ	Fracture inclination angle
µA	microamp
ρ	Density
σ_I	Major principal stress
σ_{II}	Intermediate principal stress
σ_{III}	Minor principal stress
σ_m	Mean normal stress
σ_n	Normal stress

τ	Shear stress
$\tau_{D,i}$	Initial dynamic shear yield stress
$\tau_{S,i}$	Initial static shear yield stress
φ	Friction angle
φ_r	Residual friction angle
ψ	Dilatancy angle
κ_p	Equivalent relative displacement
ν	Poisson's ratio

CHAPTER 1: **Introduction**

In a world where the continually burgeoning population has resulted in an immense demand for sustainable infrastructure, innovative construction solutions are increasingly sought. It is recognised that infrastructure investment is positively correlated to economic growth, and dignified housing directly contributes to physical and mental health, safety, and socio-economic prosperity. Specifically, the impact of social housing investment is multi-dimensional, providing inclusive economic growth through job creation, increased gross value-added, and multiplier effects [1]. Additionally, it addresses inequalities such as poverty and homelessness, improves health and well-being, and provides community anchors that strengthen resilience [1].

Providing adequate, cost-effective, and durable housing is an imminent challenge in the Republic of South Africa [2] and most developing nations, where rapid population expansion is most often witnessed [3]. A General Household Survey conducted by Statistics South Africa in 2018 reports that 13.1 % of South African households reside in informal dwellings [4]. Currently, a 2.3-million-unit housing backlog persists, rising at a rate of 178 000 units per year. Strikingly, 18 % of households living in state-subsidised housing declare that they are dissatisfied with the structural condition [4]. Evidently, collate efforts to innovate in housing finance models, construction technology and materials, subsidy mechanisms and institutional arrangements driven by lean construction frameworks are required to redress this exorbitant need for adequate housing [4]. It is reasoned that the high cost of construction materials and processes is responsible for the fact that low to middle-income individuals, which constitute 95% of the South African populace, cannot meet the expense of their accommodation needs [2].

These high construction costs are attributed to the construction industry's adversity to change in the 21st century, with materials and processes remaining essentially unchanged. As a result of such fixation, the associated benefits of modern construction processes and materials have not been exploited [5]. Innovative construction processes and materials could stimulate the production of more affordable homes, which has the potential to reduce the number of individuals constrained to the rental market, promoting homeownership, and thereby effectively increasing personal prosperity and financial security at a mass scale [6].

The increased strain imposed on natural resources and the associated effects of climate change profoundly impact businesses, society, and individuals, and it is appreciated that a transition towards a circular low-carbon economy is required. Cooperation in the construction sector is essential towards this shift since approximately 40 % of global greenhouse gas emissions can be attributed to the industry [7]. In order to provide sustainable infrastructure, i.e., for infrastructure to be economically feasible, environmentally friendly, and to promote societal prosperity, it must embody resilient design

approaches. In this light, the author opines that authorities, designers, and clients are obligated to advocate for new design philosophies that address the growing demands for sustainable infrastructure while mitigating the environmental impact caused by its implementation.

Owing to this growing need for the rapid realisation of infrastructure, attention has been directed towards alternative construction methodologies. The potential to employ advanced industrialised manufacturing techniques, such as the additive manufacturing technology 3D concrete printing (3DCP), within the architectural, engineering, and construction industry has provided a new paradigm for clients, designers and contractors. Additionally, it is postulated that certain sectors of the construction industry could benefit from a 500 to 1000 % productivity increase by transitioning to a manufacturing-style production system [8]. With proposed advantages such as enhanced structural efficacy, reduced construction duration, reduced cost, optimum material usage, reduced waste, quality improvements, and the possibility to construct custom geometries without the need for bespoke formwork solutions, 3DCP, in particular, has attracted significant attention in the emerging digital construction era. For instance, Dubai has indicated that it intends on constructing 25 % of its new buildings with 3DCP technology by 2030 [6].

Although the value added by this novel approach is undoubtedly set to revolutionise the construction industry, 3DCP is still in the developmental phase and will first have to surmount the current hurdles impeding its widespread adoption [9–16]. Predominantly, 3DCP faces challenges such as impaired interlayer bonding between filaments, contesting rheological requirements for pumping and buildability, anisotropic material characteristics in the hardened-state, a non-exclusive interrelation between material, process, and fresh- and hardened-state design requirements, and demands for the development of non-standard reinforcement techniques. The consequence of unbalanced material, process, and design parameters is multifaceted and poses various fresh-state and hardened-state considerations from a structural engineering perspective.

For 3DCP to extend its position in the building and construction industry, a fundamentally deeper physics-based understanding of the multifaceted fresh-state rheological and hardened-state mechanical behaviour of 3DCP elements is required. It is contended that pertinent testing, design, computational or numerical analysis procedures are critical to the widespread adoption of this new construction technique. Designers will need to understand how to design structures to be manufactured with printed material and process constraints, requiring novel material prescriptions, design standards, and standardised mechanical assessment protocol to be developed. To elucidate the mechanical characterisation and numerical simulation of 3DCP elements, synergy between experimental and computational mechanics is required. Such activities should characterise the unique linear and non-linear material properties of printed components to permit limit state design procedures and the correct prescription of finite element (FE) model parameters.

1.1 Research Motivation

Ensuing the various motives presented above, the structural use of 3DCP systems has globally gained traction over the past five years; however, no standardised hardened-state mechanical characterisation or design guidelines are available due to the anomalous nature of this novel technology. Moreover, sparse research has been conducted on the non-linear hardened-state FE analysis of 3DCP components. This research proposes to facilitate the development of the mechanical testing protocols required for computational modelling and FE analysis strategies that provide critical insights into the design of 3DCP systems by evaluating the fundamental failure mechanisms in 3D printed concrete (3DPC).

The benefit of suitably calibrated computational simulation strategies is contended to reside in the potential optimisation of structures and verification of their performance. Parametric studies can facilitate reliability determination exercises by providing a means to generate data to probabilistically measure the effects of geometric, defect, and material characteristic aberrations over various timeframes and environmental conditions. The envisaged increase in design complexity is hampered by the ability to conduct analytical design calculations which favour simple geometries. Therefore, to harness the full potential of spatial and shell structures with complex geometric configurations, suitable computational modelling strategies are indispensable.

Additionally, the ability to conduct computational analysis procedures that accurately capture the response of reinforced 3DCP components under design loading conditions is considered paramount to the scalability of 3DCP. Bearing in mind that the development of compatible numerical simulation strategies for reinforced 3DCP elements would permit structural verification of building components without large-scale destructive testing practices, it is contended that these research activities evoke significant cost-saving potential. Furthermore, to push the boundaries of the structural design of reinforced concrete structures and facilitate the development of parametrically optimised buildings, a deeper understanding of the structural mechanics at play in 3DCP elements under numerous loading conditions is necessary.

Consequently, through this research, a comprehensive and holistic understanding of the experimental and computational mechanics of 3DCP is established and envisioned to contribute towards the accelerated adoption of the technology, which has the potential to provide a host of economic, socio-economical, and environmental benefits.

1.2 Problem Statement

Due to the novelty of 3DCP, no standardised hardened-state mechanical characterisation or design specifications have been established. Moreover, research regarding the non-linear hardened-state FE analysis of 3DCP components is limited. Therefore, this research intends to develop hardened-state

mechanical characterisation procedures that support the proposal of pragmatic, yet accurate, computational modelling strategies to facilitate the establishment of rational design guidelines for extrusion-based 3DCP.

1.3 Aim and Objectives

This research aims to **propose, experimentally evaluate and validate computational modelling strategies for 3DCP structural systems**. Therefore, (1) linear and non-linear hardened-state mechanical characteristics are required, and (2) suitable computational modelling strategies are investigated. A dynamic approach is adopted, where based on the outcomes of objectives (1) and (2), objectives (3) and (4) arose, which are intended to (3) elaborate the effects of porosity on the fundamental failure mechanisms in 3DCP and (4) assess the pertinence and accuracy of existing failure criteria thereto. Elaborations on the four key objectives are presented below:

(1) Characterise the anisotropic hardened-state material properties required for the computational analysis of 3D concrete printed elements.

Laboratory scale experimental procedures are proposed in Chapter 3 which consider the interrelated physico-chemical, process, and design parameters prominent in 3DCP. The material aspects of the fibre-reinforced printable concrete (FRPC) utilised can be divided into (i) fresh-state rheological and (ii) hardened-state mechanical characteristics. The rheological properties refer to the thixotropic characteristics of the FRPC, i.e., the static and dynamic yield shear stress evolution of the material employed. The hardened-state mechanical properties are categorised as (i) bulk, or *intralayer,* material properties and (ii) composite interaction, or *interlayer*, characteristics.

(2) Propose computational modelling strategies for extrusion-based 3D concrete printing.

The computational modelling strategies presented in Chapter 4 aim to predict the anisotropic non-linear structural response of reinforced 3DCP elements at a component scale. For this purpose, the extensively developed non-linear modelling frameworks for masonry are adopted and related to 3DCP, which include: (i) a multi-surface anisotropic continuum macro-modelling strategy [17] and (ii) a multi-surface interface micro-modelling strategy [18]. Additionally, this serves as a validation of the presented hardened-state mechanical characterisation procedures by highlighting the fundamental mechanisms influencing the structural behaviour of the experimentally evaluated members, which allows the applicability of the attained material parameters and compatibility of the reinforcement methodology to be verified.

Based on the results of the computational modelling strategies in Chapter 4, it is established that the shear capacity of the members is overestimated. This overestimation in shear capacity is postulated to originate from both or either of two sources: (i) the effects of porosity and spatial nonuniformity (pores) at predominantly interlayer locations throughout the member, or (ii) the intrinsic assumption of the

constitutive models, which employ the Mohr-Coulomb failure criterion that might not be as suited as the Mohr-Griffith criterion considering the observed ellipsoidal morphology of pores in a 3DCP medium.

(3) Study the effects of porosity and spatial nonuniformity on the mechanical characteristics of 3D printed concrete.

Microstructural morphology and constituent characteristics of the mixture are at the root of all mechanical properties. It has been shown that the 3DCP process influences the ensuing microstructural morphology, and it is known that constituent type, constituent proportion, porosity content and void morphology affect a porous medium's bulk strength and elasticity. Therefore, the correlation between such observations warrants additional investigation concerning the influence of porosity on the anisotropic mechanical properties of 3DCP components. Thus, in Chapter 5 the effects of porosity metrics are quantitatively investigated via X-ray computed tomography and related to the elasticity, compressive strength and observed fracture patterns of mould-cast and concrete printed specimens consisting of the same FRPC matrix.

(4) Evaluate the suitability of the assumed failure criteria in the respective computational modelling strategies.

To further extend the experimental database on the hardened-state material properties, the research in Chapter 6 aims to quantify the compression-shear capacity of the FRPC mixture via a direct shear testing (DST) methodology. Additionally, Chapter 6 seeks to critically evaluate the microstructural morphology of 3DPC inter and intralayers via X-ray computed tomography and provide a theoretical basis for the often observed anisotropic strength characteristics. Finally, Chapter 6 intends to propose a suitable failure criterion based on the experimentally attained results for improved FE modelling accuracy.

1.4 Limitations

The scope of this research is subject to the below-listed constraints:

(i) Material characterisation and evaluation procedures are limited to a single fibre-reinforced printable concrete mixture.

(ii) Experimental procedures must conform to the geometric constraints of the 3DCP objects, and therefore a deviation from existing standards is required. Samples need to be extracted from actual 3DCP elements to ensure that the effect of the employed additive manufacturing process parameters is accurately reflected.

(iii) Computational modelling strategies are limited to commercially available finite element analysis packages to ensure that the implementation thereof is practical and accessible to the industry.

1.5 Dissertation Structure

This dissertation comprises written chapters as well as published and/or unpublished journal articles to follow the PhD by publication structure of Stellenbosch University.

Chapter 1 provides the reader with a broad introduction to this research. The motivation for this research is presented, and the problem is stated. Thereafter, the main aim and objectives of the study are outlined and discussed in further detail.

Chapter 2 presents the necessary literature for the reader's benefit and provides perspective to the following chapters' content.

Chapter 3 addresses objective (1) by elaborating mechanical characterisation procedures for the numerical simulation of extrusion-based 3DCP. The mechanical characterisation procedures demonstrate the anisotropic material characteristics of the FRPC mixture. These procedures comprise direct tensile, uniaxial compression, Young's modulus, and four-point bending (FPB) crack mouth opening displacement (CMOD) tests. From the mechanical characterisation tests, two elastic parameters, seven strength parameters and five inelastic parameters are ascertained. The experimental findings relating to the material characteristic parameters are validated via supplementary numerical evaluation, and suitable constitutive relations are selected.

Chapter 4 addresses objective (2) by proposing and describing two FE modelling strategies for the numerical analysis of 3DCP building elements. The models predict the hardened-state structural capacity and failure mechanisms of singularly and dually reinforced concrete deep beams under various loading configurations. An analogy between masonry and 3DCP structures is presented, and succinct descriptions of the respective modelling strategies, adaptions to the 3DCP design space, and material model prescriptions are provided.

Chapter 5 addresses objective (3) by presenting the effects of porosity on the mechanical properties of extrusion-based fibre-reinforced 3D printed concrete. Porosity metrics such as total defect content, 3D void topology (shape, size, and orientation), pore spatial, size and compactness distributions, and interconnectivity are quantitatively investigated via X-ray computed tomography and related to the elasticity, compressive strength and observed fracture patterns of mould-cast and concrete printed specimens consisting of the same FRPC matrix.

Chapter 6 addresses objective (4) by evaluating the constant compression-shear capacity of the FRPC mixture via a DST methodology and proposing novel modified Mohr-Griffith failure criterion based on the experimentally attained results.

Chapter 7 presents conclusions and recommendations for identified future research needs in 3DPC.

Author contribution declarations for each journal article, as well as legal approval by the publisher for re-use of publications, can be found in the respective Addenda.

1.6 References

[1] K. Gibb, L. Lawson, J. Williams, Michael McLaughlin, The Impact of Social Housing : Economic, Social, Health and Wellbeing, (2020).

[2] R. Legida, K. Ntakana, S.A. Alabi, Research Report on Availability of 3D Concrete Printing Technologies for Sustainable Human, (2020).

[3] Consultancy.uk, 97% of population growth to be in developing world, (2015). https://www.consultancy.uk/news/2191/97-percent-of-population-growth-to-be-in-developing-world (accessed June 28, 2021).

[4] J. Chakwizira, Low-income housing backlogs and deficits “blues” in South Africa. What solutions can a lean construction approach offer? , Journal of Settlements and Spatial Planning. 10 (2019) 71–78. https://doi.org/10.24193/JSSP.2019.2.01.

[5] A. Luxien, N. Reynecke, J. Mahachi, 3D-PRINTED HOUSES PILOT PROJECT Research Report 1: Pre-production Phase, 2020.

[6] P.A. Raices, All Things Real Estate: Will 3D printing of homes may become mainstream?, The Island Now. (2021). https://theislandnow.com/business-106/all-things-real-estate-will-3d-printing-of-homes-may-become-mainstream/ (accessed June 28, 2021).

[7] M. Müller, T. Krick, J. Blohmke, Putting the construction sector at the core of the climate change debate| Deloitte Central Europe, Deloitte. (2020) 2–3. https://www2.deloitte.com/ce/en/pages/real-estate/articles/putting-the-construction-sector-at-the-core-of-the-climate-change-debate.html.

[8] McKinsey & Company, Re-inventing Construction In Brief, McKinsey & Company. (2017).

[9] C. Menna, J. Mata-Falcón, F.P. Bos, G. Vantyghem, L. Ferrara, D. Asprone, T. Salet, W. Kaufmann, Opportunities and challenges for structural engineering of digitally fabricated concrete, Cement and Concrete Research. 133 (2020) 106079. https://doi.org/10.1016/j.cemconres.2020.106079.

[10] T. Wangler, E. Lloret, L. Reiter, N. Hack, F. Gramazio, M. Kohler, M. Bernhard, B. Dillenburger, J. Buchli, N. Roussel, R. Flatt, Digital Concrete: Opportunities and Challenges, RILEM Technical Letters. 1 (2016) 67. https://doi.org/10.21809/rilemtechlett.2016.16.

[11] R.A. Buswell, W.R. Leal de Silva, S.Z. Jones, J. Dirrenberger, 3D printing using concrete extrusion: A roadmap for research, Cement and Concrete Research. 112 (2018) 37–49. https://doi.org/10.1016/j.cemconres.2018.05.006.

[12] D. Avrutis, A. Nazari, J.G. Sanjayan, Industrial Adoption of 3D Concrete Printing in the Australian Market, Elsevier Inc., 2019. https://doi.org/10.1016/b978-0-12-815481-6.00019-1.

[13] B. Panda, Y.W.D. Tay, S.C. Paul, M.J. Tan, Current challenges and future potential of 3D concrete printing, Materialwissenschaft Und Werkstofftechnik. 49 (2018) 666–673. https://doi.org/10.1002/mawe.201700279.

[14] Y.W.D. Tay, B. Panda, S.C. Paul, N.A. Noor Mohamed, M.J. Tan, K.F. Leong, 3D printing trends in building and construction industry: a review, Virtual and Physical Prototyping. 12 (2017) 261–276. https://doi.org/10.1080/17452759.2017.1326724.

[15] F. Bos, R. Wolfs, Z. Ahmed, T. Salet, Additive manufacturing of concrete in construction: potentials and challenges of 3D concrete printing, Virtual and Physical Prototyping. 11 (2016) 209–225. https://doi.org/10.1080/17452759.2016.1209867.

[16] S.C. Paul, G.P.A.G. van Zijl, M.J. Tan, I. Gibson, A review of 3D concrete printing systems and materials properties: current status and future research prospects, Rapid Prototyping Journal. (2018) 0. https://doi.org/10.1108/RPJ-09-2016-0154.

[17] P.B. Lourenço, J.G. Rots, J. Blaauwendraad, Continuum model for masonry: Parameter estimation and validation, Journal of Structural Engineering. 124 (1998) 642–652. https://doi.org/10.1061/(ASCE)0733-9445(1998)124:6(642).

[18] P.B. Lourenço, J.G. Rots, Multisurface interface model for analysis of masonry structures, Journal of Engineering Mechanics. 123 (1997) 660–668. https://doi.org/10.1061/(ASCE)0733-9399(1997)123:7(660).

CHAPTER 2 : Literature Review

2.1 Introduction

This Chapter presents the necessary background and fundamental concepts required to comprehend the following Chapters in this dissertation. An initial context is provided to the current status of the construction industry and why innovation is needed. Thereafter, 3D printing and specifically 3D concrete printing (3DCP) are introduced, and comprehensive discussions presented. The fresh-state rheological and hardened-state mechanical characteristics and their influential underlying mechanisms are elucidated. Finally, the status of computational and numerical simulation procedures pertaining to 3DCP are presented and discussed.

2.2 Current Status of the Construction Industry

Notwithstanding the developments in most other industries, the construction industry has been averse to change in the 21st century. The employed construction materials and processes have remained monotonous, and as a result of such fixation, the associated benefits of modern construction processes and materials have not been exploited [1]. McKinsey and Company report that the construction industry accounts for 13 % of the global gross domestic product, with an approximate annual expenditure of $10 trillion for construction-related goods and services [2]. However, the annual productivity of the sector has only increased 1 % over the past 20 years, compared to a 2.8 % increase in the global economy and a 3.6 % increase in manufacturing [2]. Although meeting the global demand for infrastructure and housing is no simple task, bridging the demand deficit presents a $1.6 trillion annual market opportunity [2].

The construction industry is a vital component in the economy and is a significant contributor to economic growth [3]. This is largely because the industry impacts various industries, including finance, design consultancies, material and equipment manufacturers, and additional related service providers. Moreover, the construction industry is labour and capital intensive, resulting from inherent risk involved, labour costs, material consumption, and equipment expenses [4]. The construction sector is critical to the production of civil engineering structures and is responsible for the extent to which investment efforts in a resource-rich country are translated into investment outcomes [5]. Additionally, infrastructure is essentially the foundation upon which modern society is built and is critical to service delivery, resource security, education, shelter, and the global economy.

Adequate housing is correlated to physical and mental health, safety, and socio-economic prosperity. Specifically, the impact of social housing investment is multi-dimensional, providing inclusive economic growth through job creation (particularly to the unskilled workforce), increased

gross value added per region, and multiplier effects [6]. A survey conducted by Statistics South Africa reports that 13.1 % of South African households reside in informal dwellings [7]. This corresponds to approximately 8 million individuals who do not have access to the basic human need of shelter for physical security and comfort. Since 1994, the government has provided 4.3 million state-subsidised dwellings, yet a 2.3 million backlog persists, rising at a rate of 178 000 units per year. Strikingly, 18 % of households living in state-subsidised housing declare that they are not satisfied with the structural condition [7]. Evidently, collate efforts to innovate in housing finance, construction technology and materials, subsidy mechanisms and institutional arrangements driven by lean construction frameworks are required to redress this exorbitant need for housing [7]. The main challenges faced in the South African construction industry are presented by Windapo and Cattell [3] and include:

- The management and skills-related capacity of the public sector is lacking,
- Deficient correlation between available and required skills,
- Globalisation instigating the importation of construction services to the detriment of the local construction sector,
- Unbalanced procurement practices and the capacity for sustainable empowerment,
- Limited access to affordable mortgage, credit, and interest rates,
- Poverty and its contribution to the destabilisation of the economy,
- Technology and end-user perceptions regarding alternative building methods and innovative building systems,
- Lack of suitable privately owned land for construction,
- Lack of sufficient infrastructure for human settlements,
- High rate of state enterprise failure and its effects on the cash-flow of the sector,
- Increased cost of building materials,
- Over regulation as an impediment to rapid development.

Considering the South African context, with an official unemployment rate of 32.6 %, amidst a period of societal and economic transformation, it is foreseen that the enablement of technological skills development in sustainable employment and career paths holds immense socio-economic potential. An opportunity to redress the significant backlog in formal housing resides in highly productive, economically resilient, industrialised construction activities to be employed as a strategic construction development strategy [8]. Such a strategic construction strategy would facilitate the delivery of standard and affordable housing which forms part of the South African National Development Plan 2030 [9]. Such a strategy could aid by sustainably strengthening the labour market by providing job opportunities specifically to South African youth which comprise an alarming unemployment rate of 46.3 % in the 15 - 34-year-old age category [10].

Climate change has a profound impact on businesses, society, and individuals, and it is appreciated that a transition towards a low-carbon economy is required. Cooperation in the construction sector is essential towards this shift since approximately 40 % of global anthropogenic greenhouse gas emissions can be attributed to the industry [11]. The American Institute of Architects ascribe the predominant fraction of the emissions of the sector to the energy consumed during the production of materials, followed by their transportations, and the operation and maintenance of buildings [4]. Evidently, such emission metrics should be considered and redressed first in order to provide sustainable infrastructure.

2.3 Three-Dimensional Printing

3D printing, a lineage technique of additive manufacturing (AM), is a prominent industrialised manufacturing technology of the 4th industrial revolution. This digitally native technology embodies computer-controlled production processes to realise three-dimensional (3D) objects from a multitude of materials in a layer-wise fashion. Applied techniques can be reduced to two salient approaches: extrusion-based and selective binding methods [12]. Both methods consist of a Standard Tessellation Language (STL) file obtained from a meshed 3D computer-aided design (CAD) model, which is converted to multiple contours; this process is conventionally referred to as ‘slicing’. Note that contour spatial configuration can be either planar or non-planar [13]. The state of the art comprises combining the Cartesian coordinates corresponding to the contour path with specific printing parameters, such as printing head speed, filament layer height, the rate of material deposition (deposition/extrusion rate) and generating the machine-readable language (G-code) [12]. Thereafter, the printing facility interprets the G-code and deposits, or solidifies, filament on a printing surface to obtain the final 3D printed object. The process flow is visually depicted in Fig. 2.1.

Fig. 2.1: General overview of 3D printing process.

2.4 3D Concrete Printing

The implementation of 3D printing in concrete construction is generally termed digital fabrication of concrete (DFC). The pivotal concept of automated solid freeform construction was initially introduced by Pegna [14] in 1997 and further popularised by Khoshnevis [15] in 2004. A detailed overview of the technology is provided by [16]. Fuelled by the prospects of a fully automated construction process, DFC has experienced significant technological developments, been implemented in the construction sector, and fundamentally changed the trajectory of concrete construction, ensuing the associated advantages. This notion is substantiated by the proliferation of available literature on

DFC [17]. However, compared to 3D printing technology, DFC is still in the nascency of implementation and must first surmount the current hurdles impeding its widespread adoption.

Buswell et al. [18] present an overview of the DFC suite of processes and propose a process classification framework founded on existing International Standards Organisation (ISO) guidelines in manufacturing industries. The RILEM classification is illustrated in Fig. 2.2. However, the current research is exclusively directed towards extrusion of cementitious materials, often referred to extrusion-based 3DCP.

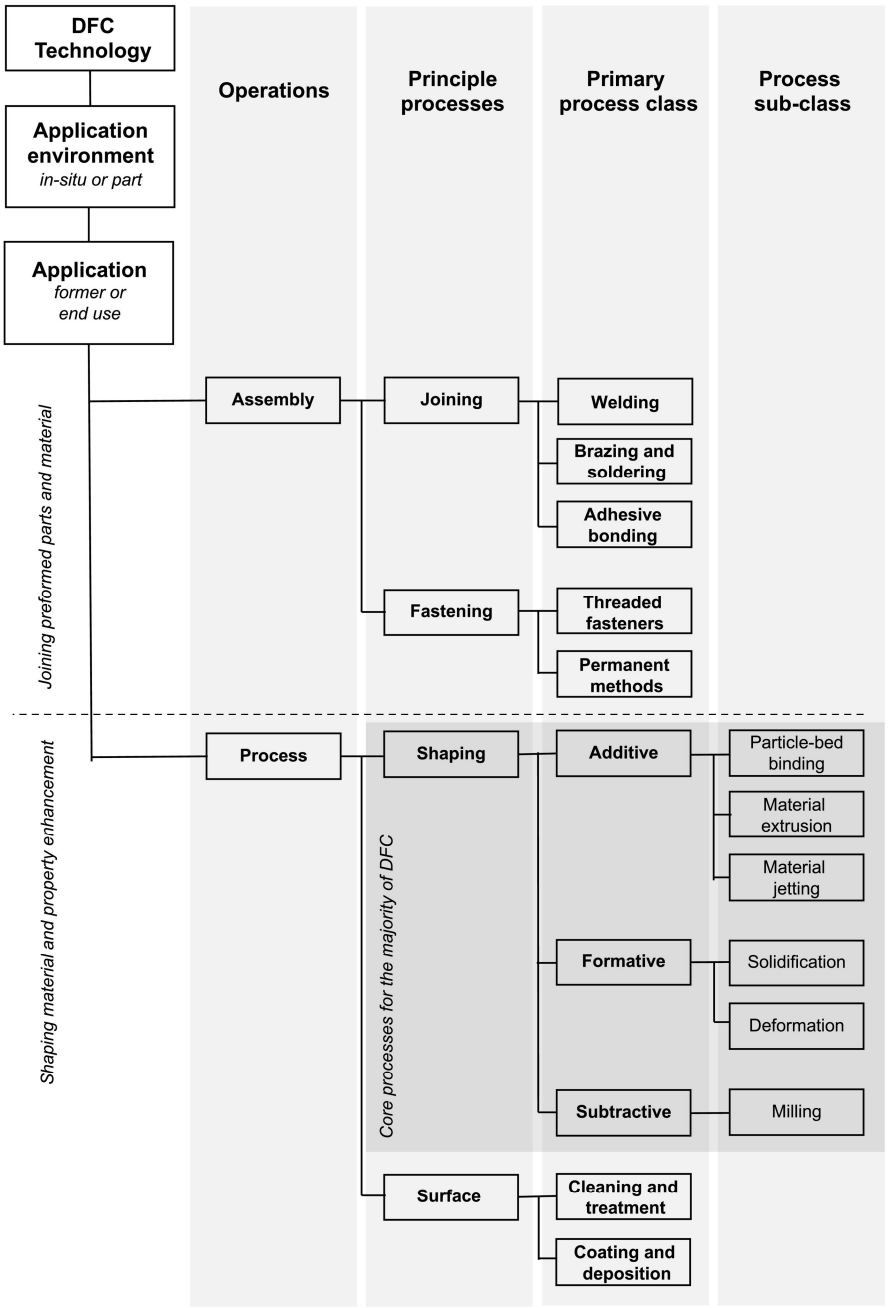

Fig. 2.2: RILEM classification framework for DFC processes. Reproduced from [18].

2.4.1 Extrusion-based 3DCP system classifications

Three major categories of 3D concrete printers are currently employed in industry and academia, namely gantry, robotic, and crane systems, as shown in Fig. 2.3. Facilities generally vary in size from laboratory scale to ultra-large-scale (17 x 50 x 10 m) systems [19]. As shown in Fig. 2.4, combinations that superimpose gantry and robotic systems have been commissioned as well as mobile robotic and crane systems that increase the building envelop of the printing facility. Evidently, a multitude of industrial grade 3DCP processes are commercially available, which demonstrates interest in the industry.

(a) (b) (c)

Fig. 2.3: 3D concrete printing systems, illustrating (a) gantry [19]*, (b) robotic* [20]*, and (c) crane systems* [21]*, respectively.*

(a) (b) (c) (d)

Fig. 2.4: Superimposed and mobile 3DCP systems, illustrating (a) robotic-gantry [22]*, (b) robotic-rail* [23]*, (c) mobile crane* [24]*, and (d) mobile robotic systems* [20]*, respectively.*

It is generally considered that robotic systems present the most significant design flexibility resulting from the 6-axis degree of freedom (DOF) capabilities such a system. However, it should be noted that specific end effectors with additionally specified DOFs can be mounted to any of the presented systems. Due to the primarily planar layer stacking methodology employed in the 3DCP industry, 3-DOF and 4-DOF systems generally suffice, depending on the nozzle geometry. When utilising non-circular nozzle geometries, a fourth DOF is required to maintain a consistent layer width.

Another influential factor is the delivery system used, where in smaller systems, a continuous connection between the concrete pump and the nozzle is often employed, and in larger systems, a two-part delivery system is employed, Fig. 2.5. Larger systems require the two-part system, incorporating a

hopper and auger system above the deposition effector to negate the lag, or pumping latency, in the pumping phase while pumping over expansive distances. Employing a hopper and auger system, Fig. 2.6, permits more significant control over material deposition and renders non-continuous print paths feasible since the extrusion can be halted [25,26]. Additionally, regardless of the size of the system, it might be advantageous to employ a two-part delivery system since the effects of pumping [27] are negated by shearing and deflocculating the plastic microstructure of the material directly before deposition. Two-part systems are also precursor when utilising hydration accelerating admixtures [28] because the accelerator must be incorporated after the main pumping action to prevent system blockages, ensure adequate dispersion of admixtures in the printhead [29], and improve rheological control [30].

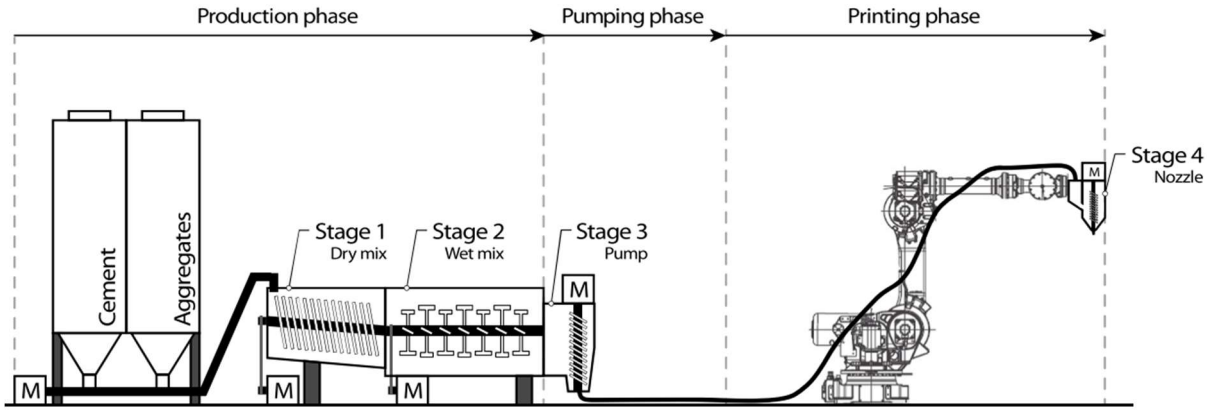

Fig. 2.5: Continuous production, pumping, and printing system. Reproduced from [25].

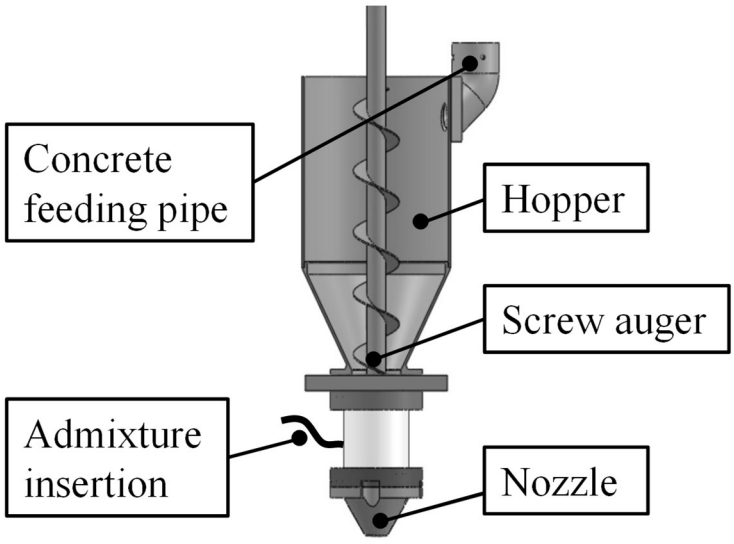

Fig. 2.6: Hopper and auger end effector system. Adapted from [31].

Suitable 3DCP systems are primarily selected considering the desired construction scale, geometric complexity of the elements to be manufactured, and the capital expense of the system. Secondary considerations comprise the maximum print speed and the ease with which the nozzle size and geometry can be interchanged. Finally, the degree of flexibility of the 3DCP systems could be of importance in advanced 3DCP applications [32].

2.4.2 Advantages of 3DCP

Bester et al. [33] present ten advantages of extrusion-based 3DCP obtained from a data collection exercise that considers 51 relevant publications. The below list of benefits is obtained:

- Increased design freedom, customisation, or object complexity.
- Increased productivity, or the labour intensity of construction is decreased.
- Decreased construction or object realisation duration.
- Reduced waste, or more effective material usage.
- Reduced formwork requirements, i.e., freeform construction.
- Decreased overall project cost of construction.
- Increased level of safety on-site.
- Increased quality or precision of components.
- Reduced environmental impact.
- Increased availability of skilled labour.

Additionally, considering the structural behaviour of 3DCP components, the focus is directed to fabrication methods that facilitate mass reduction while maintaining the desired component stiffness obtained through the fabrication of topologically optimised hollow sections [34]. This objective originates from structural dynamics, highlighting that mass reductions lower the seismic demand, or inertial forces imposed, on the structure, by limiting the base shear. Feng and Yuhong [35] validate this notion concluding that an increased strength-to-weight ratio improves the seismic resistance of structures. It is contended that suitable ductility can be provided through appropriate reinforcement strategies, which permits the capacitive design of structures that can withstand the peak global displacement demands of the induced seismic action.

2.4.3 Challenges of 3DCP

Despite the foreseen advantages of extrusion-based 3DCP, challenges exist regarding the successful execution of projects. These challenges originate from and are specific to the construction application of 3DCP. Foremost technical challenges include the availability of compatible building materials, 3DCP process particularities and their effects on structural integrity, the incorporation of reinforcement, and scalability. Regulatory challenges include the lack of standardised protocol for material design and

testing, no analytical structural design procedures specific to 3DCP, and the inherent conservatism that resides within the construction industry. In this section, an elaboration of the challenges above is presented.

2.4.3.1 Compatible Building Materials

Due to the unique manufacturing methodology exploited by 3DCP, specialist cement-based materials are required, which poses a challenge for the adoption of DFC since tailored constituent compositions will have to be manufactured at an industrial scale [36]. Currently, the material expense of printable concretes exceeds their conventional counterparts due to high binder content and the use of rheology modifying agents. Additionally, the high cement content and associated CO_2 footprint essentially negate gains achieved by reduced material use made possible by 3DCP.

2.4.3.2 3DCP Process Particularities

Material, process, and design particularities are all intrinsically interrelated and collectively contribute to the quality of the end product [17] (see Fig. 2.10). Panda et al. [37] confirm the interdependence of printable materials, the fabrication system, and the design of the components. They further state that "it is necessary to maintain proper coordination between these three components rather than optimising individual components." In this regard, many researchers have conducted trial and error experimental approaches to determine the rheological and mechanical properties affecting the quality of the printed object [38].

In the fresh state, these factors include five benchmark properties: interlayer bond strength (IBS) or interlayer adhesiveness, extrudability, pumpability, open time, and buildability [39]. Since the 3DCP process requires no formwork, fresh concrete must be capable of supporting its own weight, as well as that of subsequently deposited filament layers, without excessive deformation [40]. Moreover, a 3D printable material must have a certain level of workability, allowing for it to be pumped without the application of excessive pressure to avoid segregation [41]. Similarly, the filament must be extrudable to allow for the desired surface quality and ensure the structural integrity of the component. As comprehensively discussed by Kruger and van Zijl [42] the combination of the aforementioned parameters influences the IBS of the element and, therefore, also affects its structural integrity. Evidently, a comprehensive and holistic understanding of the inter-related benchmark properties is required to digitally fabricate components successfully.

2.4.3.3 Scalability

Scalability issues are prominent in most 3DCP applications since the dimensions of the object under construction are limited by the build volume of the 3D printing system. Geometric fabrication constraints stem from the fact that most fabrication systems rely on stationary gantry-based or robotic

arm-based printing systems, where the span and reach are the limiting factors. Zhang et al. [43] report that when considering large-scale applications, it becomes impractical to upscale the size of the 3D printing system each time larger objects are to be manufactured. Possible resolution methods include modular printed elements that can be installed on-site, as mentioned in Section 2.4.4. However, particular consideration is required for inter-member connections to ensure structural integrity. In-situ concrete fabrication methods have employed rail, movable frame and other translation strategies that allow printing setups to be moved around on-site to create continuously printed elements. Furthermore, Zhang et al. [43] proposed a 3D printing system consisting of a mobile robot team that can concurrently construct uniform parts. This promising method is illustrated in Fig. 2.7 and warrants further research on this topic.

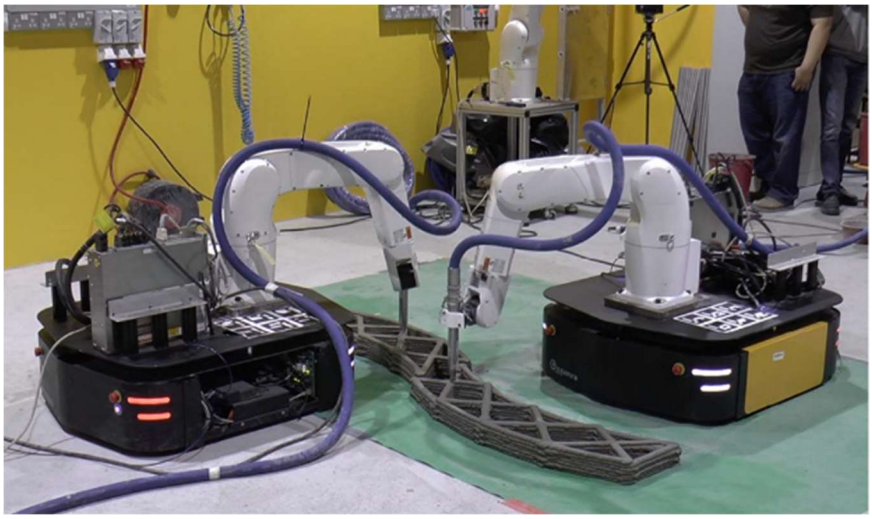

Fig. 2.7: Concurrent 3D concrete printing concept demonstrated by [43].

2.4.3.4 Lack of Standardised Protocols

Building code compliance presents another critical limitation for the espousal of large-scale automated concrete fabrication methods. The lack of standardised design and testing protocol is inherent to the novelty of this automated manufacturing procedure and the utilisation of anomalous cement-based composites [12]. Therefore, designers and regulatory bodies have no standardised design codes or guidelines for new design endeavours; thus, existing building codes and policies related to conventional manufacturing and construction techniques are adopted [44]. As large-scale DFC gains traction in the construction industry, specific design, fabrication and construction policies will need to be implemented. For this to realise, comprehensive mechanical and durability assessments are required if the necessary acumens regarding the long-term performance of 3DCP structures are sought [36].

Furthermore, owing to the rapid advances and esoteric nature of automated concrete fabrication technologies, existing construction materials are not suitable for extrusion-based systems; this necessitates the development of new material compositions and new compliance benchmarks [12,45].

Standardisation is also complicated by institutions that are unwilling to share the exact mixture of constituents and their proportions in fear of revealing their intellectual property. This is comprehensible but ultimately limits the broader adoption of the technology.

Additionally, standardised testing protocols are required to ensure that reproducible rheologic and mechanical assessment methods are introduced, which will aid both the development of new printable composites and demonstrate the appropriateness of existing mixtures. Concerning the development of standardised assessment criteria for rheo-mechanical [32] and mechanical performance, it should be noted that suitable design tools for buildability and structural analysis are imperative to the successful implementation of construction standards for 3DCP elements.

2.4.3.5 Reinforcement

Reinforced concrete (RC) has revolutionised modern infrastructure development, by providing tensile capacity and consequently ductility, to a quasi-brittle concrete matrix. Ductility, in turn, affords predictable local component and global system response, ensuring that buildings can effectively withstand an assortment of loading conditions. Considering that 3DCP extrudes predominantly cementitious pastes, incorporating reinforcement presents a critical aspect that should be addressed for large-scale adoption to persist. Asprone et al. [46] support this notion and state that for 3DCP technology to reach maturity, effective reinforcement integration strategies are mandatory.

Currently, methods to incorporate conventional reinforcement such as rebar, entrained polymer fibres and cables, as well as post-tension cables have been demonstrated [46–48]. Furthermore, it is suggested that the incorporation of passive reinforcement strategies can produce code-compliant structures [46]. The challenge is to bridge the interlayer interface and construct amalgamate concrete composites with the desired mechanical properties but still endorse the proposed advantages of automated construction. Recent focus has been directed towards methods that incorporate embedded reinforcement strategies that breach the interlayer interface [49–55]; however, deficient verification is presented regarding their performance. The absence of certified ancillary products, such as anchors, is a considerable impediment in the general structural use of DFC.

In a recent review, Bester et al. [33] present a systems approach for assessing 12 unique reinforcement methods. The methods are evaluated based on their degree of system integration and their ability to concurrently deliver the proposed benefits of 3DCP. The study reports that some methodologies are more appropriate to reinforcing particular objects than others. Evidently, reinforcement specifications will be case-specific.

2.4.4 Current 3DCP applications

Existing 3DCP construction applications can be subdivided into offsite (prefabricated) and in situ printed structures, respectively. The prefabricated 3DCP process utilises the concept of modular construction, where structures are produced in 'modules' that are erected and assembled on-site. The significant variation between modular construction and 3DCP of components is that the prefabrication of components is automated, which benefits quality and precision in conjunction with cost and time efficiencies. Nonetheless, the advantages associated with modular construction include increased quality and control, reduced waste production, fewer site disturbances and the possibility of building on a smaller footprint. Furthermore, by manufacturing elements in an industrialised factory setting, the potential to produce components for multiple projects arises, promoting overall efficacy since site and factory work can operate in tandem. Since the manufacturing process is automated, current eight-hour workdays are prolonged with no loss of efficiency or quality.

Additionally, opportunities for optimised project scheduling, on-time executions, and better preliminary cost estimations are envisioned to have a profound impact on the construction industry. Notwithstanding the aforementioned advantages of prefabricated 3DCP, challenges such as high initial capital investment requirements, unique considerations for connection detailing, the provision of installation utilities, and safe transportation methods need to be addressed to ensure the successful implementation and adoption of this technique. Demonstrated offsite 3DCP applications are illustrated in Fig. 2.8.

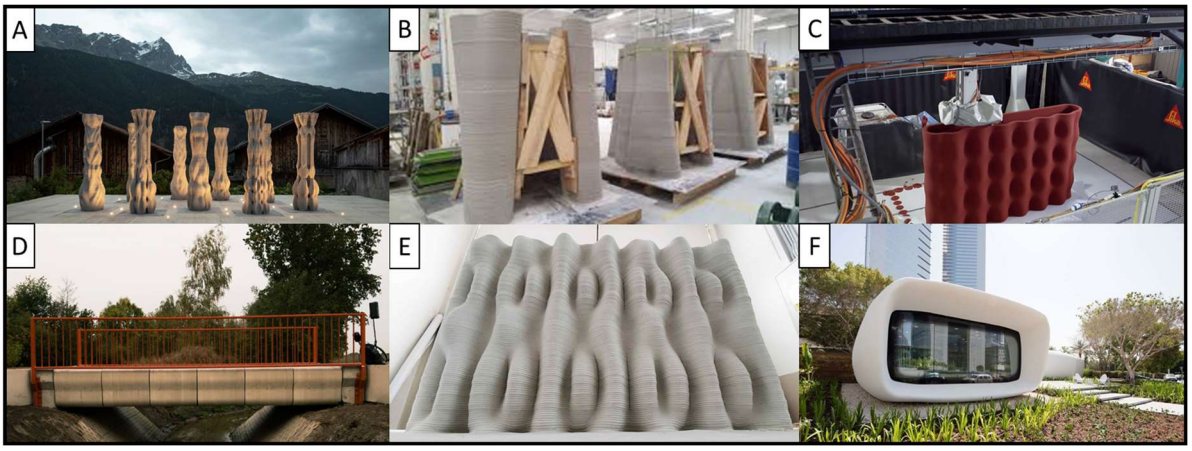

Fig. 2.8: Offsite 3D concrete printing examples. A) ETH Zurich – Concrete Choreography [56]*, B) XTreeE – Telecommunication Towers* [57]*, C) Sika – Flexible Shape for Concrete Structures* [58]*, D) TU Eindhoven and BAM Infra bowed* [59]*, E) BESIX 3D – DNA* [60]*, and F) Winsun – 3D Printed Office Park* [61].

Many private enterprises have effectively employed in situ printing; Fig. 2.9 presents examples of such endeavours. This approach has been preferred due to its seemingly instantaneous realisation of infrastructure, minimising waste, storage requirements and transportation costs. Furthermore, on-site

safety is improved via the automated construction process [62]. Labour productivity is increased via synergies of a human-mechanical workforce, ultimately augmenting and amplifying conventional construction procedures.

However, to create and control suitable environmental conditions for 3DCP, temporary structures must be erected over the constructed component or structure. This is considered an eminent constraint, hindering the scalability of on-site 3DCP construction. Although examples have been presented where in situ printing is conducted in the absence of temporary sheltering [48], this would most certainly reduce the efficiency of the project in the case of weather delays and reductions in the integrity of the structure due to improper curing.

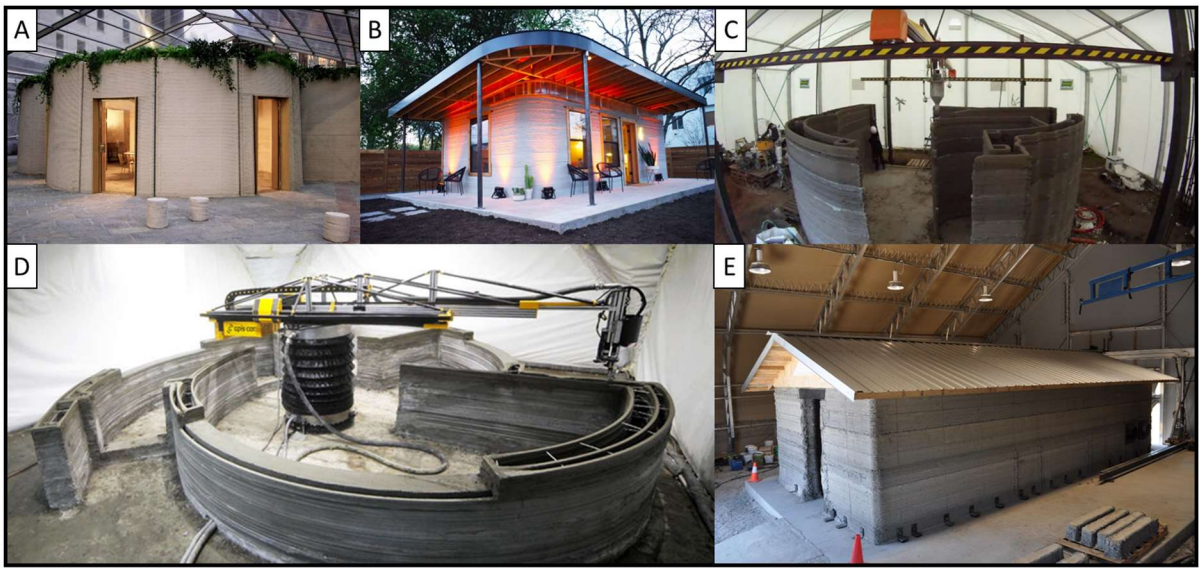

Fig. 2.9: On-site 3D concrete printing examples. A) Arup – 3D housing 05 [63]*, B) ICON – The First 3D-Printed Home in America* [64]*, C) 3D Printhuset – Printing for Building on Demand (BOD)* [65]*, D) Apis Cor - $10,000 house in 1 day* [66]*, and E) US Army Engineering Research and Development Center* [67]

Menna et al. [68] present a review of documented structural applications of DFC and report that DFC is being implemented in general-use structures such as short-span bridges, entire buildings printed in situ, and freestanding structures/components. The number of executed DFC examples is increasing rapidly and is contended to continue, considering the amount of newly announced projects [68]. Currently, extrusion-based 3DCP seems the most widely implemented process methodology for large scale DFC. Table 2.1 presents a summary of additional structural extrusion-based 3DCP projects that have been undertaken in the period between 2014 and 2020, which are not all presented in Fig. 2.8 and Fig. 2.9.

Table 2.1: Implemented structural extrusion-based 3DCP projects. Adapted from [68] *and extended.*

Project description	Location, year	Fabricator	Process type	Product type	Ref.
3D-Printed Concrete Castle	USA, 2014	TotalKustom Total	Extrusion	Building/house	[69]
Leward Grand Hotel, Hotel Suite	Angeles City Pampanga, The Philippines, 2015	TotalKustom Total, USA	Extrusion	Building/house	[70]
Office Building	Dubai, 2016	Winsun, China	Extrusion	Building/house	[71]
Krypton Post	Aix-en-Provence, France, 2016	XtreeE, France	Extrusion	Structural element	[72]
USH Sinusoidal Wall	Paris, France, 2016	XtreeE, France	Extrusion	Building component	[73]
R&Drone Laboratory	Dubai, 2017	CyBe, The Netherlands	Extrusion	Building/house	[74]
Bicycle Bridge	Gemert, The Netherlands, 2017	TU/e, The Netherlands	Extrusion	Bridge structure	[75]
Apis Cor Printed House, Russia	Moscow, Russia, 2017	Apis Cor, Boston, USA	Extrusion	Building/house	[66]
Maison Concept YRYS	Alençon, France, 2017	XtreeE, France	Extrusion	Building/house	[76]
Stormwater Collector	Lille, France, 2017	XtreeE, France	Extrusion	Infrastructure component	[77]
3D Housing 05	Milan, Italy, 2018	Italcementi with CyBe, Italy	Extrusion	Building/house	[78]
The BOD	Denmark, 2018	COBOD, Denmark	Extrusion	Building/house	[79]
Gaia	Italy, 2018	WASP, Italy	Extrusion	Building/house	[80]
3D-Printed Concrete Pedestrian Bridge	Shanghai, China, 2019	Tsinghua University (School of Architecture)	Extrusion	Bridge structure	[81]
'De vergaderfabriek', Meeting Room	Teuge, The Netherlands, 2019	CyBe, The Netherlands	Extrusion	Building/office	[82]
Cohesion Pavilion	Innsbruck, Austria, 2019	Increamental3D, Austria	Extrusion	Architectural element	[83]
Building Apis Cor, Dubai	Dubai, The UAE, 2019	Apis Cor, Boston, USA	Extrusion	Building/office	[84]
3D-Printed Community	Tabasco, Mexico, 2019	ICON, USA	Extrusion	Building/house	[85]
3D-printed Post-tensioned Concrete Girder Designed by Topology Optimisation	Ghent, Belgium, 2019	Ghent university (Concre3DLab), Belgium with vertigo, The Netherlands	Extrusion	Bridge structure	[86]
32 m^2 house	Benguérir, Morocco, 2019	Be More 3D, Spain with Polytechnic University of Valencia	Extrusion	Building/ house	[87]
175 m^2 house	Long island, USA, 2019	SQ4D	Extrusion	Building/house	[88]
Community First! Village	Austin, Texas, USA, 2020	ICON and logan Architecture	Extrusion	Building/house	[89]
Prvok	Ceske Budejovice, Czech Republic, Prague	Michal Trpak, Scoolpt	Extrusion	Building/house	[90]
Kamp C 2-Storey House	Westerlo, Belgium	Kamp C and COBOD	Extrusion	Building/house	[91]

2.5 Fundamental Design Considerations for 3DCP

3DCP engages the building material in the transition from fluid to solid phase [17], hence the interrelation between material, process, and design particularities and how they affect the quality and integrity of the manufactured product are pertinent issues in 3DCP [68]. Originating from the (partial) absence of formwork that defines most DFC processes, new challenges arise in the field ranging from material design (including reinforcement), process and hardened-state modelling, quality control, and product application.

As mentioned by Bos et al. [17], "The complete interaction between, design, material, process, and the product need to be rethought". In this light, Fig. 2.10 presents a framework illustrating the fresh-state and hardened-state design considerations for 3DCP and shows the influence of the interlinking process, material, and product properties and requirements within the design space. The following section presents the "*consideration pyramid*", and detailed descriptions of the individual fresh and hardened-state tetrahedra follow. The premise for the extension of the diagram presented by Bos et al. [17] resides in the structural application of extrusion-based 3DCP, where fresh and hardened-state design considerations are nonexclusively correlated and often competing by nature. These considerations and their consequences are essential to the performance of the components or structures, and a holistic understanding of the underlying concepts is required to comprehend the content covered in Chapters 3-6. For the reader's benefit, these underlying concepts are presented upfront.

2.5.1 Fresh-state design considerations

Fresh-state design consideration revolves around the physico-chemical phenomena exhibited by printable mixtures, the structural integrity of the printed product, and the fabrication constraints. All these aspects are influential on the hardened-state mechanical performance and therefore affect the associated design considerations.

2.5.1.1 Material-process-product

The physico-chemical phenomena exploited in 3DCP operate in the triangle of material-process-product, and here consideration should be lent to the mix design; the resulting rheological (thixotropic) parameters; that affect the structural build-up of the material; and therefore, effectively which printing parameters can be used; to ensure that the mixture is pumpable, extrudable, and ascertains the required buildability for high-rate digital fabrication [38,92]; with an acceptable surface finish.

Mix design: When designing the printable material composition, engineers should consider the particle packing density, the material constituents utilised (referring to their physical properties, availability, and embodied energy) [17], if reinforcement will be entrained, and whether accelerators and retarders are required [30].

Rheological parameters: The rheological parameters are a direct result of the mix design employed. Here thixotropic factors such as the rate of reflocculation (R_{thix}), structuration rate (A_{thix}), dynamic shear yield stress evolution over time, and material open time are of interest [41]. Consideration should be directed towards balancing the aforementioned to ensure that the printable material attains the desired rate of structural build-up while remaining pumpable and extrudable.

Structural build-up: The structural build-up of 3DCP materials is well described in [28] and affords the freshly deposited filament a certain level of shape retention and buildability [93]. Buildability affects the rate at which the object can be fabricated, and shape retention affects the aesthetic quality of the fabricated component [41]. Again, if structural build-up proceeds too rapidly, the plastic viscosity increases, and the mixture's pumpability and extrudability are compromised [32]. It is also apparent that the rate of structural build-up influences interlayer adhesion [94].

Printing parameters: The printing parameters of interest include the layer height, nozzle standoff distance, nozzle velocity, and extrusion rate. Suitable numerical and computational modelling approaches that can be employed for optimisation procedures are presented in Section 2.7.1. Additionally, depending on whether a continuous or discontinuous print path is employed, appropriate seam locations should be prescribed. The selection of appropriate printing parameters is material and system-dependent and should be optimised to negate fresh state collapse [92,95–97] and ensure suitable interlayer adhesion [98].

Pumpability, extrudability, and buildability: Pumpability refers to the capability of the mixture to be mobilised and remain stable under pressure without segregating. Considering that viscous mixtures are employed in 3DCP, one must ensure that the pump has sufficient capacity and that segregation of water and fines from the bulk plastic mixture does not occur [32]. Pumpability is related to all the items above and limits the maximum aggregate/particle size and practicably entrained fibre lengths. Extrudability is coupled to the rheological and printing parameters, where a high nozzle velocity and low extrusion rate cause filament tearing and horizontal forces, and a low nozzle velocity and high extrusion rate cause layer bulging and compressive forces [38]. Unbalanced extrusion is shown to augment the microstructural morphology and surface roughness of filaments [99] and imposes the risk of air entrapment which negatively affects the IBS [42]. Buildability refers to the ability of a material to resist the weight of successively deposited filaments during the 3DCP process. Therefore, this metric is a crucial consideration in a formwork-free additive manufacturing process as it affects the vertical building rate [28].

Surface finish: Filament surface finish is a primary aesthetic consideration, which is linked to the printing parameters, paste viscosity (filament shape retention), and the mix design (aggregate size and presence of fibres) employed.

2.5.1.2 Design-material-product

Fresh-state consideration in the triangle of design-material-product relating to the structural integrity of the manufactured product comprises the material open time, layer pass time, interlayer bond strength, and the incorporated reinforcement to hinder plastic shrinkage cracking.

Material open time: The open time of a material refers to the initial setting time of the mixture, whereafter the material transitions from the fluid to the solid state [32]. Evidently, this metric dictates the utilisable material timeframe in which successful 3DCP can be performed and dictated by the structural build-up of the material [28].

Layer pass time: Layer pass time refers to the time increment between successively deposited filaments and is dictated by the object geometry and print speed [92]. The consideration of appropriate layer pass times is paramount to the structural integrity of the printed product since a layer pass time exceeding the material open time results in cold jointing [100,101]. Cold jointing has the consequence of reduced IBS [42] and durability [102] performance and should be considered when generating print paths for large scale applications.

Interlayer bond strength: IBS is arguably the most significant contributing factor to the anisotropic mechanical properties in 3DCP [42]. However, it is reported that in the fresh-state interlayer bond is also critical from a buildability perspective [103]. Additionally, improper interlayer adhesion increases the likelihood of interlayer delamination due to differential plastic (free) shrinkage [104].

Entrained reinforcement: It has been demonstrated that 3DCP elements are particularly susceptible to plastic shrinkage, resulting from the lack of formwork, minimal bleeding water, low aggregate to binder ratio and high quantities of fines in the mixture [104]. As a result, compatible reinforcement strategies such as well dispersed microfibres are required to mitigate the risk of plastic shrinkage cracking, particularly in harsh environmental conditions and when restraint is present [105].

2.5.1.3 Design-process-product

Fresh-state consideration in the triangle of design-process-product relating to the fabrication constraints of the manufactured product comprises the fabrication setting, required manufacturing tolerances, object geometry, print path, process parameters, and how these features affect the buildability of the 3DCP product.

Fabrication setting and tolerances: Whether the 3DCP element/structure is fabricated in situ or in a factory setting poses pertinent consideration attributes pertaining to the environmental conditions and quality control of the materials and printing process. In an offsite fabrication setting, the element/structure is subject to variable humidity, temperature, and evaporation conditions that are known to affect the quality of the printed object heavily. Additionally, high wind speeds could

compromise deposition accuracy or deform the non-cured elements inducing instability issues [95] if no wind screening is provided. In contrast, the environmental conditions in offsite printing can be controlled, and the quality assurance of materials and component geometric tolerances are contended to be higher.

Print path, process parameters, and buildability: Constructability design models [92,95,96] or fresh-state FE simulation methods [97,106–111] should be consulted to determine suitable print path, speed, and filament layer height combinations that render rapid vertical building rates while ensuring the successful construction of the element/structure. Literature consultation reveals that the underlying physics of flow, pumping, part behaviour during printing, and time-dependent fresh-state material properties are well understood but require extensive consideration [38]. Nonetheless, this provides a solid basis for optimising process conditions, such as maximising the print speed, minimising the material needed for successful 3DCP, and conformity to specific manufacturing tolerances [17].

2.5.2 Hardened-state design considerations

In the hardened-state, design consideration revolves around the ensuing microstructural morphology, the structural capacity of the printed product, and the fabrication constraints. Menna et al. [68] provide a comprehensive review of this topic from a structural engineer's perspective, including a notable section, Section 2.2. therein, where Hans Laagland of Witteveen + Bos Consulting Engineers shares his insights.

2.5.2.1 Material-process-product

In the triangle of material-process-product, hardened-state design considerations are dictated by the ensuing microstructural morphology of the printed element/structure. As extensively covered in Chapters 5 and 6, the 3DCP process influences the microstructural morphology. It is known that constituent type, constituent proportion, porosity content and void topology affect the bulk strength and elasticity of a porous medium. Therefore, the influence of porosity on the anisotropic mechanical properties and durability performance of 3DCP components is a central consideration.

Durability: It is apparent that the interconnectivity of voids (or permeability) is highest at interlayer locations [102,112,113]. Such findings hold significant implication for both durability and mechanical capacity. Prolonged interconnected pore systems establish transportation networks for water, chloride or oxygen and carbon ingress, which impact durability. Even if interlayer regions are mechanically reinforced [33], premature cracking and interconnectivity will allow aggressive chemical corrosion compounds to reach the reinforcement items and deteriorate their capacity [42]. If extensive interlayer pore interconnectivity persists, structural designers should reconsider appropriate concrete cover depths or the use of external sealants to mitigate the imparted adverse effects.

Porosity: Resulting from the variation in fresh-state properties and manufacturing processes, the air void systems in 3DCP differ from their conventionally cast counterparts. This is ascribed to the more viscous mixtures employed in 3DCP, the fact that no compaction or vibration is present after deposition, and the effects of pumping [27,38]. Reduced porosity is empirically related to higher compressive strength [114]. The presence of entrapped air voids is shown to create a network of macro defects that prompts localised weak points that reduce concrete strength [115]. Evidently, material design endeavours should consider methods to reduces the porosity in 3D printed concrete.

Void topology: Irregularly shaped but approximately ellipsoidal pores within filament inter and intralayer matrices have been observed and quantitatively evaluated [112]. It has been shown that larger air voids are located at interlayer locations, with a more significant number of small to medium-sized air voids found randomly dispersed within extruded filaments [116]. Such effects profoundly influence the mechanical characteristics (strength, elasticity, and failure patterns) of concrete printed elements due to the effects of stress concentrations at void boundaries and the deformability of certain topological configurations (see Chapters 5 and 6).

Spatial uniformity: Mechanical anisotropy in 3DCP is a consequence of the inadequate adhesion between vertically stacked and horizontally adjacent filaments, which by and large originates from air entrapment during filament stacking [42,117] and the nonhomogeneous features of porosity (defects) in and in-between filaments [99,112,116]. Such aspects affect the reliability of the mechanical properties attained and require careful consideration in structural modelling with customised material properties [68]. Additionally, a detailed risk inventory is necessary to reduce the probability of failure in practice [68].

2.5.2.2 Design-material-product

Hardened-state considerations in the triangle of design-material-product relating to the structural capacity of the manufactured product comprise the imposed loading, curing conditions, anisotropic mechanical properties, interlayer bond strength, reinforcement specifications (type, detailing, and bond), and code compliance.

Imposed loading: As in conventional RC construction and design, the loading imparted on the element/structure dictates the proportions and required characteristic material properties to ensure that a rational design approach is followed under serviceability and ultimate loading states, to guarantee the essential performance requirements to protect the citizen [68]. Within the 3DCP design space, engineers should consider how the structural/component topology should be comprised to sustain the imposed loading conditions, rendering the design fit for its intended purpose whilst upholding the advantages of 3DCP presented in Section 2.4.2.

Curing conditions: Proper curing is critical to the hydration kinetics of cementitious compositions and affects the mechanical capacity of the employed materials. Again, the fabrication setting becomes relevant and influences the quality assurance of the material. Alternatively, appropriate curing provisions should be provided. The material characteristics should thus be specified with the fabrication setting in mind (e.g., either larger sectional geometries or more robust materials are required in offsite printing applications for suitable strength gain).

Anisotropic mechanical properties: Stemming from the augmented air void systems and entrained reinforcement methodologies encountered in 3DCP components, anisotropic mechanical behaviour in compression, tension, flexure, and shear is prominent [34,42,101,118–125]. Additionally, local stability and strength effects such as local and plate buckling have become highly relevant and possibly governing [68]. From a design perspective, load orientation concerning the characteristic material axis should be considered. Clearly, this necessitates the advent of anisotropic yield criteria for extensive non-linear FE analysis procedures and directionally dependant design protocol. Furthermore, whilst generating the print path to meet the component/structural topology, designers should consider configurations that harness the maximal functionality of the technology. Here factors such as modular construction (allowing the extrusion and layering direction to be altered according to the principal stress directions) and non-planar print paths become attractive [13].

Reinforcement specification: In a recent review, Bester et al. [33] present a systems approach for assessing 12 unique reinforcement methods. The methods are evaluated based on their degree of system integration and their ability to concurrently deliver the proposed benefits of 3DCP. The study reports that some methodologies are more appropriate to reinforcing particular objects than others; evidently, reinforcement specifications will be case-specific. Designers should consider when the reinforcement is incorporated (before, during, or after printing), as well as the mechanical capacity, failure mechanisms, anchorage, and bond characteristics of the reinforcement.

Code compliance: In the absence of extensive knowledge and confidence from personal experience, codes, and guidelines, an approach that significantly deviates from the industry norm is required [68]. Presently, Annex D of EN-1990 [126] provides a standardised procedure to support design by testing; this procedure is outlined for a post-tensioned bridge and discussed by Menna et al. [68]. Additionally, *fib Task Group 2.11 Structures made by digital fabrication* has been established to provide testing and design guidelines for DFC to describe preliminary structural code prescriptions. These preliminary structural code prescriptions will likely take on annexes to *fib* Model Code 2010/2020 and aim to comply with ISO 22966:2009 – Execution of concrete structures [127]. Additionally, existing standards, such as EN 1996-1-2 for reinforced and unreinforced masonry, or EN 1996-1-1 for load-bearing walls, could present feasible analogies to the 3DCP design space. Chapter 4 demonstrates how computational

modelling strategies can be employed to verify the conformity of a component or structure to the above-listed standards, amongst others.

2.5.2.3 Design-process-product

Hardened-state consideration in the triangle of design-process-product relating to the fabrication constraints of the manufactured product comprises the fabrication setting, required tolerances, object geometry, structural topology, size of the printing facility, constructability, transportation to site, and installation on-site.

Manufacturing tolerances: Resulting from the interrelated fresh-state particularities presented in Section 2.5.1, manufactured components/structure often deviate from the computer-generated model., which has implications for the design and analysis of the manufactured components. For instance, the entire filament cross-section does not adhere to upper and lower filaments (reference Chapter 4); therefore, the material density must be artificially increased to account for the additional self-weight, but the section width cannot be increased because this provides a non-conservative increase in stiffness [68] and resistance. Additionally, fresh-state settlement, partial buckling type deformation (without collapse), and process deposition inaccuracy would increase the '*out-of-straightness*', or P-delta, effects in the case of axial loading and lead to premature buckling of the member [95–97]. Finally, over extrusion could decrease the utilisable cavity size provided for services and reinforcement ducts, which negatively affects installation ease and impair buildability performance.

Setting: In the hardened-state, the fabrication setting requires consideration pertaining to the environmental (curing) conditions that influence the deposited material's long-term strength gain and durability. In a factory setting, various curing methods such as steam curing, ponding, saturated coverings, wrapping, coating with membrane compounds, and fogging are feasible, whilst on-site, mainly saturated coverings, coatings, and fogging are possible but require supervision.

Object geometry/structural topology and the size of printing facility: The object/structural topology is limited to the size of the 3DCP facility and, if it exceeds the build volume, requires modularisation. The wealth of knowledge contained in the prefabrication industry should be applied to determine suitable locations for intercomponent discontinuities and connection detailing. Additionally, in on-site fabrication settings, the advent of mobile printing facilities, shown in Fig. 2.4, might present an opportunity to extend the building envelope of the facility.

Constructability: Although this feature is not exclusive to extrusion-based 3DCP and resonates with general construction considerations, the constructability of the component assembly or structure should be considered. The insertion of passive reinforcing strategies, temporary formwork provisions at openings, and accessibility to service and grouting ducts should be considered during the structural

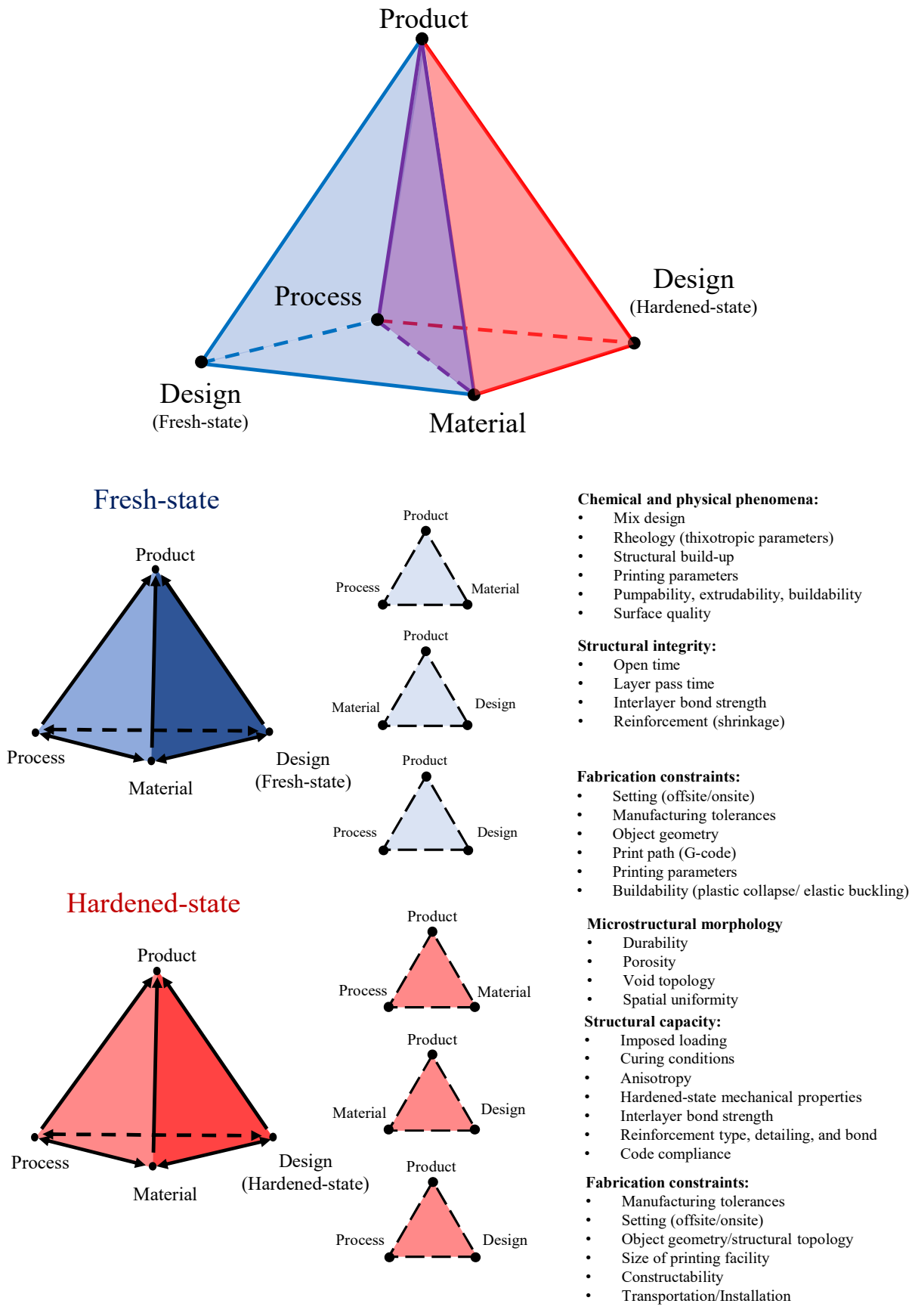

Fig. 2.10: Diagram illustrating the concurrent consideration of fresh-state and hardened-state design considerations and the influence of interlinking process, material, and product properties and requirement.

design phase. These aspects will influence the geometry and thus the print path of the object, which should again be considered in the fresh-state design.

Transportation and installation: The transportation and installation feature is primarily applicable to offsite printing applications. Here designers should specify safe transportation procedures and provide suitable fastening and damage prevention solutions. Additionally, the maximum transportable size of elements should be considered to negate the costs associated with utilising abnormally sized vehicles (if possible). Furthermore, appropriately positioned and detailed hoisting points are required for lifting and installation activities. Site access for the establishment of cranes, or other installation machinery, should be provided. Apt temporary support provisions should be specified to ensure safety during the installing and curing phase. Quality control specifications should be set and met. Finally, discontinuities should be appropriately sealed to prevent leakages.

2.6 Hardened-state Properties of 3D Printable Cementitious Materials

3DCP operates as a unique paradigm within the realm of concrete construction; therefore, novel cement-based composites are required to realise digitally fabricated components. Due to the interrelation between the process particularities presented in Section 2.5, the hardened-state mechanical properties are dictated by the mixture's fresh-state material, process, and design properties. Chapter 3 presents a detailed discussion on the hardened-state mechanical attributes in extrusion-based 3DCP. However, in brief, most hardened-state material characterisation endeavours have focused on macroscale characteristics [42,119–123,125,128–132] and a few investigations have aimed to determine the microstructural and interfacial properties [100,101,124,133,134]. Microstructural characterisation of 3DCP materials via X-ray computed tomography and surface scanning techniques is presented in [99,112,116,117,130] and discussed in Chapters 5 and 6. The mechanical parameters relevant to this study are presented below:

2.6.1 Interlayer bond and bulk tensile strength

As a result of the discrete layer deposition procedure employed in 3DCP, weak interlayers are often formed between subsequently and adjacently deposited filaments. The adhesion dictates the IBS between layers, which is related to a multitude of factors that constitute an intricate combination of mechanical interaction, chemical bond and intermolecular forces between filaments, as shown in Fig. 2.11. More specifically, factors such as surface moisture, air entrapment, thixotropy, and surface roughness are reported and reviewed at length by Kruger et al. [42]. Additionally, the bulk material tensile resistance in the extrusion direction is of interest to attain the level of anisotropy (LOA) and prescribe suitable anisotropic constitutive relations.

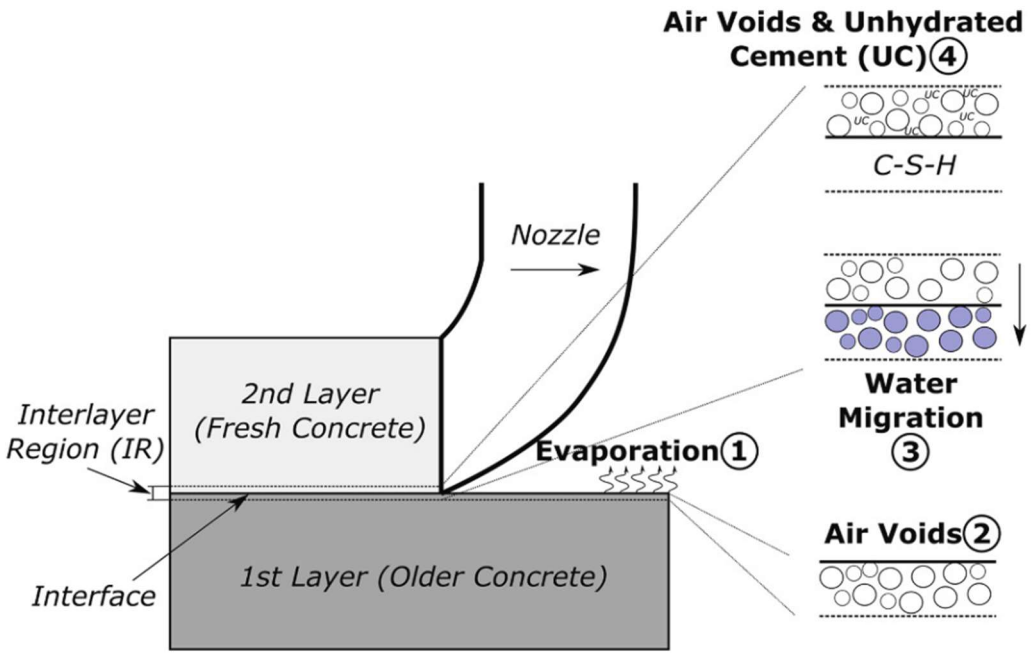

Fig. 2.11: The loss of surface moisture on the previously deposited filament resulting from evaporation, resulting in air voids, which suck water from the newly deposited filament due to capillary absorption, yielding increased porosity, permeability, and anhydrous cement in the interlayer regions, which reduces interlayer adhesion. Reproduced from [42].

2.6.2 Compressive strength

It is widely reported that 3DCP elements display anisotropic behaviour in compression (f_{cu}) with the capacity in the layer stacking direction often lowest and highest in the extrusion direction [42]. This necessitates the determination of the compressive resistance about the orthotropic axes of the material to evaluate the LOA. It is widely agreed that the reduced interlayer capacity affects the compressive capacity of composite configuration [42]. However, the origin and fundamental mechanisms are still disputed. Paul et al. [12] ascribe this phenomenon to interlayers failing in tension due to Poisson's effects, Nerella et al. [101] contend that the extent of the (weak) interface area lying beside the tri-axial compressive zone, and the size of individual defects located at the intersection of shear planes are decisive factors. Xiao et al. [135] corroborate these assertions via a parametric FE study, stating that lateral expansion results in interfacial shear-slip between filaments. From this research, it is apparent that when the tangential orientation of the interlayer region aligns with the direction of lateral expansion, the compressive capacity is affected most. In Chapter 5, it is demonstrated that defect and pore morphology, localised increases in porosity, and the orientation of interlayer regions with respect to loading affects the compressive capacity. Note that in this dissertation defects are considered the consequence of either (i) entrapped air, causing large, irregular voids or (ii) surface tears caused by under-extrusion and pores comprise entrained air, in the form of dispersed air voids, which are incorporated by mixing and pumping processes.

2.6.3 Shear strength

Anisotropic shear strength (f_s) is also observed in additively manufactured concrete, which is expected since shear is a combination of competing tensile and compressive principal stresses, which are reportedly anisotropic as presented above [118]. The shear capacity of cementitious materials is proportional to the normal stress applied to the fracture surface and the intrinsic material resistance to shear or cohesion. To this end, the Mohr-Coulomb failure criterion is most often employed for civil engineering applications [136]. However, as presented in Chapter 6, the Mohr-Coulomb failure criterion is not suited to all cementitious materials and for the particular FRPC utilised in this research a non-linear modified Mohr-Griffith criterion more aptly describes the constant compression-shear performance.

2.6.4 Tensile and flexural strength

Similarly, 3DCP samples display directionally dependant tensile (f_t) and flexural capacities when loaded parallel or orthogonally to the interlayer interface, with the parallel loading direction depicting the lowest flexural resistance and orthogonal loading depicting the lowest tensile strength. This phenomenon is ascribed to the reduced interlayer capacity and a unidirectional increase in the intralayer capacity resulting from preferentially aligned fibre entrainment or cable reinforcement in the extrusion direction [42].

2.6.5 Fracture energy

Fracture energy (G_f) is the energy required to open a unit area of crack surface [137]. Since this parameter is normalised to a unit area, the size influence is nullified. Four independent fracture energies (compressive and tensile) are required to describe the non-linear strain-softening behaviour for the non-linear orthotropic computational analysis procedures presented in Chapter 4.

2.6.6 Elasticity

The elastic, or Young's, modulus (E) is the measure of the resistance of the material to elastic deformation under loading and is a fundamental parameter in the structural design of buildings. Therefore, Young's modulus in the respective material axes is sought for design consideration. Resulting from the mortar-like materials generally employed in 3DCP, with high paste-to-aggregate ratios and aggregate sizes less than 4 mm, lower elastic moduli are observed.

2.6.7 Poisson's ratio

Poisson's ratio (ν) describes the transverse strain to longitudinal strain ratio in a specimen subject to elastic axial loading. This value is dimensionless, unique to the material utilised and is generally assumed equal in compressive and tensile stress states. For normal strength concrete in the hardened-state, a value of 0.2 is often taken without detailed experimental data [138].

2.7 Numerical Analysis and Computational Modelling of 3D Printed Concrete

Numerical analysis and computational modelling afford critical insight into the multiple, multiscale, and multi-physics (physical and chemical) phenomena that constitute the final material properties and permits the exploration of an infinitely large design space resulting from the intrinsic parametric capabilities [16]. To date, significant interest and progression are seen in the fresh-state numerical simulation of 3DCP. However, literature relating to the computational evaluation and simulation of the hardened-state mechanical performance of concrete printed components is sparse.

2.7.1 Fresh-state numerical simulation procedures

Analytical buildability models have been presented which elucidate the fundamental mechanisms responsible for fresh-state constructability performance [95–97,139]. By means of a comparison with various 3DCP experiments and FEM simulations it has been demonstrated in [95–97] that the referenced parametric model is able to accurately predict the elastic buckling behaviour and plastic collapse behaviour of various straight forward configurations (e.g., single wall, rectangular and square layouts). Further the model can be applied for a a-priori, efficient estimation of safe 3D printing design conditions for practical, geometrically complex structures, as demonstrated in the last example presented in [95]. Moreover, the plastic collapse model proposed by Suiker [96] can be applied for arbitrary 3D printed configurations, as it is geometrically independent. Contrastingly, Bos et al. [17] suggest that such models generally fall short in predicting the actual behaviour of complex geometries.

Khan et al. [16] present a detailed review pertaining to the current advances in the development of numerical methods to address the shortcomings of analytic methods. Therein attention is directed towards material models, multiscale models, physics-driven models, and data-driven models, which showcase tremendous potential. Roussel et al. [111] review available numerical methods for the modelling of extrusion-based 3DCP and assess their potential to evaluate and optimise material and process particularities. It is shown that Computational Fluid Dynamics modelling is capable of simulating the complex effects of flow, extrusion, and shape retention [16]. Additionally, notable FE modelling procedures have been proposed which are capable of predicting fresh-state buildability performance [106,107,109,110]. From these contributions, it is established that numerical modelling methods are able to predict the fresh-state failure-deformation performance accurately, as well as the critical height at which failure (elastic bucking and/or plastic collapse) occurs for relatively small objects [111]. In contrast, numerical prediction accuracy declines for larger objects and/or longer printing processes [111]. Such observations are ascribed to the effect of friction induced thermal heating of the 3DCP system over long printing durations, which has currently not yet been incorporated in the experimental fresh-state characterisation procedures nor numerical analyses [97].

2.7.2 Hardened-state computational modelling procedures

Resulting from the anisotropic material properties exhibited in 3DCP compatible computational modelling strategies are sought. These modelling strategies are therefore required to capture directional dependence to specific loading configurations. Currently, there are three main methods to simulate anisotropy computationally: (1) anisotropic continuum smeared cracking macro-models, (2) the combination of discrete interface elements, with either elastic or isotropic inelastic continuum, smeared cracking elements (micro-modelling), or (3) discrete element modelling methods. The following section presents the methods implemented within the 3DCP context and discusses their suitability.

2.7.2.1 Anisotropic continuum smeared cracking macro-models

Anisotropic continuum macro-models have been proposed for the computational simulation of masonry structures and other layered structures and are implemented in FE simulations packages, such as DIANA FEA [140] and ATENA FEA [141]. DIANA FEA contains an anisotropic Rankine-Hill cap plasticity continuum crack model, presented by Lourenco et al. [142] and ATENA FEA contains a similar Rankine-Menétrey-William material constitutive formulation [143], and an anisotropic damage-based Tsai-Wu formulation [144]. These models cannot distinguish between filament layers and interfacial regions. Instead, a smeared cracking approach is adopted where the inelastic deformation within continuum elements approximates deformation patterns. This approach entails significantly reduced modelling and computational efforts compared to 3D solid, interface-based, and discrete element simulations; however, the location of the interlayer plane is not explicitly definable. Note that these formulations only hold for planar applications as the influence of the out-of-plane direction is generally unknown. This is not considered a severe limitation within the 3DCP context since the formulations are compatible with curved shell elements that resonate with the shell-like geometries typically fabricated using the technology.

To date, no continuum anisotropic computational simulation procedures for DFC are reported in the literature, other than the Rankine-Hill plasticity model, which is implemented in Chapters 3 and 4. The detailed deliberations applicable to its implementation are discussed in Section 4.2.1.

2.7.2.2 Discrete interface element micro-models

Discrete interface element micro-models, often termed cohesive zone modelling, predict the onset of failure and its growth within regions of continuous materials or interfaces between different materials, resulting in more detailed results [145]. Such functionality appeals to the research conducted in this dissertation since the weak interlayer interface between successively deposited filaments is synonymous with the aforementioned failure phenomena. The manner in which the cracks propagate is controlled by constitutive cohesive laws denoted as traction-separation laws. These phenomenological laws quantify the extent to which an interface can be stressed or deformed before yielding, its behaviour

after yielding, and the attainable maximum stress, or deformation, magnitude before final fracture (or delamination) occurs [146].

Lourenco et al. [147] present an interface elastoplastic constitutive model for modelling masonry structures, which can be extended to the 3DCP framework (see Chapter 4). The non-linear interface element material model is assigned a Coulomb-friction envelope for shear failure, is limited by a tension cut-off for tensile failure, and a cap model for compression failure. Additionally, softening behaviour is widely reported as a principal characteristic in quasi-brittle materials and is therefore implemented in all failure modes, with the compression regime preceded by hardening. The reader is directed to Section 4.2.2 for more detailed elaborations on the proposed micro-modelling framework.

The advantage of these methods resides in the fact that the locations of discontinuities are explicitly definable and that such a method can be paired with a host of constitutive relations describing the bulk material, such as elastic, damage-plasticity, isotropic total-strain based continuum formulations, or anisotropic continuum formulations accounting for intralayer anisotropy. Cohesive interface elements are also suitable for 2D and 3D analysis procedures.

Considering computational analysis in DFC, the fissile nature of 3DCP components is characterised by van den Heever et al. [118] and the interlayer tensile failure mode is computationally simulated via the cohesive zone method. A maximum stress traction-separation damage initiation criterion is implemented, accompanied by an energy-based mixed-mode fracture criterion. This strategy yields solid agreement with the experimental results. Xiao et al. [135] considered the interfacial bond properties via a maximum displacement-based traction-separation law combined with the Concrete Damage Plasticity material model for the bulk concrete. The strategy is employed to conduct a parametric analysis on the influence of nozzle dimensions, interfacial bond strength and bulk concrete material properties on the response of the composite in compression and flexure. This study demonstrates the value of parametric analysis to elucidate the mechanics of failure in 3DCP.

2.7.2.3 Discrete element modelling

In discrete element modelling, heterogeneous materials are modelled using discrete particles with bonding between them. Newton's second law determines the motion of the particles, and interaction laws define the behaviour between particles. Such a modelling strategy is highly detailed, albeit reportedly computationally expensive [148].

Wang et al. [34] explored the discrete element method to numerically simulate the failure mechanisms of 3D printed lightweight concrete elements with hollow sections. The authors conclude that discrete element modelling is an effective strategy to assess the mechanical behaviour of a cellular component, with positions and orientations of macrocracks well correlated to the experimental results. Valle-Pello et al. [148] provide a discrete element model to predict the mechanical behaviour of 3DCP

members. Here a novel discrete model of a multilayer geometry is presented where filaments comprise randomly placed particles to simulate the heterogeneous nature of concrete. The numerical model is developed to simulate the flexural behaviour of multilayer specimens and fair agreement with the experimental results is found.

2.7.2.4 Other computational methods employed in 3DCP

In contrast to the anisotropic computational methodologies presented above, isotropic damage-based and elastic-maximum stress initiation methods have been proposed.

Bos et al. [132] investigated the ductility of 3DPC reinforced with short steel fibre, which employed the renowned Concrete Damage Plasticity material model of Abaqus to simulate the flexural response of 3DCP beams with reasonable agreement. Feng et al. [123] implemented a FE analysis procedure, founded on the experimentally determined compressive stress-strain response and a maximum stress criterion, to investigate the effect of printing direction on the load-carrying capacity of a 3D printed arch structure.

However, these methods are suitable to simulate the structural response of members, that exhibit principally dominated pure modes of failure and will misrepresent the structural response of members subject to multifaceted failure mechanisms.

2.8 References

[1] A. Luxien, N. Reynecke, J. Mahachi, 3D-PRINTED HOUSES PILOT PROJECT Research Report 1 : Pre-production Phase, 2020.

[2] McKinsey & Company, Re-inventing Construction In Brief, McKinsey & Company. (2017).

[3] A.O. Windapo, K. Cattell, The South African construction industry: Perceptions of key challenges facing its performance, development and growth, Journal of Construction in Developing Countries. 18 (2013) 65–79.

[4] Y. Weng, M. Li, S. Ruan, T.N. Wong, M.J. Tan, K.L. Ow Yeong, S. Qian, Comparative economic, environmental and productivity assessment of a concrete bathroom unit fabricated through 3D printing and a precast approach, Journal of Cleaner Production. 261 (2020) 121245. https://doi.org/10.1016/j.jclepro.2020.121245.

[5] UNIDO, Industrial Development Report 2009, 2009. http://www.worldcat.org/title/breaking-in-and-moving-up-new-industrial-challenges-for-the-bottom-billion-and-the-middle-income-countries/oclc/317717289&referer=brief_results.

[6] K. Gibb, L. Lawson, J. Williams, Michael McLaughlin, The Impact of Social Housing : Economic, Social, Health and Wellbeing, (2020).

[7] J. Chakwizira, Low-income housing backlogs and deficits “blues” in South Africa. What solutions can a lean construction approach offer?, Journal of Settlements and Spatial Planning. 10 (2019) 71–78. https://doi.org/10.24193/JSSP.2019.2.01.

[8] G.P.A.G. van Zijl, TOWARDS SUSTAINABLE EMPLOYMENT IN INDUSTRIALISED CONSTRUCTION, (2018) 3–5.

[9] D. Aghimien, C. Aigbavboa, L. Aghimien, W.D. Thwala, L. Ndlovu, Making a case for 3D printing for housing delivery in South Africa, International Journal of Housing Markets and Analysis. ahead-of-p (2020). https://doi.org/10.1108/ijhma-11-2019-0111.

[10] Statistics South Africa, Quarterly Labour Force Survey (QLFS) – Q1:2021 The, (2021). http://www.statssa.gov.za/publications/P0211/Media release QLFS Q1 2021.pdf.

[11] M. Müller, T. Krick, J. Blohmke, Putting the construction sector at the core of the climate change debate| Deloitte Central Europe, Deloitte. (2020) 2–3. https://www2.deloitte.com/ce/en/pages/real-estate/articles/putting-the-construction-sector-at-the-core-of-the-climate-change-debate.html.

[12] S.C. Paul, G.P.A.G. van Zijl, M.J. Tan, I. Gibson, A review of 3D concrete printing systems and materials properties: current status and future research prospects, Rapid Prototyping Journal. (2018) 0. https://doi.org/10.1108/RPJ-09-2016-0154.

[13] J. Allum, J. Kitzinger, Y. Li, V. v Silberschmidt, A. Gleadall, ZigZagZ: Improving mechanical performance in extrusion additive manufacturing by nonplanar toolpaths, n.d.

[14] J. Pegna, Exploratory investigation of solid freeform construction, Automation in Construction. 5 (1997) 427–437. https://doi.org/10.1016/S0926-5805(96)00166-5.

[15] B. Khoshnevis, Automated construction by contour crafting - Related robotics and information technologies, Automation in Construction. 13 (2004) 5–19. https://doi.org/10.1016/j.autcon.2003.08.012.

[16] M.S. Khan, F. Sanchez, H. Zhou, 3-D printing of concrete: Beyond horizons, Cement and Concrete Research. 133 (2020). https://doi.org/10.1016/j.cemconres.2020.106070.

[17] F. Bos, R. Wolfs, T. Salet, CCR Digital Concrete 2020 SI: Editorial, Cement and Concrete Research. 135 (2020) 106157. https://doi.org/10.1016/j.cemconres.2020.106157.

[18] R.A. Buswell, W.R.L. da Silva, F.P. Bos, H.R. Schipper, D. Lowke, N. Hack, H. Kloft, V. Mechtcherine, T. Wangler, N. Roussel, A process classification framework for defining and describing Digital Fabrication with Concrete, Cement and Concrete Research. 134 (2020) 106068. https://doi.org/10.1016/j.cemconres.2020.106068.

[19] Size list of BOD2 construction printer Pricelist construction printer, Cobod. (2020) 1–5. https://cobod.com/wp-content/uploads/2020/07/BOD2-Size-chart-2020.pdf.

[20] CyBe, 3D concrete printers, Technology. (n.d.). https://cybe.eu/technology/3d-printers/ (accessed June 19, 2021).

[21] WASP, Crane Wasp, 3D Printers. (n.d.). https://www.3dwasp.com/en/3d-printer-house-crane-wasp/ (accessed June 19, 2021).

[22] T.H.E.M. For, O.F. Mc-bauchemie, 3D concrete printing A brave new world of building, (2018).

[23] Bruil, 3D geprint architectonisch beton op Material Xperience 2016, (2016). https://www.bruil.nl/over-ons/actuele-berichten/3d-geprint-architectonisch-beton-op-material-xperience-2016 (accessed June 19, 2021).

[24] Apis cor printers, (n.d.). https://www.apis-cor.com/ (accessed June 19, 2021).

[25] W.R. Leal da Silva, 3D Concrete Printing-Technological issues in concrete mix design and extrusion, Danish Technological Institute. (2017). https://www.dti.dk/projects/3d-printed-buildings/36993.

[26] J.H. Jo, B.W. Jo, W. Cho, J.H. Kim, Development of a 3D Printer for Concrete Structures: Laboratory Testing of Cementitious Materials, International Journal of Concrete Structures and Materials. 14 (2020). https://doi.org/10.1186/s40069-019-0388-2.

[27] E. Secrieru, D. Cotardo, V. Mechtcherine, L. Lohaus, C. Schröfl, C. Begemann, Changes in concrete properties during pumping and formation of lubricating material under pressure, Cement and Concrete Research. 108 (2018) 129–139. https://doi.org/10.1016/j.cemconres.2018.03.018.

[28] L. Reiter, T. Wangler, N. Roussel, R.J. Flatt, The role of early age structural build-up in digital fabrication with concrete, Cement and Concrete Research. 112 (2018) 86–95. https://doi.org/10.1016/j.cemconres.2018.05.011.

[29] V. Mechtcherine, F.P. Bos, A. Perrot, W.R.L. da Silva, V.N. Nerella, S. Fataei, R.J.M. Wolfs, M. Sonebi, N. Roussel, Extrusion-based additive manufacturing with cement-based materials – Production steps, processes, and their underlying physics: A review, Cement and Concrete Research. 132 (2020) 106037. https://doi.org/10.1016/j.cemconres.2020.106037.

[30] L. Reiter, T. Wangler, A. Anton, R.J. Flatt, Setting on demand for digital concrete – Principles, measurements, chemistry, validation, Cement and Concrete Research. 132 (2020) 106047. https://doi.org/10.1016/j.cemconres.2020.106047.

[31] M. Hoffmann, S. Skibicki, P. Pankratow, A. Zieliński, M. Pajor, M. Techman, Automation in the construction of a 3D-Printed concrete wall with the use of a lintel gripper, Materials. 13 (2020). https://doi.org/10.3390/MA13081800.

[32] J. Kruger, Rheo-mechanics modelling of 3D concrete printing constructability, 2019. https://scholar.sun.ac.za.

[33] F.A. Bester, M. van den Heever, P.J. Kruger, G.P.A.G. van Zijl, Reinforcing digitally fabricated concrete: A systems approach review, Additive Manufacturing. 37 (2021). https://doi.org/10.1016/j.addma.2020.101737.

[34] L. Wang, H. Jiang, Z. Li, G. Ma, Mechanical behaviors of 3D printed lightweight concrete structure with hollow section, Archives of Civil and Mechanical Engineering. 20 (2020) 1–17. https://doi.org/10.1007/s43452-020-00017-1.

[35] L. Feng, L. Yuhong, Study on the Status Quo and Problems of 3D Printed Buildings in China, Global Journal of HUMAN-SOCIAL SCIENCE. 14 (2014).

[36] C. Holt, L. Edwards, L. Keyte, F. Moghaddam, B. Townsend, Construction 3D Printing, 3D Concrete Printing Technology. 42 (2019) 349–370. https://doi.org/10.1016/b978-0-12-815481-6.00017-8.

[37] B. Panda, Y.W.D. Tay, S.C. Paul, M.J. Tan, Current challenges and future potential of 3D concrete printing, Materialwissenschaft Und Werkstofftechnik. 49 (2018) 666–673. https://doi.org/10.1002/mawe.201700279.

[38] V. Mechtcherine, F.P. Bos, A. Perrot, W.R.L. da Silva, V.N. Nerella, S. Fataei, R.J.M. Wolfs, M. Sonebi, N. Roussel, Extrusion-based additive manufacturing with cement-based materials – Production steps, processes, and their underlying physics: A review, Cement and Concrete Research. 132 (2020) 106037. https://doi.org/10.1016/j.cemconres.2020.106037.

[39] Z. Li, L. Wang, G. Ma, Method for the Enhancement of Buildability and Bending Resistance of 3D Printable Tailing Mortar, International Journal of Concrete Structures and Materials. 12 (2018). https://doi.org/10.1186/s40069-018-0269-0.

[40] R.J.M. Wolfs, F.P. Bos, T.A.M. Salet, Early age mechanical behaviour of 3D printed concrete: Numerical modelling and experimental testing, Cement and Concrete Research. 106 (2018) 103–116. https://doi.org/10.1016/j.cemconres.2018.02.001.

[41] J. Kruger, S. Zeranka, G. van Zijl, An ab initio approach for thixotropy characterisation of (nanoparticle-infused) 3D printable concrete, Construction and Building Materials. (2019). https://doi.org/10.1016/j.conbuildmat.2019.07.078.

[42] J. Kruger, G. van Zijl, A compendious review on lack-of-fusion in digital concrete fabrication, Additive Manufacturing. 37 (2021) 101654. https://doi.org/10.1016/j.addma.2020.101654.

[43] X. Zhang, M. Li, J.H. Lim, Y. Weng, Y.W.D. Tay, H. Pham, Q.C. Pham, Large-scale 3D printing by a team of mobile robots, Automation in Construction. 95 (2018) 98–106. https://doi.org/10.1016/j.autcon.2018.08.004.

[44] D. Avrutis, A. Nazari, J.G. Sanjayan, Industrial Adoption of 3D Concrete Printing in the Australian Market, Elsevier Inc., 2019. https://doi.org/10.1016/b978-0-12-815481-6.00019-1.

[45] S. Hou, Z. Duan, J. Xiao, J. Ye, A review of 3D printed concrete: Performance requirements, testing measurements and mix design, Construction and Building Materials. 273 (2021) 121745. https://doi.org/10.1016/j.conbuildmat.2020.121745.

[46] D. Asprone, C. Menna, F.P. Bos, T.A.M. Salet, J. Mata-Falcón, W. Kaufmann, Rethinking reinforcement for digital fabrication with concrete, Cement and Concrete Research. 112 (2018) 111–121. https://doi.org/10.1016/j.cemconres.2018.05.020.

[47] R.A. Buswell, W.R. Leal de Silva, S.Z. Jones, J. Dirrenberger, 3D printing using concrete extrusion: A roadmap for research, Cement and Concrete Research. 112 (2018) 37–49. https://doi.org/10.1016/j.cemconres.2018.05.006.

[48] V. Carlota, Apis Cor collaborates on world's largest 3D printed building, 3Dnatives. (2019). https://www.3dnatives.com/en/apis-cor-largest-3d-printed-building-261020194/ (accessed November 7, 2019).

[49] M. Küppers, Unlimited 3D Printing Possibilities with Concrete, Construction Printing Technology 1 | 2019. (2019).

[50] T. Marchment, J. Sanjayan, Mesh reinforcing method for 3D Concrete Printing, Automation in Construction. 109 (2020) 102992. https://doi.org/10.1016/j.autcon.2019.102992.

[51] T. Marchment, J. Sanjayan, Bond properties of reinforcing bar penetrations in 3D concrete printing, Automation in Construction. 120 (2020) 103394. https://doi.org/10.1016/j.autcon.2020.103394.

[52] A. Perrot, Y. Jacquet, D. Rangeard, E. Courteille, M. Sonebi, Nailing of layers: A promising way to reinforce concrete 3D printing structures, Materials. 13 (2020). https://doi.org/10.3390/ma13071518.

[53] C. Matthäus, N. Kofler, T. Kränkel, D. Weger, C. Gehlen, Interlayer reinforcement combined with fiber reinforcement for extruded lightweight mortar elements, Materials. 13 (2020) 1–17. https://doi.org/10.3390/ma13214778.

[54] V. Mechtcherine, J. Grafe, V.N. Nerella, E. Spaniol, M. Hertel, U. Füssel, 3D-printed steel reinforcement for digital concrete construction – Manufacture, mechanical properties and bond behaviour, Construction and Building Materials. 179 (2018) 125–137. https://doi.org/10.1016/j.conbuildmat.2018.05.202.

[55] F. Bester, M. van den Heever, J. Kruger, S. Cho, G. van Zijl, Steel fiber links in 3D printed concrete, Second RILEM International Conference on Concrete and Digital Fabrication - Digital Concrete 2020. 2 (2020) 1–9.

[56] ETH Zurich, Digital Building Technologies, (2018). http://dbt.arch.ethz.ch/project/concrete-choreography/ (accessed October 23, 2019).

[57] T. Boissonneault, XTreeE 3D printing 12-meter-tall telecoms towers that blend into landscape, 3D Printing Media Network. (2019). https://www.3dprintingmedia.network/xtreee-3d-printing-telecoms-towers/ (accessed October 23, 2019).

[58] Sika, Flexible shapes for concrete structures possible thanks to 3D printing, BFT International. (2018). https://www.bft-international.com/en/artikel/bft_Flexible_shapes_for_concrete_structures_possible_thanks_to_3D_printing_3242361.html (accessed October 23, 2019).

[59] E. de Bruijn, Wereldprimeur voor Gemert: fietsen over een 3D-geprinte brug, NOS. (2017). https://nos.nl/artikel/2198400-wereldprimeur-voor-gemert-fietsen-over-een-3d-geprinte-brug.html (accessed October 23, 2019).

[60] A. Say, Luai Kurdi Experiments With 3D Printing Concrete by Using Parametric Design And Digital Fabrication Tools, Parametric Architecture. (2019). https://parametric-architecture.com/3d-printing-concrete-by-luai-kurdi/ (accessed October 23, 2019).

[61] M. Molitch-Hou, Dubai Unveils First 3D-Printed Office Building, Engineering.Com. (2016). https://www.engineering.com/BIM/ArticleID/12225/Dubai-Unveils-First-3D-Printed-Office-Building.aspx (accessed October 23, 2019).

[62] J.G. Sanjayan, B. Nematollahi, 3D Concrete Printing for Construction Applications, Elsevier Inc., 2019. https://doi.org/10.1016/b978-0-12-815481-6.00001-4.

[63] E. Pollock, Europe's First On-Site 3D-Printed House Is Unveiled, (2018). https://www.engineering.com/BIM/ArticleID/16830/Europes-First-On-Site-3D-Printed-House-Is-Unveiled.aspx (accessed October 23, 2019).

[64] Icon Build, ICON BUILD, (2018). https://www.iconbuild.com/ (accessed October 23, 2019).

[65] R. Haria, 3D PRINTHUSET COMPLETES 3D PRINTING FOR BUILDING ON DEMAND, 3D Printing Industry. (2017). https://3dprintingindustry.com/news/3d-printhuset-completes-3d-printed-building-demand-copenhagen-124932/ (accessed October 23, 2019).

[66] Apis Cor, Mashable Deals. (2017). https://www.apis-cor.com/gallary (accessed October 23, 2019).

[67] M. Jazdyk, US Army Corps of Engineers, U.S. ARMY ENGINEER RESEARCH AND DEVELOPMENT CENTER, PUBLIC AFFAIRS. (2017). https://www.erdc.usace.army.mil/Media/News-Stories/Article/1281737/3-d-printing-a-building/ (accessed October 23, 2019).

[68] C. Menna, J. Mata-Falcón, F.P. Bos, G. Vantyghem, L. Ferrara, D. Asprone, T. Salet, W. Kaufmann, Opportunities and challenges for structural engineering of digitally fabricated

concrete, Cement and Concrete Research. 133 (2020) 106079. https://doi.org/10.1016/j.cemconres.2020.106079.

[69] 3D Printed Concrete Castle is Complete, Total Kustom. (2015). http://www.totalkustom.com/3d-castle-completed.html (accessed June 19, 2021).

[70] Alec, Lewis Grand Hotel teams with Andrey Rudenko to develop world's first 3D printed hotel, planning 3D printed homes, (2015). http://www.3ders.org/articles/20150909-lewis-grand-hotel-andrey-rudenko-to-develop-worlds-first-3d-printed-hotel.html (accessed June 19, 2021).

[71] Winsun, Winsun is the world's first 3D printed office building, Winsun News. (2016). http://www.winsun3d.com/En/News/news_inner/id/465 (accessed June 19, 2021).

[72] XtreeE, Krypton, a column in Aix-en-Provence, (2016). https://xtreee.com/en/project/krypton/ (accessed June 19, 2021).

[73] XtreeE, Double sine wall, (2016). https://xtreee.com/en/project/mur-sinusoidal/ (accessed June 19, 2021).

[74] 3DPrint.com, CyBe construction announces that 3D printing is complete for Dubai's R&drone laboratory, The Voice of 3D Printing/Additive Manufacturing. (n.d.). https://3dprint.com/176561/cybe-3d-printed-dubai-laboratory/ (accessed June 19, 2021).

[75] T.A.M. Salet, Z.Y. Ahmed, F.P. Bos, H.L.M. Laagland, Design of a 3D printed concrete bridge by testing, Virtual and Physical Prototyping. 0 (2018) 1–15. https://doi.org/10.1080/17452759.2018.1476064.

[76] XtreeE, PROJECTS – Yrys Concept House, (n.d.). http://www.xtreee.eu/projects- yrys-concept-house/ (accessed June 19, 2021).

[77] XtreeE, Stormwater regulator in Lille, (2017). https://xtreee.com/en/project/deversoir-dorage/ (accessed June 19, 2021).

[78] Massimiliano Locatelli, 3dhousing05, CLS ARCHITETTI. (n.d.).

[79] 3DPrint.com, 3D Printing Completed on 3D Printhuset's Building On Demand, The Voice of 3D Printing/Additive Manufacturing. (n.d.). https://3dprint.com/ 195020/3d-printhuset-building-on-demand/ (accessed June 19, 2021).

[80] WASP, 3d Printing Architecture, (n.d.). https://www.3dwasp.com/en/3d-printing-architecture/ (accessed June 19, 2021).

[81] Tsinghua University News, (n.d.). https://news.tsinghua.edu.cn/publish/thunewsen/9670/2019/20190116161602224500923/ 20190116161602224500923_.html (accessed June 19, 2021).

[82] Construction of first 3D-printed building to start, De Ingenieur. (n.d.).

[83] G. Grasser, L. Pammer, H. Köll, E. Werner, F.P. Bos, Complex Architecture in Printed Concrete: The Case of the Innsbruck University 350th Anniversary Pavilion COHESION, RILEM Bookseries. 28 (2020) 1116–1127. https://doi.org/10.1007/978-3-030-49916-7_106.

[84] Dubai is now home to the largest 3D-printed building in the world, Business Insider. (2019). https://www.businessinsider.com/dubai-largest-3d-printed- building-apis-cor-photos-2019-12?international=true&r=US&IR=T (accessed June 19, 2021).

[85] ICON, ICON + New Story + ECHALE Unveil First Homes in 3D-Printed Community, ICON. (2019). https://www.iconbuild.com/updates/icon-new-story-echale-unveil-first-homes-in-3d-printed-community (accessed June 19, 2021).

[86] G. Vantyghem, W. de Corte, E. Shakour, O. Amir, 3D printing of a post-tensioned concrete girder designed by topology optimization, Automation in Construction. 112 (2020) 103084. https://doi.org/10.1016/j.autcon.2020.103084.

[87] Be More 3D, First house, Projects: Be More 3D. (2020). https://bemore3d.com/language/en/projects/ (accessed June 19, 2021).

[88] Technologies.org, ARCS Robot Builds World's Largest 3D Printed Home, Technologies.Org. (2020). https://technologies.org/arcs-robot-builds-worlds-largest-3d-printed-home/ (accessed June 19, 2021).

[89] S. Rener-Roth, 3D-printed houses completed for Austin's homeless population, The Architect's Newspaper. (2020). https://www.archpaper.com/2020/03/3d-printed-houses-completed-for-austins-homeless-population/ (accessed June 19, 2021).

[90] V.B. Ramirez, This Tiny House Is 3D Printed, Floats, and Will Last Over 100 Years, SingularityHub. (2020). https://singularityhub.com/2020/06/30/this-house-is-3d-printed-floats-and-will-last-over-100-years/ (accessed June 19, 2021).

[91] C. Carlson, Kamp C completes two-storey house 3D-printed in one piece in situ, De Zeen. (2020). https://www.dezeen.com/2020/12/22/kamp-c-completes-two-storey-house-3d-printed-one-piece-onsite/ (accessed June 19, 2021).

[92] J. Kruger, S. Cho, S. Zeranka, C. Viljoen, G. van Zijl, 3D concrete printer parameter optimisation for high rate digital construction avoiding plastic collapse, Composites Part B: Engineering. 183 (2020) 107660. https://doi.org/10.1016/j.compositesb.2019.107660.

[93] N. Roussel, Rheological requirements for printable concretes, Cement and Concrete Research. (2018) 1–10. https://doi.org/10.1016/j.cemconres.2018.04.005.

[94] T. Pan, Y. Jiang, H. He, Y. Wang, K. Yin, Effect of structural build-up on interlayer bond strength of 3d printed cement mortars, Materials. 14 (2021) 1–17. https://doi.org/10.3390/ma14020236.

[95] A.S.J. Suiker, R.J.M. Wolfs, S.M. Lucas, T.A.M. Salet, Elastic buckling and plastic collapse during 3D concrete printing, Cement and Concrete Research. 135 (2020) 106016. https://doi.org/10.1016/j.cemconres.2020.106016.

[96] A.S.J. Suiker, Mechanical performance of wall structures in 3D printing processes: Theory, design tools and experiments, International Journal of Mechanical Sciences. 137 (2018) 145–170. https://doi.org/10.1016/j.ijmecsci.2018.01.010.

[97] R.J.M. Wolfs, A.S.J. Suiker, Structural failure during extrusion-based 3D printing processes, The International Journal of Advanced Manufacturing Technology. (2019). https://doi.org/10.1007/S00170-019-03844-6.

[98] Y. Weng, M. Li, D. Zhang, M. Jen, S. Qian, Investigation of interlayer adhesion of 3D printable cementitious material from the aspect of printing process, Cement and Concrete Research. 143 (2021) 106386. https://doi.org/10.1016/j.cemconres.2021.106386.

[99] J. van der Putten, M. Deprez, V. Cnudde, G. de Schutter, K. van Tittelboom, Microstructural characterization of 3D printed cementitious materials, Materials. 12 (2019). https://doi.org/10.3390/ma12182993.

[100] J.G. Sanjayan, B. Nematollahi, M. Xia, T. Marchment, Effect of surface moisture on inter-layer strength of 3D printed concrete, Construction and Building Materials. (2018). https://doi.org/10.1016/j.conbuildmat.2018.03.232.

[101] V.N. Nerella, S. Hempel, V. Mechtcherine, Effects of layer-interface properties on mechanical performance of concrete elements produced by extrusion-based 3D-printing, Construction and Building Materials. 205 (2019). https://doi.org/10.1016/j.conbuildmat.2019.01.235.

[102] J. van der Putten, M. Azima, P. van den Heede, T. van Mullem, D. Snoeck, C. Carminati, J. Hovind, P. Trtik, G. de Schutter, K. van Tittelboom, Neutron radiography to study the water ingress via the interlayer of 3D printed cementitious materials for continuous layering, Construction and Building Materials. 258 (2020) 119587. https://doi.org/10.1016/j.conbuildmat.2020.119587.

[103] R.J.M. Wolfs, F.P. Bos, E.C.F. van Strien, T.A.M. Salet, High tech concrete: Where technology and engineering meet!, High Tech Concrete: Where Technology and Engineering Meet - Proceedings of the 2017 Fib Symposium. 1 (2017) v. https://doi.org/10.1007/978-3-319-59471-2.

[104] G.M. Moelich, J. Kruger, R. Combrinck, Plastic shrinkage cracking in 3D printed concrete, Composites Part B: Engineering. 200 (2020) 108313. https://doi.org/10.1016/j.compositesb.2020.108313.

[105] G.M. Moelich, P.J. Kruger, R. Combrinck, Mitigating early age cracking in 3D printed concrete using fibres, superabsorbent polymers, shrinkage reducing admixtures, B-CSA cement and curing measures., Cement and Concrete Research. (Submitted (2021).

[106] T. Ooms, G. Vantyghem, R. van Coile, W. de Corte, A parametric modelling strategy for the numerical simulation of 3D concrete printing with complex geometries, Additive Manufacturing. 38 (2021) 101743. https://doi.org/10.1016/j.addma.2020.101743.

[107] G. Vantyghem, T. Ooms, W. de Corte, VoxelPrint: A Grasshopper plug-in for voxel-based numerical simulation of concrete printing, Automation in Construction. 122 (2021) 103469. https://doi.org/10.1016/j.autcon.2020.103469.

[108] R.J.M. Wolfs, F.P. Bos, T.A.M. Salet, Triaxial compression testing on early age concrete for numerical analysis of 3D concrete printing, Cement and Concrete Composites. (2019) 103344. https://doi.org/10.1016/j.cemconcomp.2019.103344.

[109] F.A. Bester, M. van den Heever, P.J. Kruger, S. Zeranka, G.P.A.G. van Zijl, Benchmark structures for 3D concrete printing, Proceedings of the Fib Symposium 2019: Concrete - Innovations in Materials, Design and Structures. (2019) 305–312.

[110] A. van den Bos, P. van der Aa, Practical approach to assess buildability of 3D concrete printed object using finite element analysis, (2019) 2019.

[111] N. Roussel, J. Spangenberg, J. Wallevik, R. Wolfs, Numerical simulations of concrete processing: From standard formative casting to additive manufacturing, Cement and Concrete Research. 135 (2020) 106075. https://doi.org/10.1016/j.cemconres.2020.106075.

[112] J. Kruger, A. du Plessis, G. van Zijl, An investigation into the porosity of extrusion-based 3D printed concrete, Additive Manufacturing. 37 (2021) 101740. https://doi.org/10.1016/j.addma.2020.101740.

[113] B. Anleu, Quantitative micro XRF mapping of chlorides: possibilities, limitations, and applications, from cement to digital concrete, 2018. https://doi.org/https://doi. org/10.3929/ethz-a-010782581.

[114] T.C. Powers, Structure and Physical Properties of Hardened Portland Cement Paste, Journal of the American Ceramic Society. 41 (1958) 1–6. https://doi.org/doi:10.1111/j.1151-2916.1958.tb13494.x.

[115] J.D. Birchall, A.J. Howard, K. Kendall, Flexural strength and porosity of cements, Nature. 289 (1981) 388–390. https://doi.org/10.1038/289388a0.

[116] Y. Chen, O. Çopuroğlu, C. Romero Rodriguez, F.F. de Mendonca Filho, E. Schlangen, Characterization of air-void systems in 3D printed cementitious materials using optical image scanning and X-ray computed tomography, Materials Characterization. 173 (2021) 110948. https://doi.org/10.1016/j.matchar.2021.110948.

[117] H. Lee, J.H.J. Kim, J.H. Moon, W.W. Kim, E.A. Seo, Correlation between pore characteristics and tensile bond strength of additive manufactured mortar using X-ray computed tomography, Construction and Building Materials. 226 (2019) 712–720. https://doi.org/10.1016/j.conbuildmat.2019.07.161.

[118] M. van den Heever, F. Bester, M. Pourbehi, J. Kruger, S. Cho, G. van Zijl, Characterizing the Fissility of 3D Concrete Printed Elements via the Cohesive Zone Method, 2nd RILEM International Conference on Concrete and Digital Fabrication. 3 (2020) 1–10.

[119] B. Panda, S. Chandra Paul, M. Jen Tan, Anisotropic mechanical performance of 3D printed fiber reinforced sustainable construction material, Materials Letters. (2017). https://doi.org/10.1016/j.matlet.2017.07.123.

[120] G. Ma, Z. Li, L. Wang, F. Wang, J. Sanjayan, Mechanical anisotropy of aligned fiber reinforced composite for extrusion-based 3D printing, Construction and Building Materials. (2019). https://doi.org/10.1016/j.conbuildmat.2019.01.008.

[121] M. Sonebi, S. Amziane, A. Perrot, Mechanical Behavior of 3D Printed Cement Materials, 3D Printing of Concrete. (2019) 101–124. https://doi.org/10.1002/9781119610755.ch4.

[122] S.C. Figueiredo, C.R. Rodrıguez, Z.Y. Ahmed, D.H. Bos, Y. Xu, T.M. Salet, O.C. Opurog˘lu, E. Schlangen, F.P. Bos, Mechanical behaviour of printed strain hardening cementitious composites, Materials. 13 (2020).

[123] P. Feng, X. Meng, J. Chen, L. Ye, Mechanical properties of structures 3D printed with cementitious powders, CONSTRUCTION & BUILDING MATERIALS. 93 (2015) 486–497. https://doi.org/10.1016/j.conbuildmat.2015.05.132.

[124] B. Nematollahi, P. Vijay, J. Sanjayan, A. Nazari, M. Xia, V.N. Nerella, V. Mechtcherine, Effect of polypropylene fibre addition on properties of geopolymers made by 3D printing for digital construction, Materials. 11 (2018). https://doi.org/10.3390/ma11122352.

[125] J. Yu, C.K.Y. Leung, Impact of 3D Printing Direction on Mechanical Performance of Strain-Hardening Cementitious Composite (SHCC) Jing, Springer International Publishing, 2019. https://doi.org/10.1007/978-3-319-99519-9.

[126] C. Müller, Eurocode – EN 1990 Basis of Structural Design Structural Analysis and Design by Testing, (2008) 18–20.

[127] ISO/TC 71/SC 3, ISO 22966:2009 - Execution of concrete structures, ISO ICS: 91.080.40. (2021). https://www.iso.org/standard/41262.html (accessed June 21, 2021).

[128] S.C. Paul, Y.W.D. Tay, B. Panda, M.J. Tan, Fresh and hardened properties of 3D printable cementitious materials for building and construction, Archives of Civil and Mechanical Engineering. (2018). https://doi.org/10.1016/j.acme.2017.02.008.

[129] J. Xiao, S. Zou, Y. Yu, Y. Wang, T. Ding, Y. Zhu, J. Yu, S. Li, Z. Duan, Y. Wu, L. Li, 3D recycled mortar printing: System development, process design, material properties and on-site printing, Journal of Building Engineering. 32 (2020) 101779. https://doi.org/10.1016/j.jobe.2020.101779.

[130] T.T. Le, S.A. Austin, S. Lim, R.A. Buswell, R. Law, A.G.F. Gibb, T. Thorpe, Hardened properties of high-performance printing concrete, Cement and Concrete Research. 42 (2012) 558–566. https://doi.org/10.1016/j.cemconres.2011.12.003.

[131] R.J.M. Wolfs, F.P. Bos, T.A.M. Salet, Hardened properties of 3D printed concrete: The influence of process parameters on interlayer adhesion, Cement and Concrete Research. 119 (2019) 132–140. https://doi.org/10.1016/j.cemconres.2019.02.017.

[132] F.P. Bos, E. Bosco, T.A.M. Salet, Ductility of 3D printed concrete reinforced with short straight steel fibers, Virtual and Physical Prototyping. 14 (2019) 160–174. https://doi.org/10.1080/17452759.2018.1548069.

[133] A. Vespalec, J. Novák, A. Kohoutková, P. Vosynek, J. Podroužek, D. Škaroupka, T. Zikmund, J. Kaiser, D. Paloušek, Interface behavior and interface tensile strength of a hardened concrete mixture with a coarse aggregate for additive manufacturing, Materials. 13 (2020) 1–20. https://doi.org/10.3390/ma13225147.

[134] L. He, W.T. Chow, H. Li, Effects of interlayer notch and shear stress on interlayer strength of 3D printed cement paste, Additive Manufacturing. 36 (2020) 101390. https://doi.org/10.1016/j.addma.2020.101390.

[135] J. Xiao, H. Liu, T. Ding, Finite element analysis on the anisotropic behavior of 3D printed concrete under compression and flexure, Additive Manufacturing. 39 (2021) 101712. https://doi.org/10.1016/j.addma.2020.101712.

[136] J.F. Labuz, A. Zang, Mohr-Coulomb failure criterion, Rock Mechanics and Rock Engineering. 45 (2012) 975–979. https://doi.org/10.1007/s00603-012-0281-7.

[137] J.G. Rots, Computational Modeling of Concrete Fracture, 1988.

[138] European Committee for Standardization, EN 1992-1-1, Brussels, 2004.

[139] J. Kruger, S. Zeranka, G. van Zijl, 3D concrete printing: A lower bound analytical model for buildability performance quantification, Automation in Construction. 106 (2019) 102904. https://doi.org/10.1016/j.autcon.2019.102904.

[140] DIANA FEA, (n.d.). https://dianafea.com/.

[141] V. Červenka, L. Jendele, J. Červenka, ATENA Program Documentation Part 11, (2013) 1–33. https://www.cervenka.cz/assets/files/atena-pdf/ATENA_Theory.pdf.

[142] P.B. Lourenço, J.G. Rots, J. Blaauwendraad, Continuum model for masonry: Parameter estimation and validation, Journal of Structural Engineering. 124 (1998) 642–652. https://doi.org/10.1061/(ASCE)0733-9445(1998)124:6(642).

[143] P. Menetrey, K.J. Willam, Triaxial Failure Criterion for Concrete and its Generalization, ACI Structural Journal. (1996) 311–318.

[144] S.W. Tsai, E.M. Wu, A General Theory of Strength for Anisotropic Materials, Journal of Composite Materials. 5 (1971) 58–80. https://doi.org/10.1177/002199837100500106.

[145] S. Sanchez-saez, L.M. Fern, Fernández-Cañadas , L . M ., Iváñez , I ., & Sánchez-Sáez , S . (2016). Influence of the cohesive law shape on the composite adhesively- bonded patch repair behaviour . Composites Part, (2016) 414–421.

[146] M.M. Shokrieh, Residual Stresses in Composite Materials, 2014. https://doi.org/10.1533/9780857098597.

[147] P.B. Lourenço, J.G. Rots, Multisurface interface model for analysis of masonry structures, Journal of Engineering Mechanics. 123 (1997) 660–668. https://doi.org/10.1061/(ASCE)0733-9399(1997)123:7(660).

[148] P. Valle-Pello, F.P. Álvarez-Rabanal, M. Alonso-Martínez, J.J. del Coz Díaz, Numerical study of the interfaces of 3D-printed concrete using discrete element method, Materialwissenschaft Und Werkstofftechnik. 50 (2019) 629–634. https://doi.org/10.1002/mawe.201800188.

CHAPTER 3: Mechanical Characterisation for Numerical Simulation of Extrusion-based 3D Concrete Printing

Marchant van den Heever *, Frederick Bester, Jacques Kruger, Gideon van Zijl.

Structural Engineering and Civil Engineering Informatics, Department of Civil Engineering, Stellenbosch University, Stellenbosch, 7602, South Africa

Reproduced and reformatted from an article published in the *Journal of Building Engineering*. (DOI: 10.1016/j.jobe.2021.102944)

Abstract

Extrusion-based 3D concrete printing (3DCP) is experiencing exponential advancement in process, control, material, and fresh-state analysis technologies, strategically poising 3DCP to become an industrial manufacturing process for infrastructure development. To elucidate the mechanical characterisation and numerical simulation of 3DCP elements synergy among experimental and computational mechanics is required. Such activities should characterise the unique material properties of printed components to permit limit state design procedures and the correct prescription of finite element (FE) model parameters. In this research, mechanical characterisation procedures that experimentally evaluate the anisotropic material characteristics of a fibre-reinforced printable concrete (FRPC) are presented. These procedures are comprised of direct tensile, uniaxial compression, Young's modulus, and four-point bending (FPB) crack mouth opening displacement (CMOD) tests. The results portrayed anisotropic non-linear and similar elastic behaviour (in terms of Young's modulus) in all experimental tests conducted. From the mechanical characterisation tests two elastic parameters, seven strength parameters and five inelastic parameters are ascertained. The experimental findings relating to the material characteristic parameters are validated via supplementary numerical evaluation, and suitable constitutive relations are selected. The mechanical parameters are implemented in an anisotropic Rankine-Hill continuum multi-surface plasticity FE model, and the FPB-CMOD fracture response of 3DCP specimens is simulate with respectable agreement.

Highlights:

- The linear and non-linear mechanical characteristics of FRPC are experimentally evaluated
- The degree of anisotropy is determined, and suitable constitutive relations are selected
- A robust anisotropic continuum FE model adaptable to 3DCP is presented
- The employed layer pressing strategy exhibits potential for interlayer fibre breaching
- A non-rectilinear pressed interface between adjacent filaments improves tensile capacity

Keywords: 3D Concrete Printing; Mechanical Characterisation; Experimental Mechanics; Numerical Simulation; Finite Element Analysis

Introduction

Amidst global inclinations of rapid urbanisation, digitisation and climate change, it is evident that the construction sector must transform to meet the growing demand for infrastructure while mitigating the environmental impact caused by its implementation. To this end, digital fabrication of concrete (DFC), a lineage technique of the additive manufacturing suite of systems has experienced significant technological developments, providing a new paradigm for clients, designers, and contractors alike. This is substantiated by the proliferation of available literature on DFC [1]. The referenced developments are fuelled by the prospects of creating a fully automated building process, which prompts elevated levels of geometric design freedom, construction speed, reduced labour, and optimised raw material usage. The additional benefit of offering customisation at minimal to no extra expense, is truly remarkable considering the sectors in which DFC is applicable. Albeit, the value added by this novel approach is set to revolutionise the construction industry, DFC must first surmount the current hurdles impeding its widespread adoption [1–9]. The overarching consensus is that the interrelation between the design, material, fabrication and manufacturing processes and product applications need to be critically evaluated, such that the complex physicochemical phenomena influencing the material and process parameters permit the production of high-quality end products as they were designed [1,6].

Buswell et al. [10] present an overview of the DFC suite of processes and propose a process classification framework tailored to DFC that is founded on existing ISO guidelines in manufacturing industries. However, in the presented research, the focus is exclusively directed to the mechanical characterisation of extrusion-based additive manufacturing with cement-based materials, often referred to as 3DCP. Although, the cementitious compositions employed are generally classified as mortar, due to the fine aggregate sizes being less than 4 mm [11], the term “concrete” is still deemed appropriate in view of its application in the built environment and accordance with the terminology most often used in the 3DCP research arena.

Extrusion-based 3DCP is founded on the principle of discrete layer deposition, and ensuing the aforementioned interrelation between the respective design, process, and material particularities, heterogeneous layered components are often formed. The consequence of these weaker interlayer regions is anisotropic constitutive relations across various loading spectra [12–19]. Kruger and van Zijl [5] present a compendious review on the lack-of-fusion (LOF) exhibited in DFC; in this publication, the strength reduction due to the interlayer influence is studied for fifteen experimental investigations for an array of printable cementitious composites, across various research institutions. The results

portray an averaged 45.6 % maximal reduction in the mechanical performance of 3DCP elements, compared to their conventionally cast counterparts. The study further exposed the variable mechanical performance exhibited by various types of printable mixtures and fabrication processes, yielding a coefficient of variation of 53.8 %, indicating that the effect on the mechanical performance is specific to the loading direction, print process, and materials employed to digitally fabricate the desired components. The differential interlayer and intralayer matrix capacities are attributed to a variety of mechanisms, classified by Kruger and van Zijl [5] as a combination of mechanical interaction, chemical bonding, and physical forces. These mechanisms include surface moisture evaporation, air entrapment causing lens-shaped microstructural voids, thixotropy, and surface roughness. Additionally, densification of the intralayer matrix, stemming from the amplified pressure induced by the extrusion process, enhances the mechanical properties of the printed concrete filament, and so too the degree of anisotropy prevalent in the printed composite [20]. Furthermore, the entrainment of fibres causes additional differences in the elastic and post-peak responses of a 3DCP component, which stems from the alignment of fibres in the extrusion direction [16] and the increase in apparent porosity observed [21].

An appraisal of recent literature on reinforcement strategies for extrusion-based 3DCP reveals that fibre entrainment is the commonly adopted technique employed to enhance the mechanical capacity of 3D printable materials [22]. Numerous geometric and material forms of fibres such as polymeric, carbon, steel, basalt, and glass fibres, ranging in mechanical properties and aspect ratios are entrained [23]. Fibre-reinforced printable concrete/cementitious composites (FRPC) display improved mechanical properties, particularly considering the post-crack ductility and plastic shrinkage of printable compositions. Some institutions have developed printable strain-hardening cementitious composites (SHCC), which allows for significantly enhanced stress and strain capacity in the extrusion direction [15]. The efficiency of fibre entrainment is more pronounced when tensile forces are imposed in the extrusion direction, attributed to the preferential alignment of fibres in the longitudinal intralayer direction. Conversely, the addition of fibres is reported to either not affect or reduce the interlayer capacity of 3DCP elements [21], a probable result of the reduced workability resulting from a stiffened intralayer matrix and the lesser tendency of fibres to breach the interlayer regions [24]. Figueiredo et al. [15] rightfully mention that it is imperative to consider the compatibility of certain fibre types to the printing process employed.

Furthermore, comparing the thixotropic characteristics presented in Table 3.3, for a standard high-performance concrete (HPC) printable mixture [25] and the FRPC utilised in this study, it is evident that the initial static ($\tau_{S,I}$) and dynamic ($\tau_{D,I}$) shear yield stresses are mutually increased by fibre inclusion, as often reported in literature [26]. These results depict a relatively high reflocculation rate (R_{thix}) and moderate structuration rate (A_{thix}) [27–29]. The observed increase in R_{thix} and A_{thix}, portrays a decrease in the material open time [30]. Thereby, resulting in interlayer regions with increased

porosity and reduced interlayer capacity, since the rapid stiffening of the substrate layers hinders their capability to fuse [5,21]. Accordingly, it is recommended that the mechanical assessment of extrusion-based 3DCP elements utilising FRPC mixtures be conducted in their respective orthotropic components.

Cementitious materials, such as concrete and mortar, are classified as quasi-brittle materials since they are not perfectly brittle in the Griffith sense, but exhibit slight residual load-carrying capacity after the tensile strength is reached [31]. Quasi-brittle material behaviour in tension displays reversible deformation prior to fracture, and once coalescence of micro-cracks has occurred, forming a macro-crack, non-linear strain-softening commences which is associated with stable crack propagation until final fracture [32]. Strain-softening refers to diminishing stress under increasing deformation, which exists in a narrow zone within the specimen, the fracture process zone (FPZ). The remaining undamaged portion of the sample simultaneously contracts elastically when the stress is relieved. It is thus essential that the specimen geometry, measurement gauge length, and deformation rate be considered for strength tests to ensure snap-back (unstable crack propagation) is prevented. Moreover, the non-linear behaviour of concrete in compression is predominantly ascribed to the increasing contribution of micro-cracking to the strain under increasing load. The constitutive post-peak response is governed by spontaneous unstable crack propagation in the interfacial transition zone (ITZ) between the hardened cement paste and aggregates, also resulting in strain-softening behaviour [33]. On the other hand, the fracture mechanics of concrete is still not entirely comprehended due to the complexity caused by the heterogeneous microstructural configurations within the matrix [34]. Likewise, knowledge pertaining to the impact on the mechanics of fracture in weaker interlayer regions is sparse. Therefore, the combination of numerical techniques, such as the finite element method (FEM), and experimental procedures, such as to characterise the stress-CMOD curve, are required to theoretically investigate the FPZ and structural response of 3DCP elements, as done for a variety conventionally cast cementitious compositions [35].

The predominant failure mechanisms exhibited in concrete structures are (1) tension, (2) compression, (3) shear, and (4) combined failure modes, where the compressive strength of concrete is generally the most widely used property in empirical formulations. Although the tensile capacity is not explicitly used in design calculations, it remains an essential property of concrete which is used indirectly in shear strength design of slabs, splitting under concentrated loads, and anchorage of deformed bars [35]. Still, not only the various strength parameters but also the behaviour at tensile fracture is of importance, as the safety and durability of the structure depend on the tensile toughness of concrete.

The expected failure modes in 3DCP elements are interfacial delamination, interface shear-slip, intralayer tensile cracking, intralayer cracking under compression-shear, and crushing as shown in Fig. 3.24. These assertions are derived from an analogy between masonry structures and 3DCP

components and are based on established principles presented for the computational evaluation of masonry structures [36]. It is inferred that mechanical characterisation procedures for 3DCP should experimentally investigate the above-mentioned potential failure modes.

In this light, various mechanical testing procedures have been employed and a recent review presenting LOF characterisation methods can be found in [5]. It is reported that to appropriately characterise the capacity of 3DCP components, the interrelated physico-chemical, process, and design parameters should be considered [1]. Thus, it is imperative that samples be extracted from actual 3DCP parts to ensure that these factors are appropriately represented, which has been the strategy employed in several research endeavours [5,12,13,15–18,21,23,37–39]. However, procedures employing various geometric configurations and boundary conditions have been proposed, making inter-institutional evaluations problematic. It is envisioned that the development of standardised mechanical assessment criteria would significantly contribute to the collective advancement of material characterisation procedures in extrusion-based 3DCP. Nevertheless, it is appreciated that mechanically sawing specimens from 3DCP elements adds additional difficulties regarding geometric tolerances and could compromise mechanical performance induced by the extraction process.

Consequently, synergy among experimental and computational mechanics is paramount to the future development of extrusion-based 3DCP. In this regard, Wang et al. [40] recently explored the discrete element method to numerically simulate failure mechanisms of 3D printed lightweight concrete elements with hollow sections. Bos et al. [39], investigated the ductility of short steel fibre reinforced 3D printed concrete, which employed the eminent Concrete Damage Plasticity (CDP) material model of Abaqus to simulate the flexural response of 3DCP beams with reasonable agreement. However, they concluded that accurate models based on constitutive relations obtained from uniaxial tensile testing are required to simulate larger separations. Likewise, Xiao et al. [41], employ the CDP model in combination with a discrete element traction-separation constitutive relation to investigate the effects of interlayer bonding on the anisotropic mechanical behaviour of 3DCP elements in compressive and flexural loading. Feng et al. [13], implemented a FE analysis, founded on the experimentally determined compressive stress-strain response and a maximum stress criterion, to investigate the effect of printing direction on the load-carrying capacity of a 3D printed arch structure. The fissile nature of 3DCP components is characterised by van den Heever et al. [18] and the tensile failure mode over the interlayer is computationally simulated via the cohesive zone method. Though various approaches have been proposed, many drawbacks need to be resolved if robust, accurate and validated numerical simulation procedures are to be developed for 3DCP. Considering that either discrete element models, associated with great computational expense, discrete interface models, requiring the crack-path to be known apriori, or isotropic continuum models, which disregard the anisotropic behaviour of 3DCP elements, are employed; it is evident that a computational model for the analysis of the multifaceted failure in 3D printed concrete elements needs to be explored.

Therefore, if 3DCP shells are not just to be considered as permanent, or lost, formwork, robust methods founded in appropriate scientific bases for characterising the mechanical strength and fracture parameters are required.

Materials and Proportions

The FRPC mixture developed at Stellenbosch University is employed containing the specific constituent proportions presented in [18]. The grading of the mixture is tailored to achieve maximum particle packing density and approximates Fuller-Thomson's ideal grading [42]. The binder is comprised of PPC Suretech 52.5 N (CEM II) Portland cement, micro-silica fume, and DuraPozz class F fly-ash as extenders. Continuously graded Malmesbury coarse aggregate with a 4.75 mm maximum particle size is utilised. The incorporated additives are comprised of Chryso Premia 310, a modified polycarboxylate polymer-based superplasticiser, and Chryso Quad 20, a liquid hydroxypropyl methyl-cellulose viscosity modifying agent (VMA), respectively. Furthermore, 6-mm polypropylene (PP) microfibers with the specific properties listed in Table 3.2 are entrained during mixing at a 1 % dosage by volume. The mixture has a water to cement ratio of 0.45 and a 28-day cast compressive capacity of 78 MPa, therefore qualifying as a high-performance concrete (HPC). Note that due to the entrained fibre length and volume fraction, the material is contended to exhibit strain-softening behaviour [43]. The thixotropic characteristics of the mixture are summarised in Table 3.3 and the procedure followed to attain the rheological parameters is presented in [44].

Table 3.1: Fibre-reinforced printable concrete (FRPC) mixture constituent proportions.

Constituent	kg
PPC Suretech CEM II/A-L 52.5 N	562
Durapozz Fly Ash (Class F)	162
Micro Silica Fume	81.4
Fine Aggregate (Malmesbury)	1144
Water	256
Superplasticizer	0.6 % by binder mass
VMA	0.3 % by binder mass
6 mm PP Microfibres	1 % by mixture volume

Table 3.2: Polypropylene (PP) microfibre properties.

Description	Value
Young's Modulus (E_f)	3 GPa
Yield Stress (f_t)	300 MPa
Diameter (Ø)	30 µm
Length (L)	6 mm

Table 3.3: Thixotropic characteristics for two 3D printable mixtures developed at Stellenbosch University. Note that a representative printable base mixture is employed in both cases.

Mixture	$\tau_{S,I}$ (Pa)	$\tau_{D,I}$ (Pa)	R_{thix} (Pa/s)	A_{thix} (Pa/s)
Standard HPC [25]	1545	560	2.04	0.32
PP FRPC	2152	1789	7.29	1.13

Experimental Methodology

In this research, four mechanical characterisation experiments are conducted. These include direct tensile tests (DTT), uniaxial compressive tests (UCT), Young's modulus (E_{mod}), and four-point bending (FPB) crack mouth opening displacement (CMOD) fracture tests. The experimental programme seeks to attain a host of intrinsic material characteristic parameters, which are essential to numerically simulate the linear and non-linear response of elements realised by extrusion-based 3DCP. The secondary objective of the presented experimental programme is to elucidate the anisotropic mechanical attributes portrayed by 3DCP components. Furthermore, through the acquisition of the aforementioned parameters, suitable constitutive relations in compression and tension can be selected and implemented in state-of-the-art FEM packages, which is envisioned to enable comprehensive, yet pragmatic, computational modelling strategies to be developed for 3DCP.

All specimens are extracted from the 3DCP object shown in Fig. 3.1, to ensure that the material, process and design parameters employed are accurately represented. The mixture has the rheological properties presented in Table 3.3. The item is fabricated in a 3 degree of freedom gantry-type 3D printer with one cubic meter build volume [45] and has a building height of 250 mm, comprising 10 mm layer heights, a print path length of 4 m, and is printed at 60 mm/s in 22 min with a Ø25 mm nozzle. Samples are extracted from the 3DCP object to ensure that the interdependent material, fabrication process, and design parameters (i.e., rheological properties of the mixture, layer height, print speed, nozzle standoff distance, print time interval, and climatic conditions) remain consistent. Table 3.4 presents a summary of the experimental programme indicating the number of samples experimentally evaluated. Due to the anisotropic nature of 3DCP elements, samples are extracted in the respective zones illustrated in Fig. 3.1(b), in the directions shown. Direction 1 (D1) coincides with the longitudinal printing direction in which the entrained PP microfibres are predominantly aligned, Direction 2 (D2) is associated with the bond between adjacent filaments representing the transverse capacity of the element in zone 2. Finally, Direction 3 (D3) corresponds to the layer stacking direction and is indicative of the interlayer bond strength (IBS). All specimens are cured in a climate-controlled room (23 ± 2 °C and 65 ± 5% relative humidity) and tested at a 28-day concrete curing age. Furthermore, an Aramis DIC system [46] is utilised to capture the in-plane 2D displacement and deformation fields within loaded specimens. Before testing, the samples are sprayed white, and an evenly dispersed matte-black speckled stochastic

pattern for DIC measurement is applied. Note that only qualitative photographic data of the observed failure planes is extracted from DIC measurement.

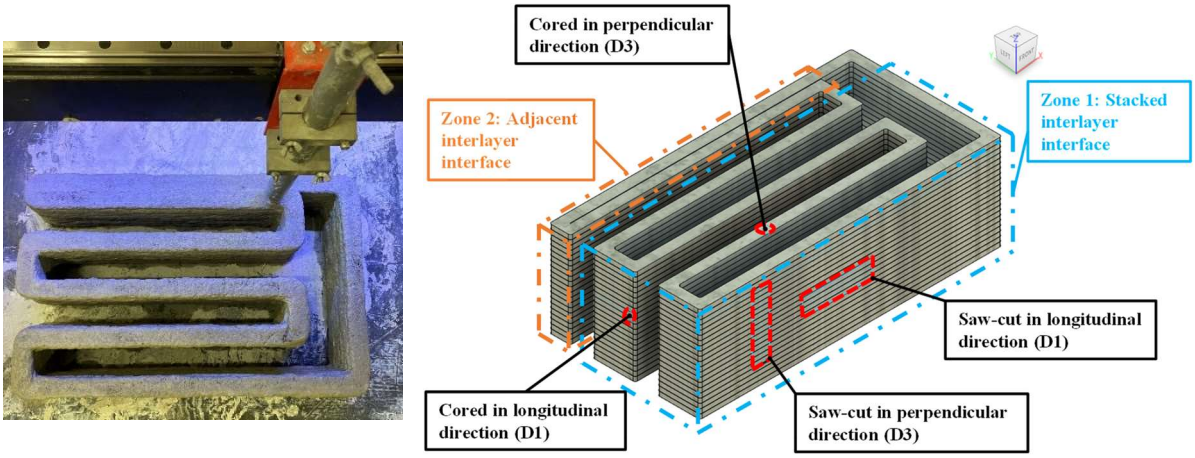

(a) (b)

Fig. 3.1: 3DCP object from which samples are extracted, (a) Plan view of the actual item, (b) Isoparametric view of the 3DCP object illustrating the various zones from which specimens are extracted and their respective orientations.

Table 3.4: Summary of experimental testing procedure at a 28 concrete curing age.

Test	Samples
Direct Tensile Test (D1)	6
Direct Tensile Test (D2)	4
Direct Tensile Test (D3)	4
Compression (D1)	6
Compression (D3)	6
E_{mod} (D1)	3
E_{mod} (D3)	3
FPB-CMOD fracture (D1)	6
FPB-CMOD fracture (D3)	6

Direct tension test

Direct tensile tests are conducted to experimentally investigate the mechanics of fracture in 3DCP components. In these tests, the linear strength and deformation parameters, as well as, the non-linear fracture parameters of the 3DCP samples are ascertained. Since 3D printed concrete is a cementitious engineering material, a quasi-brittle fracture response is expected [31]. The linear strength parameters are assessed via the maximum tensile strength ($f_{t,i}$) and corresponding deformation ($\delta_{peak,i}$), exhibited in the respective loading directions. The characteristics of the non-linear strain-softening branch are evaluated based on the fracture energy ($G_{ft,i}$) and maximum crack mouth opening displacements ($\delta_{f,i}$)

attained in the respective loading directions. These specific material parameters are required for the computational simulation procedures presented in Section 3.5.

Specimen geometry and boundary conditions

The presented DTTs are performed on 40 x 30 x 60 mm (b x d x L) notched and on 40 x 40 x 60 (b x d x L) unnotched samples, as illustrated in Fig. 3.3. The unnotched samples correspond to the transverse direction since while printing the authors appreciated that the interface between adjacent interlayers (printed with a circular nozzle) is not completely rectilinear but instead curved (s-shaped), as presented in Fig. 3.2. For this reason, the samples are not notched, allowing the interfacial failure surface to be investigated. Additionally, only the peak load is a measurable parameter, as the irregular and non-coincidental failure surface would distort the stress distribution and fracture energy over a section of the failure surface.

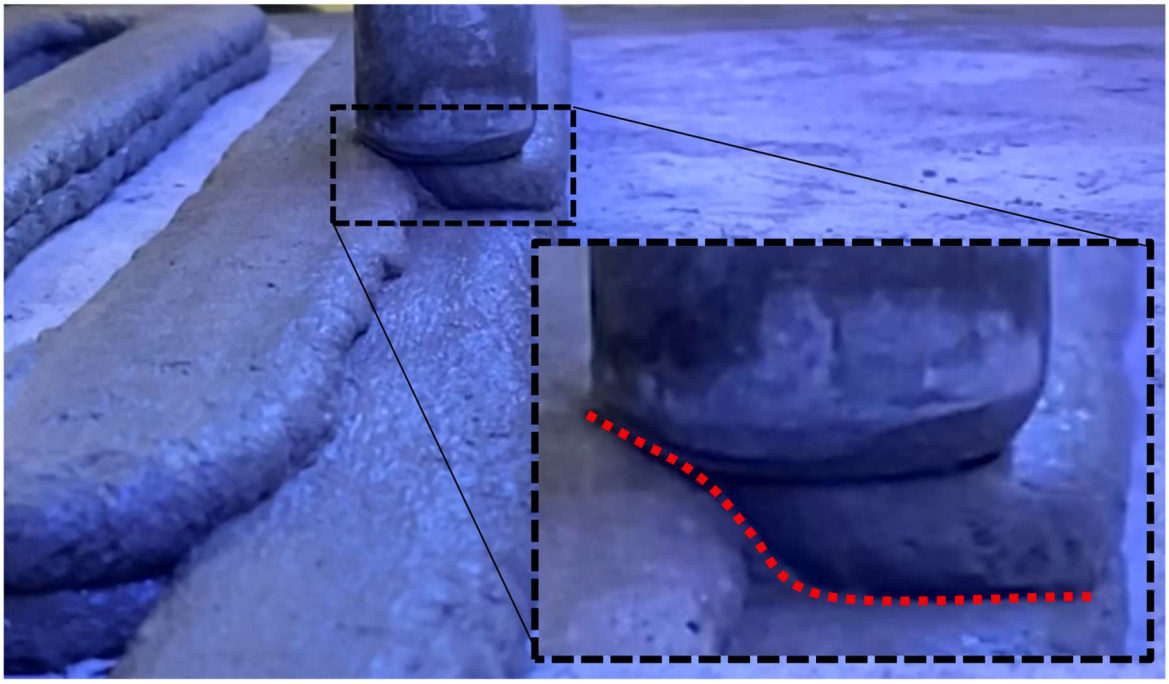

Fig. 3.2: Illustration of the formation of an S-curved interface between adjacently deposited filaments.

The DTTs are performed in the respective directions, utilising a 50 kN Instron stand-alone servo-hydraulic actuator, accompanied by a 5 kN HBM load cell, and an 8 mm Instron clip-gauge extensometer. The prisms are aligned, epoxy glued to symmetric steel T-sections, and cured for five days in a climate-controlled room. Fixed end constraints ensure that rotation is not prevalent on the fracture interface, warranting the representation of independent mode conditions. Additionally, a 3.5 mm wide mid-height notch (L_n), with a 1.75 mm tip radius, ensures a predictable failure plane. The notch depth is approximately 5 mm on either side of the specimen, rendering a notched specimen width (b_n) equal to 30 mm. Care is taken whilst extracting and preparing the samples, ensuring that the integrity of the interlayer regions is not compromised.

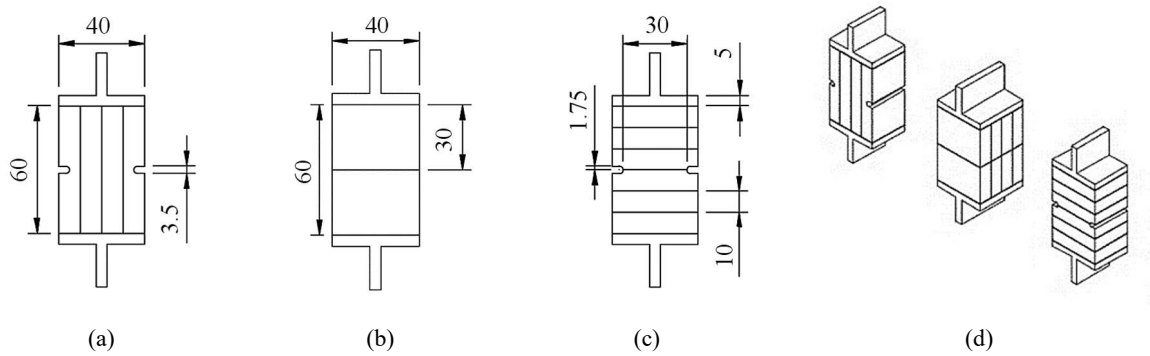

(a) (b) (c) (d)

Fig. 3.3: Direct tensile test (DTT) specimen geometry, illustrating the (a) Longitudinal (D1), (b) Transverse (D2), (c) Perpendicular (D3), and (d) an isoparametric view of the respective configurations.

Loading rates and sequence

Preliminary investigations on specimens with identical geometric and material attributes, displayed a $\delta_{peak,D3}$ approximately equal to 0.002 mm at a $f_{t,D3}$ of 1214 N, and a $\delta_{peak,D1}$ roughly equal to 0.0046 mm at a $f_{t,D1}$ of 2743 N [18]. However, snap-back behaviour is observed under the test configuration previously employed. Therefore, a closed-loop displacement-based loading sequence comprising of the three-phase loading sequence presented in Table 3.5 is used, accompanied by a constant data acquisition rate of 20 Hz for all DTTs.

Table 3.5: Loading sequence in respective test directions.

Loading phase	Loading rate	End of phase indicator
D1 - elastic	0.1 mm/min	F = 1800 N
D1 - peak	0.002 mm/min	CMOD = 0.03 mm
D1 - tail	0.1 mm/min	CMOD = 3 mm / failure
D2 - elastic	20 N/s	failure
D3 - elastic	0.1 mm/min	F = 800 N
D3 - peak	0.002 mm/min	CMOD = 0.015 mm
D3 - tail	0.1 mm/min	CMOD = 2 mm / failure

The three phases are diagrammatically simplified and shown in Fig. 3.4 as *elastic*, the reversible portion of the F-CMOD response, *peak*, the upper 30 % of the linear region where tensile fracture occurs and softening commences, and *tail*, expresses the evolution of the softening branch until complete failure occurs.

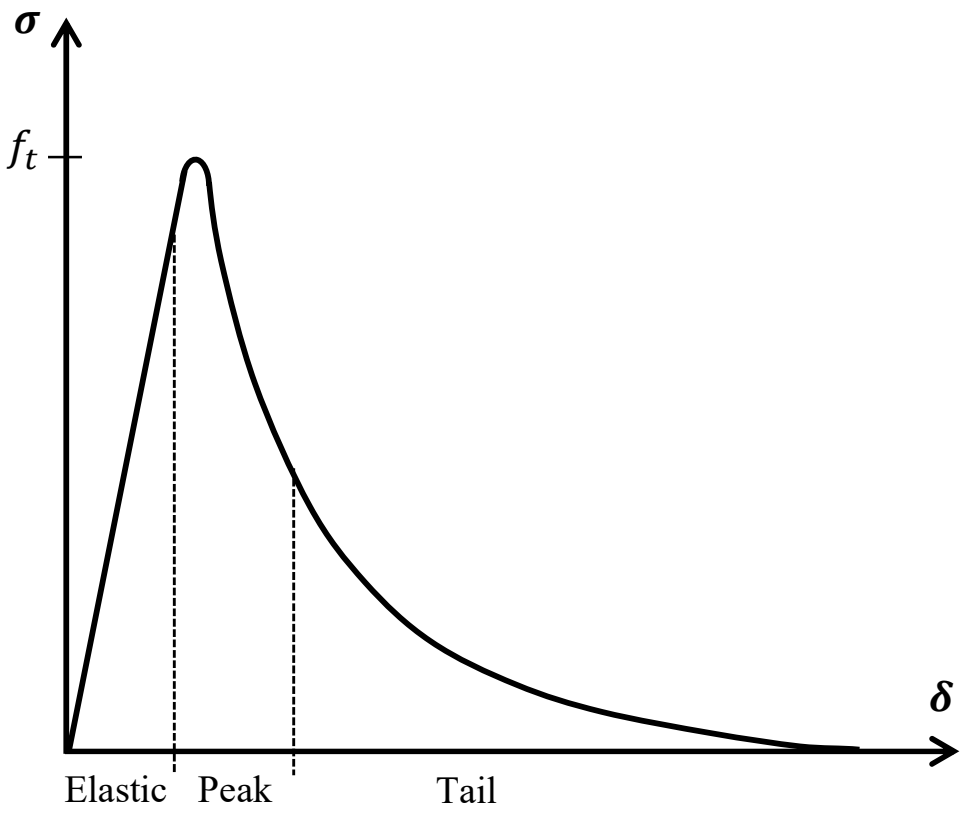

Fig. 3.4: Simplified representation of typical stress vs. displacement response exhibited under uniaxial tension loading of a quasi-brittle material, illustrating the respective phases of the loading sequence.

Uniaxial compression tests

Uniaxial compression tests are conducted on cored samples to determine the compressive strength in the respective loading directions, and the experimental procedure is founded on the ASTM C 39/C 39M – 03 Standard Testing Method for Compressive Strength of Cylindrical Concrete Specimens [47]. In this experiment, six 28 x 60 mm cored cylinders, per orientation, are extracted from the 3DCP object presented in Fig. 3.1 and tested at a 28-day concrete curing age. The top and bottom ends of the compressive samples are surface ground to ensure that the loading surfaces are flat and parallel to one another. The UCTs are conducted in a Zwick Z250 universal material testing machine (MTM) with an open-loop force-controlled test configuration, presented in Fig. 3.5, at a continually increasing rate of 150 N/s. The tests are terminated upon complete specimen failure, and the failure type is recorded. Furthermore, the compressive strength is computed by dividing the ultimate load attained during the test by the specimen specific cross-sectional area. Note that the compressive fracture energy is computed using Equation 3.7.

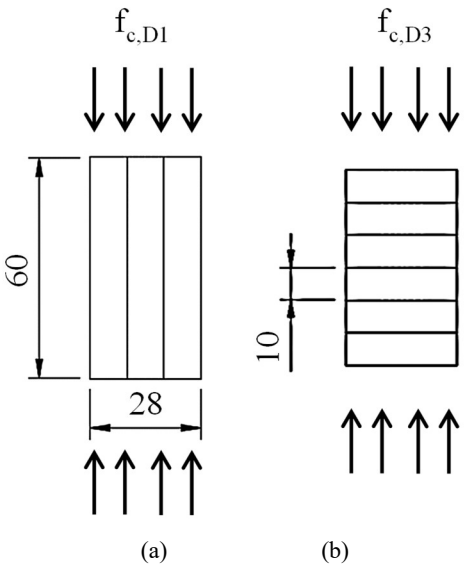

Fig. 3.5: Compression test sample geometry, illustrating (a) the Longitudinal (D1) and (b) Perpendicular (D3) configurations, respectively.

Young's modulus determination

The Young's Moduli (E_{mod}) are evaluated in the respective orthogonal directions presented in Section 3.3.2, at a 28-day concrete curing age. Samples comprise of 28 x 60 mm (diameter x height) cored cylinders extracted from the 3DCP object presented in Fig. 3.1. Three 300-ohm linear strain gauges, with a 6 mm gauge length, are circumferentially positioned at 120-degree increments to ensure that the three-dimensional deformation of the loaded samples is effectively captured, as illustrated in Fig. 3.6. Strain gauges are epoxied to samples using the X60 two component adhesive of HBM, suitable for strains ≤ 4%, rough concrete surfaces, and testing temperatures ≤ 60 ℃. The strain readings are captured using a quarter-bridge configuration via a Quantum MX840b data acquisition system at a sampling rate of 20 Hz, and the corresponding applied axial load is acquired using an HBM 5 kN load cell attached to the crosshead of the Zwick Z250 MTM. The force-based loading regime is repeated three times and conducted at a loading rate of 150 N/s up until 40 % of the maximum compressive capacity of the material, corresponding to the respective loading directions, is reached.

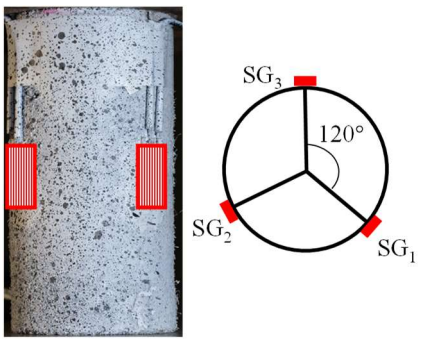

Fig. 3.6: Illustrates the cored E_{mod} samples and the strain gauge (SG) configuration.

CMOD four-point bending fracture test

FPB tests are conducted in the respective loading directions, on 40 x 30 x 160 mm samples. Six samples per orientation are tested at a 28-day concrete curing age. The FPB test is performed using a 50 kN Instron servo-hydraulic testing frame under the closed-loop displacement-controlled loading regime presented in Table 3.6. A clip-gauge placed within the notched region controls the loading rate, ensuring a predetermined rate of CMOD. A 5 kN HBM load cell is installed on the actuator head to continuously monitor the transmitted load with high accuracy in the low-force range applied, at a 20 Hz sampling rate.

Specimen geometry and boundary conditions

Fig. 3.7 depicts the specimen geometry and layer orientation. A notch with of width 3.5 mm and height 10 mm is created. The load inducing rollers are equally spaced at 50 mm third points, creating a frictionless lateral support condition. FPB is selected since pure bending is prevalent between the inner support points (i.e. theoretically no shear is induced between internal supports); thus the results obtained from the DTTs can be interpreted and compared to the FPB test results in terms of tensile behaviour.

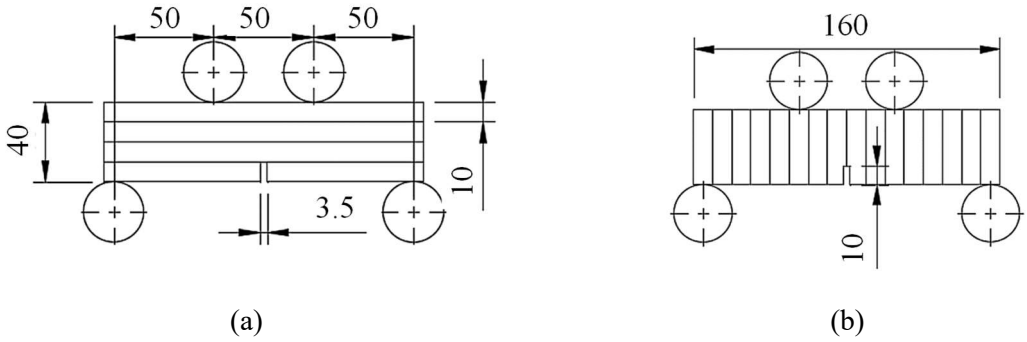

Fig. 3.7: Crack mouth opening displacement fracture samples, illustrating the (a) Longitudinal (FPB-D1) and (b) Perpendicular (FPB-D3) configurations, respectively.

Loading rates and sequence

Preliminary tests on companion specimens provided insights concerning suitable loading rates and transition points for the three-phase sequence presented in Table 3.6. The three phases are somewhat similar to those shown in Fig. 3.4, but the *elastic* portion (ending at the limit of proportionality) is proceeded by a more pronounced non-linear deflection hardening *peak* phase with higher strain capacity before reaching the modulus of rupture, the softening portion (*tail*) displays decaying load-carrying capacity at increasing CMOD.

Table 3.6: Loading sequence in respective flexural test directions.

Loading phase	Loading rate	End of phase indicator
D1 - elastic	0.2 mm/min	F = 800 N
D1 - peak	0.01 mm/min	CMOD = 0.5 mm
D1 - tail	0.1 mm/min	CMOD = 3 mm / failure
D3 - elastic	0.2 mm/min	F = 400 N
D3 - peak	0.01 mm/min	CMOD = 0.2 mm
D3 - tail	0.1 mm/min	CMOD = 2 mm / failure

Results and Discussions

Direct tension test

In this section, the DTT results, conducted in the respective loading directions, are illustrated and interpreted. A two-fold degree in anisotropy is observed between samples loaded in D1 and D2 versus D3. All specimens displayed linear elastic behaviour up until their maximal loads, where after strain-softening behaviour typical of quasi-brittle materials, is observed [32]. In all instances, the tensile failure mechanism manifests as a single hairline fracture over the notched region, as depicted in Fig. 3.8. It is observed that some PP microfibres breach the interlayer region between subsequently deposited filaments, Fig. 3.9. In contrast, the PP microfibres are preferentially aligned in the extrusion direction, and randomly orientated over the region between adjacent interlayers, thereby partially elucidating the degree of anisotropy prevalent under tensile loading. Albeit, the above-mentioned effects pertaining to the mechanical interaction, chemical bonding, or physical forces between filaments should not be excluded [5].

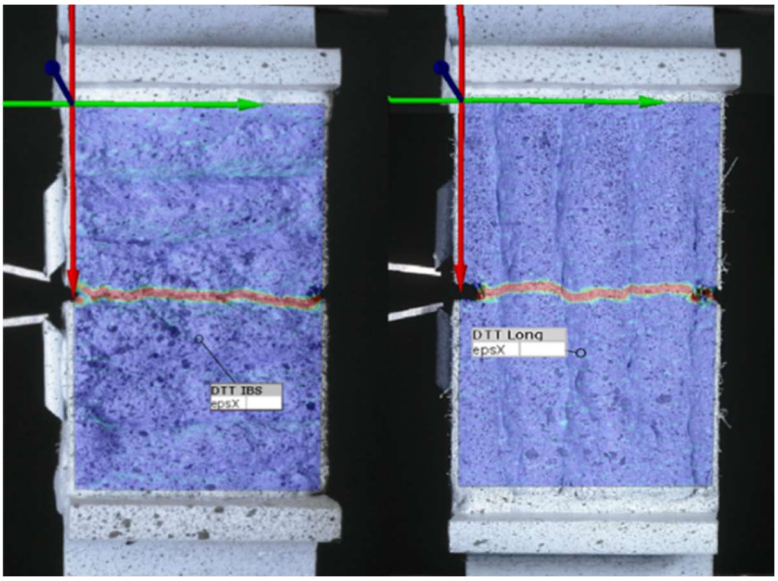

Fig. 3.8: Fracture pattern observed under direct tensile loading in D3 (left) and D1 (right), respectively.

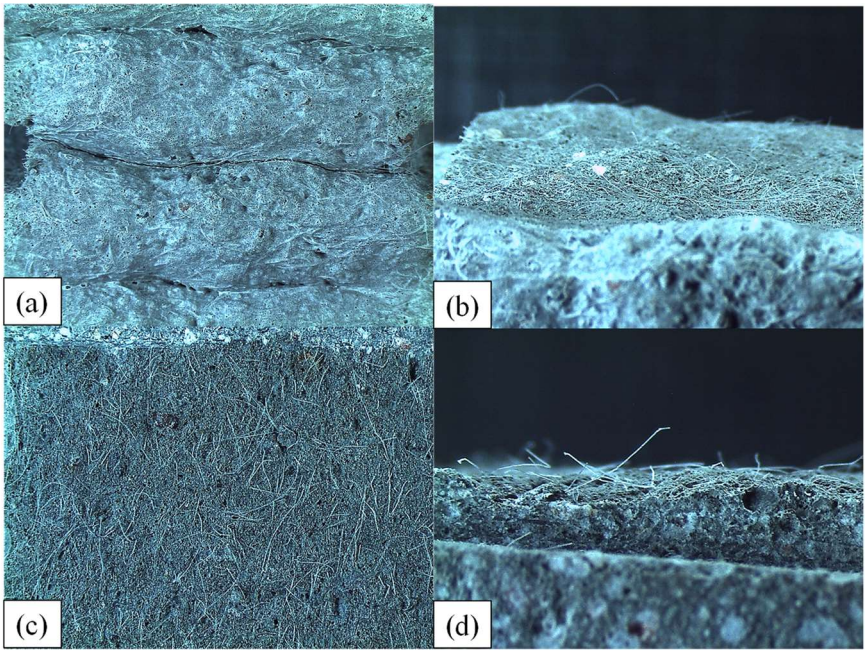

Fig. 3.9: Interfacial fibre breaching detected during DTT in D3. (a) illustrates the fracture plane between filaments, (b) shows the bottom half of the specimen, (c) depicts a plan view of the fracture surface, and the presence of PP microfibres, and (d) shows an elevation of the top half of the specimen (indicating the presence of fibres on the respective halves of the fractured interface).

Direction 1 direct tensile strength

The results of specimens loaded in D1 are illustrated in Fig. 3.10 and display a mean peak load of 2113 ± 204 N, attained at a mean CMOD of 0.0064 mm. Measuring the fracture surface geometry of individual specimens yields an average fracture area of 863 mm^2, comprising of an average notch width (b_n) of 30.5 mm and average layer width (d) equal to 28.3 mm. A mean tensile capacity ($f_{t,D1}$) of 2.45 ± 0.31 MPa is computed assuming a uniform stress distribution over the surface. However, $f_{t,D1}$ is 36 % lower than the expected (f_{ctm} = 3.82 MPa) tensile capacity considering the EN 1992-1-1:2004 [48] nominal value for concrete. A credible explanation may lie in the fact that the FRPC used in this study exhibits material behaviour more consistent with cementitious mortars than concrete, likely brought by the reduced aggregate sizes included in the mixture and associated crack tortuosity. One can further deduce that the entrainment of PP microfibres does not increase the tensile strength of the mixture employed but only improves the post-crack ductility. The reasoning is that the mortar-like matrix of the composite reaches its strain capacity and ruptures before comparative strain is built up in the PP microfibres, ascribed to the difference in stiffness (30 GPa vs. ≈22 GPa for the general FRPC) between the two materials.

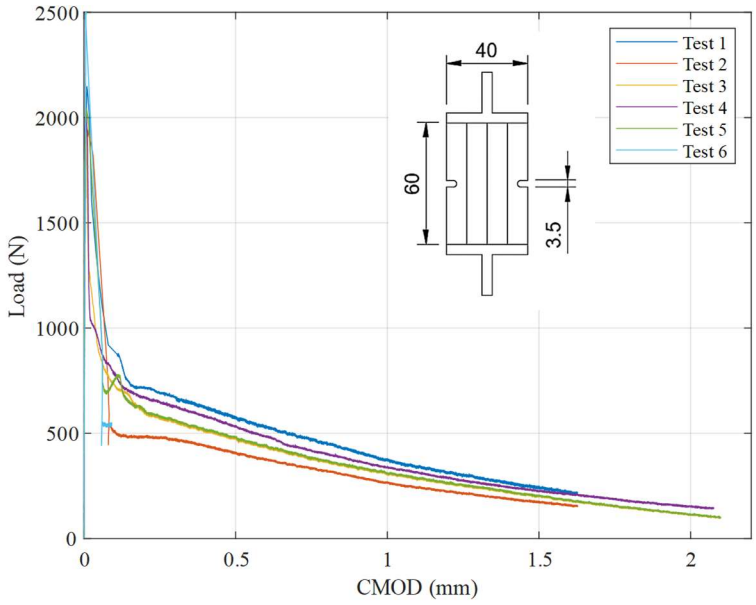

Fig. 3.10: Illustrates the raw data load vs. CMOD response of the specimens loaded in direction 1 (D1), representing the longitudinal intralayer capacity of the 3DCP samples in tension.

Considering the strain-softening portion of the F-CMOD response presented in Fig. 3.11, the experimentally determined loads are converted to corresponding tractions, using the original mean area of the DTT specimens, and averaged, a two-term exponential expression is fitted with a regression (R^2) equal to 0.99̇. The independent variable of the fitted expression (x = CMOD) extends from 0.0064 mm to 2.8 mm, respectively.

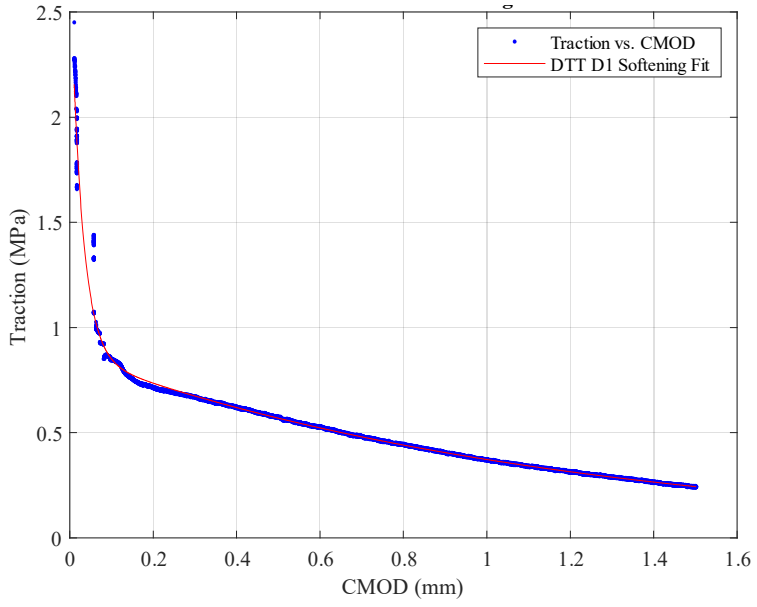

Fig. 3.11: Illustrates the average traction vs. CMOD pertaining to the strain-softening regime of the specimens loaded in D1.

$$f_{t,D1}(x) = a \cdot exp^{b \cdot x} + c \cdot exp^{d \cdot x} \tag{3.1}$$

Where: $a = 1.91$ $b = -36.05$ $c = 0.87$ $d = -0.85$

The expression is integrated over the bounds of the independent variable rendering a specific fracture energy ($G_{ft\text{-}D1}$) equal to 0.956 N/mm, notably higher than the fracture energy in direction 3 ($G_{ft\text{-}D3}$). The differential interlayer and intralayer fracture capacities are ascribed to the preferential alignment of the PP microfibres in the extrusion direction. Fig. 3.12 presents the approximated traction-CMOD relation obtained from the DTTs in D1. Find that the maximum CMOD ($\delta_{f,D1}$) is capped at 2.8 mm since no significant increase in $G_{f,D1}$ is prevalent beyond this point. An acute decline in tensile capacity persists straight after the maximal load is reached followed by a later addition in tensile ductility. It is theorised that this relation is attributed to two successive mechanisms: plain concrete fracture, with a comparatively lower energy dissipation potential, and then fibre activation at larger tensile separations, providing the additional ductility to the composite. It is understood that the favourable alignment of 3DCP elements relative to the induced loading components would yield superior structural performance and material efficacy.

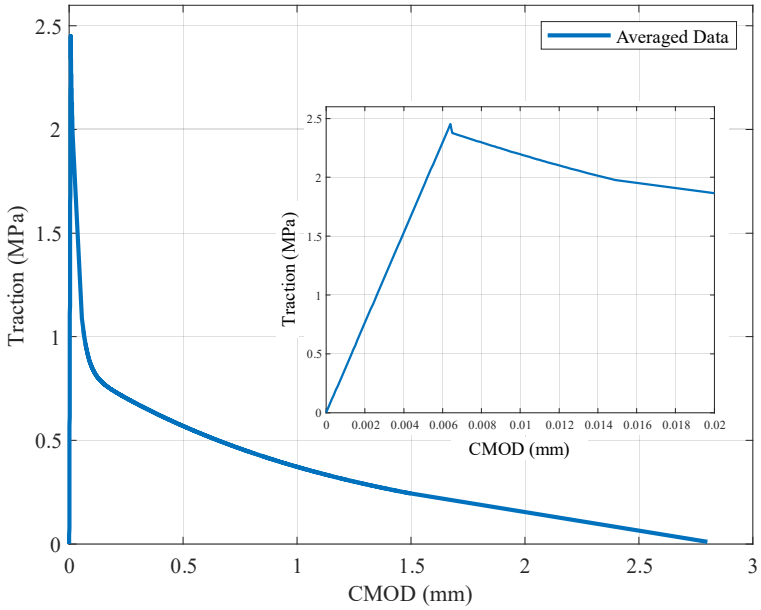

Fig. 3.12: Approximated traction-CMOD response pertaining to the longitudinal direction (D1).

Numeric evaluation of the presented approximate traction-CMOD response in D1 reveals that a Rankine type yield criterion and exponential softening is a suitable constitutive relation to be implemented in succeeding computational simulation procedures. As presented in Fig. 3.13, the implemented yield criterion effectively captures the elastic, peak, and ultimate displacements and tractions of the traction-CMOD response, but somewhat distorts the phases in which the available fracture energy is expended. It is deduced that the presented continuum approach will not impact the overall ductility prediction for larger elements (e.g., beams and walls) but might misrepresent corresponding deformations at certain post-peak loads. Evaluating the suitability of other softening

traction-separation regimes, such as the Hordijk, JSCE, and multi-linear formulations [49] it is determined that only the multi-linear formulation allows the post-crack traction-separation response to be precisely captured. However, it is appreciated that in the commercial DIANA FEA software package used, such functionality is only compatible with a discrete cracking model that employs cohesive elements at predefined interfacial locations. The continuum approach used in this research has exponential softening intrinsically embedded in its numeric framework and therefore disregards the potential advantages of an interface-based, discrete crack modelling strategy, such as the strategy successfully implemented in a recent study by van den Heever et al. [18].

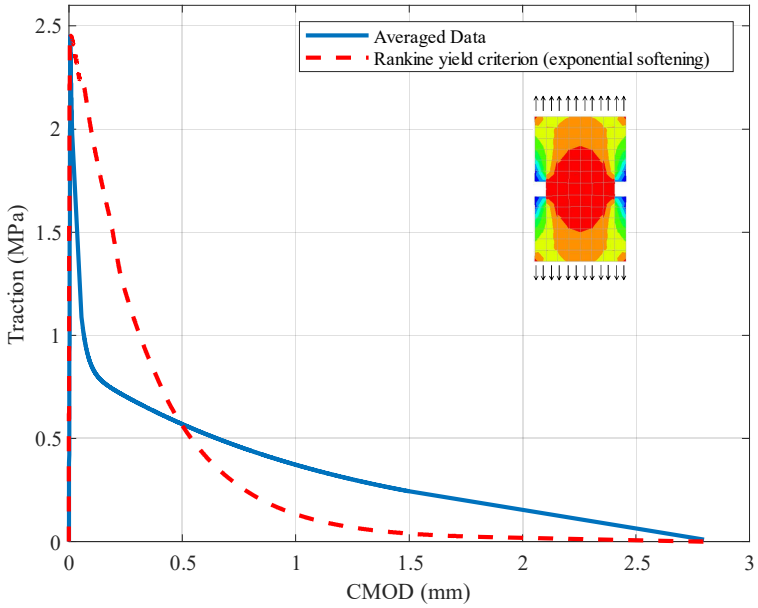

Fig. 3.13: Numeric validation of proposed Rankine yield criterion with exponential softening in D1.

Direction 3 direct tensile strength

The results relating to the DTTs in D3 are presented in Fig. 3.14; a mean peak load of 1007 ± 242 N is exhibited at a mean CMOD of 0.0032 mm. The interlayer fracture surface is approximately 805 mm^2, including an average notched width (b_n) equal to 29.1 mm and layer width (d) of 27.7 mm. Dividing the average peak load by the mean area, an interlayer tensile capacity ($f_{t,D3}$) of 1.25 ± 0.12 MPa is attained. The sizeable tensile load variance (24 %) is chiefly ascribed to geometric erraticism, presumably induced by inconsistent material extrusion, and the lower tensile strength variance substantiates this. The experimental result is in reasonable agreement with the 1.4 MPa presented by van den Heever et al. [18] in a preliminary study utilising the same material. The variation is ascribed to the 125 times higher loading rate (0.25 mm/min) applied in [18]. Conversely, $f_{t,D3}$ is 64 % lower than the expected (f_{ctm} = 3.43 MPa) nominal tensile capacity given by the EN 1992-1-1:2004 [48] for concrete, indicating that current guidelines should be revised and adapted for 3DCP specific guidelines.

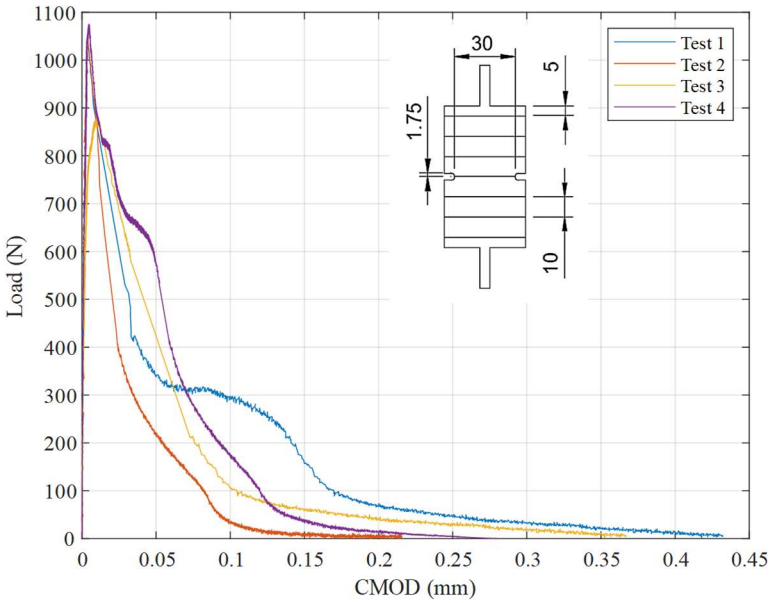

Fig. 3.14: Raw data presenting the load vs. CMOD response of the specimens loaded in direction 3 (D3), representing the interlayer bond strength (IBS) of the 3DCP samples.

To attain the strain-softening portion of the F-CMOD response presented in Fig. 3.15, the experimentally determined loads are converted to corresponding tractions, using the original mean area of the DTT specimens, and averaged, again a two-term exponential expression is fitted with a R^2 equal to 0.99̇. The independent variable of the fitted expression (x = CMOD) extends from 0.0032 mm to 0.43 mm, respectively.

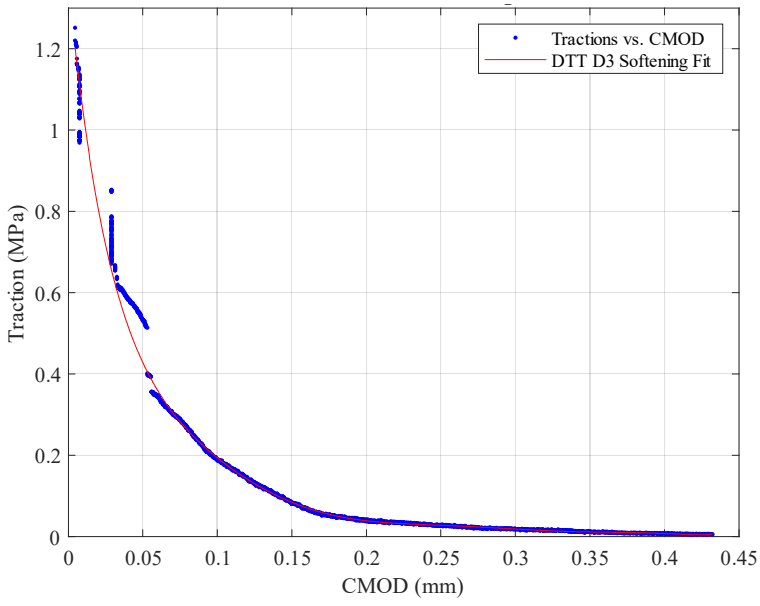

Fig. 3.15: Illustrates the average traction vs. CMOD pertaining to the strain-softening regime of the specimens loaded in D3.

$$f_{t,D3}(x) = a \cdot exp^{b \cdot x} + c \cdot exp^{d \cdot x} \tag{3.2}$$

Where: *a = 1.198* *b = -20.3* *c = 0.049* *d = -4.338*

Expression 2 is integrated over the bounds of the independent variable rendering a specific fracture energy ($G_{ft\text{-}D3}$) equal to 0.063 N/mm, notably less than $G_{ft\text{-}D1}$. Additionally, comparing the experimentally determined $G_{ft\text{-}D3}$ to the deterministic expression presented in [50] for G_{ft}, in Equation 3.3, it is inferred that the obtained result is in reasonable agreement with the stipulations for plain concrete (0.047 N/mm). Interestingly, $G_{ft\text{-}D3}$ is 34 % higher than the codified value, although the tensile capacity is less. Considering the microscopic visualisations presented in Fig. 3.9, it is deduced that the occurrence of a reasonable amount of interfacial fibre breaching (through the employed layer pressing strategy) marginally increases the interfacial ductility. Future studies aimed at exploiting this phenomenon, via an enhanced degree of thixotropy, could yield a comparative reduction in the degree of anisotropy portrayed in 3DCP structures. Fig. 3.16 shows the approximated traction-CMOD relation attained from the DTTs in D3.

$$G_{ft} = 0.025(2 \cdot f_t)^{0.7} \tag{3.3}$$

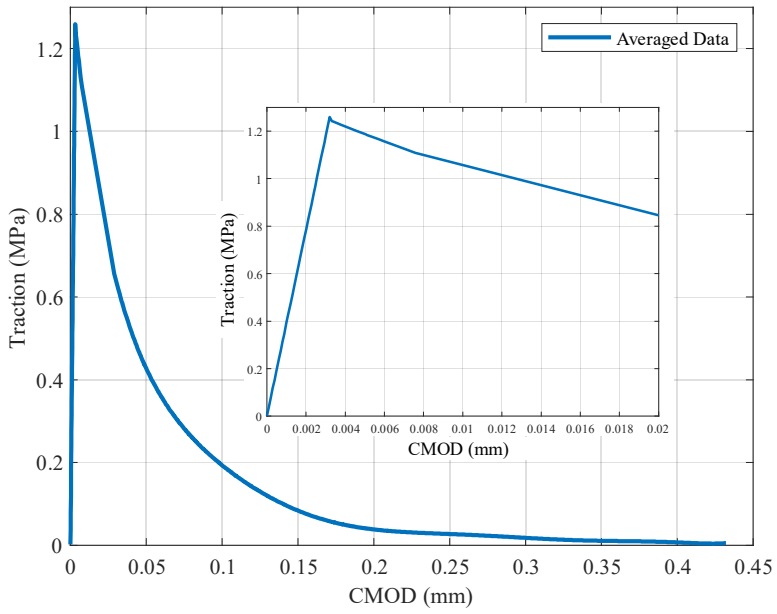

Fig. 3.16: Approximated traction-CMOD response pertaining to the perpendicular direction (D3).

Numeric evaluation of the presented approximate traction-CMOD response reveals that a Rankine type yield criterion and exponential softening is an eligible constitutive relation to be implemented for the simulation of the response in D3. This assertion is validated by the traction-CMOD plot presented in Fig. 3.17.

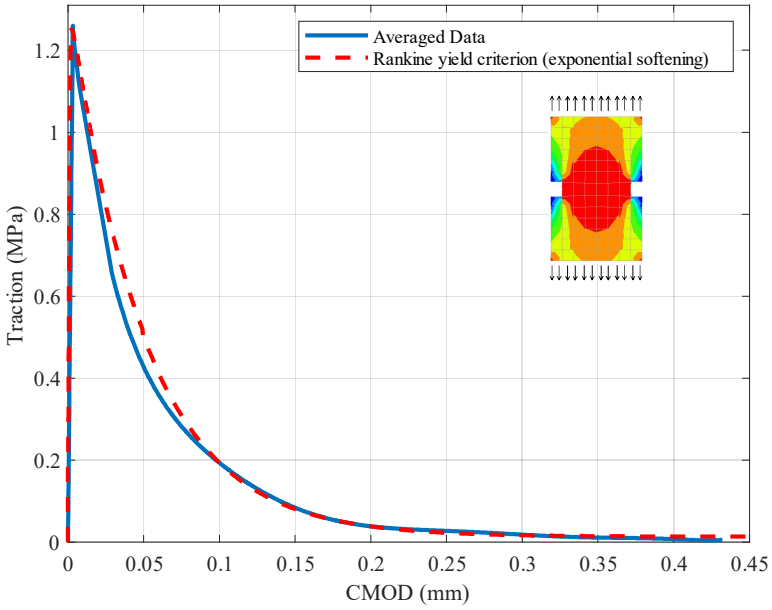

Fig. 3.17: Numeric validation of proposed Rankine yield criterion with exponential softening for D3.

Direction 2 direct tensile strength

Table 3.7 presents the peak loads obtained from the unnotched samples extracted in the transverse direction (D2); as shown an average peak load of 4349 ± 145 N is obtained, rendering an average tensile strength of 2.43 ± 0.05 MPa. Interestingly, this capacity is consistent with the intralayer (D1) capacity presented above. A likely result of the mechanical connection between neighbouring filaments induced by the transverse pressing action imposed when the centre line distance between adjacently deposited filaments is less than the expected layer width. The low coefficient of variation provides confidence in this assertion. Furthermore, this transverse pressing action in combination with a vertical folding action (resulting in the s-shaped interface) also induces sufficient disturbance on the contact interface allowing fibres to breach the interlayer zone. Fig. 3.18 illustrates the observed corrugated fracture pattern and depicts the presence of fibres. It is recommended that a parametric study be conducted to determine the optimal centre line spacing for a particular part manufactured via extrusion-based 3DCP. This study should consider the designed object, the rheological properties of the mixture, the process particularities, and the end-effector employed.

Table 3.7: Summary of direct tension tests in the transverse direction (D2).

Sample	F_{max} (N)	b (mm)	h (mm)	A (mm^2)	f_t (MPa)
S1	4464	42.5	42.3	1799	2.48
S2	4148	42.3	41.6	1748	2.37
S3	4447	42.5	42.4	1800	2.47
S4	4337	42.5	42.6	1812	2.39
Mean	4349	42.5	42.16	1790	2.43
				CoV	2.2%

Fig. 3.18: illustrates the undulating tensile failure surface for specimens loaded in the transverse direction (D2).

Compressive strength

The compressive strength of samples loaded in D1 ($f_{cu,1}$) is 17 % higher than D3 ($f_{cu,3}$). Both sets portray limited variance confirming the suitability of cored cylinders for characterising the compressive strength of 3DCP samples. Measuring individual specimens displays an average aspect ratio (height/diameter) equal to 1.9; therefore, an interpolated adjustment factor is applied to all specimens [47]. Although the dimensionality of the respective samples differed, the results are within a 4% variation of those presented in [18,47], and within the CoV of the data presented hereafter. The analysis of variance (ANOVA) indicates that the population means are distinctly different ($\alpha = 0.05$, P-value = 0.0019); accordingly, the anisotropy in D1 and D3 is statistically verified. The UCT validate that the heterogeneous qualities of 3DCP are also portrayed in compression.

Direction 1 Compressive Strength

The results obtained for the UCTs conducted in D1 are summarised in Table 3.8. A mean compressive strength of 45.1 $\pm$ 2.6 MPa is observed. As depicted in Fig. 3.19(a), all specimens exhibited a distinct columnar failure pattern induced by interlayer delamination. Interlayer delamination is ascribed to additional porosity on interlayer regions, causing reduced tensile capacity [21]. Kruger and van Zijl [5] report that the formation of lens-shaped voids, elongated in the extrusion direction (D1) and squeezed in the stacking direction (D3), imposes reduced chemical and physical bonding between filaments, and thus lowers interlayer adhesion. Nerella et al. [17] substantiate this assertion and provide SEM images that visually illustrate the effects of air enclosure between a subsequently deposited filament and the undulating surface of a previously deposited substrate layer.

Table 3.8: Compressive strength in the longitudinal direction (D1).

Specimen	F_{max} (N)	D (mm)	h (mm)	A (mm²)	f_{cu} (MPa)
Specimen 1	30170	30.5	58.7	730.6	41.0
Specimen 2	31223	30.2	58.6	716.8	43.4
Specimen 3	33174	30.4	58.6	723.9	45.6
Specimen 4	33634	30.4	58.6	725.8	46.1
Specimen 5	33457	30.3	58.6	721.5	46.1
Specimen 6	34767	30.1	58.7	713.0	48.6
				Average	45.1
				CoV	5.7%

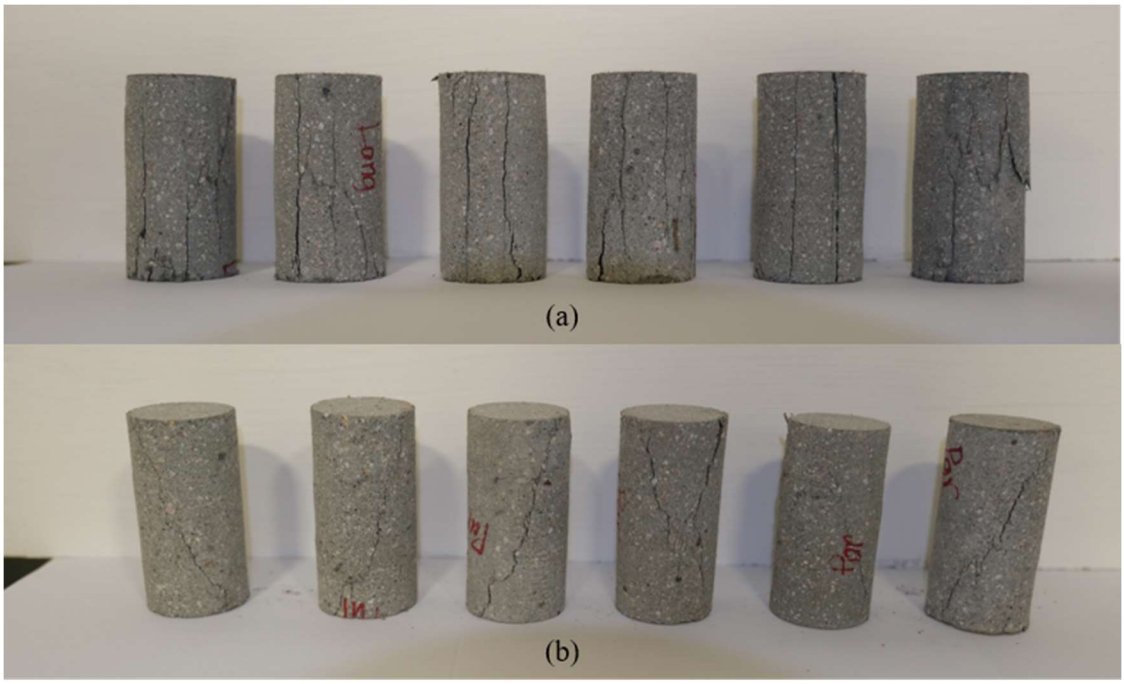

Fig. 3.19: illustrates the compressive failure modes for, (a) the longitudinal direction (D1) and (b) the perpendicular direction (D3).

Direction 3 Compressive Strength

The compressive strength in D3 is summarised in Table 3.9. An average compressive strength of 38.2 ± 3.6 MPa is attained. As illustrated in Fig. 3.19(b), conventional conical, and shear failure patterns are observed. The reduction in compressive strength can be due to a fibre-induced increase in the entrapped air, thereby increasing the porosity of the mixture. Nematollahi et al. [21] validate this postulation and present a 3.7 % (from 10.4 % to 14.1 %) increase in the apparent porosity of a fibre-reinforced geopolymer matrix.

Table 3.9: Compressive strength in the perpendicular direction (D3).

Specimen	F_{max} (N)	D (mm)	h (mm)	A (mm²)	f_{cu} (MPa)
Specimen 1	24934	30.4	58.4	725.8	34.1
Specimen 2	27431	30.7	58.5	739.2	36.8
Specimen 3	27255	30.3	57.0	721.0	37.4
Specimen 4	28299	30.4	56.6	724.9	38.6
Specimen 5	29224	30.3	58.1	719.6	40.3
Specimen 6	30908	30.3	51.4	720.1	41.9
				Average	38.2
				CoV	7.1 %

It is still uncertain precisely why the compressive strength of extrusion-based 3DCP elements differs in the respective directions. However, leaning on the principles presented for the bulk strength of rock the authors propose that pore shape and orientation affect the bulk strength of the printed composite. Therefore, the observation that elliptically shaped microstructural voids consequently reduces the mechanical capacity in D3 appears to have a scientific basis. The theory suggests that tensile stress nucleation arises at the poles of the oblate voids induced by the embodied extrusion and deposition process [51]. Conversely, when loaded in D1 prolate voids would be more susceptible to buckling but are constrained and therefore, can resist more load since the void walls then fail in shear [51]. The concept is illustrated in Fig. 3.20, where compression and tension concentration factors are presented for a surrounding matrix with a Poisson's ratio of 0.25. Both higher compressive and tensile concentration factors are proposed for oblate pores. However, further investigation is required to validate these assertions in the context of extrusion-based 3DCP.

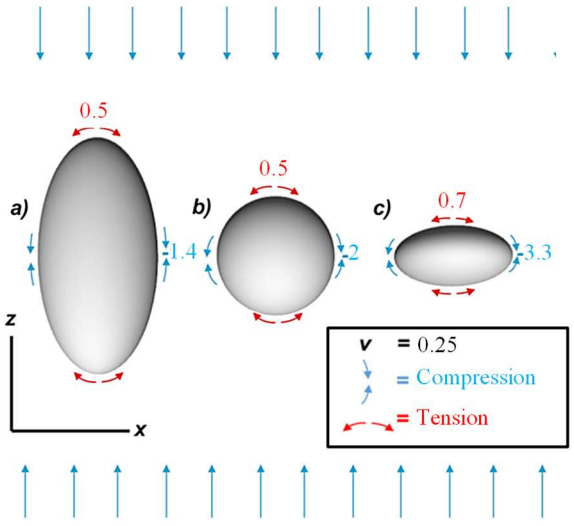

Fig. 3.20: Stress concentration factors derived from various void configurations, presenting (a) prolate, (b) spherical, and (c) oblate voids, respectively. Adapted from [51].

Young's modulus (E_{mod}) Determination

The results attained for the E_{mod} in the respective loading directions are summarised in Table 3.10. The test results show that the E_{mod} does not significantly differ in the individual orientations assessed, with D1 and D3, equal to 21.9 and 21.6 GPa, respectively. Indeed, an ANOVA suggests that the sample means are not statistically different ($\alpha = 0.05$, P-value = 0.75).

Table 3.10: Elastic modulus of cylindrical specimens.

Parallel to Interlayer (D1)			Perpendicular to Interlayer (D3)		
E1	22.4	GPa	E1	21.0	GPa
E2	20.7	GPa	E2	20.6	GPa
E3	22.6	GPa	E3	23.1	GPa
Average	21.9	GPa	Average	21.6	GPa
CoV	4.8%		CoV	6.2%	

Interestingly, the elastic moduli mutually exhibit a significantly lower stiffness considering the EN 1992-1-1:2004 [48] nominal specifications for determining the elastic modulus of plain concrete specimens presented in the equation below:

$$E_{cm} = 22\left({f_{cm}}/{10}\right)^{0.3} \tag{3.4}$$

Employing Equation 3.4, the E_{mod} in D1 and D3 should yield 34.56 and 32.89 GPa, respectively. The E_{mod} determined from cast samples utilising the same FRPC material presented in [18] is 32 GPa. This slight variation in the cast and codified nominal stiffnesses is ascribed to fibre inclusion and the mortar-like materials utilised for extrusion-based 3DCP. However, the approximately 8 GPa dissimilarity in the cast and printed samples is still ambiguous. Considering the increase in apparent porosity reported in [21] it is perceived that this phenomenon could have an adverse effect on the stiffness of the 3DCP composite. This premise is corroborated by Du et al. [52] who display that the effective elastic modulus (E^*) of porous concrete is quasi-linearly decreased with increasing porosity, with a slope of -0.67 GPa per percentage porosity (%p), between 0 and 30 %p. This requires a large disparity in porosity (≈12 %) to account for the 8 GPa distinction in the respective elastic moduli. Therefore, it is reasoned that additional effects such as pore shape and orientation may too affect the stiffness of printed concrete.

CMOD Four-Point Bending Fracture Test

The results of the respective CMOD-FPB fracture tests are presented in Fig. 3.21 and Fig. 3.22, respectively. A 2.2-fold degree of anisotropy is depicted in flexural loading, accompanied by a pronounced variation in flexural ductility. The limited flexural ductility exhibited over the interlayer

regions, and the strain-softening behaviour in the extrusion direction, calls for the development of compatible reinforcement strategies.

Direction 1 FPB Fracture Test

The F-CMOD curves obtained from specimens perpendicular to D1 exhibited negligible elastic response divergence but a rough variation thereafter. A linear branch characterises their initial loading response until micro-cracking occurs categorised by subsequent non-linear behaviour up to the peak load, where a single macrocrack is formed. Once the mean peak load (982 ∓ 56.6 N) is reached, the load-carrying capacity decayed, sharply, which indicates that a less notable FPZ exists in the vicinity of the crack tip. The sudden increase in load-carrying capacity, at a CMOD equal to 0.5 mm, is ascribed to the transition between the peak and tail loading regimes presented in Table 3.6. Evidently, loading rate dependency should be considered in subsequent experimental procedures.

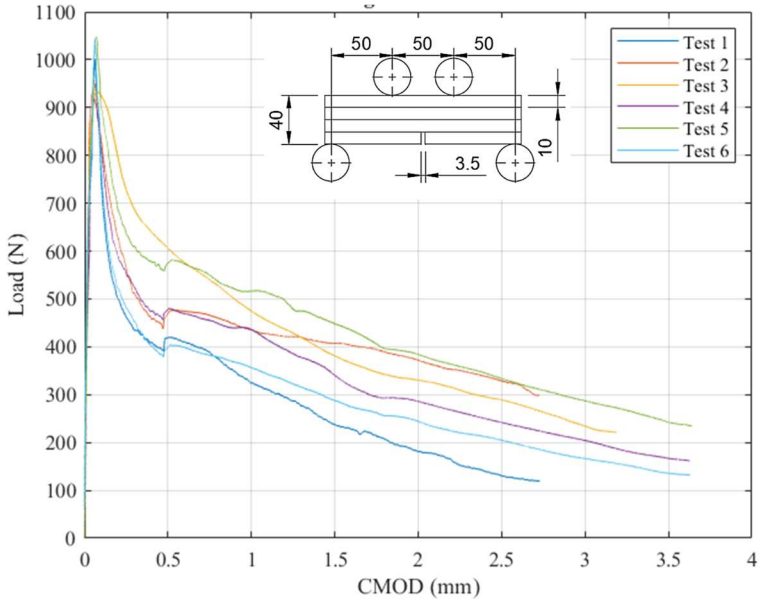

Fig. 3.21: Illustration of the four-point bending Force-CMOD response in the longitudinal direction (D1).

Direction 3 FPB Fracture Test

The F-CMOD curves obtained from specimens loaded parallel to D3 also portray insignificant elastic response divergence and acceptable variation thereafter. Their F-CMOD curves show a linear branch up to the initial micro-crack and subsequent non-linear deflection hardening behaviour until the peak load. Once the mean peak load (444 ∓ 22.7 N) is reached, the load-carrying capacity decayed, sharply, as also observed in D1. In all instances, complete fracture occurred in a somewhat inconsistent manner approaching a CMOD of 0.05 mm. The reason for the discrimination in post-peak stability between the D3 DTT and F-CMOD results is likely attributed to the increased rate at which the fracture area diminishes in the FPB-CMOD fracture test. Therefore, the presence of entrapped air voids, lack of fibre breaching, spatial non-uniformity, and other imperfections, have a more perceptible effect on the

flexural response. Loading rate dependence is visible in D1, bearing this in mind subsequent experimental procedures should consider slower loading rates if the F-CMOD response over the interlayer is desired. However, in this investigation, all tensile mechanical parameters are derived from the stable DTT procedure, and the F-CMOD is merely used for validation of the proposed numerical modelling strategy proposed in Section 0.

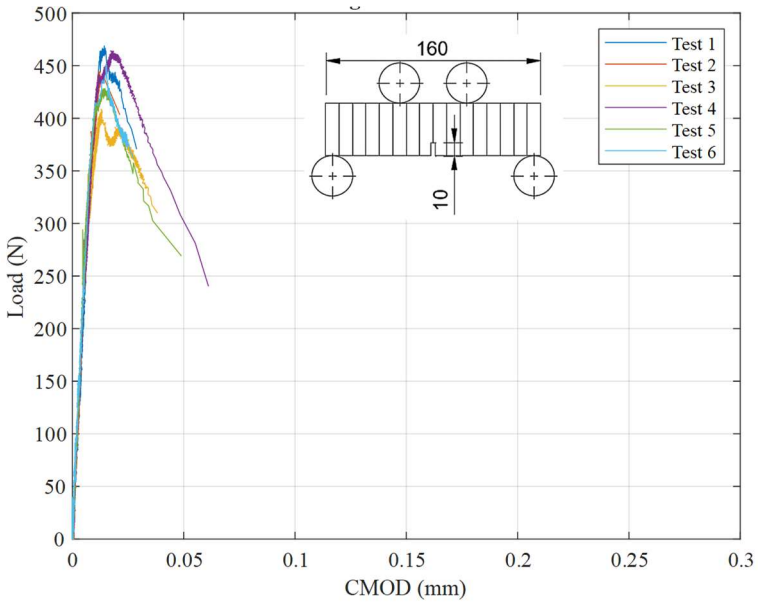

Fig. 3.22: Illustration of the four-point bending Force-CMOD response over the interlayer direction (D3).

Numerical Simulation Procedure for 3DCP

Although it is foreseen that the heterogeneous nature and associated degree of anisotropy prevalent in 3D printed elements can be mitigated to an extent by supplementary material and technological development [5,53], it is imperative that the orthotropic mechanical behaviour exhibited be considered in the development of numerical modelling strategies for 3DCP. Therefore, one should consider models that are capable of accounting for the differing capacities shown in the respective directions. Additionally, such modelling strategies and models should enable the design and analysis of 3DCP structures and contribute to the future codification of rational design guidelines specific to 3DCP. In this light, an analogy is drawn between 3DCP and more mature layered construction procedures such as masonry and laminates, where the extensively documented modelling strategies proposed for these layered construction procedures can be adopted in the design and analysis of 3DCP structures. In this research, a macro-modelling approach proposed by Lourenço et al. [36] is adopted for its potential to capture the macroscopic response of the tested elements. In this approach presented in Fig. 3.23, the deformation patterns associated with the expected failure mechanisms shown in Fig. 3.24 are approximated by the inelastic deformation of continuum elements.

Anisotropic Rankine-Hill (RH) continuum model

For the accurate analysis of 3DCP structures considered in a composite perspective, a material description for all principal stress states is required, which is complicated by the lack of standardised mechanical assessment protocol. Nevertheless, employing the aforementioned model adopted from Lourenço et al. [36] , isotropic elasticity and anisotropic plasticity and softening are combined to assess the response of 3DCP prisms under tensile and four-point flexural loading. Considering the results presented in Section 0, isotropic elasticity is a suitable assumption based on the similar Youngs' moduli ascertained and orthotropic yield criteria, with associated softening, is required. Suitably, the model permits exponential softening in the tensile (Rankine) regime and hardening, with subsequent exponential softening, in the compressive (Hill) regime [54].

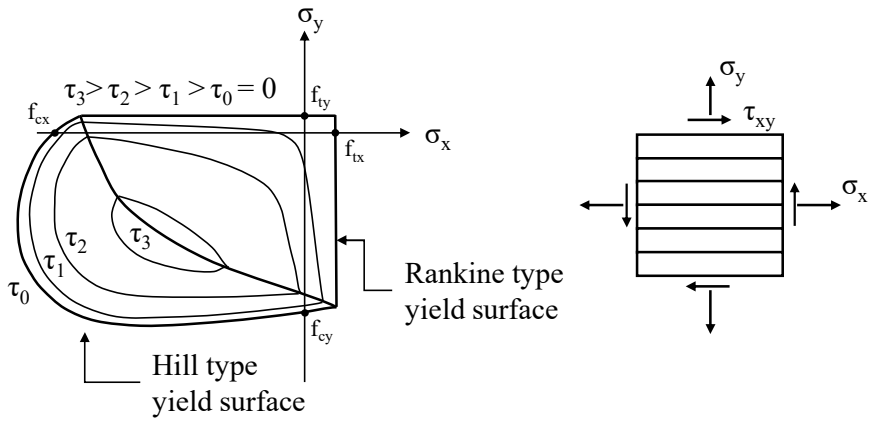

Fig. 3.23: Composite macro-modelling approach illustrating the adopted Rankine-Hill anisotropic continuum multi-surface plasticity model (adopted from [36]*).*

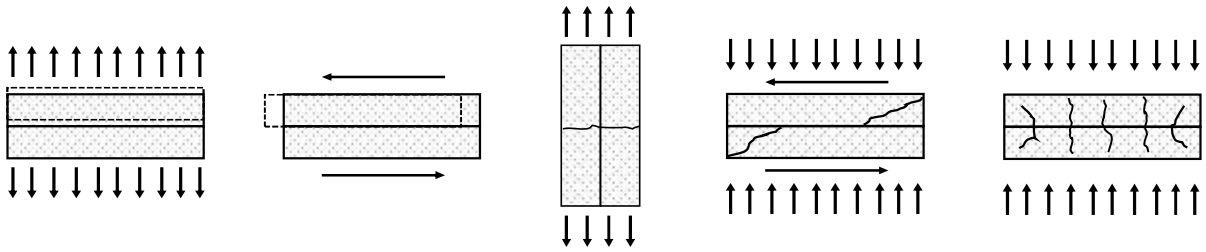

Fig. 3.24: Expected failure modes in 3DCP elements, (a) interfacial delamination, (b) interface shear-slip, (c) intralayer tensile cracking, (d) intralayer cracking under compression-shear, and (e) crushing (reworked for 3DCP from [36]*).*

Model parameters

Utilising the experimental results presented in Section 0, the two elastic parameters (E, ν), seven strength parameters (f_{tx}, f_{ty}, f_{cx}, f_{cy}, α, β, and γ), and five inelastic parameters (G_{fx}, G_{fy}, G_{fcx}, G_{fcy}, and κ_p) are ascertained. Note that the respective subscripts (x, y) refer to the orthotropic directions (D1) and

(D3) defined in Section 0. The extracted parameters are summarised in Table 3.11, supplementary reference to the theoretical basis of the employed model can be found in the DIANA FEA manual [54].

Table 3.11: Summary of Rankine-Hill model parameters.

Isotropic Elastic Parameters					
E	21.9/21.6	GPa	ν*	0.2	
Orthotropic Strength Parameters					
Direction 1 (x)			Direction 3 (y)		
f_{tx}	2.45	MPa	f_{ty}	1.25	MPa
f_{cx}	45.1	MPa	f_{cy}	38.2	MPa
Unitless Strength Parameters					
α	0.35	β**	-1	γ	0.525
Orthotropic Inelastic Parameters					
G_{fx}	0.956	N/mm	G_{fy}	0.063	N/mm
G_{fcx}	27.07	N/mm	G_{fcy}	26.17	N/mm
κ_p	0.0014	mm/mm			

**assumed based on the work presented in* [18].

*** β rotates the yield surface around the shear stress axis and can be determined from biaxial compression tests, however due to a lack of experimental data the default value of -1 is assumed.*

$$\alpha = \frac{f_{tx} \cdot f_{ty}}{\tau_u^2} \tag{3.5}$$

Where: τ_u is the interface shear-slip (Mode 2) capacity equal to 2.96 MPa from [18].

$$\gamma = \frac{f_{cx} \cdot f_{cy}}{\tau_u^2} \tag{3.6}$$

Where: τ_u is the material pure shear (Mode 2) strength equal to $1.5f_{c,y}$ MPa from [18].

$$G_{fc} = 15 + 0.43 \cdot f_c - 0.0036 \cdot f_c^2 \tag{3.7}$$

Where: G_{fc} is related to f_c the ultimate compressive capacity in the respective loading directions as presented in [50].

Model geometry and boundary conditions

The 2D plane stress FE model geometry and boundary conditions are presented in Fig. 3.25. The simulation is conducted using the commercially available FE-code DIANA FEA [55]. The model geometry is synonymous to that presented in Section 0, besides that the average specimen width (b) is adjusted to the measured means of 27.5 mm and 28.4 mm in D1 and D3, respectively. A non-linear elastic zero tension/shear interface connection is included between the respective loading and support plates, as well as, a rigid connection between the upper loading plates. In the analysis, the continuum finite elements comprise of 4 mm square eight-node quadrilateral isoparametric plane stress elements

(CQ16M), whilst compatible quadratic line interface elements (CL12I) are employed. The element mesh size (h) is well below the limiting $h \leq \frac{G_f \cdot E}{f_t^2}$, ensuring that snap-back at a constitutive level is avoided [56]. Regularisation of the energy dissipation is achieved by assuming that the inelastic work is uniformly distributed over the equivalent length h by $g_f = \frac{G_f}{h}$. Additionally, a crack bandwidth (h) equal to the notch width (3.5 mm) is manually prescribed, and the default super-hyperbolic Rankine and Rankine-Hill parameters (n = 16, m = 32) are assumed.

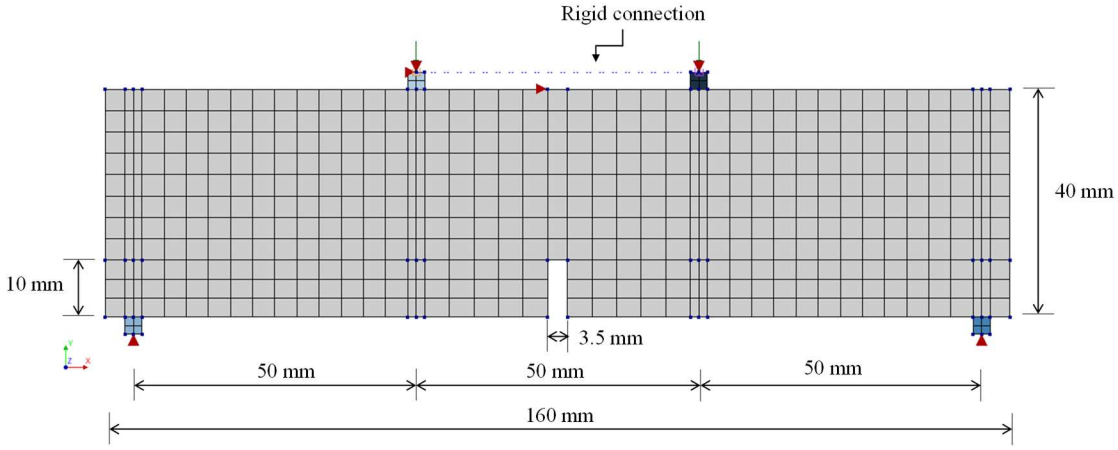

Fig. 3.25: illustrates the finite element model geometry, mesh, and boundary conditions.

The bottom support plates are constrained in the vertical direction, while the upper loading plates are constrained in the horizontal direction. A horizontal point constraint is applied to the specimen at the upper-midspan boundary to ensure that the sample remains centred relative to the loading plates. Furthermore, prescribed deformations of 1.65 mm and 0.9 mm, in the negative y-direction, are applied when simulating the flexure response in D1 and D3, respectively. To evaluate the FPB flexure response in the respective material directions, the local element orientation is varied for the two separate simulations. Wherewith layers vertically stacked (D1) the element local axes are as depicted in Fig. 3.25. In contrast, when layers are horizontally stacked (D3) the local axis system is simply rotated by 90 degrees to align the element local x-axis with the global y-axis.

Furthermore, a non-linear structural analysis, which considers material nonlinearity, in combination with an incremental-iterative secant (quasi-newton) BFGS solution procedure is utilised. Both energy and force convergence norms equal to 0.001 and 0.01 are respectively applied, and line search algorithm is employed to increase the convergence rate of the numerical analysis.

Numerical simulation results and discussions

The numerical results are presented in Fig. 3.26 and, in general, portray decent agreement with the experimental results attained. The maximum flexural loads in both D1 and D3, respectively equal to 961 N and 438 N, is within the observed standard deviation presented in Section 0. It is inferred that

the elastic and subsequent non-linear hardening permitted by the Hill regime accurately captures the pre-peak behaviour. As depicted in the DTT in D1, the acute decrease in post-peak capacity directly after the peak load is overestimated by the exponential softening constitutive relation embedded in the RH anisotropic continuum model; however, the capacity at increasing CMOD is well embodied. The FPB flexure response in D3 exhibits a substantially more appropriate post-peak response, which is expected considering the strong agreement in the DTT results in D3.

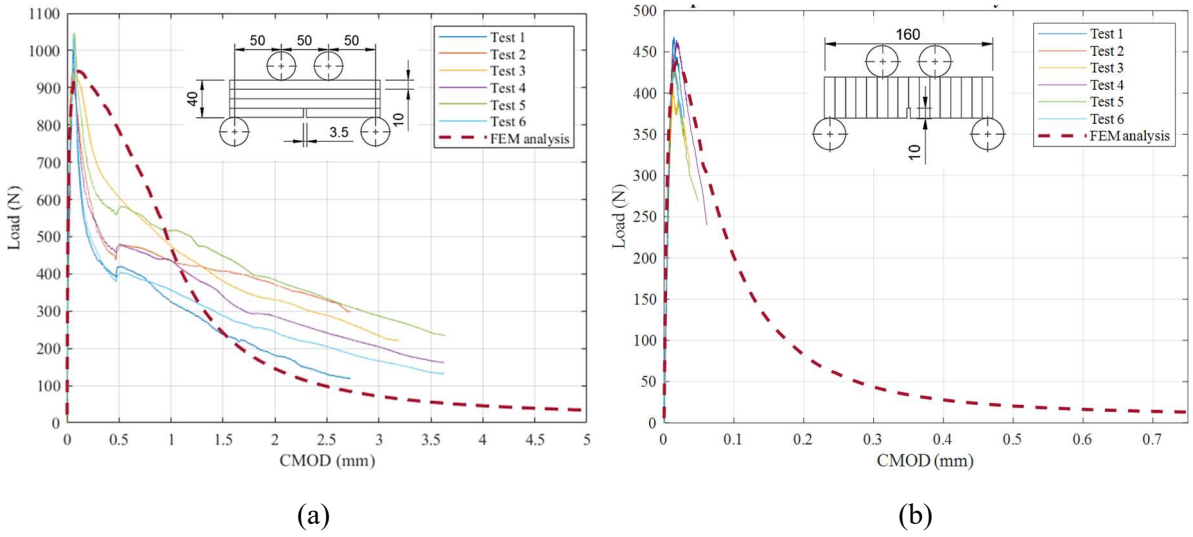

Fig. 3.26: Numerical simulation results illustrating (a) the FPB flexure response in D1, and (b) D3, respectively.

Fig. 3.27 presents the normalised displacement configurations and total Cauchy principal stress (S1) of the FPB-D3 flexural experiment. The onset of cracking and subsequent development is evident, exhibiting a trend that closely resembles the experimental results.

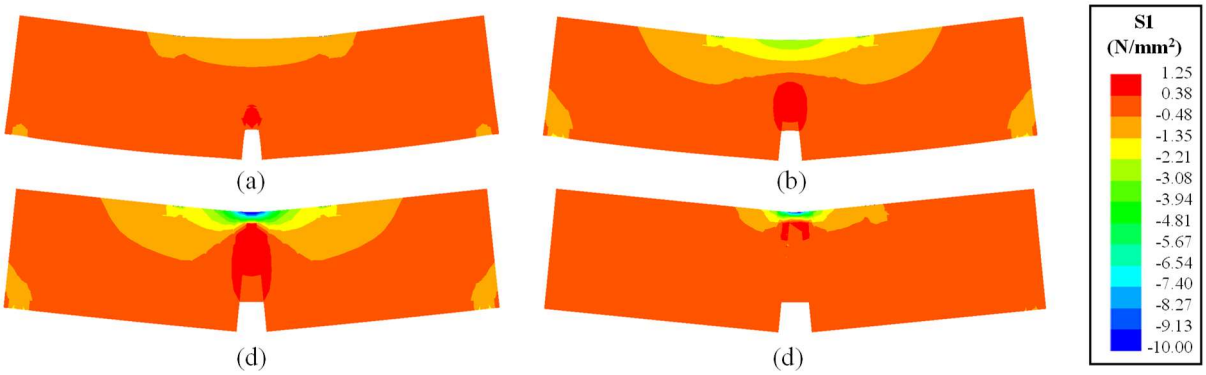

Fig. 3.27: Normalised displacement configurations attained from the FE model, indicating increasing displacement from (a) to (d). The contour plot portrays the total principal stress (S1) distribution for FPB-D3.

Conclusions

In this research, the linear isotropic and non-linear anisotropic behaviour of 3DCP specimens is mechanically evaluated via direct tension (DTT), uniaxial compression (UCT), Young's Modulus (E_{mod}), and four-point bending (FPB) crack mouth opening displacement (CMOD) fracture tests. From

the mechanical characterisation tests two elastic parameters, seven strength parameters and five inelastic parameters are ascertained. The experimental findings relating to the material characteristic parameters are validated via supplementary numerical evaluation, and suitable constitutive relations are selected. Ensuing an analogy linking 3DCP to masonry structures, the mechanical parameters are implemented in an anisotropic Rankine-Hill continuum multi-surface plasticity FE model, and the FPB-CMOD fracture response is successfully simulated. The following main conclusions are drawn from the research:

1. In the absence of standardised testing protocol, the proposed experimental methodology reveals the often reported anisotropic tensile, compressive, and flexural material characteristics of 3DCP specimens with moderate variation. It is envisaged that standardised protocol can be established, if these experimental techniques are utilised in future studies and comprehensive data sets are generated for various printable cementitious compositions.
2. The FRPC samples display a quasi-brittle strain-softening fracture response in direct tension. Where the tensile capacity in the longitudinal and transverse directions (D1 and D2) exceeds the interfacial capacity (D3) by factor two.
3. Preferential alignment of the entrained PP micro-fibres induces significant improvements in the tensile ductility of 3DCP components. A 6.5 times greater ultimate tensile CMOD and 15 times more fracture energy are depicted in D1.
4. The orthotropic compressive capacity is lowest perpendicular to the interlayer (D3), followed by the longitudinal direction. Furthermore, the comparative reduction in the compressive capacity of printed samples is contended to be correlated to the porosity, pore geometry and orientation, and presence of weakly bonded interlayer regions. However, subsequent investigation of the effects of porosity on the mechanical properties of extrusion-based fibre-reinforced 3D printed concrete is required.
5. The E_{mod} shows insignificant statistical variation and isotropic elasticity is assumed. However, a 32 % reduction in stiffness from that of reference cast specimens is mutually exhibited. The aforementioned effects of porosity, pore shape, and orientation are alleged to contribute to the reduced stiffness observed.
6. The FPB flexural capacity coincides with the tensile capacity and exhibits a 2.2-fold degree of anisotropy. The influence of spatial non-uniformity, reduced fracture energy, and interfacial imperfections has a more pronounced effect in flexure than in tension.
7. More robust 3DCP structures are viable if individual sections are orientated such that the relatively weaker interlayer region is favourable aligned relative to the induced load direction.
8. The implemented anisotropic continuum FE simulation appears a promising numerical modelling technique for simulating the FPB CMOD flexural response in the respective loading

directions. The mean peak flexural loads and associated CMOD is well represented. However, the softening regime requires additional refinement if a precise correlation is desired.

Furthermore, additional experimental evaluation at a larger scale, and under biaxial loading conditions, is recommended to assess the suitability of the proposed methodology in detail.

Acknowledgements

The support by The Concrete Institute in South Africa is gratefully acknowledged. IIBCC are partially financing this project in collaboration with Eternit (Schweiz) AG, Switzerland who are providing the Polypropylene Fibres for experimental purposes.

Disclosure statement

The authors report no conflict of interest in the presented research.

References

[1] F. Bos, R. Wolfs, T. Salet, CCR Digital Concrete 2020 SI: Editorial, Cement and Concrete Research. 135 (2020) 106157. https://doi.org/10.1016/j.cemconres.2020.106157.

[2] R.A. Buswell, W.R. Leal de Silva, S.Z. Jones, J. Dirrenberger, 3D printing using concrete extrusion: A roadmap for research, Cement and Concrete Research. 112 (2018) 37–49. https://doi.org/10.1016/j.cemconres.2018.05.006.

[3] B. Panda, Y.W.D. Tay, S.C. Paul, M.J. Tan, Current challenges and future potential of 3D concrete printing, Materialwissenschaft Und Werkstofftechnik. 49 (2018) 666–673. https://doi.org/10.1002/mawe.201700279.

[4] S.C. Paul, G.P.A.G. van Zijl, M.J. Tan, I. Gibson, A review of 3D concrete printing systems and materials properties: current status and future research prospects, Rapid Prototyping Journal. (2018) 0. https://doi.org/10.1108/RPJ-09-2016-0154.

[5] J. Kruger, G. van Zijl, A compendious review on lack-of-fusion in digital concrete fabrication, Additive Manufacturing. 37 (2021) 101654. https://doi.org/10.1016/j.addma.2020.101654.

[6] M.T. Souza, I.M. Ferreira, E. Guzi de Moraes, L. Senff, A.P. Novaes de Oliveira, 3D printed concrete for large-scale buildings: An overview of rheology, printing parameters, chemical admixtures, reinforcements, and economic and environmental prospects, Journal of Building Engineering. 32 (2020). https://doi.org/10.1016/j.jobe.2020.101833.

[7] C. Menna, J. Mata-Falcón, F.P. Bos, G. Vantyghem, L. Ferrara, D. Asprone, T. Salet, W. Kaufmann, Opportunities and challenges for structural engineering of digitally fabricated concrete, Cement and Concrete Research. 133 (2020) 106079. https://doi.org/10.1016/j.cemconres.2020.106079.

[8] D. Lowke, E. Dini, A. Perrot, D. Weger, C. Gehlen, B. Dillenburger, Particle-bed 3D printing in concrete construction – Possibilities and challenges, Cement and Concrete Research. 112 (2018) 50–65. https://doi.org/10.1016/j.cemconres.2018.05.018.

[9] V. Mechtcherine, F.P. Bos, A. Perrot, W.R.L. da Silva, V.N. Nerella, S. Fataei, R.J.M. Wolfs, M. Sonebi, N. Roussel, Extrusion-based additive manufacturing with cement-based materials –

Production steps, processes, and their underlying physics: A review, Cement and Concrete Research. 132 (2020) 106037. https://doi.org/10.1016/j.cemconres.2020.106037.

[10] R.A. Buswell, W.R.L. da Silva, F.P. Bos, H.R. Schipper, D. Lowke, N. Hack, H. Kloft, V. Mechtcherine, T. Wangler, N. Roussel, A process classification framework for defining and describing Digital Fabrication with Concrete, Cement and Concrete Research. 134 (2020) 106068. https://doi.org/10.1016/j.cemconres.2020.106068.

[11] British Standards Institution (BSI), BS EN 12620:2013 Aggregates for concrete, British Standards. (2013) 60.

[12] B. Panda, S. Chandra Paul, M. Jen Tan, Anisotropic mechanical performance of 3D printed fiber reinforced sustainable construction material, Materials Letters. (2017). https://doi.org/10.1016/j.matlet.2017.07.123.

[13] P. Feng, X. Meng, J. Chen, L. Ye, Mechanical properties of structures 3D printed with cementitious powders, CONSTRUCTION & BUILDING MATERIALS. 93 (2015) 486–497. https://doi.org/10.1016/j.conbuildmat.2015.05.132.

[14] M. Sonebi, S. Amziane, A. Perrot, Mechanical Behavior of 3D Printed Cement Materials, 3D Printing of Concrete. (2019) 101–124. https://doi.org/10.1002/9781119610755.ch4.

[15] S.C. Figueiredo, C.R. Rodrıguez, Z.Y. Ahmed, D.H. Bos, Y. Xu, T.M. Salet, O.C. Opurog˘lu, E. Schlangen, F.P. Bos, Mechanical behaviour of printed strain hardening cementitious composites, Materials. 13 (2020).

[16] G. Ma, Z. Li, L. Wang, F. Wang, J. Sanjayan, Mechanical anisotropy of aligned fiber reinforced composite for extrusion-based 3D printing, Construction and Building Materials. (2019). https://doi.org/10.1016/j.conbuildmat.2019.01.008.

[17] V.N. Nerella, S. Hempel, V. Mechtcherine, Effects of layer-interface properties on mechanical performance of concrete elements produced by extrusion-based 3D-printing, Construction and Building Materials. 205 (2019). https://doi.org/10.1016/j.conbuildmat.2019.01.235.

[18] M. van den Heever, F. Bester, M. Pourbehi, J. Kruger, S. Cho, G. van Zijl, Characterizing the Fissility of 3D Concrete Printed Elements via the Cohesive Zone Method, 2nd RILEM International Conference on Concrete and Digital Fabrication. 3 (2020) 1–10.

[19] J. Xiao, S. Zou, Y. Yu, Y. Wang, T. Ding, Y. Zhu, J. Yu, S. Li, Z. Duan, Y. Wu, L. Li, 3D recycled mortar printing: System development, process design, material properties and on-site printing, Journal of Building Engineering. 32 (2020) 101779. https://doi.org/10.1016/j.jobe.2020.101779.

[20] T.T. Le, S.A. Austin, S. Lim, R.A. Buswell, R. Law, A.G.F. Gibb, T. Thorpe, Hardened properties of high-performance printing concrete, Cement and Concrete Research. 42 (2012) 558–566. https://doi.org/10.1016/j.cemconres.2011.12.003.

[21] B. Nematollahi, P. Vijay, J. Sanjayan, A. Nazari, M. Xia, V.N. Nerella, V. Mechtcherine, Effect of polypropylene fibre addition on properties of geopolymers made by 3D printing for digital construction, Materials. 11 (2018). https://doi.org/10.3390/ma11122352.

[22] F.A. Bester, M. van den Heever, P.J. Kruger, G.P.A.G. van Zijl, Reinforcing digitally fabricated concrete: A systems approach review, Additive Manufacturing. 37 (2021). https://doi.org/10.1016/j.addma.2020.101737.

[23] M. Hambach, D. Volkmer, Properties of 3D-printed fiber-reinforced Portland cement paste, Cement and Concrete Composites. 79 (2017) 62–70. https://doi.org/10.1016/j.cemconcomp.2017.02.001.

[24] V.C. Li, F.P. Bos, K. Yu, W. McGee, T.Y. Ng, S.C. Figueiredo, K. Nefs, V. Mechtcherine, V.N. Nerella, J. Pan, G.P.A.G. van Zijl, P.J. Kruger, On the emergence of 3D printable Engineered, Strain Hardening Cementitious Composites (ECC/SHCC), Cement and Concrete Research. 132 (2020) 106038. https://doi.org/10.1016/j.cemconres.2020.106038.

[25] P.J. Kruger, M. van den Heever, S. Cho, S. Zeranka, G. van Zijl, High-performance 3D printable concrete enhanced with nanomaterials, Proceedings of the International Conference on Sustainable Materials, Systems and Structures: New Generation of Construction Materials. (2019) 533–540.

[26] A. Perrot, T. Lecompte, P. Estellé, S. Amziane, Structural build-up of rigid fiber reinforced cement-based materials, Materials and Structures/Materiaux et Constructions. 46 (2013) 1561–1568. https://doi.org/10.1617/s11527-012-9997-9.

[27] A. Perrot, D. Rangeard, A. Pierre, Structural built-up of cement-based materials used for 3D-printing extrusion techniques, Materials and Structures/Materiaux et Constructions. 49 (2016) 1213–1220. https://doi.org/10.1617/s11527-015-0571-0.

[28] J. Kruger, S. Zeranka, G. van Zijl, 3D concrete printing: A lower bound analytical model for buildability performance quantification, Automation in Construction. 106 (2019) 102904. https://doi.org/10.1016/j.autcon.2019.102904.

[29] F.P. Bos, P.J. Kruger, S.S. Lucas, G.P.A.G. van Zijl, Juxtaposing fresh material characterisation methods for buildability assessment of 3D printable cementitious mortars, Cement and Concrete Composites. 120 (2021) 104024. https://doi.org/10.1016/j.cemconcomp.2021.104024.

[30] T. Pan, Y. Jiang, H. He, Y. Wang, K. Yin, Effect of structural build-up on interlayer bond strength of 3d printed cement mortars, Materials. 14 (2021) 1–17. https://doi.org/10.3390/ma14020236.

[31] R. de Borst, Fracture in quasi-brittle materials: A review of continuum damage-based approaches, Engineering Fracture Mechanics. 69 (2001) 95–112. https://doi.org/10.1016/S0013-7944(01)00082-0.

[32] P.B. Lourenço, Experimental and numerical issues in the modelling of the mechanical behaviour of masonry, Structural Analysis of Historical Constructions II. (1998) 57–91. https://doi.org/10.1016/j.conbuildmat.2010.04.010.

[33] P. Domone, J. Illston, eds., Construction Materials: Their Nature and Behaviour, 4th ed., Spon Press, New York, 2010. https://doi.org/10.1016/B978-0-444-88887-7.50012-X.

[34] S.C. Paul, G.P.A.G. van Zijl, Assessment of fracture toughness in strain hardening cement-based composite (SHCC) made from fine and coarse sand, Research and Applications in Structural Engineering, Mechanics and Computation - Proceedings of the 5th International Conference on Structural Engineering, Mechanics and Computation, SEMC 2013. (2013) 619–624. https://doi.org/10.1201/b15963-114.

[35] A. Hillerborg, The theoretical basis of a method to determine the fracture energy GF of concrete, Materials and Structures. 18 (1985) 291–296. https://doi.org/10.1007/BF02472919.

[36] P.B. Lourenço, J.G. Rots, J. Blaauwendraad, Continuum model for masonry: Parameter estimation and validation, Journal of Structural Engineering. 124 (1998) 642–652. https://doi.org/10.1061/(ASCE)0733-9445(1998)124:6(642).

[37] F. Bester, M. van den Heever, J. Kruger, S. Cho, G. van Zijl, Steel Fiber Links in 3D Printed Concrete, 2020. https://doi.org/10.1007/978-3-030-49916-7_41.

[38] R.J.M. Wolfs, F.P. Bos, T.A.M. Salet, Hardened properties of 3D printed concrete: The influence of process parameters on interlayer adhesion, Cement and Concrete Research. 119 (2019) 132–140. https://doi.org/10.1016/j.cemconres.2019.02.017.

[39] F.P. Bos, E. Bosco, T.A.M. Salet, Ductility of 3D printed concrete reinforced with short straight steel fibers, Virtual and Physical Prototyping. 14 (2019) 160–174. https://doi.org/10.1080/17452759.2018.1548069.

[40] L. Wang, H. Jiang, Z. Li, G. Ma, Mechanical behaviors of 3D printed lightweight concrete structure with hollow section, Archives of Civil and Mechanical Engineering. 20 (2020) 1–17. https://doi.org/10.1007/s43452-020-00017-1.

[41] J. Xiao, H. Liu, T. Ding, Finite element analysis on the anisotropic behavior of 3D printed concrete under compression and flexure, Additive Manufacturing. 39 (2021) 101712. https://doi.org/10.1016/j.addma.2020.101712.

[42] W.B. Fuller, S.E. Thompson, The laws of proportioning concrete, Proceedings of the American Society of Civil Engineers. 33 (1907) 222–298.

[43] S. Chaves Figueiredo, O. Çopuroğlu, E. Schlangen, Effect of viscosity modifier admixture on Portland cement paste hydration and microstructure, Construction and Building Materials. 212 (2019) 818–840. https://doi.org/10.1016/j.conbuildmat.2019.04.020.

[44] M. van den Heever, F.A. Bester, P.J. Kruger, G.P.A.G. van Zijl, Effect of silicon carbide (SiC) nanoparticles on 3D printability of cement-based materials, Advances in Engineering Materials, Structures and Systems: Innovations, Mechanics and Applications. (2019) 1616–1621. https://doi.org/10.1201/9780429426506-279.

[45] J. Kruger, Rheo-mechanics modelling of 3D concrete printing constructability, 2019. https://scholar.sun.ac.za.

[46] GOM, ARAMIS metrology systems, (2020). https://www.gom.com/metrology-systems/aramis.html (accessed October 13, 2020).

[47] Z. Raheem, Standard Test Method for Compressive Strength of Cylindrical Concrete Specimens 1, ASTM Standard Book. (2003) 1–5.

[48] European Committee for Standardization, EN 1992-1-1, Brussels, 2004.

[49] DIANA FEA bv, DIANA User Manual: Tensile behaviour, (2015) 6.2.2.1. https://dianafea.com/manuals/d100/MatLib/node86.html (accessed May 25, 2021).

[50] G. Magenes, P. Morandi, A. Penna, Test results on the behaviour of masonry under static cyclic in plane lateral loads, Tech. Rep. ESECMaSE Work Package 7, Deliverable D7.1 c, Enhanced Safety Efficient Construction of Masonry Structures in Europe. (2008).

[51] T. Davis, D. Healy, A. Bubeck, R. Walker, Stress concentrations around voids in three dimensions: The roots of failure, Journal of Structural Geology. 102 (2017) 193–207. https://doi.org/10.1016/j.jsg.2017.07.013.

[52] X. Du, L. Jin, G. Ma, Macroscopic effective mechanical properties of porous dry concrete, Cement and Concrete Research. 44 (2013) 87–96. https://doi.org/10.1016/j.cemconres.2012.10.012.

[53] E. Hosseini, M. Zakertabrizi, A.H. Korayem, G. Xu, A novel method to enhance the interlayer bonding of 3D printing concrete: An experimental and computational investigation, Cement and Concrete Composites. 99 (2019) 112–119. https://doi.org/10.1016/j.cemconcomp.2019.03.008.

[54] DIANA FEA, Rankine-Hill Anisotropy, (2017). https://dianafea.com/manuals/d101/MatLib/node326.html#RanHil (accessed September 28, 2020).

[55] DIANA FEA, (2020). https://dianafea.com (accessed October 12, 2020).

[56] J.G. Rots, Computational Modelling of Concrete Fracture, 1988.

CHAPTER 4 : Numerical Modelling Strategies for Reinforced 3D Concrete Printed Elements

Marchant van den Heever *, Frederick Bester, Jacques Kruger, Gideon van Zijl.

Structural Engineering and Civil Engineering Informatics, Department of Civil Engineering, Stellenbosch University, Stellenbosch, 7602, South Africa

Reproduced and reformatted from an article submitted to *Additive Manufacturing*.

(DOI: Submitted)

Abstract

Extrusion-based 3D concrete printing (3DCP) prompts a new age of reinforced concrete structures by virtue of the exponential advancements in process, control, material, and fresh-state analysis technologies. Notwithstanding these advancements, latency exists in the numerical analysis of complex geometric forms produced by 3DCP technology. In this research, two finite element (FE) modelling strategies are proposed for the numerical analysis of 3DCP building elements. The objective of these models is to predict the hardened-state structural capacity and failure mechanisms of singularly and dually reinforced concrete deep beams under various loading configurations. To validate the proposed FE modelling strategies, the reinforced 3DCP deep beams are experimentally evaluated. An analogy between masonry and 3DCP structures provides premise to the presented FE modelling strategies, and succinct descriptions of the respective modelling strategies, adaptions to the 3DCP design space, and material model prescriptions are provided. Strikingly, the recommended input parameters provide sound agreement with the experimentally evaluated configurations, with all simulations exhibiting a load carry capacity within 14 % of the experimental observations. Not only is the load-displacement response deemed appropriate, but also the numerically produced cracking patterns, placing confidence in the proposed numerical simulation strategies. Furthermore, it is shown that the advent of a 2D plane stress simplification of the fibre-reinforced hollow beam geometry yields adequate agreement while significantly reducing the computational expense required to simulate the nonlinear response of anisotropic printed composites.

Highlights

- Design and fabrication rules to ensure structural integrity in 3DCP elements is presented
- The mechanical performance of reinforced 3DCP beams is experimentally investigated
- Two hardened-state anisotropic numerical simulation frameworks for 3DCP are proposed
- A 2D plane stress simplification of cellular infill geometry is proposed and validated

Keywords: 3D Concrete Printing; Hardened-State Mechanical Performance; Design and Fabrication Rules; Numerical Simulation; Finite Element Analysis; Reinforcement

4.1 Introduction

Extrusion-based 3D concrete printing (3DCP) is an additive manufacturing process that employs the computer-controlled placement of extruded cementitious mortar to realise physical objects in a layer-by-layer fashion. Here the fabricated component is a duplicate of a 3D model from which the machine control operations is derived, similar to conventional additive manufacturing processes. This digitally native construction technology enables supreme aesthetic capabilities via the cost-effective, non-laborious, rapid realisation of freeform geometrically complex parts with optimised material usage [1]. 3DCP could also lead to less CO_2 emissions and improved productivity, compared with traditional pre-casting methods [2]. Ensuing this potential, 3DCP is experiencing exponential advancement in process, control, material, and fresh-state analysis technologies [3]. Driven by the prospect of complete construction automation, 3DCP is strategically positioned to set new horisons in the built environment. This notion is substantiated by the increasing number of large-scale commercial and residential infrastructure projects successfully delivered in recent years [4]. Additionally, a current market evaluation, conducted by Allied Market Research, estimates the global 3DCP market at $310.9 million in 2019 and projects it to reach $40.6 billion by 2027, registering a cumulative annual growth rate (CAGR) equal to 106.5 % between 2020 and 2027 [5].

Foreseeable value-addition undoubtedly resides in using this technology to realise shell and spatial structures with architectural or structural function in prefabricated and in-situ fabrication settings. The opportunity to fabricate more efficient systems employing topology [6–8] and topography [9] optimisation procedures provide a new paradigm in architecture, engineering, and construction; where structures can be designed, following critical load paths, to use less material and can be tailored to existing landscapes. Additionally, 3DCP is ideal for taking advantage of bio-inspired design principles [10] and parametric design procedures could provide opportunities for mass customisation at no additional cost. Owing to the development of computational modelling, designers can produce geometrically complex structures on digital platforms. Yet, due to the properties of the fresh material and the difficulty in generating robotic toolpaths, printed geometries have remained relatively simple, and a disconnect exists between the conceptual design possibility and fabrication capabilities and constraints of 3DCP [11]. To this end, recently proposed integrated building information management (BIM) workflows provide a solution to facilitate the merger between design and fabrication activities [12]. Moreover, the synergy amongst integrated BIM workflow management for direct toolpath generation and voxel-based fresh-state numerical simulation provides scope to “as designed” fabrication procedures with superior quality control [13]. Notwithstanding the developments in design,

fabrication, and fresh-state FE modelling, latency exists in the hardened-state numerical analysis of complex geometric forms produced by 3DCP technology.

Considering that reinforced concrete (RC) has revolutionised modern infrastructure development, by providing tensile capacity, and consequently ductility, to a brittle concrete matrix, the integration of reinforcement into the digital fabrication process is essential. A detailed elaboration on the current state-of-the-art reinforcement methodologies for 3DCP can be found in [1]. To validate the efficiency of reinforcement strategies, a systems approach can be adopted, considering the degree of system integration [1]. Still, ultimately a comprehensive understanding pertaining to the interaction between the reinforcement and the printed matrix and the mechanical behaviour within the printed composite is required if 3DCP is to be used to fabricate load-bearing structures.

The ability to conduct computational analysis procedures that accurately capture the response of reinforced 3DCP components under design loading conditions is paramount to the scalability of the aforementioned design techniques. Building code compliance presents a significant limitation for the espousal of large-scale concrete fabrication methods. This is inherent to the novelty of this automated manufacturing procedure and the utilisation of anomalous cement-based composites. Therefore, designers and regulatory bodies have no standardised protocol to reference for new design endeavours; thus, existing building codes and policies related to conventional manufacturing and construction techniques are adopted [14]. It is held that suitable numerical analysis methodologies would accelerate the codification process in the absence of large experimental data sets by providing critical insights relating to the structural response and capacity of reinforced 3DCP elements.

An additional method to circumvent the arduous activity of generating entirely new building codes could be to find inspiration in analogous historical construction methodologies, such as masonry [11]. With apparent similarities stemming from the layered nature of both 3DCP and masonry structures, both comprise discrete elements (bricks and filaments) bonded together to form a composite structure. One could undoubtedly adopt the wealth of knowledge and insight gained over many centuries pertaining to the design and analysis of masonry structures within the 3DCP design space. Indeed, various studies have considered these similarities; with some looking to extend the design space of 3DCP to include cantilevers, vaults, and domes [11]; others proposing a potential link between the computational modelling strategies [15]; and another validating the applicability of an anisotropic macro-modelling approach derived from masonry [16]. Clearly, there lies potential in these considerations and thereby forms the basis from which inspiration is drawn for this research.

Eurocode 2 offers provisions for “design assisted by testing” intended for new structures in the absence of adequate calculation models [17]; however, such activities would incur substantial cost implications when an extensive array of unique elements must be designed. Considering that the development of compatible numerical simulation strategies for reinforced 3DCP elements would permit

structural verification of building components without large-scale destructive testing practices. It is contended that these research activities evoke significant cost-saving potential. Furthermore, to push the boundaries of the structural design of RC structures and facilitate the development of parametrically optimised buildings, a deeper understanding of the structural mechanics at play in 3DCP elements under numerous loading conditions is necessary. To keep pace with the rapid developments in this sector and indeed deliver the proposed benefits of 3DCP, pertinent design and numerical analysis procedures are required. As they are considered critical to the widespread adoption of this new construction technique. Effectively, engineers will need to understand how to design structures to be manufactured with printed materials, requiring new design codes and standardised mechanical assessment protocol to be developed [18].

Numerical simulation remains an effective analytical tool for studying the complex interrelation between the design, material, process, and product requirements of 3DCP structures. To date, significant interest and progression are seen in the fresh-state numerical simulation of 3DCP, which primarily considers the physicochemical aspects of the printable material, process particularities, and product quality and applications [19]. Notable fresh-state FE simulations capable of predicting the buildability performance of actual printed objects include [20–23], to name a few. However, literature relating to the numerical evaluation and simulation of the hardened-state mechanical performance of concrete printed components is sparse. In this regard, Valle-Pello et al. [24] provide a discrete element model to predict the mechanical behaviour of 3DCP members. Wang et al. [25] explored the discrete element method to numerically simulate the failure mechanisms of 3D printed lightweight concrete elements with hollow sections. Bos et al. [26] investigated the ductility of 3D printed concrete reinforced with short steel fibre, which employed the renowned Concrete Damage Plasticity material model of Abaqus to simulate the flexural response of 3DCP beams with reasonable agreement. Feng et al. [27] implemented a FE analysis procedure, founded on the experimentally determined compressive stress-strain response and a maximum stress criterion, to investigate the effect of printing direction on the load-carrying capacity of a 3D printed arch structure. The fissile nature of 3DCP components is characterised by van den Heever et al. [28] and the interlayer tensile failure mode is computationally simulated via the cohesive zone method. More recently, van den Heever et al. [16] provides perspective to the experimental and computational mechanics of extrusion-based 3DCP by presenting a range of mechanical characterisation procedures that enable the simulation of concrete printed prisms via the anisotropic Rankine-Hill continuum material model [29].

In an extension of the preceding works by van den Heever et al. [16], this research aims to (i) experimentally assess the mechanical capacity of reinforced 3DCP deep beams under three respective loading schemes; (ii) assess the compatibility and performance of a coupled reinforcing strategy comprising entrained polypropylene (PP) micro-fibres and conventional steel rebar; (iii) propose and evaluate two different numerical simulation frameworks (an anisotropic continuum macro-modelling

strategy and an interface-based micro-modelling strategy) and evaluate their accuracy and robustness; (iv) verify that the material parameters attained in [16] are applicable when modelling 3DCP elements at a larger scale, and (v) provide recommendations for future research relating to the nonlinear numerical simulation of reinforced 3DCP building elements.

4.2 Numerical Simulation Frameworks

The following section presents the numerical simulation frameworks considered, accompanied by the theoretical deliberations applicable to their selection. Considering the anisotropic mechanical properties displayed by a multitude of 3D printable materials from various institutions [15], it is evident that numerical modelling strategies capable of capturing the orthotropic constitutive relations exhibited by 3DCP elements should be employed. Additionally, suitable numerical modelling frameworks with orthotropic damage and plasticity need to be considered to fully describe the complex nonlinear behaviour of 3DCP elements. Due to the heterogeneous nature and associated degree of anisotropy prevalent in 3DCP elements, numerical simulation methodologies for 3DCP can be considered analogous to those employed for masonry and other layered structures. Adopting the extensively developed modelling frameworks for layered structures such as masonry and composite laminates, this study is the first to present and assess two such frameworks in the 3DCP context, including: (i) a multi-surface anisotropic continuum macro-modelling strategy [29] and (ii) a multi-surface interface micro-modelling strategy [30], respectively.

Since 3DCP is envisioned to permit highly customisable, complex geometric components, suitable numerical modelling strategies must assess the structural integrity of such components. Albeit complexity is often associated with great computational expense and robust numerical simulation frameworks are sought. Therefore, a simplified 2D plane-stress numerical simulation framework is proposed. Detailed descriptions of the proposed frameworks are shown in the following subsections. The respective failure mechanisms in 3DCP items are illustrated in Fig. 4.1, and Fig. 4.2 presents a simplified representation of the micro and macro-modelling approaches adopted to provide context to the proposed numerical simulation frameworks.

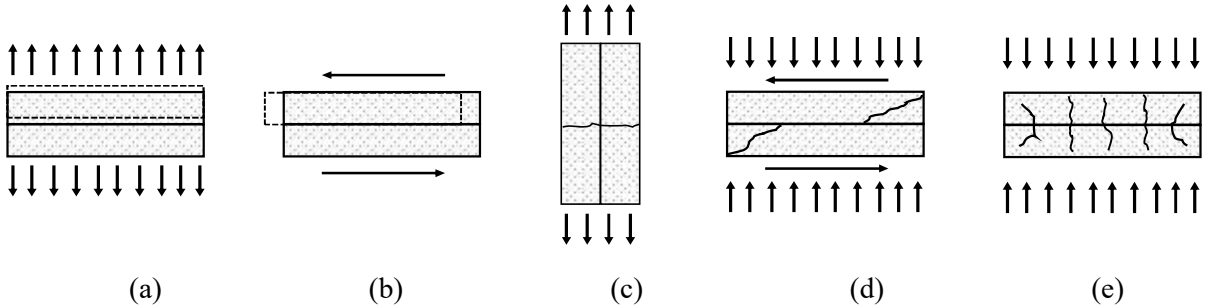

Fig. 4.1: Failure mechanisms in 3DCP elements, (a) interfacial cracking (Mode I), (b) interface shear-slip (Mode II), (c) intralayer tensile cracking, (d) intralayer cracking under compression-shear, and (e) crushing (reworked for 3DCP from [29]).

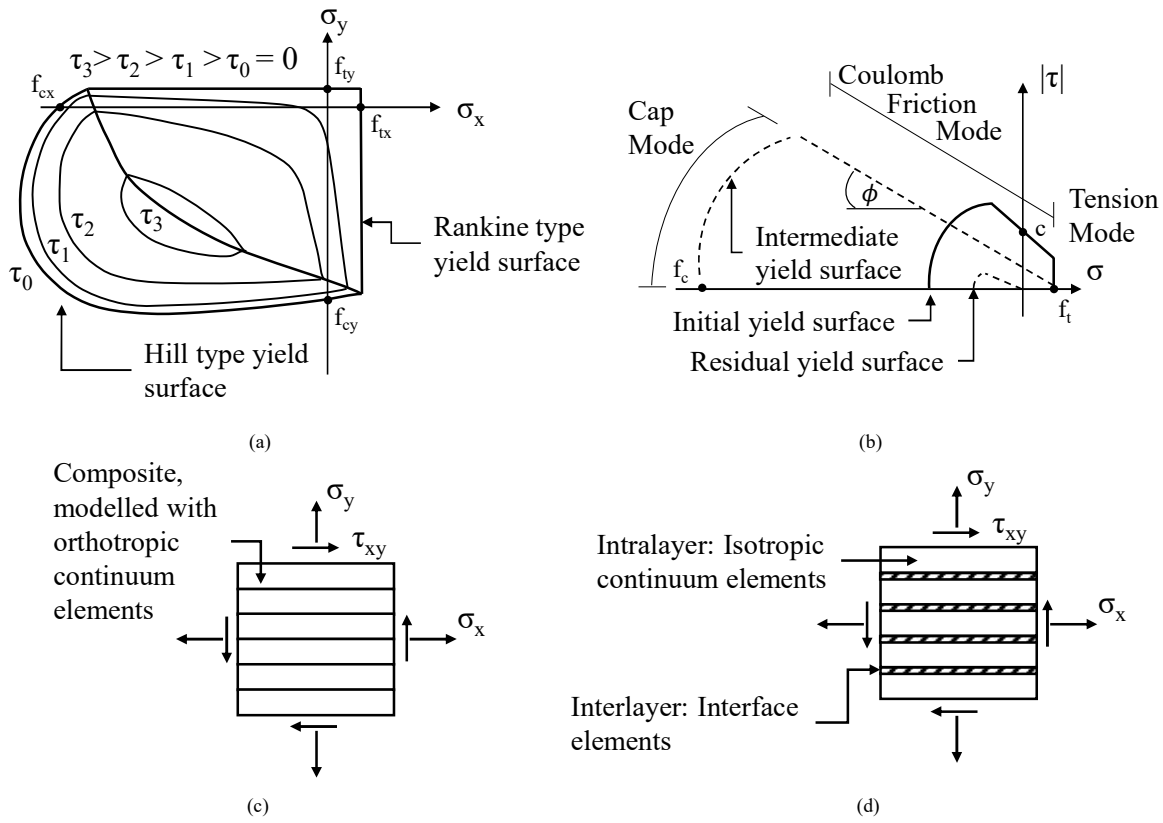

Fig. 4.2: Proposed simulation frameworks for 3D concrete printed elements illustrating, (a) continuum material model (adapted from [29]*), (b) interface material model (adapted from* [30]*), (c) proposed macro-modelling approach, and (d) proposed micro-modelling approach.*

4.2.1 Continuum model

The continuum model (CM), or macro-modelling approach (Fig. 4.2c), does not distinguish between filament layers and interfacial regions (IRs). Instead, a smeared cracking approach is adopted where deformation patterns are approximated by the inelastic deformation within continuum elements. This approach entails significantly reduced modelling and computational efforts compared to 3D solid simulations; however, the location of IRs is not definable. Here, an anisotropic Rankine-Hill cap plasticity continuum crack model, presented in Fig. 4.2a, with separate softening in tension (Rankine)

and compressive hardening-softening (Hill), is selected for its potential to capture the anisotropic inelastic response of layered objects [15]. The direction of the IR (x-direction) defines the local material axes with the y-direction orientated normal in-plane to the x-axis (i.e., vertically). Note that this formulation only holds for planar applications since the influence of the out-of-plane direction is generally unknown. Considering that in the CM, the locations of IRs are not explicitly definable, continuum elements are prescribed homogenised characteristics about their respective orthotropic axes. However, it is reported that such an approximation still yields satisfactory agreement with experimental results on masonry shear walls [29] and the homogenised characteristics used in this study are attained from the closed-loop displacement controlled direct tensile tests presented in van den Heever et al. [16].

The proposed material model is implemented in the DIANA FEA simulation package and requires two elastic parameters (E, ν), seven strength parameters (f_{tx}, f_{ty}, f_{cx}, f_{cy}, α, β, and γ), and five inelastic parameters (G_{fx}, G_{fy}, G_{fcx}, G_{fcy}, and κ_p) to define the yield criteria presented in Fig. 4.2a. Where the respective subscripts (x, y) refer to the orthotropic directions shown in Fig. 4.2c-d. The first four strength parameters represent the uniaxial tensile and compressive strength along the material axes. The experimental procedure presented in [16] is recommended to attain these parameters. Note that conducting the experimental procedures presented in [16] under precise displacement control is paramount to acquire the four independent fracture energies (tension and compression) and the peak strain in compression. Supplementary tests are required to calibrate the yield criterion fully. These tests include the shear stress contribution to tensile failure (α) calculated as per Equation 4.4; the coupling between normal stress values in the case of compressive failure (β); and parameter γ, which weights the shear stress contribution to compressive failure and is calculated via Equation 4.5 [29].

4.2.2 Interface-based model

The interface-based model (IFM), or micro-modelling approach, comprises an interface elastoplastic constitutive model presented by Lourenco and Rots [30] to analyse unreinforced masonry structures. Stemming from the additive manufacturing technique employed, 3DCP elements have IRs with comparatively lower strength when gauged against the capacity of the intralayer matrix [15]. Therefore, the proposed framework is elected for its potential in capturing the detailed response of 3DCP elements. In the preceding works by Lourenco and Rots [30], individual masonry units are discretised to form a rational unit-joint model. In this research, the filament layers are considered continuum elements and cracking and shear-slip along IRs is captured by discrete interface elements as illustrated in Fig. 4.1d. The nonlinear interface element material model (Fig. 4.2b) is assigned a Coulomb-friction envelope for shear (Mode II) failure (Fig. 4.1b), limited by a tension cut-off for tensile (Mode I) failure (Fig. 4.1a), and a cap model for compression failure (Fig. 4.1e). Additionally, softening behaviour is widely reported as a principal characteristic in quasi-brittle materials and is therefore implemented in all failure modes, with the compression regime preceded by hardening. Additionally, a

hypo-elastic isotropic total strain-based rotating crack (TSC) model is selected to describe the tensile and compressive behaviour of the intralayer continuum elements. The TSC approach is based on modified compression field theory, proposed initially by Vecchio and Collins [31], which follows a smeared cracking approach for the fracture energy.

4.2.3 2D plane stress (2D) model

In this section, the rationale behind the 2D plane stress (2D) simplification of 3DCP hollow sections, with biaxially symmetric cellular infill patterns indicated in Fig. 4.3a, is presented. This simplification permits the cellular geometry of 3DCP elements to be converted to a representative thickness with similar mechanical properties, thereby significantly reducing the computational and modelling effort required to simulate the response of such members under various loading conditions. Considering a section within the infill of the 3DCP beam yields the resultant area shown in Fig. 4.3b, which is attained from the 3D model geometry. A representative rectangular thickness (t) is derived, assuming that a constant stress state exists over the thickness of section A-A. Naturally, dividing the attained area by the object height gives a representative rectangular thickness, as presented in Equation 4.1. Additionally, it is shown that the effective contact area of a rounded filament is less than that of its square counterpart (Fig. 4.3c). Therefore, a contact factor (Δ_{CF}) is presented in Equation 4.2 to account for the reduced contact efficiency associated with specific layer geometries. Measuring the fractured samples from C1, C2, and C3, an average layer width equal to 30 mm and average effective layer width ($L_{w,eff}$) equal to 26 mm is observed. It is appreciated that, in general terms, the Δ_{CF} is related to the filament shape retention and the employed printing parameters (i.e., deposition height, nozzle geometry, extrusion rate, and print speed). Consequently, the following representation of Δ_{CF} is only applicable to empirical data. If this parameter were desired in a preprocessing step, calibration that accounts for the printing parameters and fresh-state material properties is required. The representative plane stress thickness of the element (t_{eff}) is calculated according to Equation 4.3. Furthermore, the density of components fabricated with rounded filaments should be increased by the inverse of Δ_{CF} to account for the mass of the component, which is not reduced. This effect is unpronounced in this research but will certainly become relevant in the structural design and computational evaluation of larger structures.

$$t = \frac{A_{\sec A-A}}{h} = \frac{42727}{260} = 164\ mm \tag{4.1}$$

$$\Delta_{CF} = \frac{L_{w,eff}}{L_w} = \frac{26}{30} = 0.86 \tag{4.2}$$

$$t_{eff} = \Delta_{CF} \cdot t = 141\ mm \tag{4.3}$$

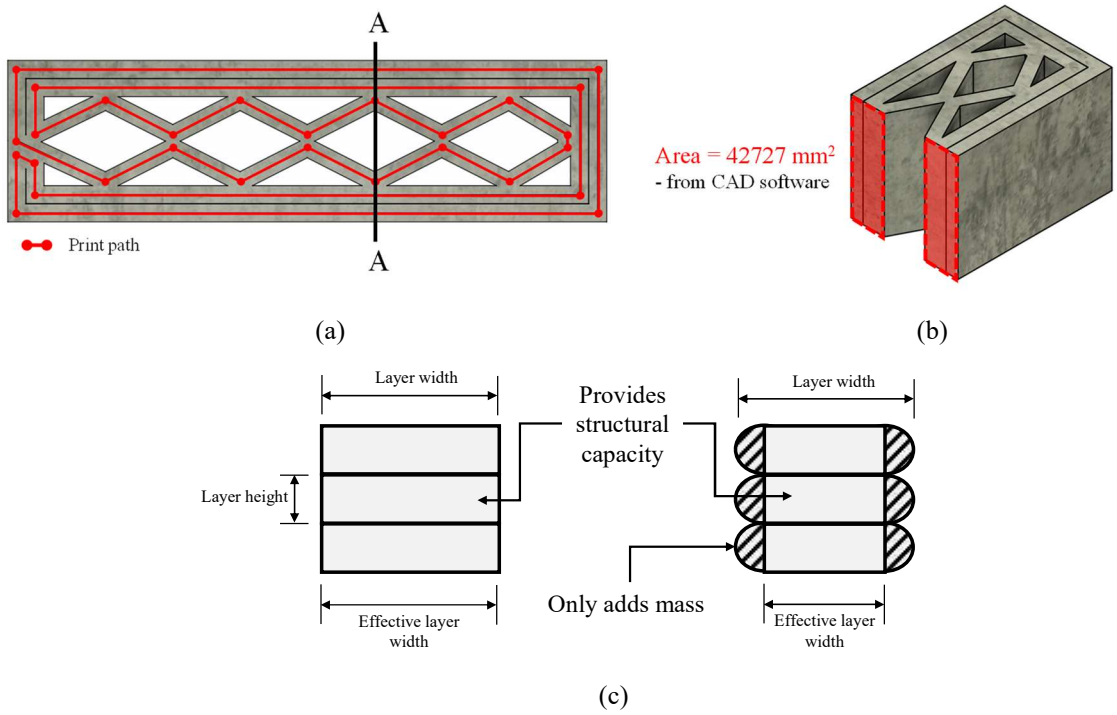

Fig. 4.3: The rationale behind the 2D simplification, (a) shows the plan view of a section within the cellular portion of the printed object, (b) presents the load resisting area derived from the infill geometry, and (c) illustrates the difference between rounded and square filaments and the effect on the effective contact area.

4.3 Experimental Methods & Materials

In this research, three geometrically identical reinforced concrete deep beams are 3D concrete printed for experimental evaluation under four-point bending and eccentrically loaded three-point bending (eTPB) configurations. All beams are fabricated with the polypropylene (PP) fibre-reinforced printable concrete (FRPC) developed at Stellenbosch University. The PP fibres have an elastic modulus of 3 GPa, a yield stress of 300 MPa, a 6 mm length, and a diameter of 0.03 mm. Detailed descriptions of the anisotropic mechanical capacity of the mixtures, grading, constituents, proportions, and rheological properties are available in [16]. The experimental programme seeks to:

i. assess the mechanical capacity and corresponding failure mechanisms of the above mentioned 3DCP deep beams;
ii. verify whether the material parameters attained from the mechanical characterisation procedures presented in [16] are applicable at the increased scale of the current experimental programme;
iii. determine whether the aforementioned continuum and interface-based FE modelling frameworks can numerically simulate the structural response of the members under the respective loading configurations presented; and
iv. evaluate the accuracy and robustness of the proposed frameworks.

4.3.1 Fabrication procedure

The 910 x 260 x 260 mm (l x w x h) reinforced concrete deep beams are 3D concrete printed at the Centre for the Development of Sustainable Infrastructure (CDSI) at Stellenbosch University. Fig. 4.4a illustrates the printed objects fabricated in the 1 x 1 x 1 m gantry type 3DCP facility presented in Fig. 4c. Two of the three beams are dually reinforced with entrained PP microfibres and manually placed Y10 reinforcement bars at a cover distance equal to 30 mm from the bottom filament, as shown in Fig. 4.4b. One of the configurations (C1) purposefully omits the steel reinforcement, as presented in Fig. 4.6a. The items illustrated in Fig. 4.4a are printed in a continuous path at 60 mm/s, with a 10 mm layer height (L_h) and 30 mm layer width (L_w), respectively. The print contour path is 6 m long, resulting in a pass time interval of 100 s and a total object print time equal to 41 min. Due to the object shape and selected print parameters, no buildability issues were encountered during the printing procedure. All objects are printed in a climate-controlled room (23 ± 2 °C and 65 ± 5 % relative humidity) and cured for 28 days in this environment prior to testing.

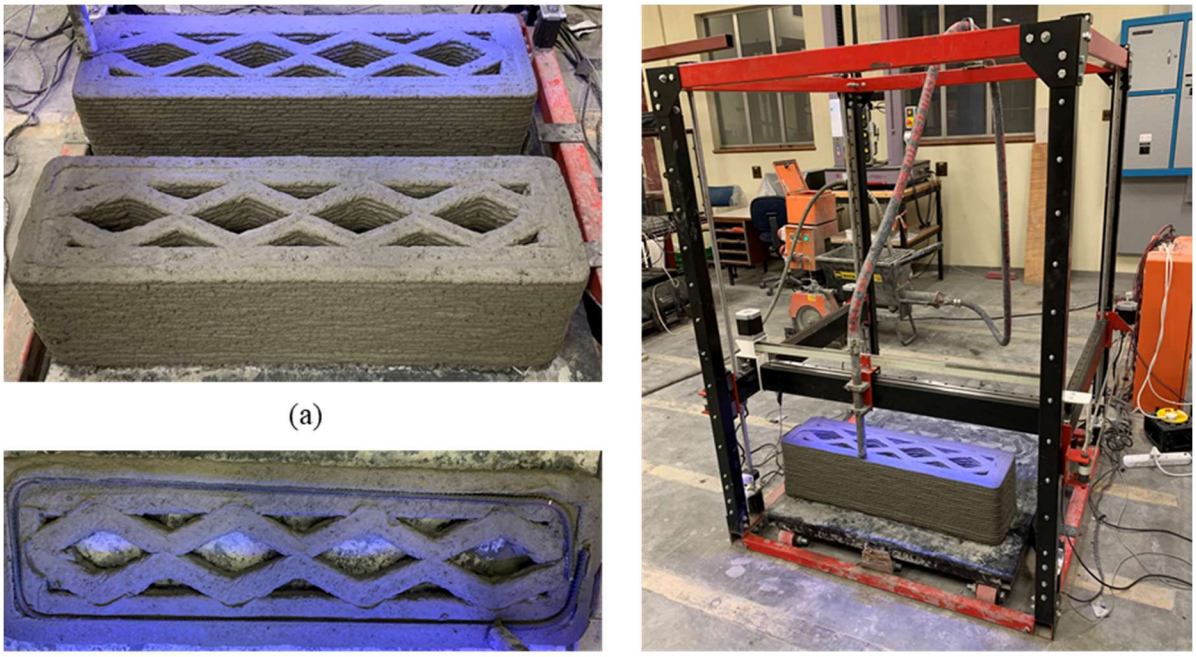

Fig. 4.4: Visual illustrations of (a) 3DCP deep beams, (b) manual placement of the Y10 steel reinforcement bars on the third layer of the objects, and (c) the gantry type 3DCP facility utilised to fabricate the components in this study.

4.3.2 Design & fabrication parameters

The following section presents the design rules by which the continuous print path must abide to ensure the structural integrity of the printed component. As depicted in Fig. 4.5a, the print path corresponds to the centre line of the extruded filament and is prescribed by the preprogrammed gcode file. From operational experience, a minimum distance $L_{collinear} = L_w - \frac{L_w}{10}$ is required to ensure

sufficient bond strength between adjacently deposited collinear filaments. Such a separation guarantees that a transverse pressing action is induced on the outer filament in Fig. 4.5c when the inner segment is printed. Note that reducing the distance "$L_{collinear}$" by more than $\frac{L_w}{10}$ compromises the ability of the outer segments to conform to the external geometric tolerances of the printed object. Note that these prescriptions are empirical to the material and fabrication setup used and may differ for other groups. Since the connection between the inner and outer components is of great importance to the overall moment of inertia of the segment, a minimum distance $L_{internal} = L_w - \frac{L_w}{3}$ is prescribed. The minimum distance "$L_{internal}$" in the inner region is less than "$L_{collinear}$" since the connected length between angular and linear filaments is less than the connected length between collinear filaments. Therefore, an increased connection depth is desired. Additionally, over-extruding at these locations has a less pronounced impact on the overall dimensions of the object and results in a suture connection between adjacent filaments, as shown in Fig. 4.5c. A layer pressing strategy is employed to ensure that vertically stacked contours disturb the top surface of the substrate layer, allowing it to deflocculate and permits, to a certain extent, interlayer fibre breaching [16]. When the extruded material reflocculates, the degree of interlayer fusion is amplified, and the tensile fracture energy of the connection increases [16]. Layer pressing is achieved when the layer height is less than the nozzle width (n_w) [32]. In this research, a nozzle width to layer height ratio equal to ($\frac{n_w}{L_h} = 2.5$) is employed.

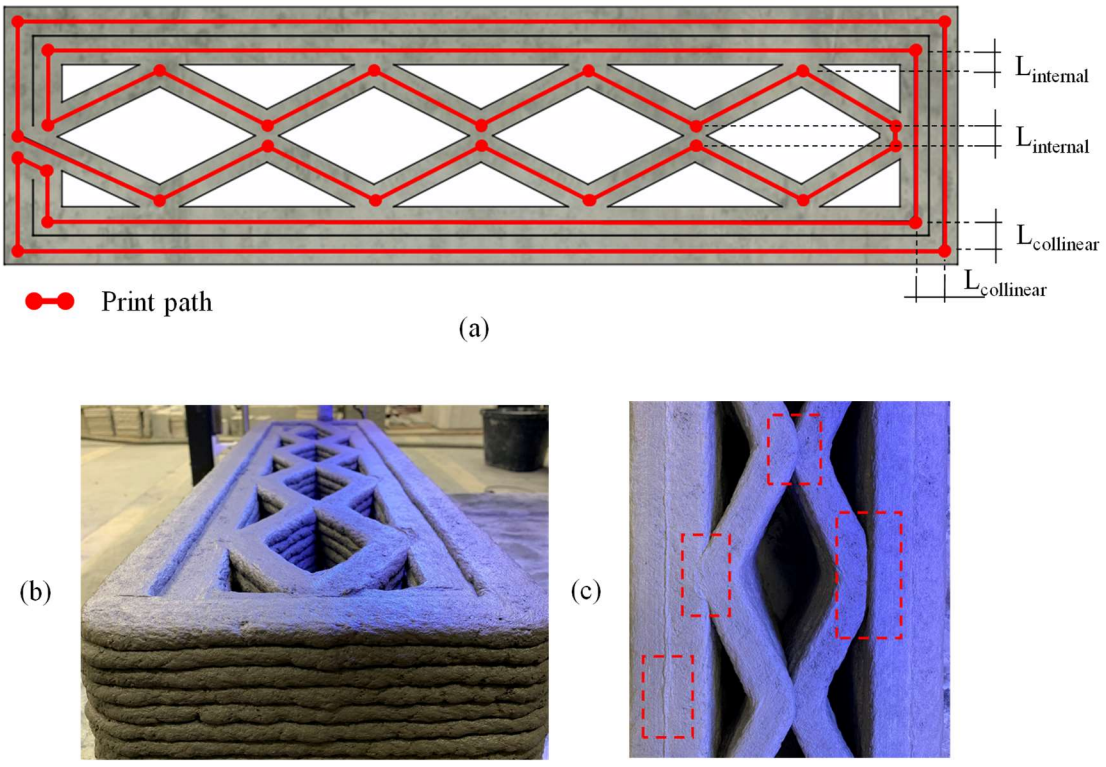

Fig. 4.5: Illustrations depicting (a) the print path and minimum separation at critical locations, (b) view of the inner segment created by the continuous print path, and (c) the results of adhering to the specified constructability design rules.

Note that flaws are known to exist in 3DCP, caused by predominantly by filament tearing and air entrainment. Special care was taken to avoid such flaws in the specimens presented here, in order to present best practise, and no observable flaws were indeed present, substantiated by relatively small coefficients of variation in characterised material parameters [16]. It is appreciated that flaws might dominate resistance to particular actions. However, the flaws are system, print parameter and material dependent, and a systematic study of the influence of flaws is required in future experimental campaigns, beyond the scope of the current contribution.

4.3.3 Loading configurations

In this section, the respective loading configurations are presented. These configurations comprise FPB at third points of dually (C1) and singularly reinforced (C2) concrete printed deep beams and an eccentrically loaded dually reinforced deep beam (C3). The FPB configurations are selected to determine the bending capacity of the printed items and verify the bonding constraint between the manually inserted reinforcement and the FRPC matrix. The eTPB configuration is proportioned to ensure that diagonal shear failure towards the right-hand side support dominates. The dimensions of the various configurations are summarised in Table 4.1. The schemes presented in Fig. 4.6a-b are notched at midspan to ensure failure at a predefined location within the constant moment region. Since shear failure is the desired failure mechanism for the eTPB configuration in Fig. 4.6c, the specimen is left unnotched. All tests are performed at a loading rate of 1 mm/min in a 250 kN Instron servo-hydraulic testing frame. A 500 kN HBM load cell is installed on the actuator head to continuously monitor the transmitted load with high accuracy in the force range applied at a 10 Hz sampling rate. Each FPB test is instrumented with 6 LVDTs (three opposing LVDTs per side), and the eTPB test is instrumented with 10 LVDTs (five opposing LVDTs per side) at the locations depicted in Fig. 4.6. The LVDTs are positioned using the LVDT frame shown in Fig. 4.6d and measure from the neutral axis of the beam in the direction of the arrowheads shown in Fig. 4.6a-c.

Table 4.1: Summary of dimensions used in the respective loading configurations.

Dimension	Value	Units	Dimension	Value	Units
a	280	mm	e	502	mm
b	338	mm	h	260	mm
c	25	mm	w	260	mm
d	230	mm	L	840	mm

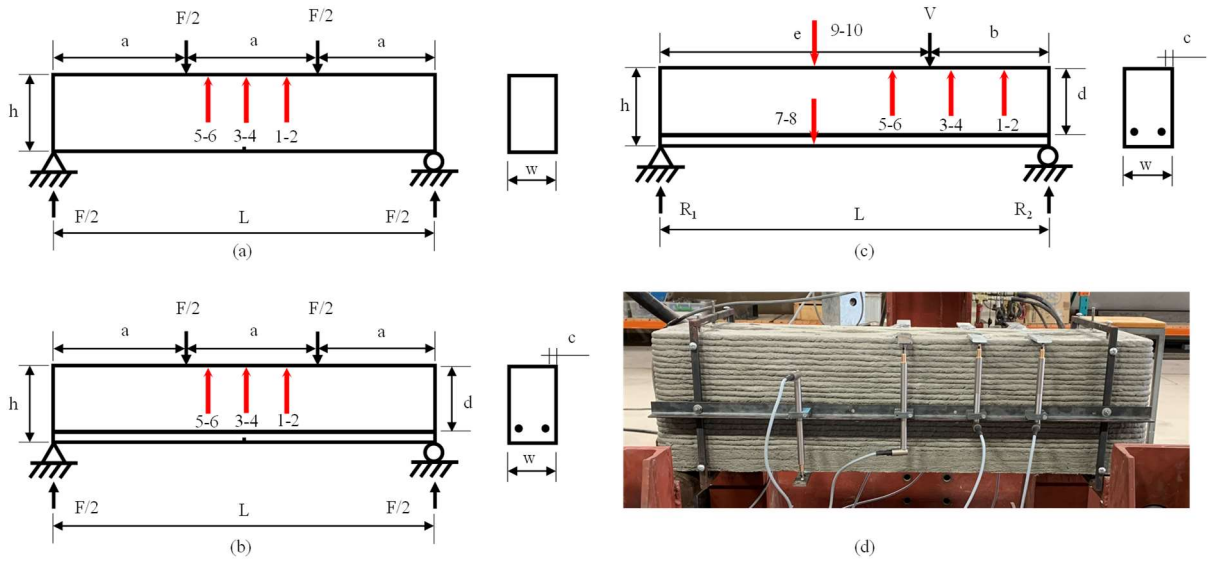

Fig. 4.6: Experimental loading configurations illustrating (a) C1: FPB of a singly (only PP microfibres) reinforced deep beam, (b) C2: FPB of a dually reinforced deep beam (2-Y10 rebars and PP microfibres), (c) C3: eTPB of a dually reinforced deep beam, and (d) a visual illustration of the eTPB configuration and LVDT frame.

4.4 Finite Element Modelling Methodology

A commercial FE analysis software product DIANA FEA [33] is used to simulate the respective loading schemes presented in Section 4.3.3. The individual models utilise the available nonlinear material models presented in Section 4.2, with the specific material parameters given below.

4.4.1 Model parameters

Utilising the extensive experimental results established in [16], the material parameters presented in Table 4.2 and Table 4.3 are prescribed for the continuum (CM) and interface-based models (IFM), respectively.

4.4.1.1 Continuum model input parameters

To exploit the anisotropic Rankine-Hill continuum model available in the DIANA FEA package, two elastic parameters (E, ν), seven strength parameters (f_{tx}, f_{ty}, f_{cx}, f_{cy}, α, β, and γ), and five inelastic parameters (G_{fx}, G_{fy}, G_{fcx}, G_{fcy}, and κ_p) are required. These parameters are summarised in Table 4.2, with detailed descriptions in Section 4.2. Supplementary reference pertaining to the underlying theoretical basis of these parameters can be found in the DIANA FEA user manual [34]. Note that these parameters are used for all the CM simulations unless explicitly stated otherwise. Poisson's ratio (ν) is assumed based on the work presented in [28]. Equation 4.4 sets out the means for determining the shear stress contribution to tensile failure (α) and β rotates the yield surface around the shear stress axis and can be ascertained from biaxial compression tests; however, due to a lack of experimental data, the default value of -1 is assumed. Equation 4.5 indicates how the shear stress contribution to compressive

failure (γ) is computed. The plastic strain at peak compressive stress is set to 0.2 % according to Eurocode 6 [28] and the default super-hyperbolic Rankine and Rankine-Hill parameters (n = 16, m = 32) are assumed. Equation 4.6 presents the calculation procedure for the compressive fracture energy in the respective orthotropic material directions.

Table 4.2: Input parameters for the anisotropic Rankine-Hill continuum model.

Isotropic Elastic Parameters					
E	21900	N/mm^2	ν	0.2	-
Orthotropic Strength Parameters					
x-direction			y-direction		
f_{tx}	2.45	N/mm^2	f_{ty}	1.25	N/mm^2
f_{cx}	45.1	N/mm^2	f_{cy}	38.2	N/mm^2
Unitless Strength Parameters					
α	0.35	β	-1	γ	0.525
Orthotropic Inelastic Parameters					
Crack bandwidth		According to Section 4.5.2			
G_{fx}	0.956	N/mm	G_{fy}	0.063	N/mm
G_{fcx}	27.07	N/mm	G_{fcy}	26.17	N/mm
κ_p	0.002	mm/mm			

$$\alpha = \frac{f_{tx} \cdot f_{ty}}{\tau_u^2} \tag{4.4}$$

τ_u is the interface shear-slip (Mode 2) capacity equal to 2.96 MPa from [28].

$$\gamma = \frac{f_{cx} \cdot f_{cy}}{\tau_u^2} \tag{4.5}$$

τ_u is the material pure shear (Mode 2) strength equal to 1.5$f_{c,y}$ MPa from [28].

$$G_{fc} = 15 + 0.43 \cdot f_c - 0.0036 \cdot f_c^2 \tag{4.6}$$

G_{fc} is related to f_c, the ultimate compressive capacity in the respective loading directions, as presented in [35].

4.4.1.2 Interface-based model input parameters

As mentioned in Section 4.2.2, the IFM is based on an interface elastoplastic constitutive model presented by Lourenco and Rots [30] to analyse unreinforced masonry structures and is adapted to include isotropic continuum elements that represent the intralayer matrix. The combined-cracking-shearing-crushing (CCSC) interface model available in DIANA FEA is implemented to define the IRs in the 3DCP composite. The intralayer filaments are prescribed an isotropic hypo-elastic total strain-based rotating crack (TSC) constitutive relation, also available in the DIANA FEA package, with properties given in Table 4.3 corresponding to the intralayer direction (x-direction) from [16]. Since the

CCSC interface elements represent the IRs (joints) in the printed composite, the direction 3 (y-direction) results for the compressive and tensile strength, and fracture energies are prescribed. Note that the cohesion (c_c) is taken as the pure shear strength of the interface (i.e., with zero normal stress) [36]. Due to the lack of experimental data explicitly pertaining to 3D printed cementitious composites, the parameters that are not attained from physical experiments follow the recommendations of [35]. Consequently, constant friction (36.87°) and dilatancy (0°) angles are assumed in this research. Furthermore, it is appreciated that the shear bond (Mode II) fracture energy (G^{II}_{fc}) depends on the level of normal stress acting on the interlayer, but due to insufficient data, an average value of $\frac{1}{10} \cdot c_c$ is assumed [35]. Currently, not much data exists about the compressive post-peak behaviour of 3DCP prisms; therefore, employing Equation 4.6 to approximate the compressive fracture energies is advised. The equivalent relative displacement (κ_p) can be calculated using Equation 4.7, ensuring that the total filament-interface strain combination equals 0.2 % at the peak compressive stress. The elastic normal stiffness in the IRs (k_{nc}) is taken as 1E+06 N/mm^3 according to [37], and the elastic shear stiffness (k_{sc}) is proportional to the shear moduli (Equation 4.8). From the definition of the compressive cap, $c_{ss,j}$ controls the shear stress contribution to the compressive failure of the IR [36] but is reported to have an insignificant influence. Nevertheless, the parameter is determined from the interface compressive strength ($f_{c,j}$) and the interface shear strength (c_c), as shown in Equation 4.9.

$$K_p = f_c \cdot \left\{0.002 - f_c \cdot \left[\frac{1}{E} + \frac{1}{k_{nc}(h_l + h_j)}\right]\right\} \tag{4.7}$$

E is the Young's modulus of the filament, k_{nc} is the elastic normal stiffness of the interface (joint), h_l is the filament layer height (h_l =10 mm), and h_j is the interface height (h_j = 0 mm).

$$k_{sc} = \frac{k_{nc}}{2(1+\nu)} \tag{4.8}$$

$$c_{ss,j} \leq \sqrt{f_c / c_c} \tag{4.9}$$

The intralayer filament regions are prescribed an exponential post-peak softening constitutive relation in tension to adhere to the intrinsic tension-softening specification of the anisotropic Rankine-Hill material model. Unless stated otherwise, Govindjee's projection method is employed for the crack bandwidth of continuum elements [36]. Furthermore, neither an increase in compressive strength due to confinement effects or reduction due to lateral cracking is included.

Table 4.3: Input parameters for the interface-based model.

Interface Parameters (CCSC interface)			Continuum Parameters (Total Strain based cracking)		
Parameter	Value	Units	Parameter	Value	Units
$f_{t,j}$	1.25	N/mm^2	E	21900	N/mm^2
$G^I_{f,j}$	0.063	N/mm	ν	0.2	-
c_c	2.96	N/mm^2	ρ	2.15E-06	T/mm^3
Friction angle (φ)	36.87	°	Crack orientation	Rotating	
Dilatancy angle (ψ)	0	°	Tensile curve	Exponential	
Residual friction angle (φ_r)	36.87	°	f_t	2.45	N/mm^2
Confining normal stress	-1	N/mm^2	G^I_f	0.956	N/mm
Exponential degradation coefficient	1	-	Crack bandwidth	According to Section 4.5.2	
G^{II}_{fc}	0.296	N/mm	Poisson ratio reduction	Damage based	
a	0	mm	f_c	45.1	N/mm^2
b	0.296	N/mm	G_{cc}	27.07	N/mm
G_{cc}	26.17	N/mm	Reduction due to lateral cracking	No	
k_{nc}	1.00E+06	N/mm^3			
k_{sc}	4.17E+05	N/mm^3	Confinement increase	No	
$c_{ss,j}$	3.5	-			
$f_{c,j}$	38.2	N/mm^2			
κ_p	0.0096	N/mm^2			

4.4.2 Geometric configurations & boundary conditions

The 2D plane stress FE model geometry and boundary conditions for the respective loading schemes are presented in Figs. 4.7-4.9. All dimensions are equivalent to those shown in Table 4.1. Each object is assigned an effective plane stress thickness (t_{eff}) equal to 141 mm. Additionally, 10 mm x 5 mm load/support blocks are positioned beneath the applied load locations to negate the effects of stress concentrations, reducing the computational effort required to simulate the respective configurations. In all instances, the continuum elements comprise quadratic eight-node quadrilateral isoparametric plane stress elements (CQ16M), whilst compatible quadratic line interface elements (CL12I) are employed in all IFMs [38]. For all loading configurations, the element mesh size (h) is well below the limiting $h \leq \frac{G_f \cdot E}{f_t^2}$, ensuring that snap-back at a constitutive level is avoided [39]. Regularisation of the energy dissipation is achieved by assuming that the inelastic work is uniformly distributed over the equivalent length of "h" by $g_f = \frac{G_f}{h}$ [39]. The particularities pertaining to each configuration are discussed in Sections 4.4.2.1-3, and the analysis procedure is outlined in Section 4.4.3.

4.4.2.1 Configuration 1

The geometric and loading configurations relating to the C1-CM-2D and C1-IFM-2D models are presented in Fig. 4.7a-b, respectively. The FE model boundary conditions are identical in both instances, comprising vertical translation (y-direction) constrains at the bottom roller supports, and a horizontal

translation (x-direction) constraint at the bottom left roller support. The upper load blocks are assigned a prescribed displacement of 4 mm in the negative y-direction, and 10 mm square mesh is prescribed to all regions shown in Fig. 4.7. Note that the central elements above the notched region are assigned 3.5 mm x 10 mm rectangular elements due to the notch geometry. Furthermore, depending on the crack bandwidth prescription applied (i.e., Rots, Govindjee, or user-specified), careful consideration relating to the regularisation of energy dissipation in the continuum elements is required. The analyst should ensure that the regularised fracture energy ($g_f = \frac{G_f}{h}$) is equal in the respective regions of the model. In this case, comparable energy dissipation is achieved by manually prescribing crack bandwidths equal to 3.5 mm and 10 mm, in the notched and unnotched regions and reducing the G_{fx} and G_{fy} according to the element size in the notched region. The C1-IFM-2D model is assigned interface constraints at 10 mm intervals (corresponding to the layer heights) at the locations shown in Fig. 4.7b. As depicted in Fig. 4.13a, two analyses are conducted for the C1-CM-2D model, initially with the material properties presented in Table 4.2, while the latter considers a lower-bound analysis (C1-CM-2D-LBA) which reduces f_{tx} to 2.3 MPa. The C1-IFM-2D model only considers the parameters given in Table 4.3.

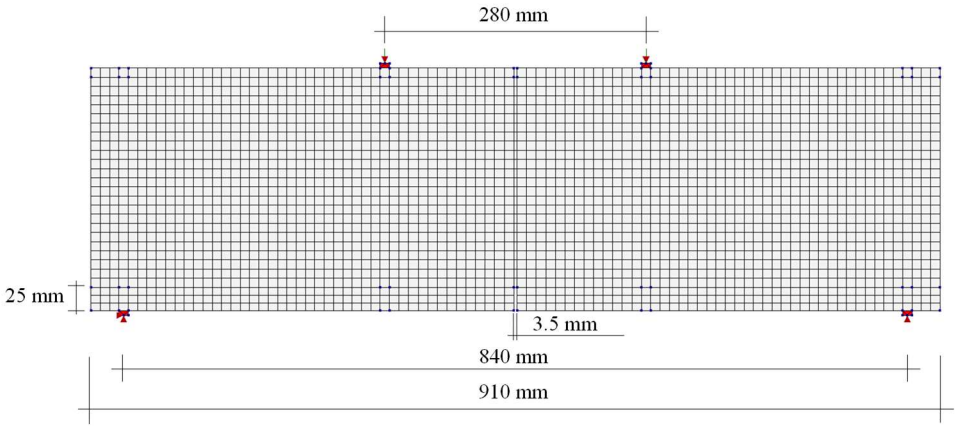

(a)

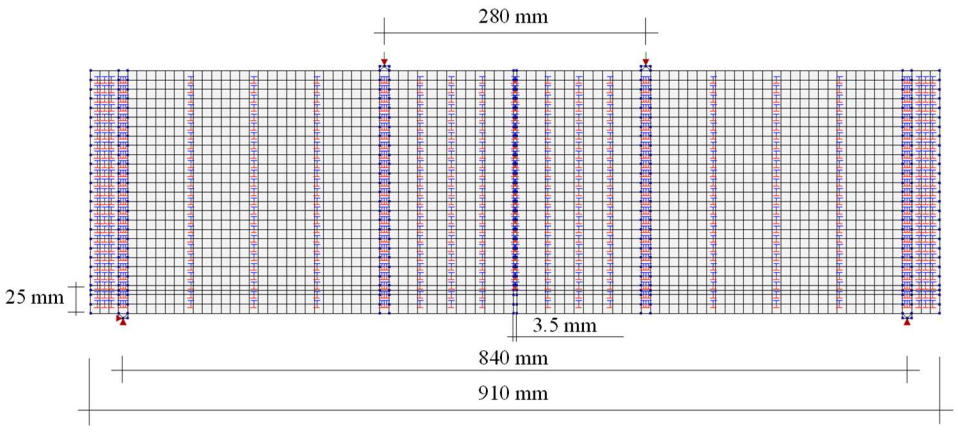

(b)

Fig. 4.7: C1 geometry and boundary conditions, presenting (a) the C1-CM-2D model and (b) the C1-IFM-2D model with interface constraints.

4.4.2.2 Configuration 2

The boundary conditions, geometry, and loading configurations relating to the C2-CM-2D and C2-IFM-2D models are presented in Fig. 4.8. The FE model boundary conditions are identical to those presented in Section 4.5.2.1, while the top load blocks are assigned a prescribed displacement of 8 mm in the negative y-direction. The C2-IFM-2D model interface constraints are applied as per Fig. 4.7b, and a 10 mm square mesh is prescribed to all regions shown in Fig. 4.8.

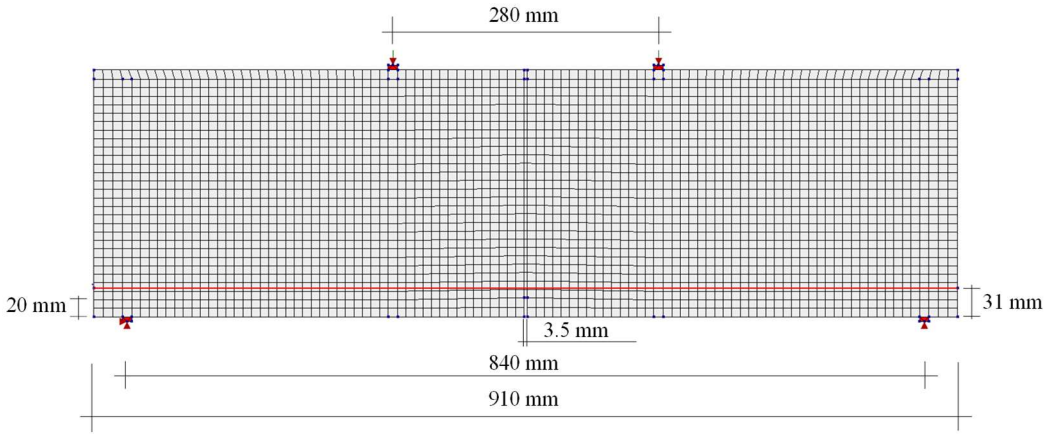

Fig. 4.8: C2 geometry and boundary conditions.

A 500 MPa yield strength embedded reinforcement element, with linear hardening properties shown in Table 4.4, is included at 31 mm from the bottom-most filament. Although 30 mm is the desired distance, the embedded reinforcement algorithm prescribes that elements must be located within surrounding continuum elements. The Y10 reinforcement represents the two reinforcement bars placed on each side of the beam and is included as one line element with twice the area (A_{rebar} = 157.08 mm^2).

Table 4.4: Reinforcement properties, reproduced from [40].

Young's modulus (E)	200E+03	N/mm^2
Yield stress (f_y)	500	N/mm^2
Ultimate strength (f_{ult})	8574	N/mm^2
Ultimate strain (ε_{su})	1*	-

**this value is prescribed to permit computational strain-hardening, but the codified fracture limit is 0.14%, according to* [41].

Accurate FE analysis of the experimentally evaluated configurations is verified based on both the load-displacement response and the attained crack patterns, representing the predominant failure mechanisms. It is noted that the parameters α and γ dictate the sequence in which the respective failure mechanisms occur, see Section 4.5.1. Therefore, a parameter study (PS) is conducted to calibrate the non-experimentally determined strength parameters α and γ to the experimentally observed crack patterns. Additionally, the crack bandwidth specification is numerically studied to assess the influence of various regularisation procedures. The user-specified case ensures comparable energy dissipation by

manually prescribing crack bandwidths equal to 3.5 mm and 10 mm, in the notched and unnotched regions and reducing the G_{fx} and G_{fy} according to the element size in the notched region. PS4 is based on Govindjee's projection method [36]. These parameters are varied, as presented in Table 4.5.

Table 4.5: C2-CM-2D parameter study of non-experimentally determined strength parameters.

Parameter Study	α	γ	Crack bandwidth
PS1	0.68	1.00	User-specified (10mm, 3.5mm)
PS2	1.00	0.53	User-specified (10mm, 3.5mm)
PS3	1.00	3.00	User-specified (10mm, 3.5mm)
PS4	1.00	3.00	Govindjee

Two parameter variations are studies for the C2-IFM-2D model. The first (C2-IFM-2D-v1) presents the standard parameters given in Table 4.3. The latter increases the interfacial friction angle ($\varphi = 40°$) and reduces the Mode II fracture energy ($G^{II}_{fc} = 0.15$ N/mm) to study the relationship between these variables.

4.4.2.3 Configuration 3

The boundary conditions, geometry, and loading configurations relating to the C3-CM-2D and C3-IFM-2D models are presented in Fig. 4.9. In both instances, the FE analysis boundary conditions include vertical constraints in the y-direction at the bottom support rollers, a horizontal constraint applied to the top load block, and a prescribed displacement of 10 mm, in the negative y-direction. The interface constraints in the C3-IFM-2D model are once again applied as per the illustration in Fig. 4.7b, and a 10 mm square mesh is prescribed to all regions shown in Fig. 4.9. An embedded reinforcement element, with properties presented in Table 4.4, is included 31 mm above the bottom-most filament. The simulation of both the C3-CM-2D and C3-IFM-2D cases is initially conducted with the standard parameters presented in Tables 4.2 and 4.3.

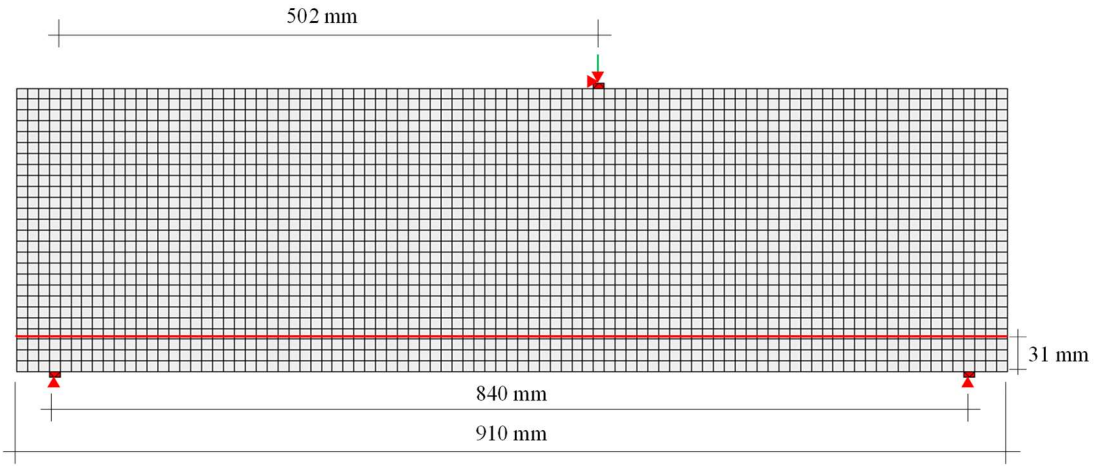

Fig. 4.9: C3 geometry and boundary conditions.

Thereafter, a parameter study relating to the non-experimentally determined strength parameters (α and γ) in the C3-CM-2D model is conducted with the respective combinations presented in Table 4.6. Additionally, a second parameter study is performed on the C3-IFM-2D model to determine the influence of lower shear bond (cohesion) at varying friction angles, and Mode II fracture energies, as shown in Table 4.7. Since the geometric configuration is proportioned to exhibit shear critical failure, forming diagonal shear cracks, Govindjee's projection method [36] is specified for all regions.

Table 4.6: C3-CM-2D parameter study of non-experimentally determined strength parameters.

Parameter Study	α	γ
PS1	0.39	1.18
PS2	0.68	3.00
PS3	0.84	3.00
PS4	1.00	3.00

Table 4.7: C3-IFM-2D parameter study of interface parameters.

Parameter Study	c_c (MPa)	Φ (°)	G^{II}_{fc} (N/mm)
PS1	2.80	38.00	0.15
PS2	2.80	36.87	1.00
PS3	2.50	36.87	1.00
PS4	2.50	36.87	0.25

4.4.3 Analysis procedure

In all instances, a nonlinear structural analysis, which considers material and geometric nonlinearity, in combination with a fixed step incremental-iterative secant (quasi-newton) BFGS solution procedure is employed. A second-order (consistent) plasticity algorithm is elected. Both energy and force convergence norms equal to 0.001 and 0.01 respectively are applied, and a line search algorithm is employed to increase the convergence rate of the numerical analysis.

4.5 Results & Discussions

The following section presents the experimental and numerical simulation results for the respective loading configurations and numerical simulation strategies presented in Sections 4.2 and 4.3.3. The presented results include the individual load-displacement responses and descriptions of the failure mechanisms associated with the various loading configurations and FE simulation strategies.

4.5.1 Experimental results

4.5.1.1 Configuration 1

The experimental load-displacement results pertaining to the singularly reinforced 3DCP beam under four-point bending (FvD-C1-XP) is presented in Fig. 4.10a, and the cracking pattern is shown in Fig. 4.10b. The FvD-C1-XP response depicts an ultimate bending capacity of 45.3 kN followed by strain-softening post-peak behaviour with limited ductility. A maximum mean mid-span deflection of 7.4 mm, in the negative Y-direction, is recorded on LVDT average (avg) 3-4. The resemblance between LVDT avg 1-2 and LVDT avg 5-6 indicates a reasonably symmetric failure mode, and the similar cracking patterns presented reinforces the notion of symmetric bending failure. Additionally, considering the experimental cracking pattern (Fig. 4.10b), it is evident that the flexural capacity of the member is the governing failure mode.

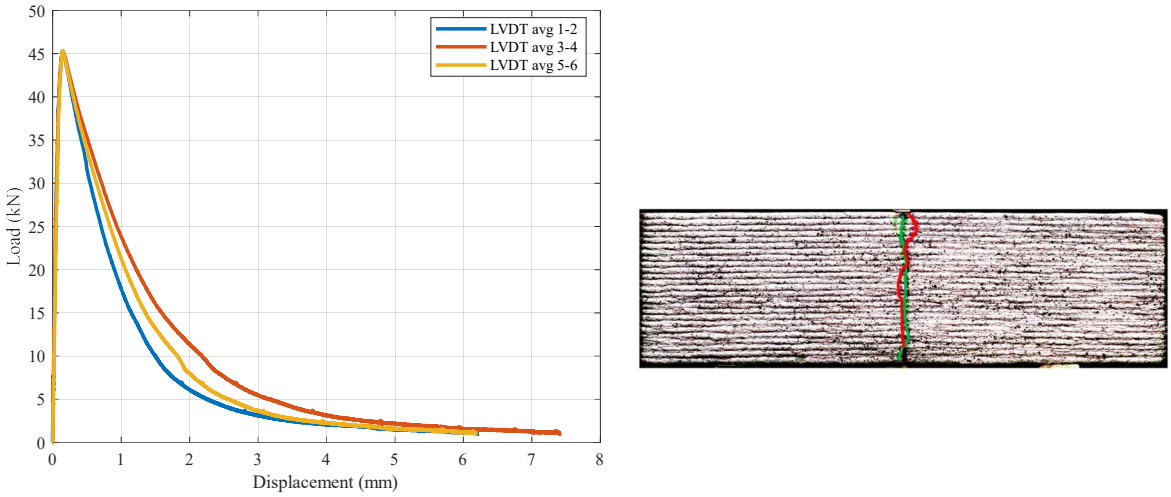

(a) (b)

Fig. 4.10: Configuration 1 experimental results showing (a) the load-displacement response (C1-XP) and (b) the experimental cracking pattern, where the front (green) and back (red) faces are overlaid to represent the entire member.

4.5.1.2 Configuration 2

The experimental load-displacement results pertaining to the dually reinforced 3DCP beam under four-point bending (FvD-C2-XP) is presented in Fig. 4.11a, and the numbered cracking pattern is shown in Fig. 4.11b. FvD-C2-XP exhibits both amplified load-carrying capacity and ductility when compared to FvD-C1-XP. Therefore, it is deduced that the manual in-laid placement of reinforcement during the printing process is an effective reinforcement strategy for 3DCP. Considering the FvD-C2-XP response, at 103 kN, the first nonlinearity is attributed to the formation of (1) diagonal shear cracks originating from the location of the load-inducing rollers. As expected, the combination of additional tensile reinforcement, no vertical shear reinforcement, and the deep beam geometric configuration evokes diagonal shear failure as the initial failure mechanism. Thereafter, at 164 kN, the limited deformability of the printed matrix induces cracking, thereby localising the tensile strains, and results in (2) yielding

of the reinforcement as depicted within the inner span. Subsequently, increased deformation and associated moment redistribution induce the formation of (3) multiple smaller flexural cracks, which further propagate to diagonal tension discontinuities. Finally, excessive deformation resulting in large curvatures triggers (4) interlayer delamination at the location of the manually inserted reinforcement. Although it is not explicitly presented, it is considered that definitive failure would occur once the reinforcement reaches its ultimate strain capacity and fractures.

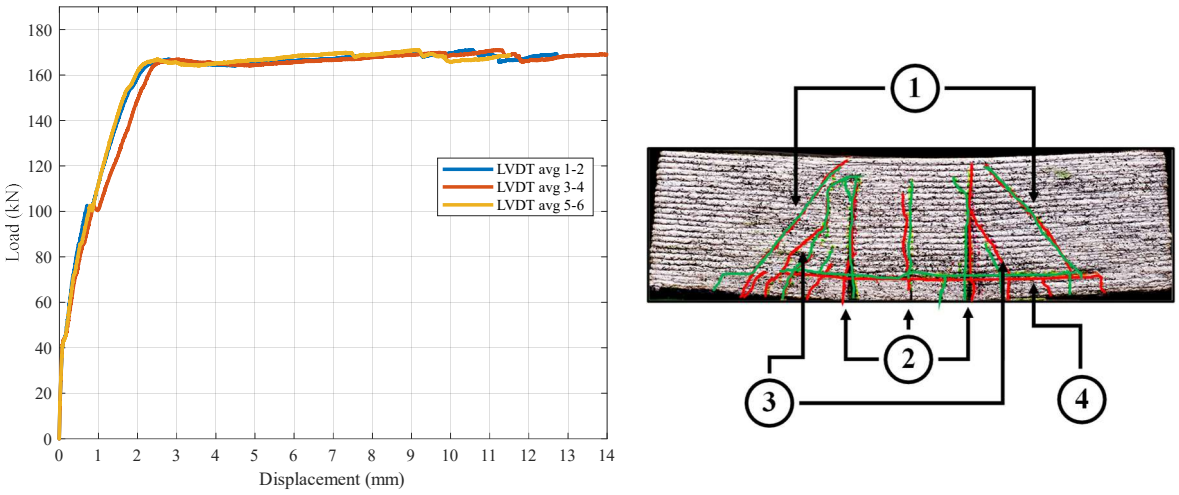

(a) (b)

Fig. 4.11: Configuration 2 experimental results showing (a) load-displacement response (C2-XP) and (b) illustrates the experimental cracking pattern, where the front (green) and back (red) faces are overlaid to represent the entire member.

4.5.1.3 Configuration 3

The experimental load-displacement results relating to the dually reinforced 3DCP beam under eccentric three-point bending (FvD-C3-XP) are presented in Fig. 4.12a, with the numbered cracking pattern shown in Fig. 4.12b. The FvD-C3-XP response presents the average LVDT readings at locations 1 to 6 (see Fig. 4.6c). The initial nonlinearity, at 93 kN, is attributed to (1) the diagonal shear crack towards the bottom right roller support. Evidently, the combination of additional tensile reinforcement, no vertical shear reinforcement, and the deep beam geometric configuration, with eccentric loading, evokes diagonal shear failure as the initial failure mechanism.

A peak load-carrying capacity of 124 kN is recorded at the initial peak before the yielding plateau is entered. After the peak load is reached, a secondary vertical bending crack (2) is formed due to the limited deformability in the printed cementitious composite, resulting in the somewhat perfectly plastic post-peak behaviour attributed to strain localisation and yielding of the tensile reinforcement. Due to excessive deformation, (3) delamination occurs on the IR where the reinforcement is situated, resulting in the horizontal crack pattern near the bottom of the vertical bending crack. After additional deformation, (4) multiple minor bending cracks are formed without any load release in the member. Ultimate failure occurs in a brittle fashion, illustrated by (5) the left shear-flexural crack in Fig. 4.12b.

The left-hand horizontal crack (6) is attributed to the loss of bonding due to cracking, large curvatures, and the reduced interlayer contact area at the location where the reinforcement is placed.

The lack of vertical shear reinforcement in conjunction with weaker IR results in a shear critical ultimate failure mechanism. From the moderate ductility exhibited, it is deduced that the reinforcement is sufficiently bonded to the 3DCP matrix to permit the formation of multiple cracks. Furthermore, the requirement for vertical shear reinforcement is highlighted by the presented results. It is envisioned that a solution may lie in vertical reinforcement strategies that bridge interlayer regions such as orthogonal straight [42,43] and corrugated [44] steel fibre links, mesh [45], nail [46], needle [1], inserted rebar [44,47], and additively manufactured reinforcement [48]. Although, the structural, durability, and reliability performance of these strategies requires additional verification for design specification to be set.

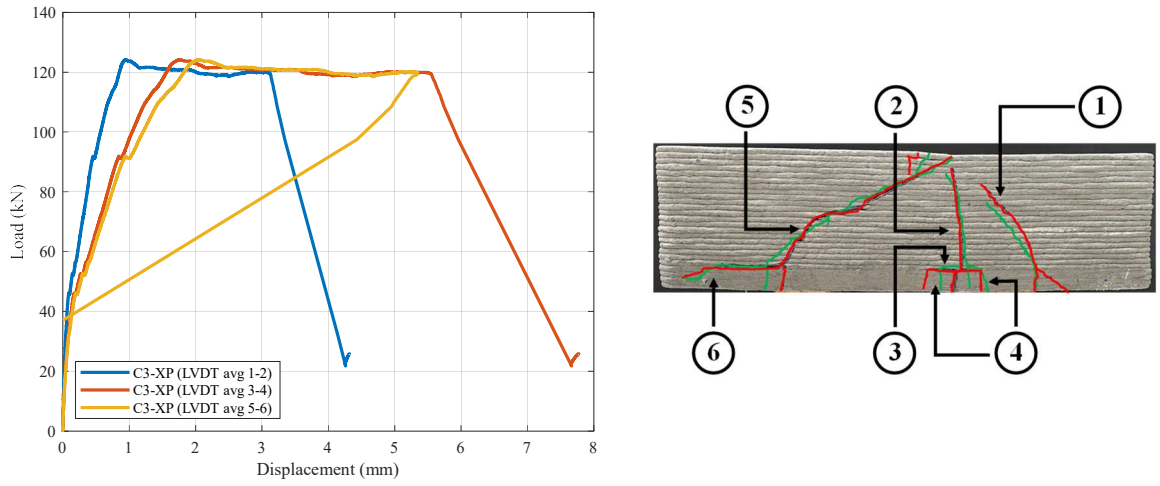

(a) (b)

Fig. 4.12: Configuration 3 experimental results presenting (a) the load-displacement response (C3-XP) and (b) the experimental cracking pattern, where the front (green) and back (red) faces are overlaid to represent the entire member.

4.5.2 Numerical simulation results

4.5.2.1 Configuration 1

The FE simulation results for C1-CM-2D and C1-IFM-2D models are presented in Fig. 4.13a-b, and the crack patterns are shown via the principal strain tensors in Fig. 4.13c-d. Applying the standard parameters given in Table 4.2, the FEM C1-CM-2D load-displacement (FvD) response is attained. A maximum flexural capacity of 53 kN is exhibited, 17 % higher than the experimental observation (C1-XP), with a reasonable agreement in the post-peak regime. The overestimation in flexural capacity is attributed to the incorrect crack pattern given in Fig. 4.13e, which forms two crack branches with collectively greater resistance. The lower bound analysis FEM C1-CM-2D-LBA, with f_{tx} equal to 2.3 MPa, yields good agreement over the entire FvD response, demonstrating a peak flexural capacity of 44.8 kN, only 1 % lower than the C1-XP. Employing the standard parameters presented in Table 4.3,

the FEM C1-IFM-2D FvD response is attained. A maximum flexural capacity of 46.2 kN (2 % higher than C1-XP) is shown with an excellent agreement in the softening regime.

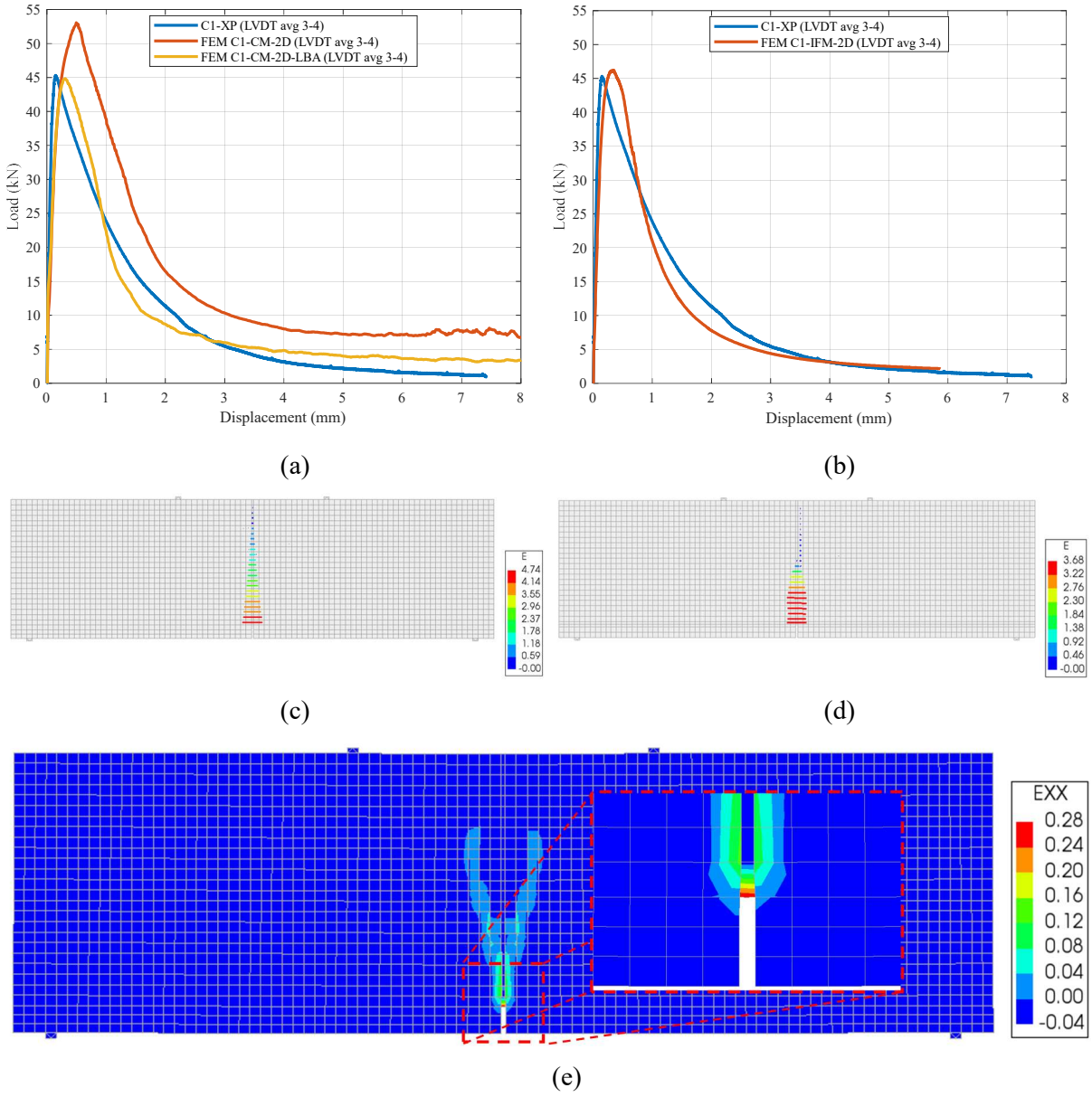

Fig. 4.13: Presents the plane stress numerical analysis load-displacement results for (a) the configuration 1 continuum model (C1-CM-2D) and (b) the configuration 1 interface model (C1-IFM-2D). The maximum in-plane principal strain components are presented as a visual representation of the predominant failure mechanism for (c) C1-CM-2D and (d) C1-IFM-2D. The attained crack pattern for (e) FEM C1-CM-2D (standard analysis) depicting the incorrect result induced by the high LOA.

An explanation relating to the variance amidst the FEM C1-CM-2D and FEM C1-IFM-2D analyses resides in the underlying theory of the anisotropic smeared cracking approach adopted in the C1-CM-2D model. Where the large level of anisotropy (LOA = 1.96) results in an inappropriate crack pattern (Fig. 4.13e) favouring the reduced strength (f_{ty}) and regularised fracture energy (g_{fy}) in the y-direction resulting from the rectangular 3.5 mm x 10 mm mesh seeding above the notched region. This is circumvented by reducing the LOA to 1.84, thereby negating the effects of the misaligned principal

stresses around the notched region. In contrast, this effect is unpronounced in the FEM C1-IFM-2D model due to the isotropic TSC material law employed, where the lower f_{ty} capacity is exclusively localised to the IRs.

Nonetheless, both models depict excellent agreement with the experimental observation in terms of both the FvD response and the attained crack patterns. Thereby, the experimentally obtained material parameters presented in [16] are validated at a larger scale. Furthermore, the proposed plane stress simplification presented in Section 4.2.3 is discerned to effectively capture the behaviour of 3DCP beams with cellular infill patterns.

4.5.2.2 Configuration 2

The FE simulation results for the C2-CM-2D and C2-IFM-2D models are presented in Fig. 4.14a-b and the crack patterns are shown via the principal strain tensors in Fig. 4.14c-f. Utilising the standard parameters given in Table 4.2, the FEM C2-CM-2D-STD FvD response is attained. Good agreement is observed in the elastic region until the initial shear nonlinearity at 103 kN, where after the stiffness of the member is overestimated. A flexural yield capacity of 186 kN is attained, 13 % higher than the C2-XP result at this location in the FvD response. It is observed that the FEM C2-CM-2D-STD model is dictated by a flexural failure mechanism (Figs. 4.14a and 4.14c) and not diagonal shear cracking, as is the case in the C2-XP results and observations.

It is deduced that the shear stress contribution to failure (α) is underestimated, or rather the pure shear capacity of the composite is overestimated with α equal to 0.35. This observation is the premise for the parameter study presented in Section 4.4.2.2. Applying the standard parameters given in Table 4.3, the FEM C2-IFM-2D-v1 FvD response is attained. A peak shear capacity of 178 kN is reached, corresponding to a 9 % overestimation of the shear capacity, where after flexural cracking and interlayer delamination describe the failure mechanisms in the plateau. Similar behaviour is exhibited by the FEM C2-IFM-2D-v2 response, which employs an increased interfacial friction angle ($\varphi = 40°$) and reduced Mode II (sliding) fracture energy ($G^{II}_{fc} = 0.15$ N/mm). A peak shear capacity equal to 181 kN is attained, where flexural yielding and interlayer delamination too describes the post-peak behaviour.

Considering the crack patterns in Fig. 4.14d and Fig. 4.14f, it is foremost noted that both simulations capture the C2-XP crack pattern well, with a marginal discrepancy in the crack distribution observed in the constant moment region. An inversely proportional relationship is recorded between the φ and G^{II}_{fc} parameters, consistent with the Mohr-Coulomb material model enforced; an increase in friction angle results in higher shear stress at corresponding normal stress states and a higher G^{II}_{fc} exhibits retentive tensile capacity in the softening regime. From these observations, it is inferred that the recommended material prescriptions in Tables 4.2 and 4.3 are suited to simulate reinforced 3DCP elements in bending.

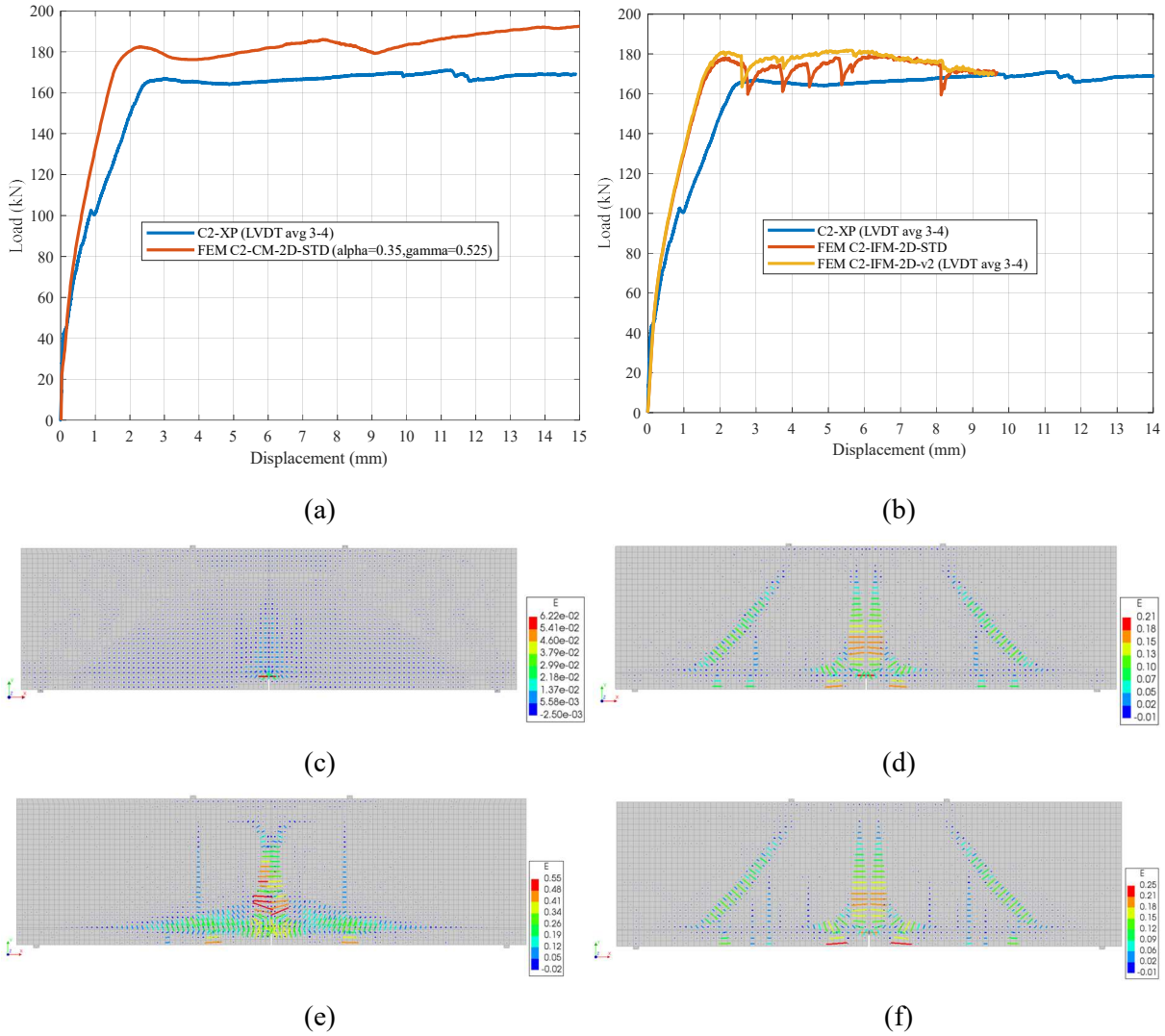

Fig. 4.14: Illustrates the plane stress FE analysis load-displacement results for (a) Configuration 2 continuum model (C2-CM-2D) and (b) Configuration 2 interface model (C2-IFM-2D). Accompanied by the failure mechanisms with (c) the tensile yielding mechanism for C2-CM-2D-STD, the final crack patterns for (d) FEM C2-IFM-2D-v1, (e) FEM-C2-CM-2D-STD, and (f) FEM-C2-IFM-2D-v2.

The results relating to the C2-CM-2D parameter study are displayed in Fig. 4.15a, and the crack patterns are shown in Figs. 4.15b-e. It is shown that increasing α to the unitary Rankine value (α=1) triggers shear failure as the initial failure mechanism at ~122 kN; the prominent oblique strain localisations reveal this in Figs. 4.15c-e. In contrast, Fig. 4.15b portrays the predominant flexural failure mechanism resulting from a lower value for α. The FEM-C2-CM-2D-PS2 simulation presents the best agreement with the experimental results, offering an initial shear capacity equal to 125 kN and flexural capacity of 169 kN, only 3 % over the C2-XP result. The crack pattern in Fig. 4.15c depicts reasonable agreement with the C2-XP cracking pattern, besides the absence of the major vertical cracks that are localised to one crack.

The post-peak yield regime is superbly matched by all parameter study alternatives. Additionally, the increased shear contribution to compressive failure (γ) is shown to only contribute to the ultimate

compressive failure beneath the load blocks. This is likely due to the geometric configuration and should be validated on object geometries where shear and compressive-shear failure modes govern.

Finally, FEM-C2-CM-2D-PS4 shows a reduction in the overall capacity of the member brought about by the crack bandwidth prescription, although excellent agreement with the experimental results is still noted. From these observations, it is apparent that supplementary calibration of parameters α and γ are required for 3DCP composites and variations of the tests proposed in [29] are recommended.

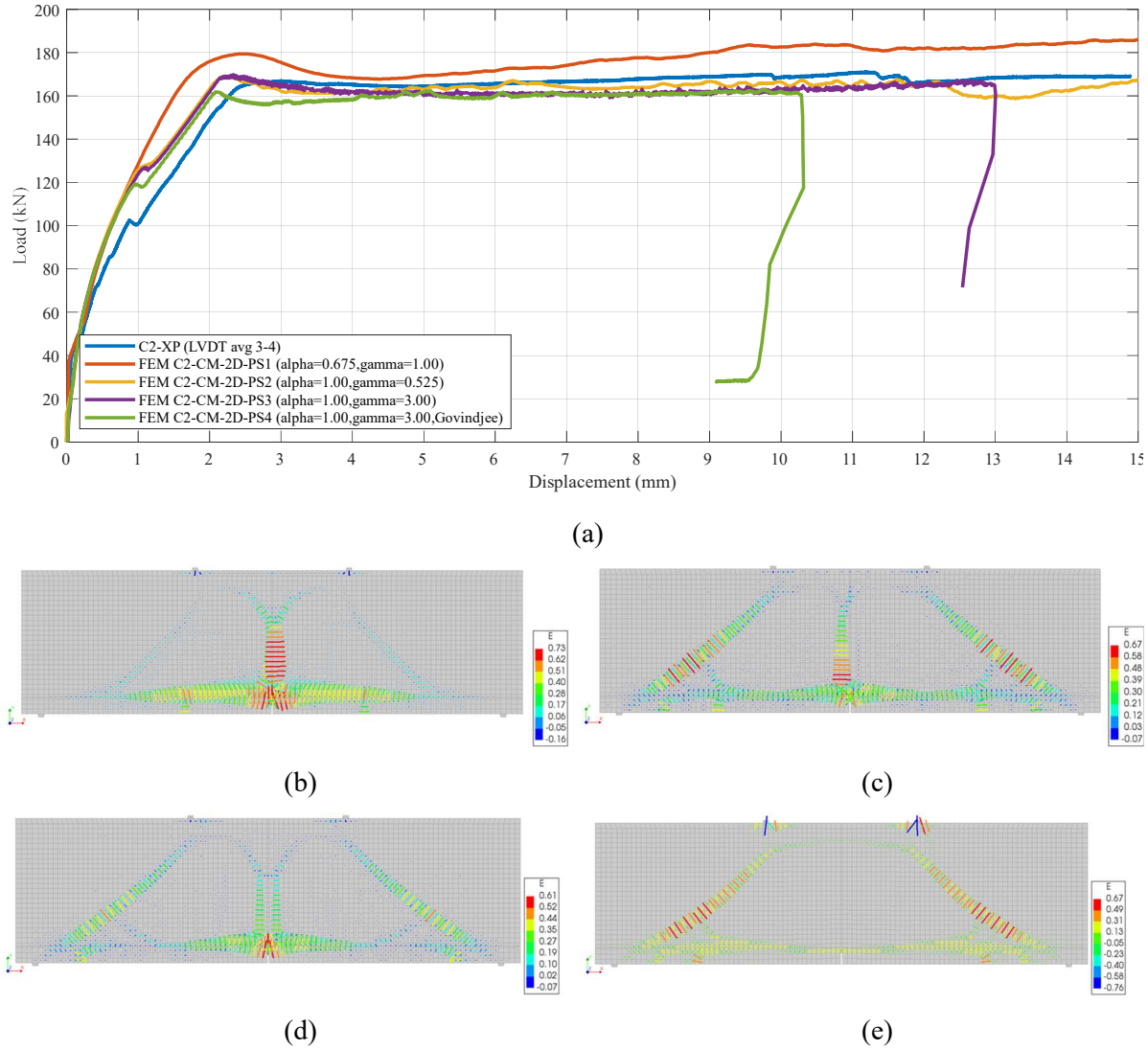

Fig. 4.15: FE analysis parameter study (PS) results of C2-CM-2D depicting (a) the load-displacement response for PS1-4 and the obtained crack patterns for (b) PS-1, (c) PS-2, (d) PS-3, and (e) PS-4.

4.5.2.3 Configuration 3

The FE simulation results for the C3-CM-2D and C3-IFM-2D models are presented in Figs. 4.16 a-b and the crack patterns are shown via the principal strain tensors in Figs. 4.16 c-d. Utilising the standard parameters presented in Table 4.2, the FEM C3-CM-2D FvD response is attained for averaged readings on LVDT 1-2. Excellent agreement is reflected in the elastic region, although the initial shear-induced

nonlinearity at 93 kN is not captured. This observation suggests that the shear stress contribution to tensile failure is underestimated and warrants the parameter investigation presented below. The initial yield capacity of 138 kN, 11 % higher than C3-XP, is attributed to the flexural resistance of the member, as illustrated in Fig. 4.16c.

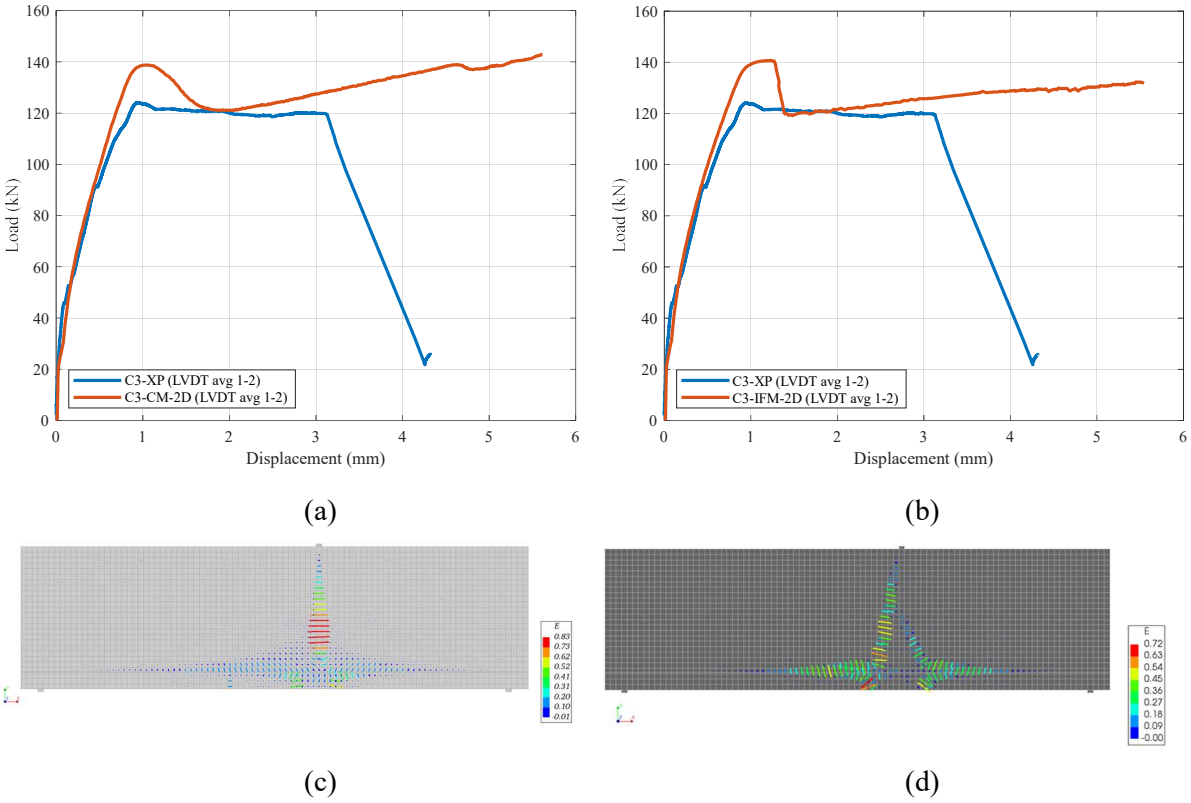

Fig. 4.16: Plane stress FE analysis load-displacement results for (a) Configuration 3 continuum model (C3-CM-2D), and (b) Configuration 3 interface model (C3-IFM-2D), as well as, the numerical cracking patterns for (c) C3-CM-2D, and (d) C3-IFM-2D.

The underestimation of α is inferred to induce flexural yielding, as opposed to diagonal shear failure. After the load release after the initial peak, additional deformation initiates interlayer delamination as recorded in the experimental observations. Thereafter, flexural hardening attributed solely to yielding of the reinforcement is shown and is considered the apparent result of the misrepresented failure mechanisms. Applying the standard parameters presented in Table 4.3, the FEM C3-IFM-2D FvD response is attained with a notable agreement in the elastic response. A peak bending capacity of 141 kN is reached, corresponding to a 14 % overestimation of the yielding capacity, where after a sudden drop in capacity is observed. Two diagonal shear-bending failure mechanisms dictate the FvD response ensuing the peak capacity, and persists until the simulation is completed. The less pronounced flexural hardening behaviour is attributed to load release via interlayer delamination. Furthermore, the similarity of the C3-CM-2D and C3-IFM-2D models indicates that the recommended standard input material parameters are suitably calibrated to one another.

The results relating to the C3-CM-2D parameter study are displayed in Fig. 4.17a, and the crack patterns are shown in Figs. 4.17b-e. It is shown that initial shear failure is induced by increasing α to values greater than 0.675, exposed by the pronounced diagonal strain localisations in Figs. 4.17d-e. In contrast, C3-CM-2D-PS2 (Fig. 4.17c) portrays the best correlation with the experimental crack pattern in C3-XP. The C3-CM-2D-PS3 simulation presents the best agreement with the experimental FvD results, offering an initial shear capacity equal to 110 kN and flexural capacity of 125 kN, only 1 % over the C3-XP result. Although, the crack patterns for α values greater than 0.675 (Figs. 4.17d-e) depict predominantly shear and shear-bending failure mechanisms and smaller multiple bending cracks induced at larger deformations. The post-peak yield regime is well matched by all CM parameter study alternatives, although the brittle ultimate shear-bending failure mode is not captured, even at large γ values. Clear justification for the latter observation is not available and would require a more extensive experimental data set to investigate this phenomenon.

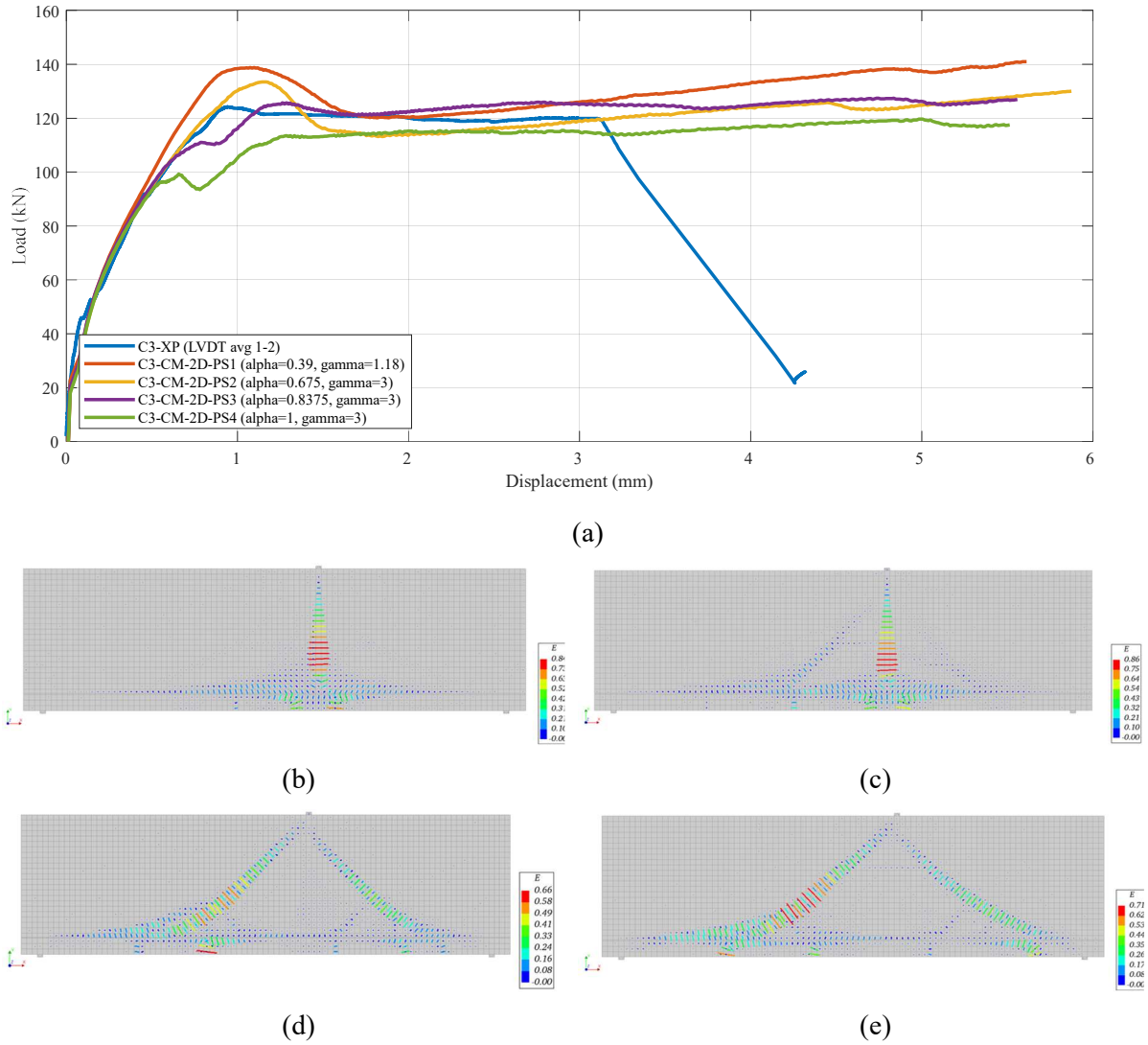

Fig. 4.17: FE analysis parameter study (PS) results pertaining to C3-CM-2D depicting (a) the load-displacement response for PS1-4 and the obtained crack patterns for (b) PS-1, (c) PS-2, (d) PS-3, and (e) PS-4.

The results relating to the C3-IFM-2D parameter study are displayed in Fig. 4.18a, and the crack patterns are shown in Figs. 4.18b-e. Similar results to those of the C3-CM-2D parameter study are attained, and the inversely proportional relationship between the friction angle and Mode II fracture energy is shown. It is observed that a high friction angle (φ =38 °) and low fracture energy (G^{II}_{fc} = 0.15 N/mm) results in a steep decline in load-carry capacity since when the shear capacity is reached, there is little retentive capacity in the IR.

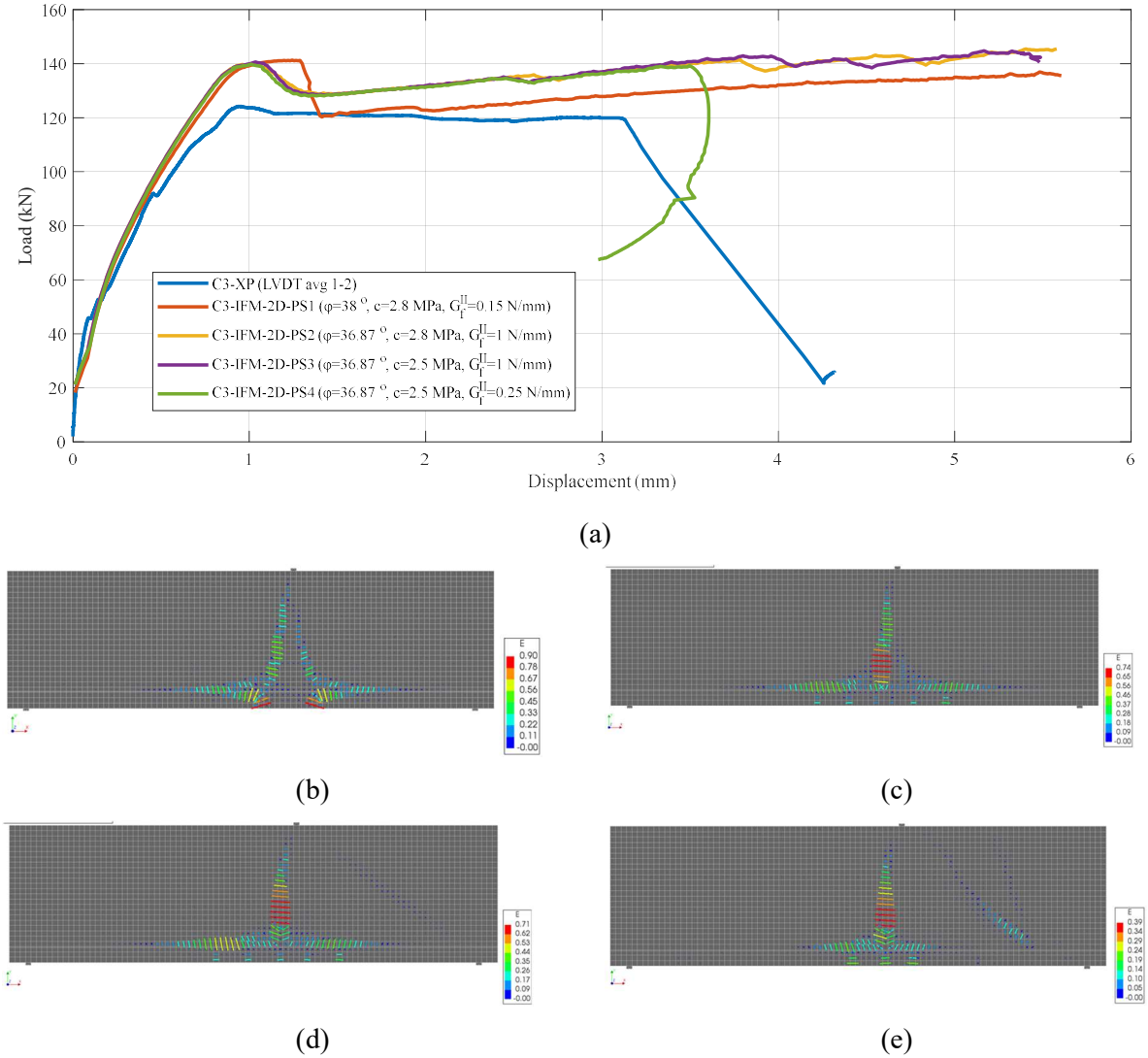

Fig. 4.18: FE analysis parameter study (PS) results pertaining to C3-IFM-2D depicting (a) the load-displacement response for PS1-4 and the obtained crack patterns for (b) PS-1, (c) PS-2, (d) PS-3, and (e) PS-4.

Conversely, assigning the recommended lower friction angle (φ =36.87 °), a smooth load decay transition, as in C3-IFM-2D-PS2 and PS3, is demonstrated. As illustrated by the C3-IFM-2D-PS4 FvD response and the crack pattern shown in Fig. 4.18e, a low friction angle and, in combination with a lower Mode II friction angle induces a brittle decrease in load-carrying capacity. None of the IFM parameter study alternatives accurately represent the experimental cracking pattern in C3-XP, with C3-IFM-2D-PS3 presenting the nearest resemblance. Therefore, it is evident that additional calibration of

the interfacial shear input parameters is required. Nevertheless, the portrayed results are still deemed appropriate from a structural design perspective and warrant further investigation with various printable cementitious compositions.

4.6 Conclusions

In this research, the mechanical performance of reinforced 3DCP deep beams with hollow cross-sections is experimentally evaluated under three respective loading configurations. Context is provided to the design, fabrication and process parameters applied to realise the printed geometries. A methodology pertaining to the simplification of fibre-reinforced three-dimensional geometries is presented for application in two-dimensional plane stress numerical simulation procedures. Furthermore, an analogy is drawn between proven numerical simulation strategies for masonry structures and adapted to comply with the material characteristics of 3DCP elements. These strategies are comprised of a multi-surface anisotropic continuum macro-modelling approach and a multi-surface interface-based micro-modelling approach with isotropic intralayer material prescriptions. These numerical simulation strategies are employed to simulate the experimentally evaluated beams under the respective loading configurations and parameter various. From these efforts, the following main conclusions are drawn:

1. The presented 3D geometric configurations can intuitively be simplified to representative 2D plane stress elements that reduce the computational expense required to simulate the structural response. Furthermore, the effective contact area between filaments should be considered for structural design endeavours.
2. The singularly reinforced configuration (C1-XP) exhibits an ultimate bending capacity of 45.3 kN followed by strain-softening post-peak behaviour with limited ductility. In comparison, the dually reinforced configuration (C2-XP) exhibits both amplified load-carrying capacity at 164 kN and ductility compared to C1-XP.
3. Adequate bond and anchorage of the reinforcement in the printed matrix is observed in both the C2 and C3 experimental loading configurations. The formation of multiple bending cracks corroborates this assertion. Therefore, it is deduced that the manual in-laid placement of reinforcement during the printing process is an effective reinforcement strategy for 3DCP.
4. The need for vertical reinforcement (over the interlayer) is highlighted by the initial shear dominant failure in both C2 and C3.
5. Pure bending is accurately simulated by both numerical simulation strategies, with the FEM-C1-CM-2D-LBA and FEM-C1-IFM-2D models presenting a peak load capacity within 2 % of the C1-XP result and sound agreement in the softening regime. Thereby validating the suitability of the employed material parameters at a larger scale.

6. Utilising the recommended input material and model parameters, fair agreement in both the FEM-C2-2D-STD and FEM-C2-IFM-2D-STD simulations is attained, with a maximum load capacity within 13 % of the C2-XP result. From the attained crack patterns, it is inferred that the shear capacity of the members is overestimated. The FEM-C2-CM-2D parameter study supports this assertion, where increased values of α are shown to capture not only initial shear failure but also the correct post-peak flexural yielding behaviour.
7. Reasonable agreement is observed under eccentric three-point bending (C3), with the recommended parameters exhibiting a maximal load capacity error smaller or equal to 14 %. Again, the calibration of the shear capacity of the member reveals better agreement with the experimental observations. It is recommended that the parameters affecting the shear capacity of 3DCP elements be critically evaluated in future studies.
8. The similarities in both the force-displacement response and crack patterns attained across all simulations indicate that the respective FE simulation strategies apply to 3DCP.

From the above conclusions, it is evident that the proposed multi-surface anisotropic continuum and interface-based FE simulations strategies show immense potential for implementation in the nonlinear design and analysis of 3DCP components. Furthermore the work done is envisioned to take an incremental step towards the detailed design and analysis of load-bearing 3DCP components and structures.

Acknowledgements

The support by The Concrete Institute in South Africa is gratefully acknowledged. IIBCC are partially financing this project in collaboration with Eternit (Schweiz) AG, Switzerland who are providing Polypropylene Fibres for experimental purposes.

Disclosure statement

The authors report no conflict of interest in the presented research.

4.7 References

[1] F.A. Bester, M. van den Heever, P.J. Kruger, G.P.A.G. van Zijl, Reinforcing digitally fabricated concrete: A systems approach review, Additive Manufacturing. 37 (2021). https://doi.org/10.1016/j.addma.2020.101737.

[2] Y. Weng, M. Li, S. Ruan, T.N. Wong, M.J. Tan, K.L. Ow Yeong, S. Qian, Comparative economic, environmental and productivity assessment of a concrete bathroom unit fabricated through 3D printing and a precast approach, Journal of Cleaner Production. 261 (2020) 121245. https://doi.org/10.1016/j.jclepro.2020.121245.

[3] F. Bos, R. Wolfs, T. Salet, CCR Digital Concrete 2020 SI: Editorial, Cement and Concrete Research. 135 (2020) 106157. https://doi.org/10.1016/j.cemconres.2020.106157.

[4] C. Menna, J. Mata-Falcón, F.P. Bos, G. Vantyghem, L. Ferrara, D. Asprone, T. Salet, W. Kaufmann, Opportunities and challenges for structural engineering of digitally fabricated concrete, Cement and Concrete Research. 133 (2020) 106079. https://doi.org/10.1016/j.cemconres.2020.106079.

[5] Allied Market Research, 3D Concrete Printing Market, (2021). https://www.alliedmarketresearch.com/3d-concrete-printing-market (accessed February 17, 2021).

[6] P. Martens, M. Mathot, F. Bos, J. Coenders, Optimising 3D Printed Concrete Structures Using Topology Optimisation, in: High Tech Concrete: Where Technology and Engineering Meet, Springer International Publishing, Cham, 2018: pp. 301–309. https://doi.org/10.1007/978-3-319-59471-2_37.

[7] T. Pastore, C. Menna, D. Asprone, Combining Multiple Loads in a Topology Optimization Framework for Digitally Fabricated Concrete Structures, RILEM Bookseries. 28 (2020) 691–700. https://doi.org/10.1007/978-3-030-49916-7_69.

[8] G. Vantyghem, V. Boel, W. de Corte, M. Steeman, Compliance, Stress-Based and Multi-physics Topology Optimization for 3D-Printed Concrete Structures, in: T. Wangler, R.J. Flatt (Eds.), First RILEM International Conference on Concrete and Digital Fabrication – Digital Concrete 2018, Springer International Publishing, Cham, 2019: pp. 323–332.

[9] B. Hall, Topography Optimization, CPT Worldwide. 0 (2020) 40. https://www.cpt-worldwide.com/.

[10] A. du Plessis, A.J. Babafemi, S.C. Paul, B. Panda, J.P. Tran, C. Broeckhoven, Biomimicry for 3D concrete printing: a review and perspective, Additive Manufacturing. (2020) 101823. https://doi.org/10.1016/j.addma.2020.101823.

[11] P. Carneau, R. Mesnil, N. Roussel, O. Baverel, Additive manufacturing of cantilever - From masonry to concrete 3D printing, Automation in Construction. 116 (2020) 103184. https://doi.org/10.1016/J.AUTCON.2020.103184.

[12] Y. Weng, N.A.N. Mohamed, B.J.S. Lee, N.J.H. Gan, M. Li, M.J. Tan, H. Li, S. Qian, Extracting BIM Information for Lattice Toolpath Planning in Digital Concrete Printing with Developed Dynamo Script: A Case Study, Journal of Computing in Civil Engineering. 35 (2021). https://doi.org/10.1061/(ASCE)CP.1943-5487.0000964.

[13] G. Vantyghem, T. Ooms, W. de Corte, VoxelPrint: A Grasshopper plug-in for voxel-based numerical simulation of concrete printing, Automation in Construction. 122 (2021) 103469. https://doi.org/10.1016/j.autcon.2020.103469.

[14] D. Avrutis, A. Nazari, J.G. Sanjayan, Industrial Adoption of 3D Concrete Printing in the Australian Market, Elsevier Inc., 2019. https://doi.org/10.1016/b978-0-12-815481-6.00019-1.

[15] J. Kruger, G. van Zijl, A compendious review on lack-of-fusion in digital concrete fabrication, Additive Manufacturing. 37 (2021) 101654. https://doi.org/10.1016/j.addma.2020.101654.

[16] M. van den Heever, F.A. Bester, P.J. Kruger, G.P.A.G. van Zijl, Mechanical Characterisation for Numerical Simulation of Extrusion-based 3D Concrete Printing, Journal of Building Engineering. 44 (2021). https://doi.org/10.1016/j.jobe.2021.102944.

[17] C. Müller, Eurocode – EN 1990 Basis of Structural Design Structural Analysis and Design by Testing, (2008) 18–20.

[18] R.A. Buswell, W.R. Leal de Silva, S.Z. Jones, J. Dirrenberger, 3D printing using concrete extrusion: A roadmap for research, Cement and Concrete Research. 112 (2018) 37–49. https://doi.org/10.1016/j.cemconres.2018.05.006.

[19] V. Mechtcherine, F.P. Bos, A. Perrot, W.R.L. da Silva, V.N. Nerella, S. Fataei, R.J.M. Wolfs, M. Sonebi, N. Roussel, Extrusion-based additive manufacturing with cement-based materials – Production steps, processes, and their underlying physics: A review, Cement and Concrete Research. 132 (2020) 106037. https://doi.org/10.1016/j.cemconres.2020.106037.

[20] T. Ooms, G. Vantyghem, R. van Coile, W. de Corte, A parametric modelling strategy for the numerical simulation of 3D concrete printing with complex geometries, Additive Manufacturing. 38 (2021) 101743. https://doi.org/10.1016/j.addma.2020.101743.

[21] F.A. Bester, M. van den Heever, P.J. Kruger, S. Zeranka, G.P.A.G. van Zijl, Benchmark structures for 3D concrete printing, Proceedings of the Fib Symposium 2019: Concrete - Innovations in Materials, Design and Structures. (2019) 305–312.

[22] A. van den Bos, P. van der Aa, Practical approach to assess buildability of 3D concrete printed object using finite element analysis, (2019) 2019.

[23] R.J.M. Wolfs, F.P. Bos, T.A.M. Salet, Early age mechanical behaviour of 3D printed concrete: Numerical modelling and experimental testing, Cement and Concrete Research. 106 (2018) 103–116. https://doi.org/10.1016/j.cemconres.2018.02.001.

[24] P. Valle-Pello, F.P. Álvarez-Rabanal, M. Alonso-Martínez, J.J. del Coz Díaz, Numerical study of the interfaces of 3D-printed concrete using discrete element method, Materialwissenschaft Und Werkstofftechnik. 50 (2019) 629–634. https://doi.org/10.1002/mawe.201800188.

[25] L. Wang, H. Jiang, Z. Li, G. Ma, Mechanical behaviors of 3D printed lightweight concrete structure with hollow section, Archives of Civil and Mechanical Engineering. 20 (2020) 1–17. https://doi.org/10.1007/s43452-020-00017-1.

[26] F.P. Bos, E. Bosco, T.A.M. Salet, Ductility of 3D printed concrete reinforced with short straight steel fibers, Virtual and Physical Prototyping. 14 (2019) 160–174. https://doi.org/10.1080/17452759.2018.1548069.

[27] P. Feng, X. Meng, J. Chen, L. Ye, Mechanical properties of structures 3D printed with cementitious powders, CONSTRUCTION & BUILDING MATERIALS. 93 (2015) 486–497. https://doi.org/10.1016/j.conbuildmat.2015.05.132.

[28] M. van den Heever, F. Bester, M. Pourbehi, J. Kruger, S. Cho, G. van Zijl, Characterizing the Fissility of 3D Concrete Printed Elements via the Cohesive Zone Method, 2nd RILEM International Conference on Concrete and Digital Fabrication. 3 (2020) 1–10.

[29] P.B. Lourenço, J.G. Rots, J. Blaauwendraad, Continuum model for masonry: Parameter estimation and validation, Journal of Structural Engineering. 124 (1998) 642–652. https://doi.org/10.1061/(ASCE)0733-9445(1998)124:6(642).

[30] P.B. Lourenço, J.G. Rots, Multisurface interface model for analysis of masonry structures, Journal of Engineering Mechanics. 123 (1997) 660–668. https://doi.org/10.1061/(ASCE)0733-9399(1997)123:7(660).

[31] F.J. Vecchio, M.P. Collins, Modified Compression-Field Theory for Reinforced Concrete Elements Subjected To Shear., Journal of the American Concrete Institute. 83 (1986) 219–231. https://doi.org/10.14359/10416.

[32] F. Bos, R. Wolfs, Z. Ahmed, T. Salet, Additive manufacturing of concrete in construction: potentials and challenges of 3D concrete printing, Virtual and Physical Prototyping. 11 (2016) 209–225. https://doi.org/10.1080/17452759.2016.1209867.

[33] DIANA FEA bv, Diana Finite Element Analysis, (2021). https://dianafea.com (accessed March 3, 2021).

[34] DIANA FEA bv, Diana User's Manual, DIANA Documentation Release 10.4. (2020). https://dianafea.com/manuals/d104/Diana.html.

[35] P.B. Lourenço, A USER / PROGRAMMER GUIDE FOR THE MICRO-MODELING OF MASONRY STRUCTURES, TNO Building and Construction Research. (1996).

[36] S. Govindjee, G.J. Kay, J.C. Simo, Anisotropic modelling and numerical simulation of brittle damage in concrete, International Journal for Numerical Methods in Engineering. 38 (1995) 3611–3633. https://doi.org/10.1002/nme.1620382105.

[37] P.B. Lourenço, Computational strategies for masonry structures, 1996. https://doi.org/ISBN 90-407-1221-2.

[38] DIANA FEA bv, Appendix D: Available Element Types, (2017). https://dianafea.com/manuals/d102/GetStart/node143.html (accessed March 3, 2021).

[39] J.G. Rots, Computational Modeling of Concrete Fracture, 1988.

[40] DIANA FEA bv, Structural Nonlinear Analysis of a Shear Wall Panel, (2019). https://dianafea.com (accessed November 21, 2020).

[41] SANS 920: 2011, South African National Standard: Steel bars for concrete reinforcement, (2011).

[42] F. Bester, M. van den Heever, J. Kruger, S. Cho, G. van Zijl, Steel fiber links in 3D printed concrete, Second RILEM International Conference on Concrete and Digital Fabrication - Digital Concrete 2020. 2 (2020) 1–9.

[43] J. Kruger, A. Cicione, F. Bester, M. van den Heever, S. Cho, R. Walls, G. van Zijl, Facilitating Ductile Failure of 3D Printed Concrete Elements in Fire, 2020. https://doi.org/10.1007/978-3-030-49916-7_46.

[44] C. Matthäus, N. Kofler, T. Kränkel, D. Weger, C. Gehlen, Interlayer reinforcement combined with fiber reinforcement for extruded lightweight mortar elements, Materials. 13 (2020) 1–17. https://doi.org/10.3390/ma13214778.

[45] T. Marchment, J. Sanjayan, Mesh reinforcing method for 3D Concrete Printing, Automation in Construction. 109 (2020) 102992. https://doi.org/10.1016/j.autcon.2019.102992.

[46] A. Perrot, Y. Jacquet, D. Rangeard, E. Courteille, M. Sonebi, Nailing of layers: A promising way to reinforce concrete 3D printing structures, Materials. 13 (2020). https://doi.org/10.3390/ma13071518.

[47] T. Marchment, J. Sanjayan, Bond properties of reinforcing bar penetrations in 3D concrete printing, Automation in Construction. 120 (2020) 103394. https://doi.org/10.1016/j.autcon.2020.103394.

[48] V. Mechtcherine, J. Grafe, V.N. Nerella, E. Spaniol, M. Hertel, U. Füssel, 3D-printed steel reinforcement for digital concrete construction – Manufacture, mechanical properties and bond

behaviour, Construction and Building Materials. 179 (2018) 125–137. https://doi.org/10.1016/j.conbuildmat.2018.05.202.

CHAPTER 5 : Evaluating the Effects of Porosity on the Mechanical Properties of Extrusion-based Fibre-reinforced 3D Printed Concrete

Marchant van den Heever [a], Anton du Plessis [b, c], Jacques Kruger [a], Gideon van Zijl [a]

[a] Structural Engineering and Civil Engineering Informatics, Department of Civil Engineering, Stellenbosch University, Stellenbosch, 7602, South Africa

[b] Research group 3D Innovation, Stellenbosch University, Stellenbosch 7602, South Africa

[c] Department of Mechanical Engineering, Nelson Mandela University, Port Elizabeth 6001, South Africa

Reproduced and reformatted from an article submitted to *Cement and Concrete Research*.

(DOI: Submitted)

Abstract

Elements fabricated by extrusion-based 3D concrete printing (3DCP) display anisotropic mechanical properties when subject to loading conditions orientated in principle Cartesian axis directions. Various studies show that the mechanical characteristics of 3DCP components are lower than their mould-cast counterparts, reportedly due to the existence of weaker, more porous, interfacial joints in-between filament layers. To promote the widespread adoption of 3DCP, the elastic response and strength parameters of 3DCP elements must be fully comprehended. Numerous attempts have been made to improve the mechanical properties of 3DCP using fibre reinforcement. At the root of all mechanical properties are the microstructural morphology and constituent characteristics of the mixture. It has been shown that the 3DCP process influences the ensuing microstructural morphology, and it is known that constituent type, constituent proportion, porosity content and void topology affect the bulk strength and elasticity of a porous medium. Therefore, the correlation between such observations warrants additional investigation concerning the influence of porosity on the anisotropic mechanical properties of 3DCP components. In this research, the effects of porosity metrics such as total porosity content; 3D void topology (shape, size, and orientation); pore spatial, size and compactness distributions; and interconnectivity are quantitatively investigated via X-ray computed tomography and related to the elasticity, compressive strength and observed fracture patterns of mould-cast and concrete printed specimens consisting of the same fibre reinforced printable concrete matrix. The experimental findings indicate higher porosity, on average and at interlayer locations, in 3DCP samples as well as alterations in the spatial and topological attributes of voids in 3DCP samples. Furthermore, it is shown

that both reductions in the elastic modulus and compressive capacity can be physically linked to the porosity metrics detected in 3DCP elements. Elasticity is dominated by porosity content and compressive capacity by the interrelation between porosity content, loading direction relative to the interlayer orientation, stress concentrations at void boundaries, and the increased deformability of the composite configuration. From the consideration and interpretation of these aspects, the anisotropic mechanical response of 3DCP samples is elucidated, and potential remedies are proposed.

Highlights:

- The 3DCP process spatially and geometrically alters the microstructural morphology.
- Pores in 3DCP are elongated in the extrusion direction and pressed in the building direction.
- The augmented microstructural morphology is a main source of anisotropy.
- Mechanical properties must be attained from actual 3DCP and not from cast specimens.

Keywords: 3D concrete printing; Computed tomography; porosity metrics; elasticity; mechanical characteristics

5.1 Introduction

Extrusion-based 3D concrete printing (3DCP) is revolutionising the construction industry by offering a host of unique advantages [1] which permit digitally-driven value-added products and services across various tiers of the construction value chain to a variety of stakeholders. There is great potential for complex architectural designs for large-scale structures, utilising the freeform design capabilities of 3D printing approaches [2]. However, 3DCP faces challenges such as reduced interlayer bonding; contesting rheological requirements; anisotropic material characteristics; a non-exclusive interrelation between material, process and design requirements; and demands for the development of non-standard reinforcement techniques. The consequence of unbalanced material, process, and design parameters is compromised structural integrity, and it is believed that at the core lies the augmentation of critical porosity metrics in concrete printed elements.

In structural design practice, strength and stiffness are arguably the most important aspects when considering structural performance. Therefore, to promote the widespread adoption of 3DCP, the elastic response and characteristic material parameters of 3DCP components must be fully comprehended. Since fostering a deeper comprehension of the material response and associated characteristics ultimately facilitates the rational design of load-bearing structures realised by this promising digital fabrication technique. Many studies have focused on ascertaining the anisotropic material parameters [3–13], but only some have postulated that porosity is at the root of the differential elastic and strength parameters observed [14–17]. None present theories that relate porosity, void topology, and laminates to the mechanical properties of fibre-reinforced concrete printed components. It is expected that the

strength and elastic properties of concrete printed elements, analogous to laminated composites, depend on their filament stacking configuration, interlayer adhesion, and thus void topological orientation relative to the applied stress. Additionally, it is assumed that the effect of porosity on the mechanical properties of the printed cementitious composite is associated with the constituent type and fractional volume of each incorporated phase.

The purpose of this research is to investigate the relationship between the mechanical strength and stiffness and the porosity metrics total porosity content, porosity distribution, shape, size, spatial orientation, and position of pores in 3DCP. As recommended by [15], the physical causes and mechanical effects of stress concentrations at micro-crack or pore boundaries in fibre-reinforced 3DCP are studied.

5.2 Porosity in cementitious materials

At any stage of hydration, hardened cement paste consists of anhydrous cement, hydrate products (containing gel pores with diameters in the order of 0.5-5 nm), portlandite crystals, unfilled capillary pores (between 5 nm - 10 μm wide), and larger entrapped voids (from 5 μm upwards) which have not been expelled from the paste during placement and compaction [18]. Factors that affect the overall porosity in hardened concrete include the type of cement [19,20], water-to-cement (w/c) ratio [18,20], incorporated additives and admixtures [20], degree of hydration [21,22], paste viscosity, coarse aggregate size, and grading, duration and intensity of vibration and compaction, along with curing conditions e [23]. It is essential to consider all these factors when investigating porosity associated effects on the mechanical properties of novel cementitious mixtures.

Porosity influences both the fresh-state rheological properties, hardened-state mechanical, and durability performance of cementitious materials. Interestingly, 3-5 % porosity is considered advantageous from a durability perspective if air voids are within the range of 10-100 μm and homogeneously dispersed within the hardened microstructure [23]. The benefits of entrained air in conventionally cast concrete include a paste volume increase, fluidification of cement paste, a decrease of absorptivity and permeability of hardened concrete, energy dissipation at crack tip fissures during the coalescence of micro-cracking, and reduced mixing water requirements prompting lower w/c ratios consequently increasing the strength of the cementitious composite at a constant cement fraction [19].

5.2.1 Porosity measurement techniques

Generally, the pore structure is evaluated via indirect measurement by fluid impregnation of pores, such as mercury intrusion porosimetry [20] and helium porosimetry [21]. However, specific gravity methods, absorption tests, 2D surface electron imaging techniques, microscopy, and capillarity determination have been employed. Yet, these methods are subject to various influential factors [20,21],

which, if not suitably accounted for, often misrepresent, or cannot express the 3D spatial porosity metrics of interest in porous media. Additionally, a single method that effectively captures all facets of porosity in porous cementitious media does not exist [14]. It is contended that when investigating the influence of porosity on the mechanical properties of cementitious materials, it is paramount to have well-characterised 3D information about the material. Therefore, 3D X-ray computed tomography (CT) has been adopted in the current study to measure the porosity metrics of interest. Table 5.1 presents the porosity determination methods and results from various institutions to accentuate the influence of different techniques and scanning resolutions on the attained porosity metrics in 3DCP components. X-ray CT is gaining wider acceptance in a variety of scientific disciplines [24] and has been used widely to characterise cementitious materials [25]. The method uses X-ray images to create full 3D datasets from which porosity information can be quantitatively extracted. The pore size range that can be detected depends on the selected voxel size and field of view, limited by sample size and equipment characteristics.

Table 5.1: Porosity investigation methods and results for 3D printable cementitious compositions by various institutions.

Institution*	Method	Porosity (Cast)	Porosity (Printed)	Voxel size/ Resolution	Reference
Stellenbosch University	3D volumetric micro-CT scanning	6.8 %	7.9 %	15 µm	[15]
Stellenbosch University	3D volumetric micro-CT scanning	-	4.2 %	22.5 µm	[15]
Loughborough University	2D surface analysis	3.8 %	1.0 % / 4.8 % [a]	0.2 – 4 mm voids	[26]
Ghent University	2D surface analysis	-	2.3-3.2 %	8 µm	[16]
Technical University Braunschweig	3D volumetric micro-CT scanning	-	3.4 %	36 µm	[27]
Korea Institute of Civil Engineering and Building Technology	3D volumetric micro-CT scanning	-	5.0-6.0 %	70 µm	[17]
Delft University of Technology	2D surface analysis	-	14.2 % / 8.5 % [b]	7.2 µm	[14]
Delft University of Technology	2D surface micro-CT scanning	-	8.7-9.2 %/ 5.2-7.5 % [c]	27 µm	[14]
Swinburne University	Apparent porosity	-	10.1% / 14.1% [d]	-	[28]

** note that only the affiliation of the first referenced author is presented. All additional information can be obtained from the cited manuscripts in the reference column.*

[a] 1.0 % porosity for "well-printed" samples and 4.8 % for "poorly-printed" samples.

[b] Values presented are for two respective mixtures M1 and M2.

[c] Values given are for two separate mixes as in [b], hyphenated ranges represent changes in 2D surface/plane orientation.

[d] Apparent porosity measurement with variations dependant on polypropene fibre dosages (0-1 %) in the 3D-printable geopolymer mixture.

5.2.2 Porosity and strength in cementitious composites

In general terms, reduced porosity is empirically related to higher compressive strength, where the interrelation is shown by Powers [19] to be of the form:

$$f_c = k(1-p)^3 \tag{5.1}$$

Note that raising the porosity to power three indicates its significant contribution to compressive strength. Yet, compression failure is convoluted and unlikely to be amply described by a single equation [29]. Instead, Griffith contends that the incidence of crack-like pores which contribute little to total porosity have a more pronounced effect on failure in brittle materials. Following this statement, the tensile and flexural strength of brittle materials is more agreeable to analysis since, in the Griffith formulation, Equation 5.2, the tensile cracking stress (f_{tc}) is related to an effective critical crack length (a_c), which could represent an elongated pore diameter. At the same time, Young's modulus (E) and the fracture energy (G_f) is taken as material constants [30].

$$f_{tc} = \left(EG_f/\pi a_c\right)^{\frac{1}{2}} \tag{5.2}$$

Considering quasi-brittle materials, such as mortar, which display nonlinear hardening to the peak load and post-peak progressive deterioration in load-carry capacity, it is established that porosity is related to the global material response (viz., elasticity, strength, and fracture energy). This notion is deduced from the fact that the number of pores included in the material is related to the deformability of the matrix, the attainable stress intensity, and the rate at which distributed micro-cracks are formed [31]. In the cementitious microstructure, the presence of entrapped air voids creates a network of macro pores that prompts localised weak points that reduce concrete strength [30]. Birchall et al. [30,32] infer that reduced strength in ordinary cement pastes is predominantly ascribed to macro pores rather than the microscopic or mineralogical qualities of the gel. Additionally, factors such as void topology have been shown to influence the bulk strength of porous media [33].

5.2.3 Porosity and elasticity in cementitious composites

Compared to strength, the elastic modulus of cementitious composites is less susceptible to reduction with increased porosity [31]. Literature suggests that microscopic (colloidal and gel) pores, rather than encapsulated macropores, have a more pronounced influence on the elastic modulus of cement pastes [32]. Since in their opinion, structural differences among pastes are mainly due to differences in capillary porosity. Additionally, the chemical composition is also of less significance since the physical characteristics of hardened cement gel are influenced to only a minor degree by such differences in chemical composition as found among different Portland cement types [22]. Thus, the elastic modulus of cement paste can be presented as:

$$E_{cmp} = V_{gel}^3 E_{gel} \tag{5.3}$$

with V_{gel} and E_{gel} representing the fractional volume and modulus of elasticity of cement gel, respectively [34]. Since 3D printed concrete is a two-phase cementitious material comprising mostly fine aggregate (< 4 mm) and binders, the Young's modulus of the printed composite material (E_{3DCP}) is expected to follow Ishai's representation for mortar [34].

$$E_{3DCP} = E_{mort} = \left(1 + kV_{agg}\right)E_{cmp} \tag{5.4}$$

Here parameter k is the ratio between the elastic properties of the aggregate and the cement paste. It is noted that Equations 5.3 and 5.4 pertain to materials which only contain colloidal porosity, and no adjustment for the influence of macro pores has been made. In Section 5.4.6.1, we show how the effects of non-colloidal porosity on elasticity can be considered.

5.2.4 Effect of the printing process on porosity metrics

Resulting from the variation in fresh-state properties and manufacturing processes, the air void systems in 3DCP differ from their conventionally cast counterparts. As extensively reported, the viscosity of printable concrete is higher than that of conventionally cast concrete [35]. Cast concrete generally has a lower viscosity because it should conform to the mould in which it is placed and printed concrete has a very high viscosity, in the unagitated state, to ensure suitable buildability performance and shape retention during the freeform deposition process [26,36]. Additionally, no vibration or compaction is present after pumping and filament deposition in the material extrusion process. Therefore, the likelihood of air entrapment or entrainment is increased within the 3DCP paradigm. Notwithstanding, the extrusion process has been reported to densify the plastic mixture, thereby reducing the total porosity fraction in the intralayer, ensuing the additionally induced pumping pressure [3,15,26]. Moreover, irregularly shaped but approximately ellipsoidal pores within filament intralayer matrices have also been observed and quantitatively evaluated [15]. It has been shown that larger air voids are located at interlayer locations, with a more significant number of small to medium-sized air voids found randomly dispersed within extruded filaments [14].

5.2.5 The link between interlayer porosity and interlayer capacity

Interlayer porosity can be attributed to mechanisms such as (i) water migration stemming from surface moisture evaporation between printed filaments [3,12,16,37], (ii) surface roughness, and (iii) the thixotropic nature of 3DCP mixtures [3] causing additional porosity [14,15] and void interconnectivity. Additionally, (iv) the formation of a lubrication layer during pumping due to the hydraulic pressure gradient within the printable cementitious composite, induced by particle migration

and segregation of water from the fines paste [3], effectively causes a higher w/c ratio and thereby increases the porosity in the outer lubrication layer [38]. Macro inclusions flattened in the building direction and elongated in the extrusion direction also stem from the embodied extrusion process. Here voids are pressed and smeared between filaments when (v) incompatible printing parameters are used (i.e., too high print speed coupled with a lower extrusion rate) [26], resulting in filament tearing.

Stemming from the augmented air void systems encountered in 3DCP components, anisotropic mechanical behaviour in compression, tension, flexure, and shear is prominent [3–13]. Mechanical anisotropy in 3DCP is a consequence of the inadequate adhesion between vertically stacked and horizontally adjacent filaments, which by and large originates from air enclosure during filament stacking [3,17] and the nonhomogeneous features of porosity in and in-between filaments [14–16]. Note, that the deployment of unidirectional reinforcement strategies accentuates the level of anisotropy [14–16]. Lee et al. [17] investigated the correlation between porosity and tensile bond strength at interlayer locations and found that no direct relationship is evident. However, Lee et al. [17] rightfully suggest that pores on failure surfaces (i.e., entrained/encapsulated air voids) induce failure on interlayer regions with lesser porosity. This statement is consistent with the Griffith formulation above and the deductions presented by Birchall et al. [30] and Kendall et al. [32] in Section 5.2.2.

5.3 Materials & methods

5.3.1 Fibre-reinforced printable concrete composite composition & properties

A fibre-reinforced printable concrete (FRPC) mixture with 6 mm polypropylene (PP) microfibres entrained at a 1 % dosage by binder volume is employed. The PP microfibre properties are presented in Table 5.2, and the specific constituent types, properties, and fractions are shown in Table 5.3 and more detail can be found in van den Heever et al. [11]. The binder consists of PPC 52.5 N (CEM II/A-L) normal hardening Portland-limestone cement, including 80-94 % clinker and 6-20 % limestone replacement [39], Chryso densified micro-silica fume, and class F DuraPozz fly-ash. The featured admixtures include a modified polycarboxylate polymer-based superplasticiser (Chryso Premia 310) and a liquid hydroxypropyl methyl-cellulose viscosity modifying agent (Chryso Quad 20) to ensure suitable workability in the fresh state. A locally mined continuously graded Malmesbury crushed granite sand with a 4.75 mm maximum particle size is utilised. The aggregates have an elastic modulus of 68-76 GPa [40] and the mixture has a w/c ratio of 0.45 to ensure adequate hardened state mechanical performance.

From preliminary investigation, it is determined that the FRPC mixture displays anisotropic behaviour in tension, compression, and shear considering the capacity over the interlayer (D3) and in the extrusion direction (D1). The shear level of anisotropy (LOA) is highest at 2.43 [4], followed by a tensile LOA of 1.96 and a compressive LOA equal to 1.18 [11]. Interestingly, similar elastic properties

(21.9 vs. 21.6 GPa) are observed [11]. The rheological properties are consistent with those utilised for 3DCP and exhibits thixotropic fresh-state behaviour with a static shear yield stress ($\tau_{S,I}$) of 2152 Pa, a dynamic shear yield stress ($\tau_{D,I}$) of 1789 Pa, as well as a relatively high reflocculation (R_{thix}) and moderate structuration (A_{thix}) rates, equal to 7.29 Pa/s and 1.13 Pa/s, respectively [11].

Table 5.2: Polypropylene (PP) microfibre properties.

Description	Value
Young's Modulus (E_f)	3 GPa
Yield Stress (f_t)	300 MPa
Diameter (Ø)	30 µm
Length (L)	6 mm

Table 5.3: Fibre-reinforced 3D printable concrete (FRPC) mixture constituents and proportions.

Constituent	Proportion (kg/m^3)	Relative Density (-)
PPC Suretech CEM II/A-L 52.5 N	562	3.14
Durapozz Fly Ash (Class F)	162	2.2
Micro Silica Fume	81.4	2.1
Aggregate (Malmesbury)	1144	2.65
Water	256	1
Superplasticizer	4.9 (0.6 % by binder mass)	1.05
VMA	2.4 (0.3 % by binder mass)	2
6 mm PP Microfibres	9.1 (1 % by mixture volume)	0.91

5.3.2 Sample preparation & configurations

Samples are extracted from the printed object shown in Fig. 5.1, thereby representing the material, design, and process parameters employed. The item has a building height of 250 mm with 10 mm layer heights, a print path length of 4 m, a layer pass time of 67 s and is printed at 60 mm/s in 28 min [11]. Printed samples are cored after 14 days from the centre of filaments in the respective longitudinal (D1) and perpendicular (D3) directions to enable assessment in orthotropic components. Cast samples are manufactured by placing the FRPC mixture into Ø100 x 200 mm cylinders and vibrating until the exposed surface is smooth. The casting procedure entails placing approximately a third of the fresh mixture into the cylindrical moulds and compacting with a tamping rod until the fraction has settled; the procedure is repeated three times until the sample is full. Cast specimens are cored from the centre of the cylindrical samples to negate the influence of fine particle migration at mould boundaries (wall effect) on the material characteristics. All specimens are air-cured in controlled environmental conditions (23 ± 2 °C and 65 ± 5 % relative humidity) and evaluated at a 28-day concrete age.

For porosity investigation via micro-X-ray CT, the extracted samples are CT scanned before and after the respective testing procedures presented in Section 5.3.4. Micro CT scans at 20 µm voxel size provide quantitative evaluation of pores larger than 60 µm in diameter (3 voxels minimum pore

diameter in any axis), while offering a reasonable representative field of view covering the entire sample [15]. Areas in the vicinity of the outer surface of the sample were not investigated via CT scanning to negate accounting for any possible influence that the coring process may have on the microstructure of the specimen.

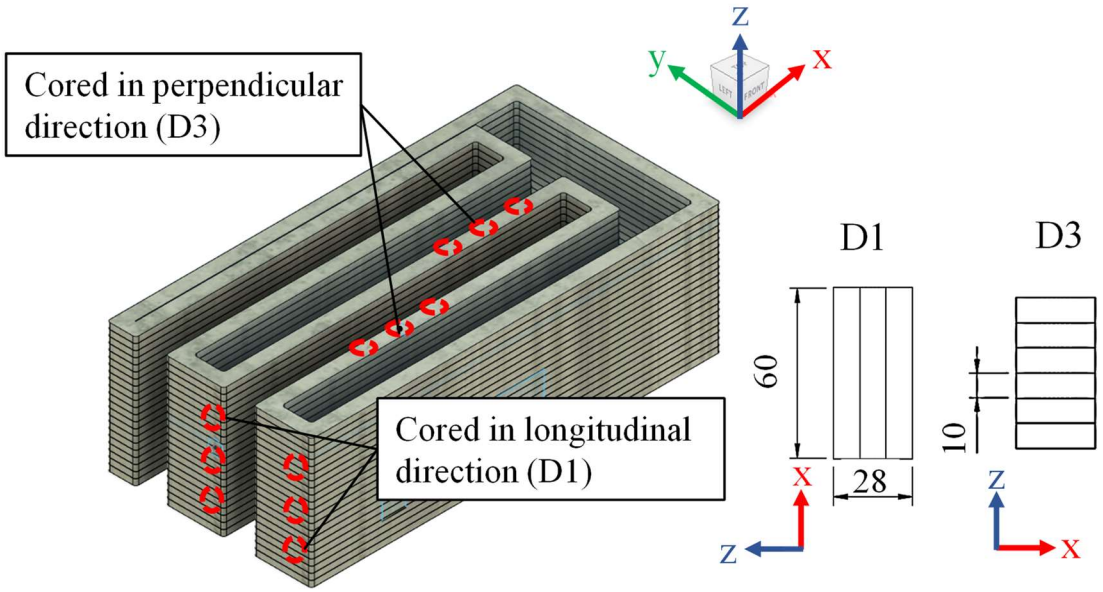

Fig. 5.1: Concrete printed sample object, indicating coring directions and extracted sample configurations.

5.3.3 CT scanning methodology

X-ray micro computed tomography was performed using a General Electric Vtomex L240 system. Reconstruction was performed in Datos 2.0 and visualization and quantitative analysis performed using Volume Graphics VGSTUDIO MAX 3.3. The procedure is described briefly below but follows the approach used in prior work on non-fibre reinforced 3DCP [15]. A region of interest is selected to exclude boundaries of the sample, and the data is subject to an adaptive Gauss de-noising filter. This is followed by porosity analysis using the defect analysis tool in VGSTUDIO MAX, providing information on pores in the sample larger than 27 voxels (3 x 3 x 3 in three orthogonal axes). In order to evaluate directional variation of porosity, an integration mesh is used with 0.3 mm thickness to provide porosity percentage values and visualization of porosity changes across the interlayer region. X-ray generation was set to 150 kV and 120 µA, with 500 ms per image acquisition time. The sample was rotated through 360 degrees in 2800 steps, at each position the first image was discarded and the next two images averaged to improve signal-to-noise ratio.

5.3.4 Mechanical testing methodology

Two mechanical characterisation experiments are conducted to ascertain the ultimate uniaxial compressive capacity and Young's modulus of 3DCP and mould-cast specimens. Six samples are

evaluated per category (3DCP-D1, 3DCP-D3, CAST) in each experimental procedure, while three samples are selected per configuration for micro-CT scanning. The experiments pertaining to 3DCP specimens have been conducted and reported on in a previous study [11] and additional evaluation of cast specimens is undertaken in this research.

5.3.4.1 Modulus of elasticity

The testing procedure to determine Young's modulus of various test specimens is conducted based on the ASTM C469-02 standard testing procedure [41]. In total, 18 samples are evaluated on an assortment of cast and printed samples, respectively. The samples comprise Ø28 x 60 mm cored cylinders orchestrated with circumferentially positioned axially orientated strain gauges at 120-degree increments, as presented in [11]. All samples are tested in a Zwick Z250 universal material testing machine (MTM) at a uniaxial loading rate of 50 N/s until 40 % of f_c is reached. Strains are recorded via a quarter-bridge configuration at a sampling rate of 20 Hz, and the axial load by an HBM 5 kN load cell attached to the crosshead. The experimental data is captured with a Quantum MX840B universal data acquisition system and post-processed to obtain the desired output. The elastic modulus (E) is determined from Equation 5.5 following Hooke's law, where the uniaxial compressive stress (f_c) is computed from the applied force and the contact area while the axial strains are attained directly from strain gauge readings.

$$E = {f_c}/{\varepsilon} \tag{5.5}$$

5.3.4.2 Compressive capacity

Unconfined uniaxial compression tests are conducted on cored samples from cast and printed specimens to determine the compressive strength in the casting and respective loading directions. The experimental procedure is founded on ASTM C39/C39M [42] but modified to suit the scale of 3DCP filaments. Six Ø28 x 60 mm cored cylinders, per category, are extracted from the mould-cast and 3DCP objects presented in Fig. 5.1. The upper and lower ends of the compressive samples are surface ground to ensure that the loading surfaces are smooth and parallel to one another. Compressive tests are conducted in a Zwick Z250 universal MTM with an open-loop force-controlled test configuration at a continually increasing rate of 150 N/s. The tests are terminated upon complete specimen failure, and the failure type is recorded. Furthermore, the compressive strength is computed by dividing the ultimate load attained during the test by the specimen specific cross-sectional area.

5.4 Results & discussions

5.4.1 Porosity content

The total porosity of cast and printed samples is presented quantitatively in Fig. 5.2 and graphically in Fig. 5.3. Total porosity is computed as the total detected pore volume ratio over the total sampled material volume of each specimen and averaged per category. 3DCP-D3 displayed the highest average total of 10.8 %, followed by 3DCP-D1 and cast samples, with 10.3 % and 6.5 % average total porosity content, respectively. As expected, 3DCP-D1 and 3DCP-D3 display similar average total porosities as samples are cored from the same printed object, Fig. 5.1, with only a variation in the core direction. Note that due to the inclusion of PP microfibres, it is expected that the average porosity measurements are increased by ≈1 %, as fibres have a lower density (910 kg/m^3) than the surrounding cement paste (≈ 2150 kg/m^3) and are thus interpreted as voids. Additionally, since a 20 µm CT scanning resolution is employed in this research, the porosity contribution of colloidal and gel pores is omitted. Nonetheless, from these results, it is affirmed that the concrete printing process introduces additional porosity in terms of pores greater than 60 µm.

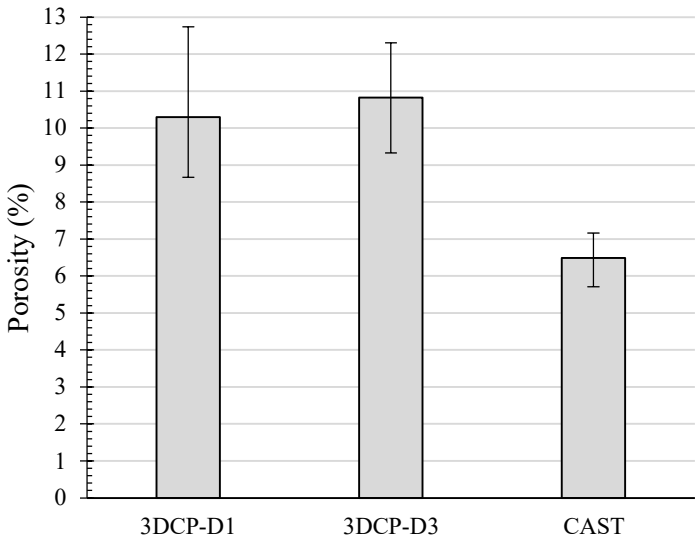

Fig. 5.2: Total porosity of evaluated samples.

These observations contradict those presented by [26], who report a reduction in porosity for well-printed samples. These porosity measurements are attained for pore sizes between 0.2 - 4 mm and therefore only represent a reduction in macropore fractions but cannot be attributed to additional pumping pressure since samples extracted from configurations comprising vertically and contiguously stacked filaments are susceptible to air enclosure between filaments. It is postulated that a more likely cause resonates with their latter notion that improved material and printing parameters reduce the fraction of macro pores in printed components.

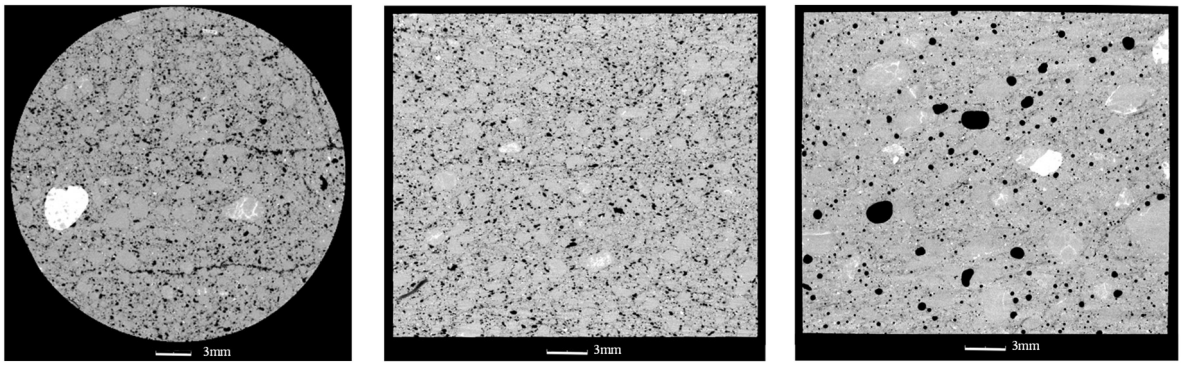

(a) (b) (c)

Fig. 5.3:Illustration of CT scan data showing (a) 3DCP-D1, (b) 3DCP-D3, and (c) CAST specimens, respectively.

On the other hand, the average porosity attained in this research is consistent with the findings presented by Kruger et al. [15] who report average total porosities of 6.8 % for mould-cast samples and 7.9 % for printed samples, respectively. Additionally, identical base mixtures are employed, except in this study, 1 % of the mixture volume is replaced by PP microfibres. Comparing the porosity of printed specimens, it is observed that the inclusion of PP microfibres results in higher porosity (+2.9 % for 3DCP-D1 and +2.4 % for 3DCP-D3); however, mould-cast specimens exhibit similar total average porosities. Considering the appraisal of recent literature presented in Table 5.1, it is necessary to point out that a larger voxel size was used in this research (20 μm vs. 15 μm), and therefore lower porosity values should be expected. Yet, contrary findings are presented, indicating that even higher porosity fractions should arise if equivalent CT scanning resolution were employed. It is deduced that fibre entrainment during the printing process induces additional porosity.

5.4.2 Porosity distribution

5.4.2.1 Pore size distribution

The pore size distribution for three specimens is presented in Fig. 5.4 to illustrate the size distribution of porosity within printed and cast specimens. Here, pore size is expressed in terms of equivalent diameter by considering the volume of a circumscribed sphere with equivalent volume to the pore volume. Evaluating the pore size distribution, it is noted that all categories display right-skewed log-normal distributions, and pores are generally in the range of 0.06-1.2 mm for printed samples, with an increased number of larger pores (> 1.2 mm) noted in cast specimens. Interestingly, cast specimens also display an increased number of pores with equivalent diameters smaller than 0.16 mm. These results indicate that mould-cast specimens contain a larger spectrum of pores, although the total porosity is less than the observations for concrete printed specimens. It is suspected that in the fresh state, the additional pumping pressure reduces the volume of individual pores by breaking up larger voids into smaller voids. In contrast, smaller pores (<< 0.16 mm) are pressed together, interconnecting to form larger pores. Therefore, during pumping and extrusion, the total porosity remains consistent, but the

embodied extrusion-based additive manufacturing process modifies the microstructural morphology of the pores.

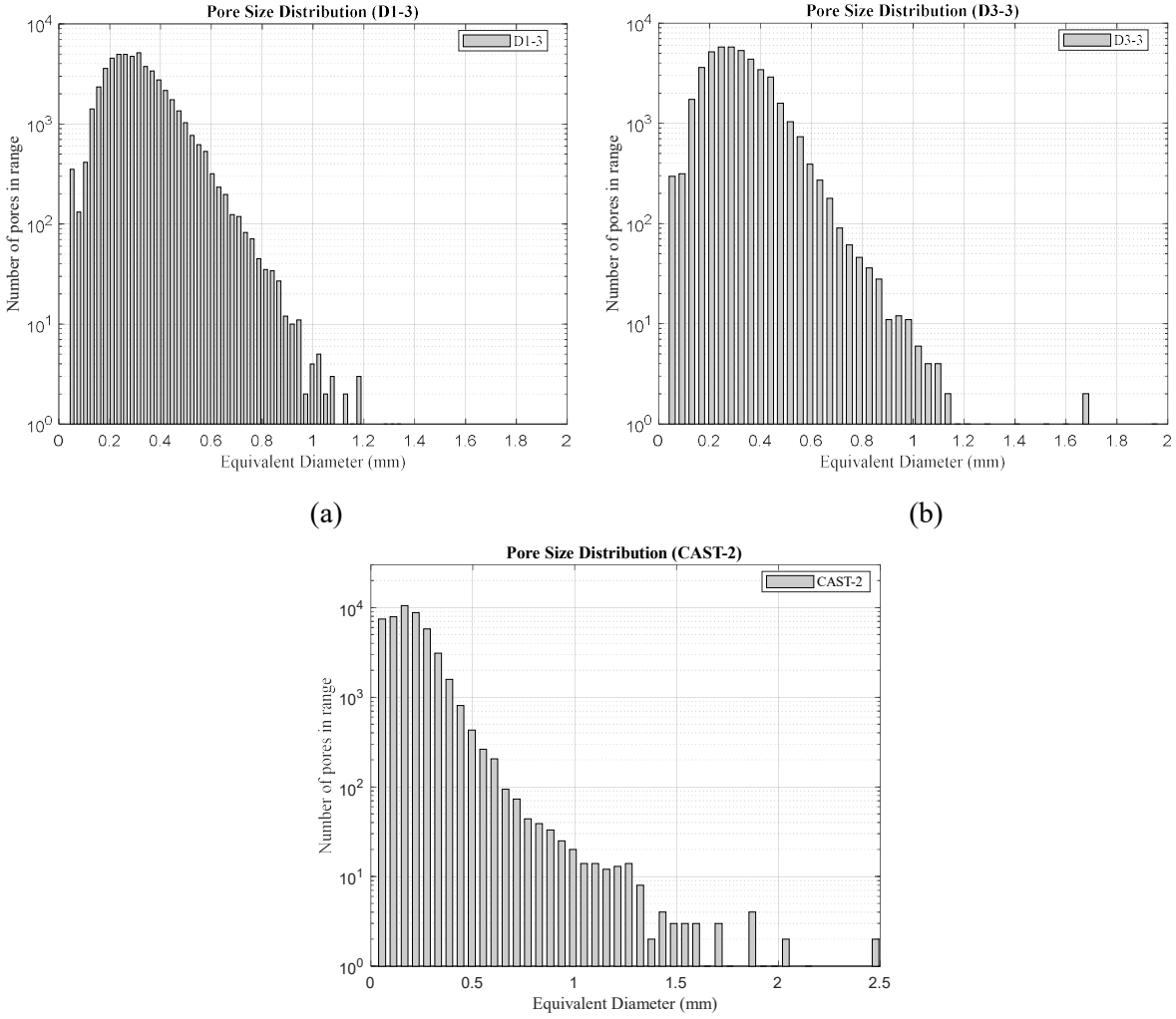

Fig. 5.4: Pores size distribution represented as a function of the equivalent diameter and the log scale of the frequency distribution. Equivalent diameter refers to the diameter of a circumscribed sphere of equal volume to the original pore volume. A supplementary Fig. S1 is provided containing the additional results per category.

5.4.2.2 Porosity vs. Position

The porosity distribution is evaluated in terms of position, in 0.3 mm integration mesh sections, over the height of all samples as presented in Fig. 5.5. Reviewing Figs. 5.5a-d higher porosity is evident at interlayer locations, shown by the definite spikes in porosity and the red coloured regions. Comparing Figs. 5.5a-d (printed samples) to Figs. 5.5e-f (cast samples), one can clearly see the more even porosity distribution for cast specimens, although spikes in integration mesh slivers can still occur due to larger pores in cast samples. As expected, the distance between porosity spikes is approximately 10 mm, which coincides with the layer height, validating that the observed porosity spikes indeed occur at interlayer locations. Additionally, apart from the even distribution of porosity in cast samples, these samples generally display lower porosity fractions (≈ 7-11 %) than printed samples (≈ 11-18 %).

Considering Figs. 5.5b, d and e, we note that pores encountered in cast samples are generally rounder as opposed to the irregularly shaped inclusions found in printed samples. Based on such observations, one can conclude that the air void fraction and shape vary based on the employed manufacturing method, both within filaments and interlayer regions.

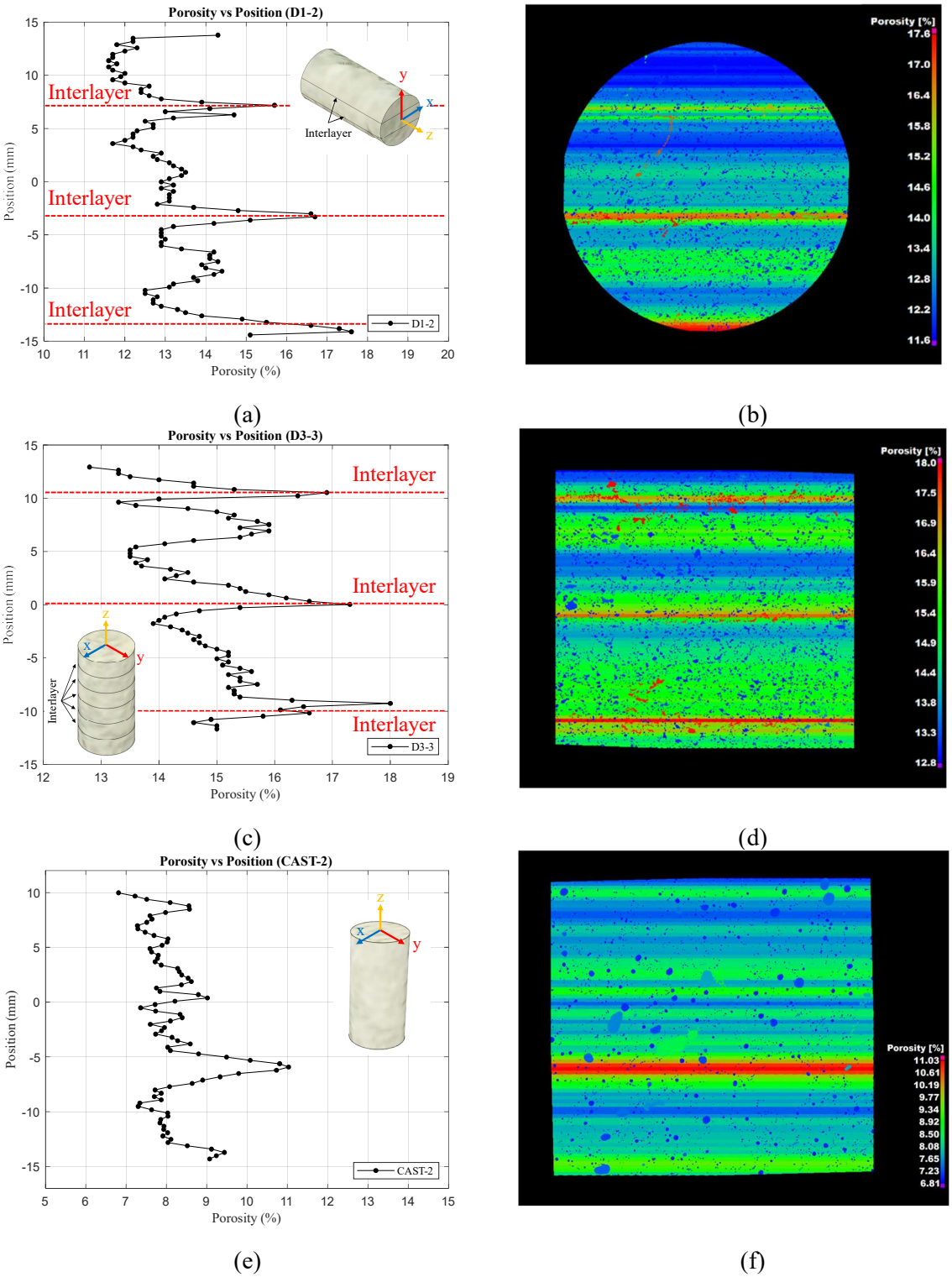

Fig. 5.5: Porosity as a function of position within the cores of printed and cast samples. Plotted porosity vs. position is presented for (a) D1-2, (c) D3-3, and (e) CAST-2 specimens. A visual depiction of porosity vs position for a 0.3 mm integration mesh over the sample build direction (upwards) is presented for (b) D1-2, (d) D3-3, and (f) CAST-2.

5.4.2.3 Equivalent diameter vs. spatial position of voids

The results for printed and cast samples pertaining to the equivalent diameter as a function of position is presented in Fig. 5.6. These results are selectively presented for pores with equivalent diameters larger than 0.5 mm.

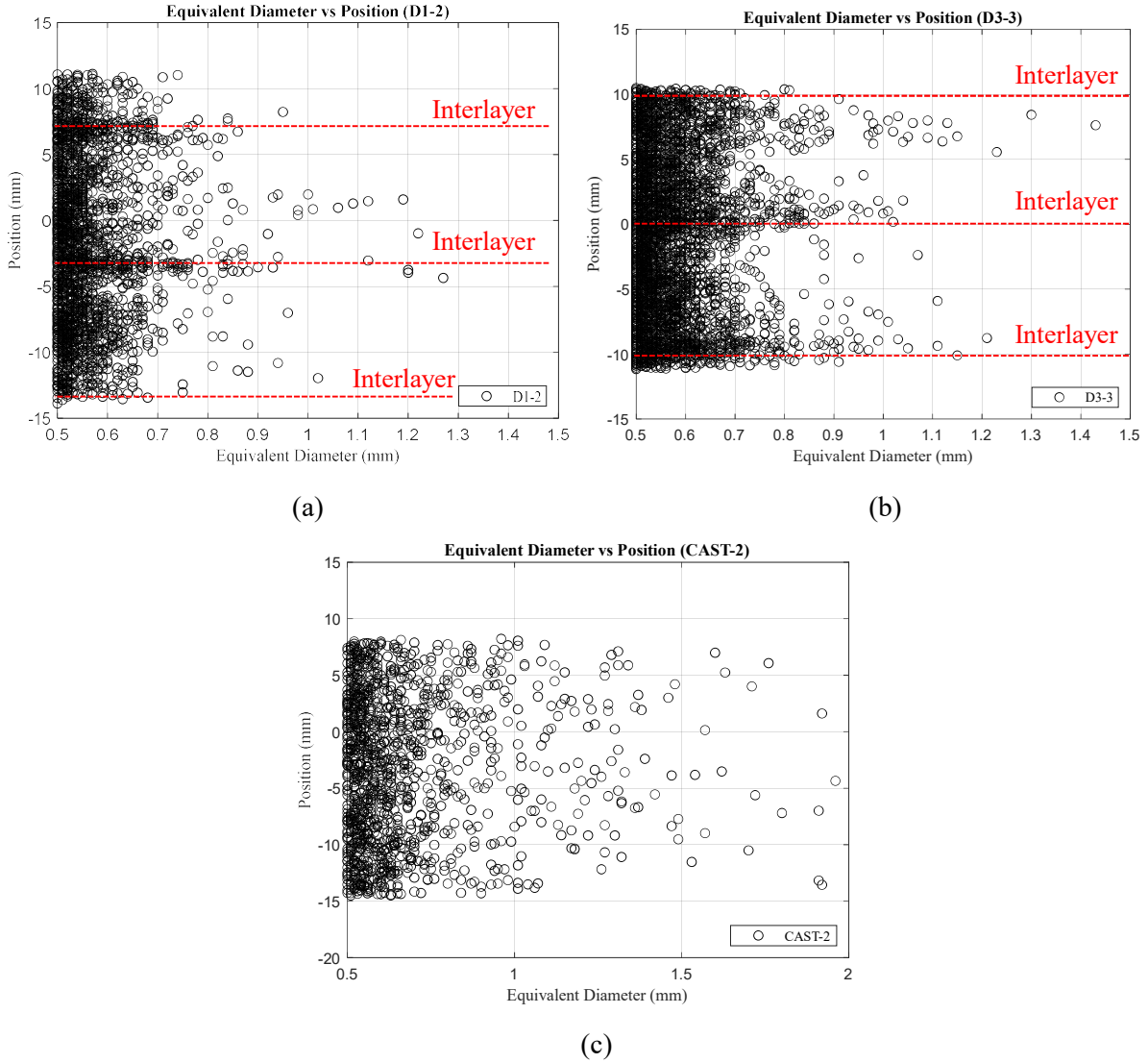

Fig. 5.6: Equivalent diameter of macro voids as a function of position within the cores of FRPC samples, illustrating the results for (a) D1- 2, (b) D3-3, and (c) CAST-2. A supplementary Fig. S2 is provided containing the additional results per category.

From these results, it is deduced that pores with larger equivalent diameters concentrate at interlayer locations, while a random distribution in larger pore sizes is observed for cast specimens. These findings are believed to be brought about by the concrete printing process, where either shear flow in the outer region of the viscous extrudate causes flow-induced particle migration, which renders pockets of encapsulated air in the lubrication layer [38], defects stemming from surface roughness or moisture migration after deposition alters the pore size distribution [3]. The pore size metric has been related to interlayer strength, where weak interlayer bonding has been correlated to larger size air voids at

interlayer locations as opposed to that of other regions [16]. It is postulated that macropores formed by the amalgamation of entrapped air voids could considerably undermine the mechanical performance of concrete printed structures [16]. Interestingly, again as in Fig. 5.4c, larger equivalent diameters (> 1 mm) are encountered for cast samples, indicating that a more significant number of smaller pores are found in printed specimens. We therefore conclude that in the concrete printing context not only is the porosity higher at interlayer locations but also the size and concentration of the encountered pores throughout the printed composite.

5.4.3 Compactness

Compactness provides a quantitate means to evaluate pore topology and is defined as the volumetric ratio between the volume of a defect and the volume of a circumscribed sphere. A compactness ratio equal to one represents a perfect sphere and compactness of zero represents a straight line with no volume.

5.4.3.1 Average compactness of voids

Here, we present the average compactness of voids, Fig. 5.7, to elucidate the topology of voids in cast and 3DCP samples. Mean compactness ratios of 0.36 and 0.33 are attained for printed samples. However, cast samples display a 19 % higher mean compactness ratio equal to 0.43. The higher compactness ratios found in cast samples, signifies that cast samples are generally morphologically more spherical. These observations are consistent with those presented in Fig. 5.5, where cast samples visually exhibit rounder air voids. Intriguingly, van der Putten et al. [16] found that voids with compactness ratios in the order of 0.1 to 0.45 concentrate at interfacial regions in printed specimens. Recalling that pore topology is related to the stress concentration magnitude at pore poles and sides contends that lower compactness ratios pair with reduced bulk material strength and increased deformability [33]. However, the spatial orientation of pores with respect to the loading direction should be considered as in Section 5.4.4.

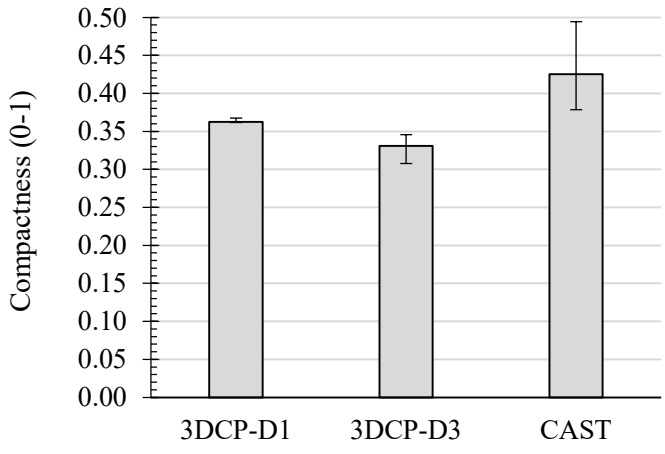

Fig. 5.7: Average compactness of evaluated samples.

5.4.3.2 Compactness vs. void diameter

Viewing compactness as a function of void diameter, Fig. 5.8, shows that printed samples only display high compactness ratios (> 0.5) in voids with diameters less than 0.5 mm, where cast samples display high compactness ratios for voids with diameters up to 2 mm. Curiously, in printed specimens, essentially all voids with diameters larger than 2 mm have compactness ratios less than 0.1 mm. It is postulated that the concrete printing process induces the mechanisms responsible for the presented microstructural morphology. These mechanisms include (i) additional vertical pressure due to compaction overlay and (ii) smearing of encapsulated voids in the extrusion direction due to non-optimised material and process parameters (viz. print speed, extrusion rate, nozzle standoff distance, and fresh state rheological properties). Higher stress concentrations occur at pore poles or corners with lower compactness ratios, and it is now also shown that less compact voids are encountered in printed samples. Therefore, given Griffith's theory, the effective critical crack length is increased relative to the void volume, indicating that the onset of failure is expected to occur earlier in printed samples as opposed to cast samples due to the variations in their microstructural porosity characteristics. Such conjecture is supported by the experimental results presented in Section 5.4.7, where cast samples showcase higher compressive capacity than printed samples evaluated in their respective orthotropic directions.

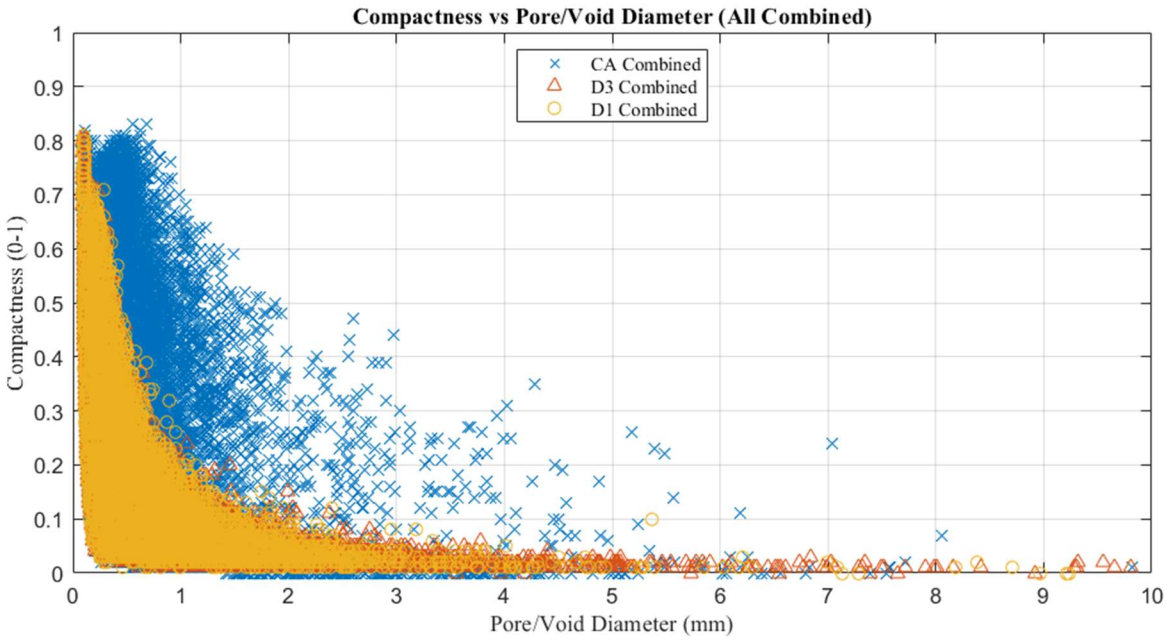

Fig. 5.8: Compactness vs. macropore diameter for the respective categories. Note all samples within a category are combined in this illustration.

5.4.4 Effect of extrusion direction on the shape and orientation of voids

To further express the differences in the microstructural topology of pores in printed and cast specimens, pore diameter vs. the projected length of voids in main Cartesian directions is presented in Fig. 5.9.

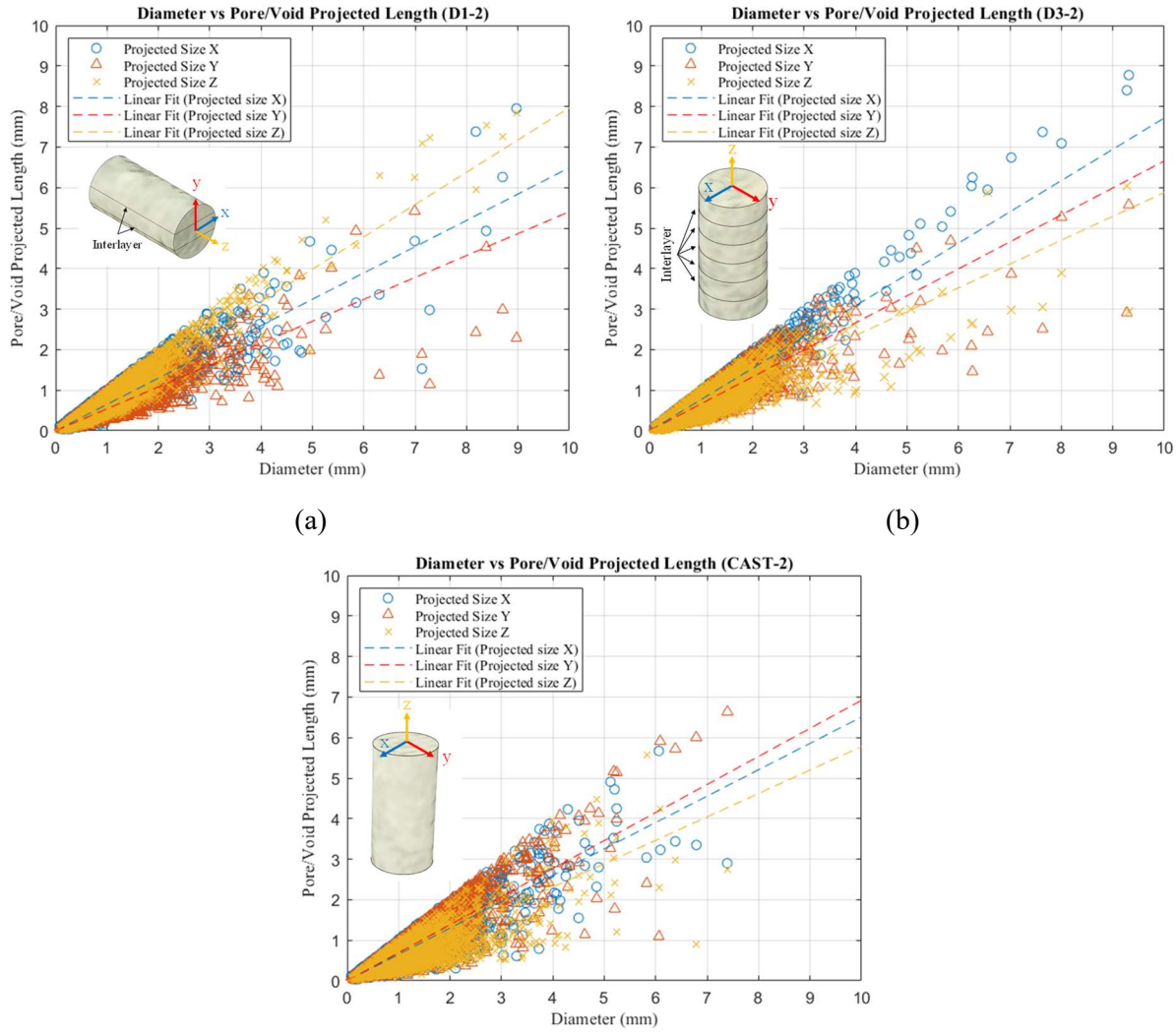

Fig. 5.9: Void projected length in the x, y, and z directions for various void diameters. Note that for D1, the z-direction corresponds to the extrusion direction, and the y-direction corresponds to the vertical building direction. For D3, the x-direction corresponds to the extrusion direction, and the z-direction corresponds with the vertical building direction. For cast samples, the z-direction corresponds to the casting direction. A supplementary Fig. S3 is provided containing the additional results per category.

For 3DCP samples, it is observed that the voids are consistently elongated in the extrusion direction and flattened in the vertical building direction, while cast specimens have similar dimension in plan (xy-plane) but are pressed in the casting direction. Considering the local coordinate systems shown in Fig. 5.9a, the z-direction corresponds to the extrusion direction, and the y-direction corresponds to the building direction normal to the deposition plane. Where in Fig. 5.9b, the x-direction corresponds to the

extrusion direction, and the z-direction parallels the building direction. In Fig. 5.9c, the z-direction corresponds to the casting direction. Additionally, it is remarked that printed specimens depict significant variations in the semi-axis or radial lengths of the elliptical voids, where cast specimens tend to show less pronounced variation, indicating that such pores are more compact, as shown in Fig. 5.7. Such observations emphasise the influence of pumping and extrusion on the microstructural configuration of printed objects. Concurrent consideration of the results presented in Sections 5.4.3 and 5.4.4 illuminates that voids are more tri-axially spheroidal than spherical, as noted by [15]. In this regard, Fig. 5.10 presents a generalised representation of pores in a concrete printed matrix.

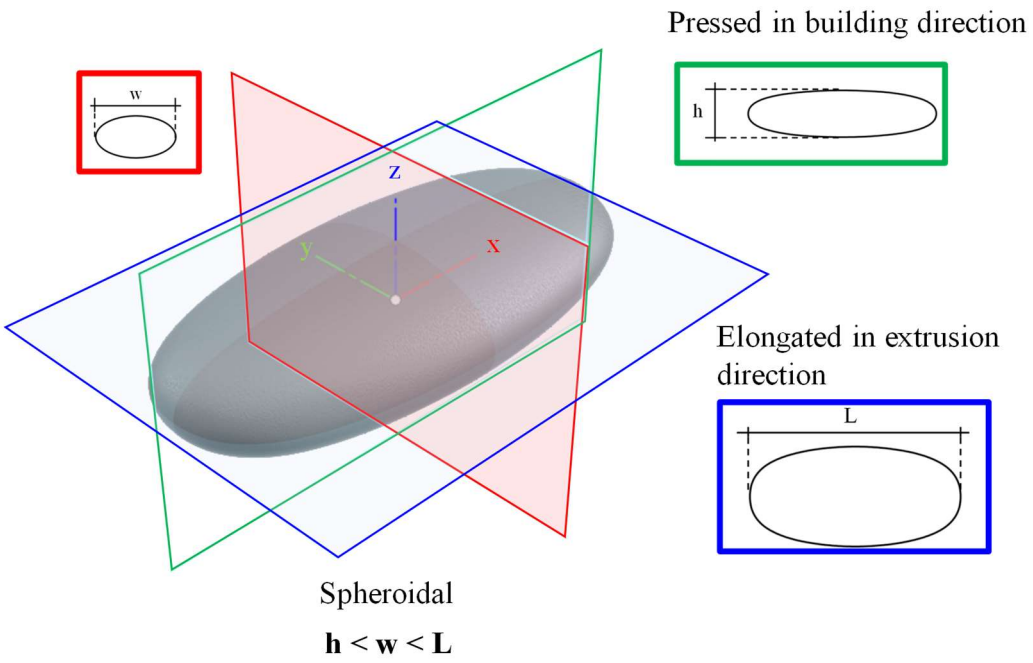

Fig. 5.10: Generalised pore shape encountered in concrete printed filaments. Note that the axis convention utilised here is independent of those presented above. Here the x-direction corresponds to the extrusion direction, the y-direction parallels the transverse direction, and the z-direction represents the vertical building direction, which is normal to the deposition plane.

5.4.5 Interconnectivity of pores/voids at interlayer locations

The results from an interconnected pore analysis are presented in Fig. 5.11. In these images, the diameter refers to the most extended interconnected length of the circumscribed sphere of the defect plane, i.e., red regions in Fig. 5.11a indicate that there is a 27.33 mm interconnected defect path at this coloured location. From these results, it is apparent that the interconnectivity of voids (or permeability) is highest at interlayer locations, which is consistent with previous literature [3,43]. Such findings hold significant implication for both durability and mechanical capacity [3,16]. Prolonged interconnected pore systems establish transportation networks for water, chloride or oxygen and carbon ingress, which impact durability. Additionally, planes of interconnected pore systems offer reduced mechanical

capacity, potentially leading to premature cracking and ultimately structural collapse in unreinforced components. Even if interlayer regions are mechanically reinforced [1], premature cracking and interconnectivity will allow aggressive chemical corrosion compounds to reach the reinforcement items and deteriorate their capacity [3]. If extensive interlayer pore interconnectivity persists, structural designers should reconsider appropriate concrete cover depths or the use of external sealants to mitigate the imparted adverse effects.

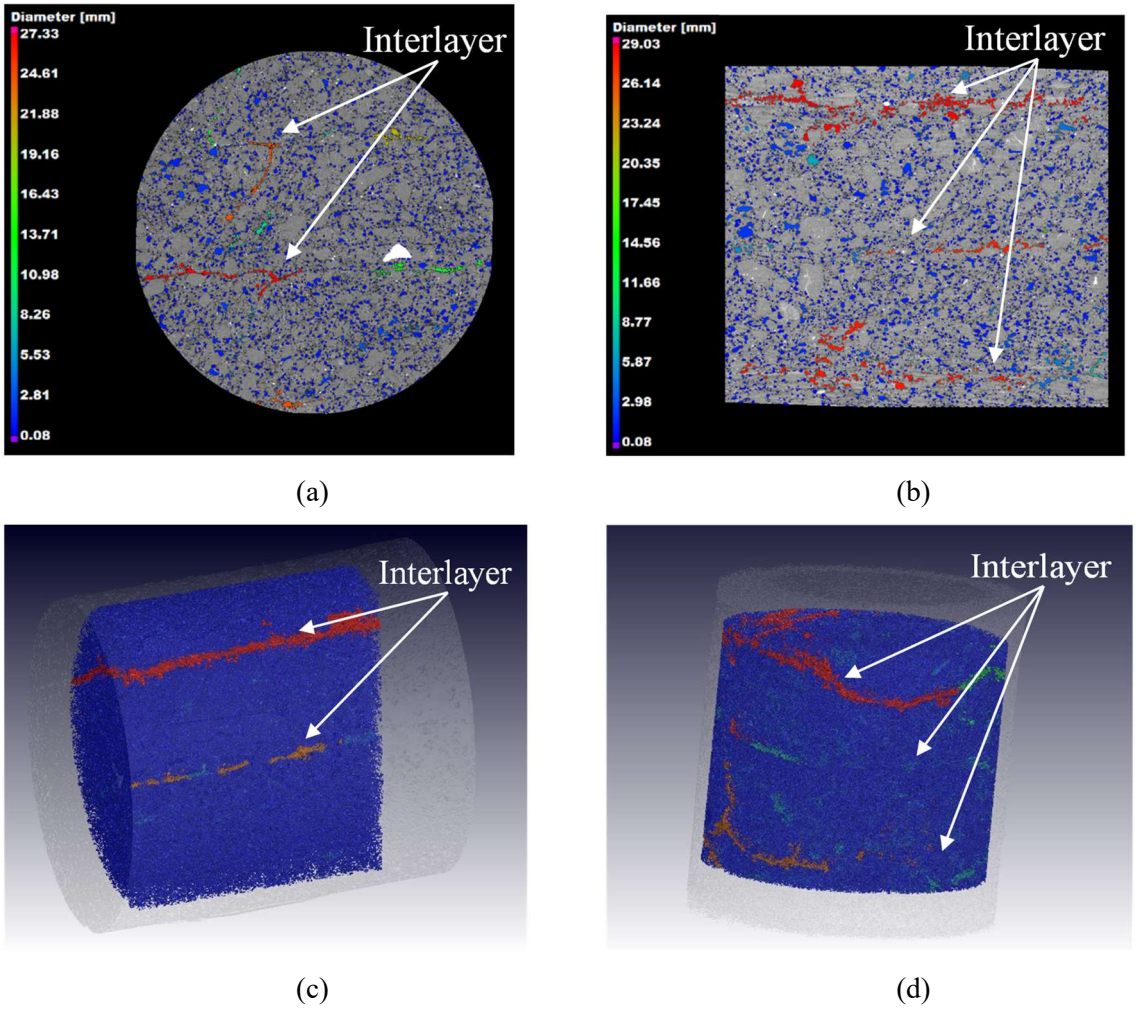

Fig. 5.11: Results from an interconnected pore analysis illustrating pore interconnectivity for samples (a) D1-2 and (b) D3-3. An isoparametric view of interconnected pores at interlayer locations is given for samples (c) D1-2 and (d) D3-3.

5.4.6 The elasticity of printed & cast samples

The E_{mod} results of cast, and printed samples are summarised in Fig. 5.12, and more detailed data of the test results can be found in [11]. Intriguingly, the E_{mod} does not significantly differ in the orthotropic orientations assessed for printed samples, with 3DCP-D1 and 3DCP-D3 equal to 21.9 and 21.6 GPa, respectively. However, a 22 % higher E_{mod} is found for cast specimens (26.7 GPa). Such changes are also believed to originate from the altered air void systems encountered in 3D printed items,

specifically increased porosity content. Furthermore, these results show that it is imperative to assess the E_{mod} of samples extracted from printed objects since cast samples misrepresent the 3DCP properties.

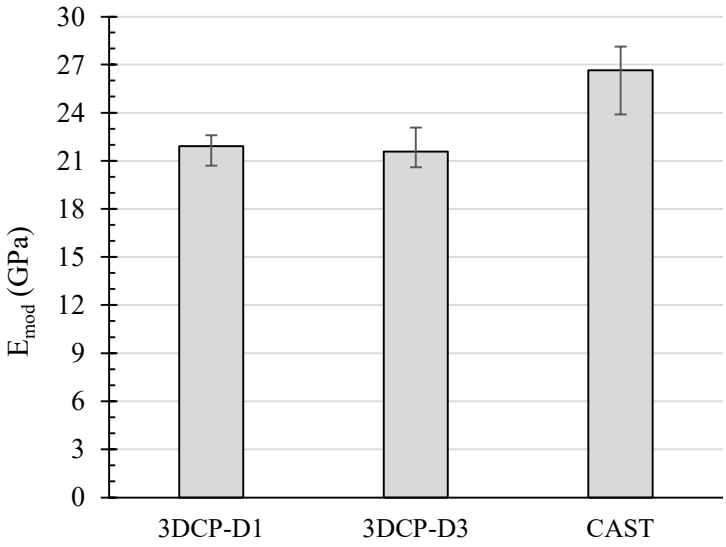

Fig. 5.12: Young's modulus of evaluated samples.

5.4.6.1 Numerical determination of Young's modulus in 3DCP samples

Since the FRPC mixture used here excludes coarse aggregate, the following numerical calculation procedure considers the fractional components of mortar (i.e., hydration products (C-S-H gel), fine aggregate (sand), and submicroscopic pores) to relate E_{mod} to the porosity in 3DCP. However, contrary to the initial formulations presented by Hansen et al. [22] and Powers [19], the given expressions extend the considered porosity domain to include the influence of meso and macropores on the elastic modulus of a FRPC mixture. Note that since porosity content is reportedly the dominating metric influencing the elasticity of cementitious composites, void topology and the associated effects of additional deformability in macropores are omitted. Employing a means to quantify the volumetric composition of hardened cement paste as a function of original w/c ratio and degree of hydration, the fractional volume of cement gel is determined from [22] as:

$$V_{gel} = \frac{0.68 \cdot m}{w/c + 0.32} \tag{5.6}$$

Parameter m is the degree of cement hydration, equal to 0.58 [21] for 28-day old air-cured concrete, and the w/c is 0.45, as presented in Section 5.3.1. Substituting Equation 5.6 into Equation 5.3, the elastic modulus of the cement paste (E_{cmp}) is attained.

$$E_{cmp} = \left(\frac{0.68 \cdot m}{w/c + 0.32}\right)^3 \cdot E_{gel} \tag{5.7}$$

$$E_{gel} \in [16\,,25]\ \text{GPa}\ [44]$$

Considering the notion that mortar is a two-phase composite comprising of aggregates with high modulus of elasticity embedded in a matrix with a lower modulus of elasticity, Ishai's [45] proposed model, Equation 5.4, is employed to express the elastic modulus of mortar (E_{mort}) as a function of the proportional volume of aggregate (V_{agg}) and E_{cmp}, respectively. Substituting Equation 5.7 into Equation 5.4, the formulation reads:

$$E_{mort} = \left(1 + k \cdot V_{agg}\right) \cdot \left(\frac{0.68 \cdot m}{w/c + 0.32}\right)^3 \cdot E_{gel} \tag{5.8}$$

$$k = \frac{E_{agg}}{E_{cmp}}$$

The V_{agg} in the mixture is calculated from the constituent proportions given in Table 5.3, equalling 0.43, and the E_{agg} is assumed equal to 68 – 76 GPa [40]. However, Equation 5.8 only considers the submicroscopic porosity domain (< 10 μm) and therefore cannot wholly describe the elastic modulus of the employed FRPC mixture, which contains substantial amounts of larger air voids greater than 60 μm (ref. Section 5.4.1). Consequently, a description of the elastic modulus based on total porosity is sought. Hansen's [34] expression, Equation 5.9, is extended to include the fractional porosity of meso and macropores attained from the CT scans performed in this research. The proportional colloidal porosity quantities of gel (P_{gel}) and empty colloidal (P_{cap}) pores are determined from Equation 5.10 and Equation 5.11, respectively [22].

$$E = E_0(1 - p)^3 \tag{5.9}$$

$$P_{gel} = \frac{0.19 \cdot m}{w/c + 0.32} \tag{5.10}$$

$$P_{cap} = \frac{0.0575 \cdot m}{w/c + 0.32} \tag{5.11}$$

The total colloidal porosity can then be computed as the sum of the fractional volume of the gel and capillary pores. Inverse determination of the elastic modulus of mortar at zero porosity (E_0) is possible by substituting p in Equation 5.9 with the total colloidal porosity and E with E_{mort}, as in Equation 5.12.

$$E_0 = \frac{E_{mort}}{(1 - (P_{gel} + P_{cap}))^3} \tag{5.12}$$

Total porosity (P_{total}) is now considered a function of both colloidal and non-colloidal pores, with non-colloidal porosity taken as the mean values given in Fig. 5.2. Finally, employing Equation 5.9 but

in terms of total porosity, ranges for the elastic modulus of cast and printed samples are obtained. Table 5.4 presents a comparison of the numerically calculated elastic moduli and the experimentally obtained results. All experimentally obtained results fit well within the calculated ranges.

Table 5.4: Comparison of numerically calculated modulus of elasticity and experimentally obtained results.

Parameter	Calculated Range (GPa)	Experimental Mean (GPa)	Experimental CoV (%)
$E_{3DCP\text{-}D1}$	20.91 – 24.00	21.90 ± 1.04	4.8
$E_{3DCP\text{-}D3}$	20.48 – 23.51	21.60 ± 1.33	6.2
E_{CAST}	24.45 – 28.07	26.70 ± 2.38	8.9

Indeed, to obtain an exact correlation between theoretical and experimental data relating to the total porosity and elastic modulus of a two-phase cementitious material, exhaustive experimental evaluations of the major components within the hardened state matrix is required. Additionally, as illustrated in Fig. 5.13, the provided formulations are inherently most sensitive to changes in total porosity followed by the degree of hydration and original w/c ratio. Yet, the proposed numerical calculation procedure provides an essentially correct, though crude, solution to the experimentally observed air void characteristics and their effect on the elastic modulus, providing insights which are founded on appropriate scientific bases and sufficiently accurate for pragmatic exposition.

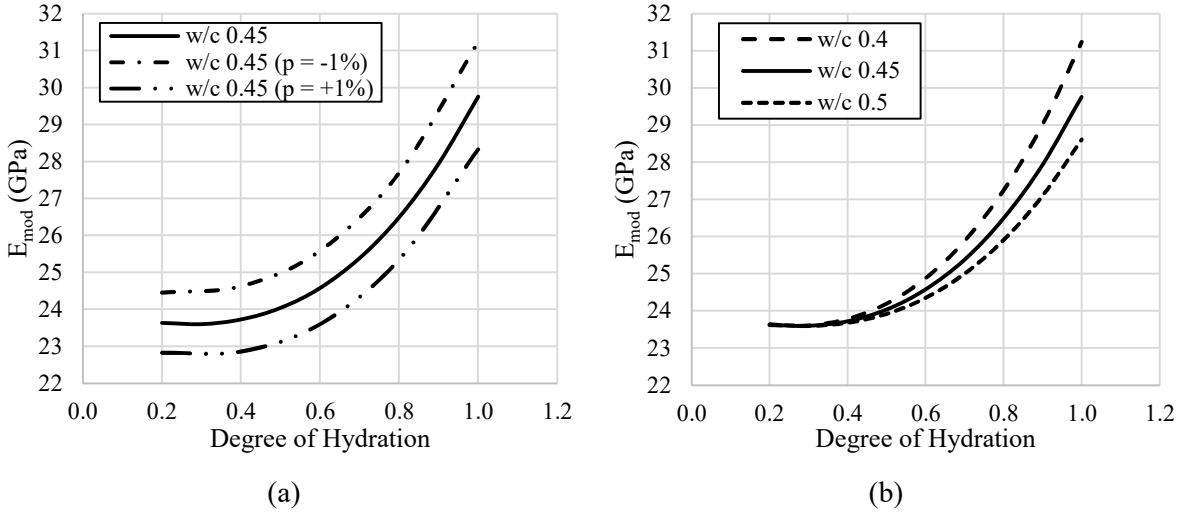

Fig. 5.13: Parameter sensitivity analysis of the upper bound curve for CAST samples, where (a) shows the sensitivity concerning changes in total porosity and (b) indicates the sensitivity of changes in the w/c ratio relative to changes in the degree of hydration.

5.4.7 Compressive capacity of printed & cast samples

The compressive capacity of cast and printed specimens is presented in Fig. 5.14, and more detailed data of the test results can be found in [11]. In these results, anisotropic compression characteristics are portrayed for printed samples, exhibiting ultimate capacities equal to 45.1 MPa and 38.2 MPa for $f_{c,D1}$ and $f_{c,D3}$, respectively. The compressive capacity of cast samples is 60.5 MPa, 34 % higher than $f_{c,D1}$

and 58 % higher than $f_{c,D3}$. It is postulated that the differences in the respective capacities can be ascribed to three main aspects: (i) void topology (shape and orientation), (ii) localised increases in porosity at interlayer locations, and (iii) the orientation of interlayer regions in 3DCP elements. All three aspects should be considered concerning the loading direction as it is contended that the capacity and observed failure patterns are influenced thereby. Additionally, Neralla et al. [12] propose that the extent of the (weak) interface area lying beside the tri-axial compressive zone, and the size of individual pores located at the intersection of shear planes are factors which decisively influence the observed compressive capacity.

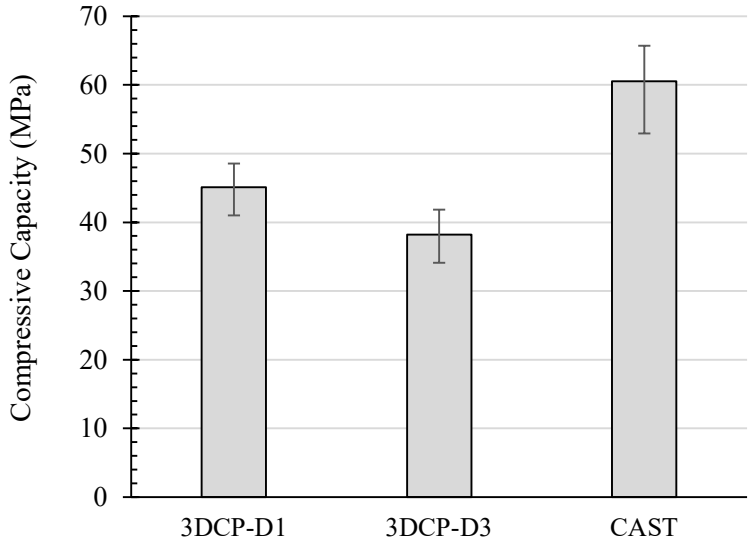

Fig. 5.14: Compressive capacity of evaluated samples.

Considering void topology in the concrete printing context, specific reference is directed towards the observed triaxial ellipsoidal shape of voids and the fact that the voids are elongated in the extrusion direction and pressed in the vertical stacking direction, as shown in Fig. 5.10. As presented in Fig. 5.15, void topology concerning the induced loading direction influences the deformability and intensity of stress concentration at pore boundaries [33]. Studying Figs. 5.7, 5.9 and 5.10, it is evident that generally, smaller oblate voids occur in 3DCP-D3, and prolate voids are found in 3DCP-D1, while larger, more compact voids are present in cast specimens. Now considering the compressive triaxial internal stress distribution presented in Fig. 5.16 in conjunction with the pore area gain and loss illustration in Fig. 5.15, it is contended that compared to 3DCP-D3, 3DCP-D1 provides greater resistance to uniaxial compressive loading because lower stress concentration occurs at void poles and sides under the same load conditions. Such observation further confirms the theory that rounder, more compact voids encountered in cast specimen have greater load-carrying capacity due to the lesser intensity of stress concentrations at pore boundaries. A secondary explanation is thought to reside in the filament-interlayer stacking configuration, where 3DCP-D1 and 3DCP-D3 are considered to represent parallel (Voight modulus) and series (Reuss modulus) arrangements, respectively [46]. Here loading along the

extrusion direction (D1) imparts equal strain on both (stiff) intralayer and (less stiff) interlayer phases, the result of localised increases in porosity, but strains due to loading in the vertical building direction (D3) differ between phases, proportional to the volumetric fraction of each phase [47]. From a composite lamellar perspective, one could say that samples loaded in D1 experience isostrain conditions (Equation 5.13), and those loaded along D3 experience isostress conditions (Equation 5.14) [46]. Furthermore, if it is assumed that the cementitious gel has a specific strain limit (ε_{lim}) it is set forth that the increased deformability and intensity of stress concentrations in printed composites provides reduced compressive capacity. This notion holds when considering the differential capacities of printed and cast samples; since cast specimens display a higher elastic modulus and no less stiff interlayer regions with higher concentrations of larger, less compact pores are present, clarifying the increased compressive strength.

$$E_{c,D3} = \frac{E_\alpha \cdot E_\beta}{V_\alpha \cdot E_\beta + V_\beta \cdot E_\alpha} \tag{5.13}$$

$$E_{c,D1} = V_\alpha \cdot E_\alpha + V_\beta \cdot E_\beta \tag{5.14}$$

$$E_{c,D1} > E_{c,D3}$$

$$\varepsilon_{lim,D1} = \varepsilon_{lim,D3}$$

$$\therefore f_{cu,D1} > f_{cu,D3}$$

where $E_{c,D1}$ and $E_{c,D3}$ are the composite elastic moduli in the respective loading directions, E_α, E_β, V_α, and V_β are the elastic moduli and volumetric fractions of the intralayer (α) and interlayer (β) phases, respectively.

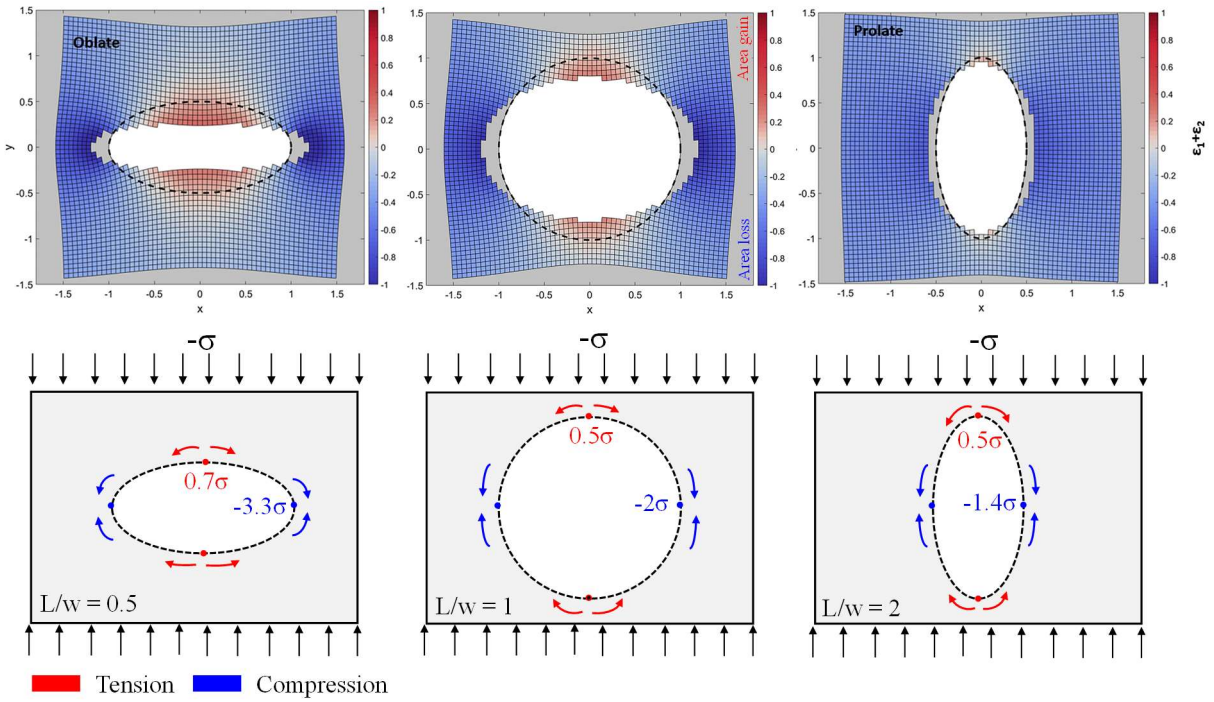

Fig. 5.15: Exposition of deformability and stress concentrations at void boundaries for various topological configurations in a surrounding elastic medium. Top from left to right represents deformability in terms of area change for loading in D3, a perfect sphere, and loading in D1. Bottom from left to right shows stress concentrations in 3D ellipsoidal voids with varying topology having axial ratios (L/w) of 0.5, 1, and 2, respectively. Note that the terms "pole" and "side" a relative to the induced loading direction, here "poles" are the top and bottom nodes of voids and "sides" are locations around the equator of voids. Adapted from [33].

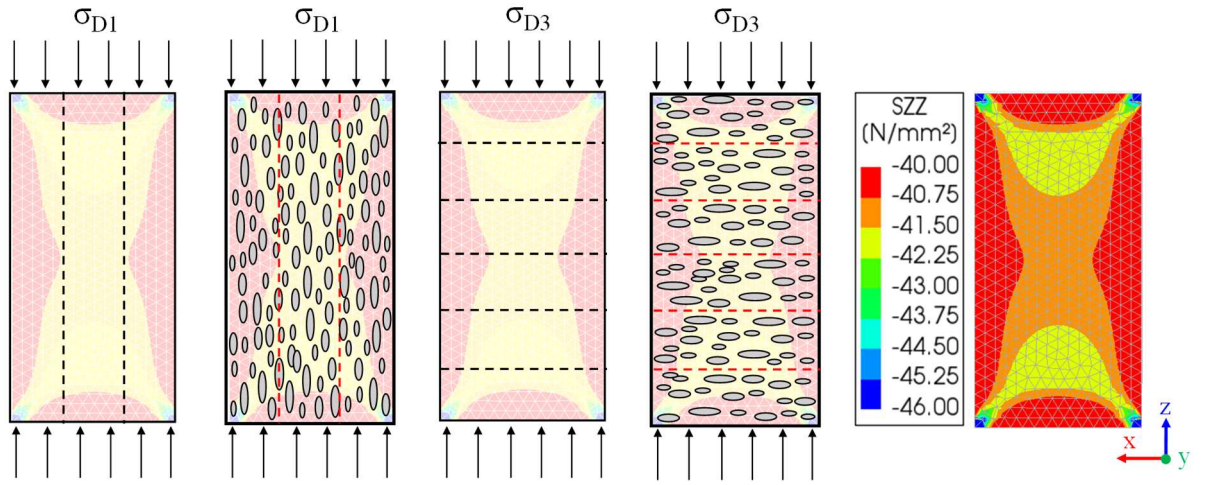

Fig. 5.16:Illustration of the uniaxial compressive loading and resultant axial stress distribution, showing interlayer orientation and void topology resulting from the extrusion-based 3D concrete printing process. Note that the pore distribution is generalised for illustrative purposes only.

5.4.8 Compressive failure patterns in printed samples

The compressive failure patterns encountered during the experimental campaign are presented in Fig. 5.17. It is shown that columnar failure occurs in samples loaded along D1 and cone/shear type failure appears in samples loaded along D3. Additionally, although not visually presented, cast samples fail similarly to samples loaded along D3. Remembering that higher porosity, increases in pore size, preferentially aligned void topology, and increased interconnectivity are prevalent at interlayer regions, it is inferred that due to the effects of porosity, reduced interlayer capacity is prominent and therefore cracks initiate and propagate along interlayers resulting in filament delamination, inducing global sample failure. This feature is particularly noticeable under compressive loading along D1, where the larger pores are elongated in the extrusion direction, causing splitting stresses that initiate tensile cracking at void poles that subsequently coalesce to form the columnar failure pattern presented in Fig. 5.17a. Since the pore topology is orientated orthogonal to the load direction in D3, a less pronounced influence of interlayer regions on the observed failure pattern is noted since the tri-axial compressive stress state shown in Fig. 5.16 dominates the failure regime. The failure mechanism for loading along D3 results from compression failure at the predominantly oblate void sides, creating shearing planes at differential stress boundaries. The rounder voids encountered in mould cast samples form a microstructural morphology similar to that of most volumetrically cast cementitious components. Therefore, the observed failure mechanisms in 3DCP-D3 and cast samples can be quantified by the Mohr-Coulomb failure criteria [48], but 3DCP-D1 samples require additional investigation.

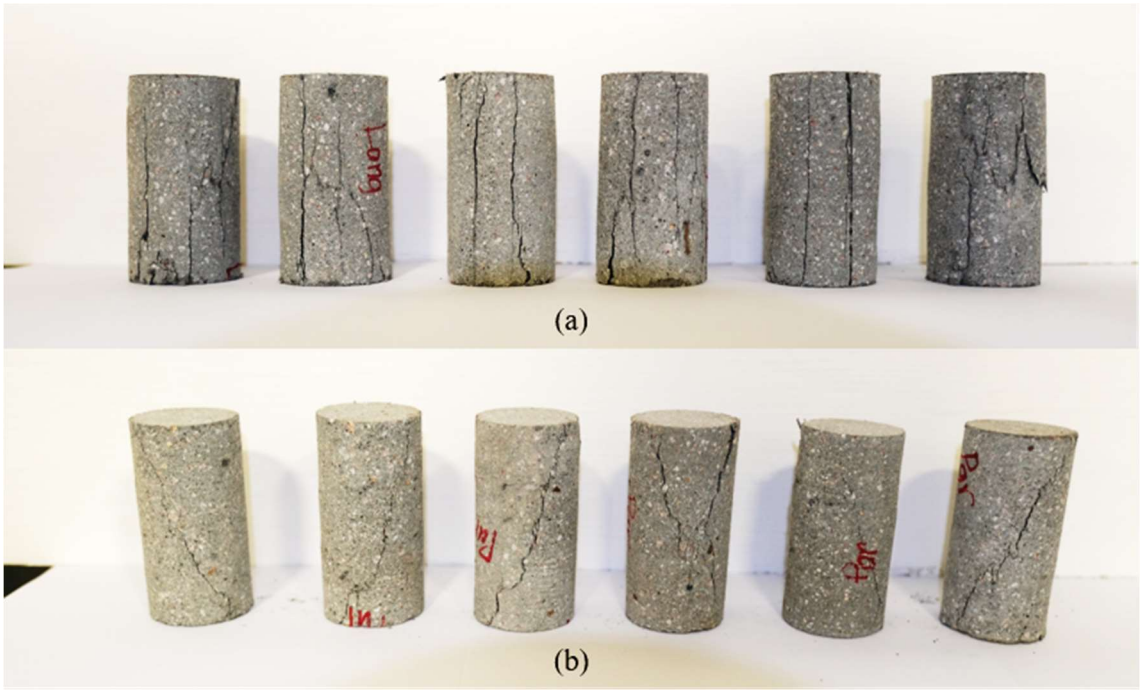

Fig. 5.17: Compression failure patterns in 3D concrete printed specimens.

Fig. 5.18 presents selected micro-CT scanning results from samples after uniaxial compressive failure has occurred. These results validate that major cracks form along interlayer regions when loading samples along D1, and diagonal shear cracks which likely occur after the initial columnar failure are prevalent in intralayer regions. The variation in the observed failure modes is thought to be the consequence of the altered microstructure. Larger ellipsoidal pores concentrate in-between filaments, and smaller, more compact pores are found in intralayers. Samples loaded along D3 illustrate predominantly tri-axial shear failure under uniaxial compressive loading. The failure pattern in D3 is more voluminous and indicative of a crushing action at ultimate loading.

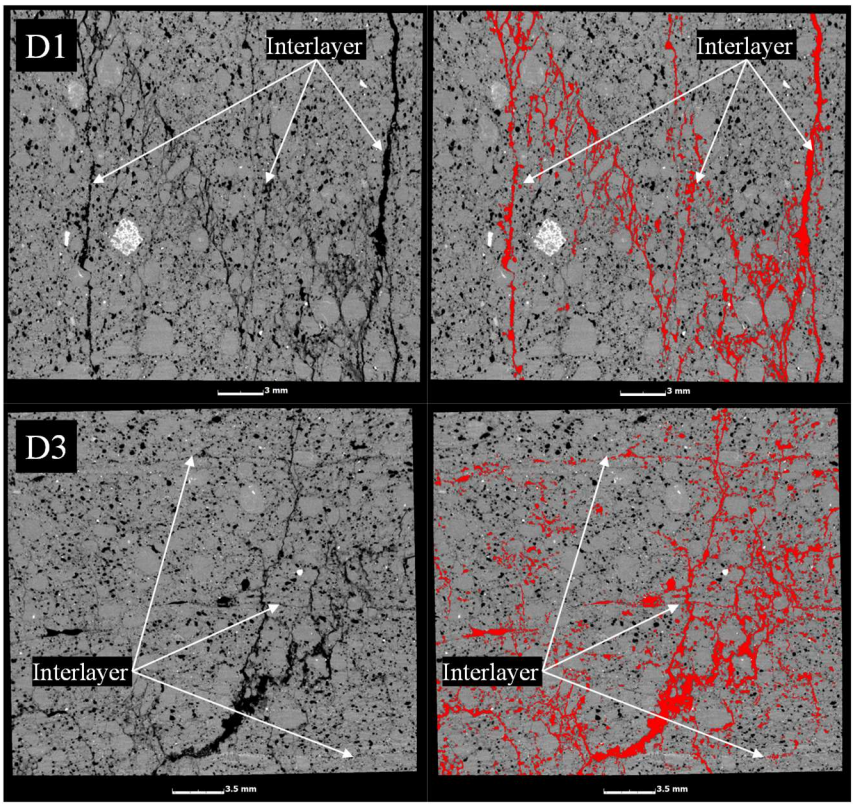

Fig. 5.18: CT scan interconnectivity analysis illustrating internal fracture patterns for (top) samples loaded along D1 and (bottom) samples loaded along D3.

5.5 Conclusions

A microstructural examination of extrusion-based 3DCP is presented in this research. Here, the effects of porosity metrics such as total porosity content; 3D void topology (shape, size, and orientation); pore spatial, size and compactness distributions; and interconnectivity are quantitatively investigated via X-ray CT and related to the experimentally determined elasticity, compressive strength and observed fracture patterns of mould-cast and 3DCP specimens consisting of a fibre-reinforced printable cementitious matrix. The microstructural effects of pumping, extrusion, and the additive manufacturing process employed are correlated to the mechanical characteristics of 3DCP. From the presented results, the following conclusions are drawn:

- Printed samples contain the highest porosity content equal to 10.8 % (D3) and 10.3 % (D1) compared to the 6.5 % total porosity of the cast specimens. Moreover, it is deduced that fibre entrainment induces additional porosity in 3DCP.
- Evaluating the pore size distribution shows that for printed samples, pores are generally in the range of 0.06-1.2 mm, with a higher number of larger (> 1.2 mm) and smaller (<< 0.16 mm) pores noted in cast specimens. Interestingly, cast samples display a larger spectrum of pore sizes, although the total porosity content is less than that of printed specimens. From these observations, it is affirmed that during pumping and extrusion, the embodied extrusion-based additive manufacturing process alters the microstructural morphology of the 3DCP matrix.
- In printed samples, higher porosity is exhibited at interlayer locations, and a more even distribution of porosity is found in cast specimens. Furthermore, pores encountered in cast samples are generally more spherical compared to the irregularly shaped inclusions observed in printed samples.
- The equivalent diameters of voids larger than 0.5 mm as a function of position indicate that pores with larger equivalent diameters concentrate at interlayer locations. In contrast, a random distribution in larger pore sizes is observed for cast specimens. Following the Griffiths formulation for tensile strength, such observations are contended to be strongly correlated to reduced interlayer capacity.
- Cast samples show higher compactness ratios (0.43) than printed samples (0.36 and 0.33), signifying that printed samples are generally morphologically less spherical. Recalling that pore topology is related to the stress concentration magnitude at pore boundaries, it is maintained that lower compactness ratios pair with reduced bulk material strength and increased deformability.
- Relating compactness to void diameter for printed samples shows that larger voids have reduced compactness, permitting the conclusion that an increased number of larger, less compact pores are present at interlayer locations.
- For concrete printed samples, it is observed that the voids are consistently elongated in the extrusion direction and flattened in the vertical building direction, while cast specimens are pressed in the casting direction. This indicates that the hydraulic pressure gradient induced by the extrusion process preferentially aligns and elongates voids in the extrusion direction while pressing/squeezing them in the vertical building direction due to compaction overlay. Additionally, larger variations in semi-axis length are seen in 3DCP samples validating their reduced compactness.
- It is apparent that the interconnectivity of voids are highest at interlayer locations which are detrimental to both durability and strength in concrete printed samples.

- Elastic moduli are similar in orthogonal directions of printed specimens, here 21.9 GPa and 21.6 GPa for E_{D1} and E_{D3}, respectively. E_{cast} is 26.7 GPa, 22 % higher than E_{D1} and 24 % higher than E_{D3}. From recognised theory, we can quantitatively correlate the apparent changes in elasticity to the fractional components of the FRPC mixture employed and show that the porosity content of macro pores appreciably contribute to the observed changes in Young's modulus.
- Anisotropic compression characteristics are observed for printed samples, with 45.1 MPa and 38.2 MPa for $f_{c,D1}$ and $f_{c,D3}$, respectively. The compressive capacity of cast samples is 60.5 MPa, 34 % higher than $f_{c,D1}$ and 58 % higher than $f_{c,D3}$. Changes in capacity are ascribed to three main factors: (i) void topology (shape and orientation), (ii) localised increases in porosity at interlayer locations, and (iii) the orientation of interlayer regions in 3D concrete printed elements concerning the loading direction.
- It is imperative to assess the mechanical characteristics of samples extracted from printed objects since cast samples misrepresent 3DCP.
- The presence and orientation of (weaker) interlayer regions influence the compression failure patterns in printed samples. Since higher porosity, increases in pore size, preferentially aligned void topology, and increased interconnectivity is prevalent at interlayer regions; it is inferred that the effects of porosity reduce interlayer capacity and therefore cracks initiate and propagate along interlayers resulting in filament delamination, inducing global sample failure. This feature is expressed by the columnar failure in 3DCP-D1 as opposed to the cone/shear type failure observed for 3DCP-D3 and cast specimens.

To stiffen and strengthen the composite matrix of 3D concrete printed components, it is recommended that void stabilisation methods either in the form of air-entraining admixtures, to transform elongated or irregularly shaped air voids to voids with smaller diameters and higher compactness, or optimised print process parameters be explored, to reduce the number and size of pores at interlayer locations.

CRediT authorship contribution statement

Marchant van den Heever: Conceptualisation, Methodology, Validation, Formal analysis, Investigation, Data curation, Writing - original draft, Writing - review & editing, Visualisation, Project administration.

Anton du Plessis: Methodology, Software, Formal analysis, Investigation, Resources, Data curation, Writing - review & editing, Visualisation, Funding acquisition.

Jacques Kruger: Conceptualisation, Resources, Writing - review & editing, Supervision.

Gideon van Zijl: Resources, Writing - review & editing, Supervision, Funding acquisition.

Declaration of Competing Interest

The authors declare the following financial interests/personal relationships which may be considered as potential competing interests:

One of the authors of this article is part of the editorial board of the journal. To avoid potential conflicts of interest, the responsibility for the editorial and peer-review process of this article lies with the other editors of the journal. Furthermore, the authors of this article were removed from the peer review process and have no access to confidential information related to the editorial process of this article.

Acknowledgements

The support by The Concrete Society in South Africa is gratefully acknowledged. Funding of Anton du Plessis through the South African Collaborative Programme in Additive Manufacturing (CPAM) is thankfully acknowledged.

5.6 References

[1] F.A. Bester, M. van den Heever, P.J. Kruger, G.P.A.G. van Zijl, Reinforcing digitally fabricated concrete: A systems approach review, Additive Manufacturing. 37 (2021). https://doi.org/10.1016/j.addma.2020.101737.

[2] A. du Plessis, A.J. Babafemi, S.C. Paul, B. Panda, J.P. Tran, C. Broeckhoven, Biomimicry for 3D concrete printing: a review and perspective, Additive Manufacturing. (2020) 101823. https://doi.org/10.1016/j.addma.2020.101823.

[3] J. Kruger, G. van Zijl, A compendious review on lack-of-fusion in digital concrete fabrication, Additive Manufacturing. 37 (2021) 101654. https://doi.org/10.1016/j.addma.2020.101654.

[4] M. van den Heever, F. Bester, M. Pourbehi, J. Kruger, S. Cho, G. van Zijl, Characterizing the Fissility of 3D Concrete Printed Elements via the Cohesive Zone Method, 2nd RILEM International Conference on Concrete and Digital Fabrication. 3 (2020) 1–10.

[5] B. Panda, S. Chandra Paul, M. Jen Tan, Anisotropic mechanical performance of 3D printed fiber reinforced sustainable construction material, Materials Letters. (2017). https://doi.org/10.1016/j.matlet.2017.07.123.

[6] G. Ma, Z. Li, L. Wang, F. Wang, J. Sanjayan, Mechanical anisotropy of aligned fiber reinforced composite for extrusion-based 3D printing, Construction and Building Materials. (2019). https://doi.org/10.1016/j.conbuildmat.2019.01.008.

[7] M. Sonebi, S. Amziane, A. Perrot, Mechanical Behavior of 3D Printed Cement Materials, 3D Printing of Concrete. (2019) 101–124. https://doi.org/10.1002/9781119610755.ch4.

[8] S.C. Figueiredo, C.R. Rodrıguez, Z.Y. Ahmed, D.H. Bos, Y. Xu, T.M. Salet, O.C. Opurog˘lu, E. Schlangen, F.P. Bos, Mechanical behaviour of printed strain hardening cementitious composites, Materials. 13 (2020).

[9] P. Feng, X. Meng, J. Chen, L. Ye, Mechanical properties of structures 3D printed with cementitious powders, CONSTRUCTION & BUILDING MATERIALS. 93 (2015) 486–497. https://doi.org/10.1016/j.conbuildmat.2015.05.132.

[10] L. Wang, H. Jiang, Z. Li, G. Ma, Mechanical behaviors of 3D printed lightweight concrete structure with hollow section, Archives of Civil and Mechanical Engineering. 20 (2020) 1–17. https://doi.org/10.1007/s43452-020-00017-1.

[11] M. van den Heever, F.A. Bester, P.J. Kruger, G.P.A.G. van Zijl, Mechanical Characterisation for Numerical Simulation of Extrusion-based 3D Concrete Printing, Journal of Building Engineering. 44 (2021). https://doi.org/10.1016/j.jobe.2021.102944.

[12] V.N. Nerella, S. Hempel, V. Mechtcherine, Effects of layer-interface properties on mechanical performance of concrete elements produced by extrusion-based 3D-printing, Construction and Building Materials. 205 (2019). https://doi.org/10.1016/j.conbuildmat.2019.01.235.

[13] J. Yu, C.K.Y. Leung, Impact of 3D Printing Direction on Mechanical Performance of Strain-Hardening Cementitious Composite (SHCC) Jing, Springer International Publishing, 2019. https://doi.org/10.1007/978-3-319-99519-9.

[14] Y. Chen, O. Çopuroğlu, C. Romero Rodriguez, F.F. de Mendonca Filho, E. Schlangen, Characterization of air-void systems in 3D printed cementitious materials using optical image scanning and X-ray computed tomography, Materials Characterization. 173 (2021) 110948. https://doi.org/10.1016/j.matchar.2021.110948.

[15] J. Kruger, A. du Plessis, G. van Zijl, An investigation into the porosity of extrusion-based 3D printed concrete, Additive Manufacturing. 37 (2021) 101740. https://doi.org/10.1016/j.addma.2020.101740.

[16] J. van der Putten, M. Deprez, V. Cnudde, G. de Schutter, K. van Tittelboom, Microstructural characterization of 3D printed cementitious materials, Materials. 12 (2019). https://doi.org/10.3390/ma12182993.

[17] H. Lee, J.H.J. Kim, J.H. Moon, W.W. Kim, E.A. Seo, Correlation between pore characteristics and tensile bond strength of additive manufactured mortar using X-ray computed tomography, Construction and Building Materials. 226 (2019) 712–720. https://doi.org/10.1016/j.conbuildmat.2019.07.161.

[18] P. Domone, J. Illston, eds., Construction Materials: Their Nature and Behaviour, 4th ed., Spon Press, New York, 2010. https://doi.org/10.1016/B978-0-444-88887-7.50012-X.

[19] T.C. Powers, Structure and Physical Properties of Hardened Portland Cement Paste, Journal of the American Ceramic Society. 41 (1958) 1–6. https://doi.org/doi:10.1111/j.1151-2916.1958.tb13494.x.

[20] R. Kumar, B. Bhattacharjee, Porosity, pore size distribution and in situ strength of concrete, Cement and Concrete Research. 33 (2003) 155–164. https://doi.org/10.1016/S0008-8846(02)00942-0.

[21] J.E. Ash, M.G. Hall, J.I. Langford, M. Mellas, Estimations of degree of hydration of portland cement pastes, Cement and Concrete Research. 23 (1993) 399–406. https://doi.org/10.1016/0008-8846(93)90105-I.

[22] T.C. Hansen, Physical Structure of Hardened Cement Paste, Materials and Structures. 19 (1986) 423–436.

[23] P.C. Aïtcin, Entrained air in concrete: Rheology and freezing resistance, Elsevier Ltd, 2016. https://doi.org/10.1016/B978-0-08-100693-1.00006-0.

[24] P.J. Withers, D. Grimaldi, C.K. Hagen, E. Maire, M. Manley, A. du Plessis, X-ray computed tomography, Nature Reviews Methods Primers. (2021). https://doi.org/10.1038/s43586-021-00015-4.

[25] A. du Plessis, W.P. Boshoff, A review of X-ray computed tomography of concrete and asphalt construction materials, Construction and Building Materials. 199 (2019) 637–651. https://doi.org/10.1016/j.conbuildmat.2018.12.049.

[26] T.T. Le, S.A. Austin, S. Lim, R.A. Buswell, R. Law, A.G.F. Gibb, T. Thorpe, Hardened properties of high-performance printing concrete, Cement and Concrete Research. 42 (2012) 558–566. https://doi.org/10.1016/j.cemconres.2011.12.003.

[27] H. Kloft, H.W. Krauss, N. Hack, E. Herrmann, S. Neudecker, P.A. Varady, D. Lowke, Influence of process parameters on the interlayer bond strength of concrete elements additive manufactured by Shotcrete 3D Printing (SC3DP), Cement and Concrete Research. 134 (2020) 106078. https://doi.org/10.1016/j.cemconres.2020.106078.

[28] B. Nematollahi, P. Vijay, J. Sanjayan, A. Nazari, M. Xia, V.N. Nerella, V. Mechtcherine, Effect of polypropylene fibre addition on properties of geopolymers made by 3D printing for digital construction, Materials. 11 (2018). https://doi.org/10.3390/ma11122352.

[29] A.A. Griffith, The phenomena of rupture and flow in solids, Royal Society. 221 (1920). https://doi.org/https://doi.org/10.1098/rsta.1921.0006.

[30] J.D. Birchall, A.J. Howard, K. Kendall, Flexural strength and porosity of cements, Nature. 289 (1981) 388–390. https://doi.org/10.1038/289388a0.

[31] D. Liu, B. Šavija, G.E. Smith, P.E.J. Flewitt, T. Lowe, E. Schlangen, Towards understanding the influence of porosity on mechanical and fracture behaviour of quasi-brittle materials: experiments and modelling, International Journal of Fracture. 205 (2017) 57–72. https://doi.org/10.1007/s10704-017-0181-7.

[32] K. Kendall, A.J. Howard, J.D. Birchall, Relation Between Porosity, Microstructure and Strength, and the Approach To Advanced Cement-Based Materials., Philosophical Transactions of the Royal Society of London. 310 (1983) 139–153. https://doi.org/10.1098/rsta.1983.0073.

[33] T. Davis, D. Healy, A. Bubeck, R. Walker, Stress concentrations around voids in three dimensions: The roots of failure, Journal of Structural Geology. 102 (2017) 193–207. https://doi.org/10.1016/j.jsg.2017.07.013.

[34] T.C. Hansen, Influence of Aggregate and Voids on Modulus of Elasticity of Concrete, Cement Mortar, and Cement Paste, Journal of the American Concrete Institute. 62 (1965) 193–216. https://doi.org/10.14359/7686.

[35] G.S. Slavcheva, O. v. Artamonova, Rheological behavior of 3D printable cement paste: Criterial evaluation, Magazine of Civil Engineering. 84 (2018) 97–108. https://doi.org/10.18720/MCE.84.10.

[36] J.H. Jo, B.W. Jo, W. Cho, J.H. Kim, Development of a 3D Printer for Concrete Structures: Laboratory Testing of Cementitious Materials, International Journal of Concrete Structures and Materials. 14 (2020). https://doi.org/10.1186/s40069-019-0388-2.

[37] J.G. Sanjayan, B. Nematollahi, M. Xia, T. Marchment, Effect of surface moisture on inter-layer strength of 3D printed concrete, Construction and Building Materials. (2018). https://doi.org/10.1016/j.conbuildmat.2018.03.232.

[38] E. Secrieru, D. Cotardo, V. Mechtcherine, L. Lohaus, C. Schröfl, C. Begemann, Changes in concrete properties during pumping and formation of lubricating material under pressure, Cement and Concrete Research. 108 (2018) 129–139. https://doi.org/10.1016/j.cemconres.2018.03.018.

[39] Cement and Concrete Institute, Cementitious Materials for Concrete : Standards , selection and properties, Concrete. (2009) 1–6.

[40] J.R. Mackechnie, Quality of Western Cape Sandstone as Concrete Aggregate, Concrete Beton. 104 (2003) 11–13.

[41] ASTM Standard C469-02, Standard Test Method for Static Modulus of Elasticity and Poisson's Ratio of Concrete in Compression, ASTM International. 04 (2002) 1–5. https://doi.org/10.1520/C0469-02.

[42] Z. Raheem, Standard Test Method for Compressive Strength of Cylindrical Concrete Specimens 1, ASTM Standard Book. (2003) 1–5.

[43] B. Anleu, Quantitative micro XRF mapping of chlorides: possibilities, limitations, and applications, from cement to digital concrete, 2018. https://doi.org/https://doi. org/10.3929/ethz-a-010782581.

[44] H. Manzano, J.S. Dolado, A. Ayuela, Elastic properties of the main species present in Portland cement pastes, Acta Materialia. 57 (2009) 1666–1674. https://doi.org/10.1016/j.actamat.2008.12.007.

[45] O. Ishai, Influence of Sand Concentration on deformations of Mortar Beams Under Low Stresses, ACI Journal Proceedings. 58 (1961) 611–624. https://doi.org/10.14359/8000.

[46] C.J.R. Verbeek, W.W. Focke, Modelling the Young's modulus of platelet reinforced thermoplastic sheet composites, Composites Part A: Applied Science and Manufacturing. 33 (2002) 1697–1704. https://doi.org/10.1016/S1359-835X(02)00184-7.

[47] H. Kuhn, D. Medlin, Mechanical Testing and Evaluation, ASM International, Ohio, 2000.

[48] J.F. Labuz, A. Zang, Mohr-Coulomb failure criterion, Rock Mechanics and Rock Engineering. 45 (2012) 975–979. https://doi.org/10.1007/s00603-012-0281-7.

Supplementary Information

Pore distribution

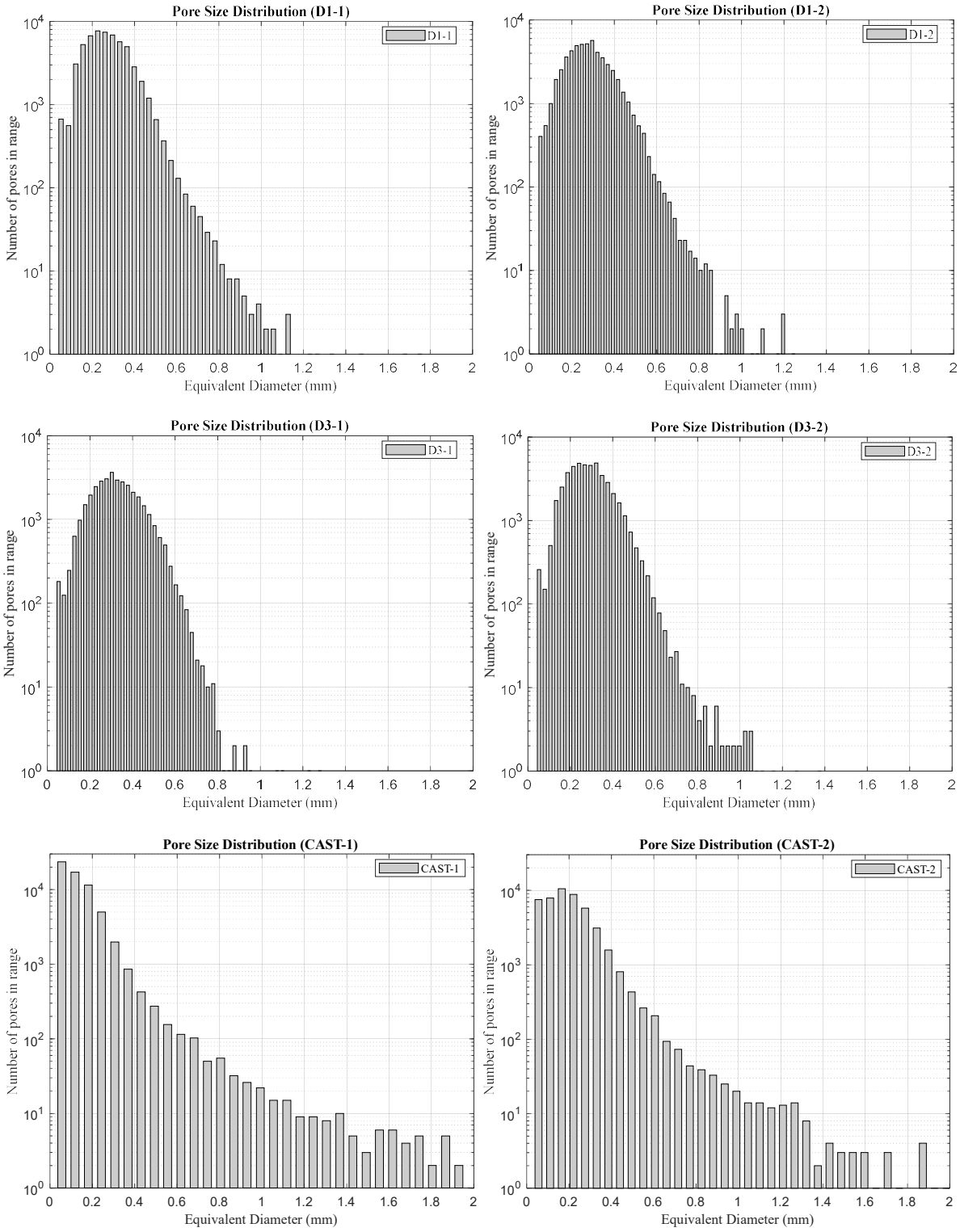

Figure S1: Supplementary pore size distributions per category.

Equivalent diameter vs. spatial position of voids

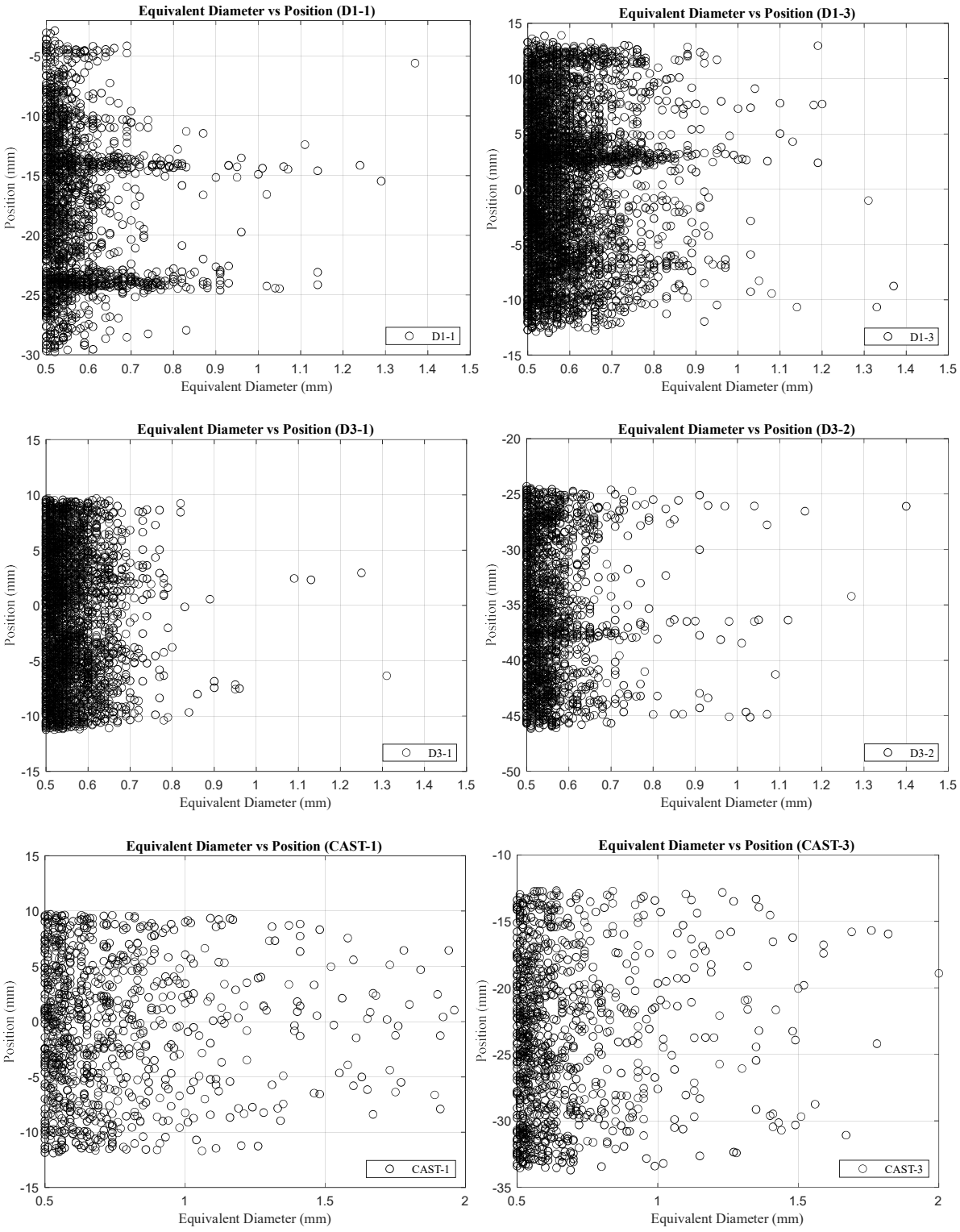

Figure S2: Supplementary equivalent diameter vs. spatial position of voids.

Pore shape

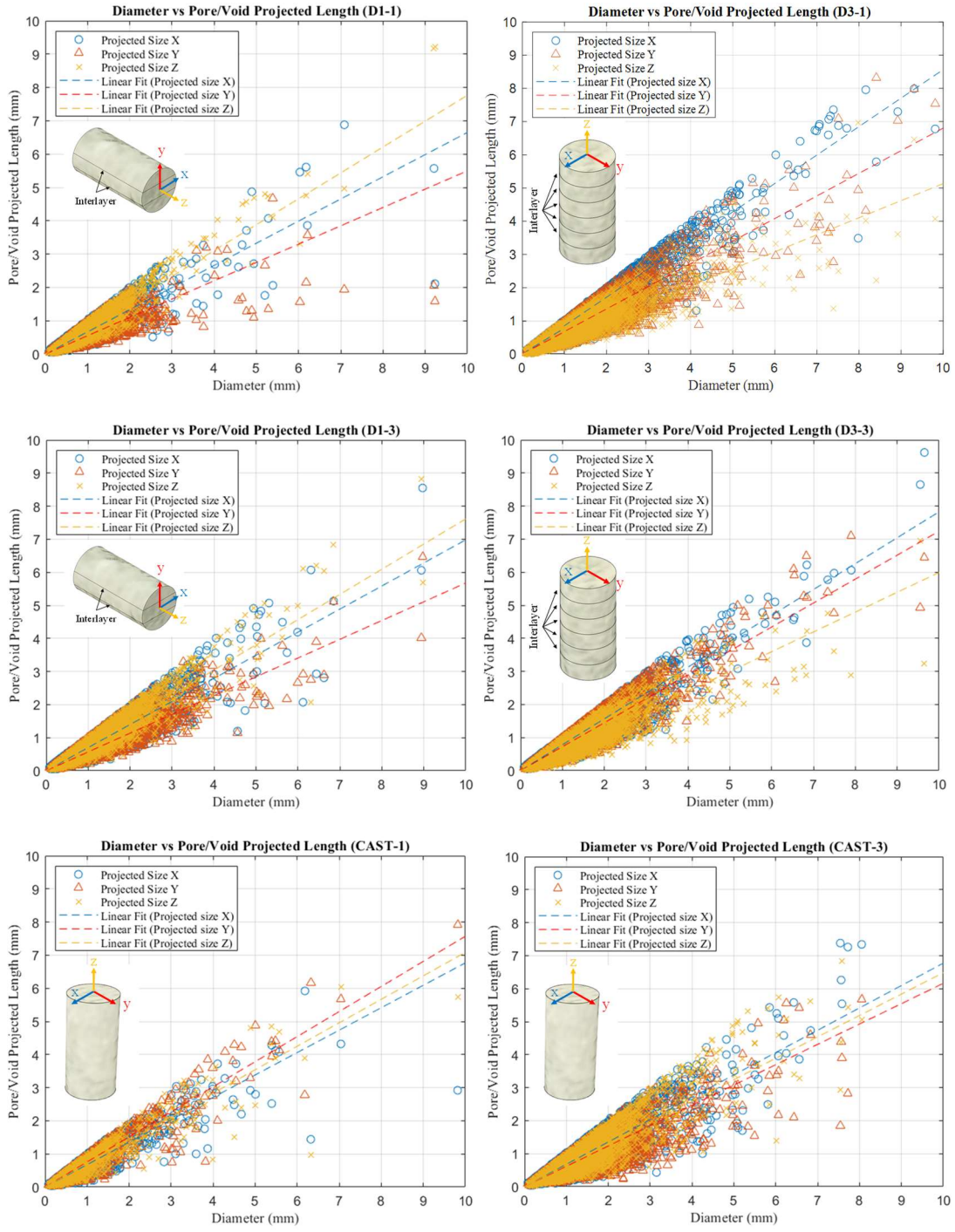

Figure S3: Supplementary diameter vs. pore projected length.

CHAPTER 6 : A Mechanistic Evaluation relating Microstructural Morphology to a modified Mohr-Griffith compression-shear constitutive model for 3D Printed Concrete

Marchant van den Heever [a], Anton du Plessis [b, c], Frederick Bester [a], Jacques Kruger [a], Gideon van Zijl [a]

[a] Structural Engineering and Civil Engineering Informatics, Department of Civil Engineering, Stellenbosch University, Stellenbosch, 7602, South Africa

[b] Research group 3D Innovation, Stellenbosch University, Stellenbosch 7602, South Africa

[c] Department of Mechanical Engineering, Nelson Mandela University, Port Elizabeth 6001, South Africa

Reproduced and reformatted from an article submitted to *Construction and Building Materials*.

(DOI: Submitted)

Abstract

The hardened-state mechanical characteristics of 3D printable concrete (3DPC) mixtures exhibit a strong dependence on the employed extrusion-based process, material, and design parameters and are predominantly anisotropic by nature. It has been shown that at the heart of the observed mechanical anisotropy lies the microstructural morphology of the manufactured component. Additionally, it is hypothesised that a linear Coulomb friction assumption misrepresents the interfacial compression-shear constitutive behaviour exhibited in 3DPC. Thus, additional calibration of the shear model parameters is sought, forming the basis for the current investigation. In this regard, the present contribution offers a comprehensive investigation of the constant compression-shear performance of a fibre-reinforced printable concrete (FRPC) mixture via a direct shear test (DST) methodology for concrete samples additively manufactured by extrusion-based 3D concrete printing (3DCP). The anisotropic material strength is studied in the three orthogonal material planes, then suitable failure criteria are considered, and a novel modified Mohr-Griffith criterion is proposed. X-ray computed tomography (CT) is employed to explore the microstructural morphology (pore size, shape, orientation, and total porosity content), fracture surface angle, and fracture surface area of 3DCP inter and intralayers compared to specimens cast from the same FRPC mixture. A mechanistic evaluation of the constant compression-shear performances relates the ensuing shear strength to the microstructural morphology observed in the experimentally assessed samples. Thereby, this contribution provides the basis for a fundamentally more detailed understanding of the hardened-state mechanical capacity of 3DPC, which is supported

by a novel failure criterion and solid theoretical explanations of the influential microstructural features affecting the mechanical characteristics. Finally, it is postulated that improved mechanical performance and reduced anisotropy, conjuring less material complexity and uncertainty, is permitted by stabilising the microstructural morphology in 3DPC.

Highlights:

- The constant compression-shear performance of 3DCP specimens is evaluated
- 3DCP elements display non-linear anisotropic behaviour over the entire experimental regime
- A modified Mohr-Griffith failure criterion with a material scaling factor is proposed and validated
- Strength is related to porosity, pore topology, and orientation w.r.t the imposed stress state
- Enhanced mechanical performance is permitted by void stabilisation

Keywords: 3D concrete printing; Griffith failure criterion; Porosity metrics; void topology; mechanical characteristics

6.1 Introduction

The mechanical characteristics of 3D printable concrete (3DPC) mixtures exhibit a strong dependence on the employed extrusion-based process [1–7], material rheological [1,8–10], design [9,11–15], reinforcement [16–23], fabrication parameters [4,5,15,24–31], and curing conditions [11,32] and are therefore predominantly anisotropic by nature. Regarding such a fact, many investigations have sought to attain the anisotropic material properties of 3DPC mixtures utilising a variety of methods over an array of loading spectra [4,13,16,26,31,33–42]. Additionally, it has been shown that at the heart of the observed mechanical anisotropy lies the microstructural topology of the manufactured component [43]. To extend the experimental database on the hardened state material properties, this research aims to quantify the constant compression-shear capacity of a fibre reinforced printable concrete (FRPC) mixture via a DST methodology and propose a suitable failure criterion based on the experimentally attained results.

Failure criteria are established to identify the maximum utilisable strength of a material for design purposes. Hence, it is imperative that a suitable criterion be selected, specific to the material and associated microstructural mechanics of the object under consideration. Consequently, design efficacy is dependent on the extent to which modes of failure and the degree to which the magnitudes and distributions of stresses and strains can be numerically or computationally predicted under specific loading regimes and geometric configurations [44]. It can indeed be argued that for 3DCP to be adopted as a widespread construction manufacturing technology, a fundamentally deepened understanding of the material microstructural, strength, and failure characteristics are required. It is envisaged that with amplified knowledge pertaining to the hardened-state micromechanics of 3DPC materials, more

suitable constitutive relations can be developed and utilised, which permits well-calibrated numerical and computational simulation strategies to be established for high accuracy modelling. In turn, this would enable and expedite the development of optimised yet rational design procedures that harness the full potential and indeed deliver the acclaimed benefits of this automated construction methodology [45–49].

The Mohr-Coulomb failure criterion, a combination of the efforts presented by Mohr and Coulomb [50], is the most often implemented failure criterion in civil engineering applications since it is well adapted to characterise the modes of failure encountered in intact isotropic solid materials, such as soil, rock, and concrete [51]. An expanded version of the Mohr-Coulomb failure criterion, including time-dependent development of the material properties, based on the DST, has been investigated as a potential method to measure the rheological parameters of 3DCP mixtures and is proven applicable to 3DCP in the fresh state [52–54]. Additionally, in the hardened condition, it is found that the Mohr-Coulomb criterion performs best under total compressive principal stress states when the uniaxial compressive capacity (f_c) is significantly larger than the uniaxial tensile capacity (f_t), e.g., $f_c/f_t > 10$ [55]. The Mohr-Coulomb failure criterion, Eq. (6.1), relates the shear stress (τ) to the effective normal stress (σ_n) at failure, given the internal friction angle of the material (φ) and intrinsic resistance to shear or cohesion (c) as illustrated in Fig. 6.1. The Mohr-Coulomb criterion predicts failure in planar applications based on the condition of major (σ_I) and minor (σ_{III}) principal stresses and disregards the effect of the intermediate principal stress (σ_{II}).

$$\tau = \sigma_n tan\varphi + c \tag{6.1}$$

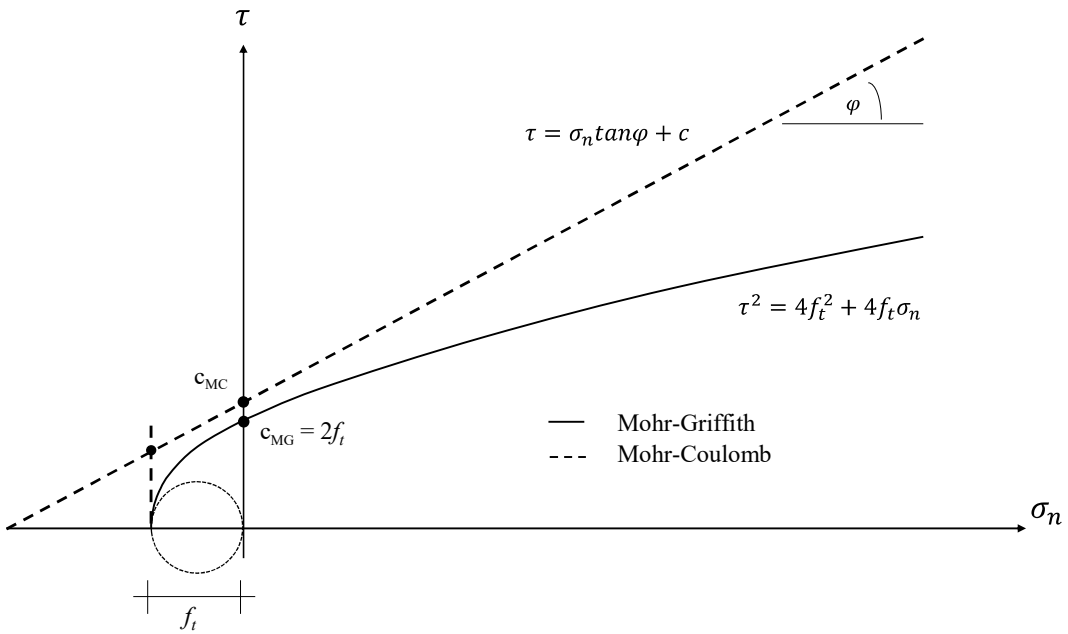

Fig. 6.1: Various failure criteria considered for isotropic materials.

However, a linear relationship between compressive normal and shear stress states is not always portrayed in experiments [56] and Mohr's general expression of the failure envelope, $\tau = f(\sigma_n)$, could be more appropriate since it can take on a non-linear form. Moreover, it is nonphysical to admit a frictional resistance under a tensile normal stress state. Ensuing this notion, tension cut-off formulations have been proposed, which retain physical validity while the average normal stress ($\sigma_m = \frac{1}{2}[\sigma_I - \sigma_{III}]$) remains compressive. Considering the augmented (approximately tri-axially ellipsoidal, see Fig. 6.21 and 6.22) microstructural morphology observed in 3DCP filaments [43,57–59], it is suspected that a non-linear failure criterion is required to express the compression-shear response in planar 3DCP elements such as shear walls, partition walls, framed structures, and shells. In this regard, Griffith's [60] failure theory for brittle materials is postulated to resonate with the observed failure mechanisms in 3DCP [43,57]. Here, failure is contended to initiate via tensile fracture induced by stress concentrations located around the corners of pores and micro-cracks in the material matrix [44]. Others extended Griffith's criterion to biaxial and triaxial stress states in rocks and explain the mechanisms of failure around a closed crack [44]. Murrell [61] presents an expression of a Mohr envelope, Eq. (6.2), which relates the shear stress at failure (τ) to the materials uniaxial tensile capacity (f_t) and the normal stress at failure (σ_n), as shown in Fig. 6.1. This formulation assumes that the pore retains its ellipsoidal topology until failure is initiated and that the material intrinsic shear strength (c) equals $2f_t$.

$$\tau^2 = 4f_t^2 + 4f_t\sigma_n \tag{6.2}$$

Suppose it is assumed that the pores do not retain their ellipsoidal topology and suffer excessive deformation until closure prior to failure, a modified Mohr-Griffith criterion, similar to the Coulomb-Navier criterion [44], including an internal frictional coefficient might be a more appropriate formulation for the compressive part of the described response [62]. Such a criterion follows Griffith's criterion in the tensile regime and Mohr-Coulomb's criterion in the compressive regime. Eq. (6.3) presents a numerical formulation for the described response.

$$\tau = \sigma_n tan\varphi + 2f_t \tag{6.3}$$

Most layered construction materials such as masonry, laminates, and 3DCP components display distinct directional material properties, and thus anisotropic failure criteria are sought. In this light, researchers have proposed continuum-based anisotropic constitutive relations such as the multi-surface plasticity-based Rankine-Hill formulation [63], a similar Rankine-Menétrey-William formulation [64], and a damage-based Tsai-Wu formulation [65]. Such formulations are reportedly well-calibrated to anisotropic construction materials such as masonry [63,66] and could therefore be considered in the 3DCP context [42,67]. Discrete interface element modelling presents another promising methodology to express the anisotropic mechanical characteristics observed in 3DCP components [67–69]. In the 3DCP context, these methods have been based on either traction-separation constitutive relations in

combination with a maximum stress criterion [68,69] or an elastoplastic multi-surface cap constitutive model, which includes a tension cut-off for tensile cracking, a linear Coulomb friction envelope for shear sliding, and a cap model for compressive crushing failure [67]. However, it is found that for reinforced 3DCP deep beams experiencing mixed shear-tension and shear-compression stress states, the capacity of the beam is overestimated [67]. It is postulated that the linear Coulomb friction assumption misrepresents the interfacial compression-shear constitutive behaviour exhibited in 3DCP. Thus, additional calibration of the shear model parameters is sought, forming the basis for the current investigation.

6.2 Materials & Methods

6.2.1 Fibre-reinforced printable concrete composite composition & properties

A FRPC mixture including 1 % by binder volume of polypropylene (PP) microfibres is utilised throughout this research. Detailed descriptions of the constituent types and proportions are available in [42]. The PP fibres have a length of 6 mm, a diameter of 0.03 mm, an elastic modulus of 3 GPa, and a yield strength of 300 MPa and are included to increase the fracture energy of the matrix. The binder consists of PPC 52.5 N (CEM II/A-L) normal hardening Portland-limestone cement, Chryso densified micro-silica fume, and class F DuraPozz fly-ash. The incorporated admixtures include Chryso Premia 310, a modified polycarboxylate polymer-based superplasticiser, and Chryso Quad 20, a liquid viscosity modifying agent. The sand comprises a continuously graded Malmesbury crushed granite with a maximum particle size of 4.75 mm, and the mixture has a water-cement ratio of 0.45.

The FRPC mixture displays anisotropic behaviour when loaded along principal Cartesian axes. The shear level of anisotropy (LOA) is highest at 2.43 [69], followed by a tensile LOA of 1.96 and a compressive LOA equal to 1.18 [42]. Comparable elastic properties ($E_{D1} = 21.9$ vs. $E_{D3} = 21.6$ GPa) are observed [42]. The rheological properties align with those generally utilised for 3DCP exhibiting thixotropic fresh-state behaviour with a static shear yield stress ($\tau_{S,I}$) of 2152 Pa, a dynamic shear yield stress ($\tau_{D,I}$) of 1789 Pa, as well as comparatively high reflocculation (R_{thix}) and moderate structuration (A_{thix}) rates, equal to 7.29 Pa/s and 1.13 Pa/s, respectively [42].

6.2.2 Sample preparation & configurations

Ø21.6 ± 0.1 x 20 mm cylinder specimens are extracted via core drilling from the mould-cast and 3D printed objects shown in Fig. 6.2. Care is exercised during core drilling, handling, and sawing to minimise the mechanical damage to test specimens. The printed items comprise two and four-layered specimens with a 5 m print path length and 83 s layer pass-time. The print parameters are consistent with those utilised in previous research [42,67] to ensure comparative mechanical performance and consist of a 60 mm/s nozzle velocity, 10 mm layer height, and 30 mm nominal layer width. The two-layered sample object is manufactured to evaluate the interlayer shear capacity in the extrusion (D3-x)

and transverse (D3-y) directions. The four-layer printed sample is fabricated to evaluate the intralayer shear capacity (D1). The mould-cast specimen is made from the same FRPC mixture to provide reference specimens (Cast) for the constant compression-shear experimental campaign. The sample testing configurations are presented in Fig. 6.2. Cored specimens are extracted at a 21-day curing age, from the centre of filaments, in the respective directions as shown in Fig. 6.3. The cast samples are fabricated by placing the FRPC mixture into a 400 x 400 x 20 mm mould and vibrating until the exposed surface is smooth. Final finishing is conducted with a mortar trawling paddle. The top surface of the extracted cores is surface ground to ensure that the top and bottom surfaces of the specimens are flat and parallel to one another. All specimens are air-cured in controlled environmental conditions (23 ± 2 °C and 65 ± 5 % relative humidity) and evaluated at a 28-day concrete age.

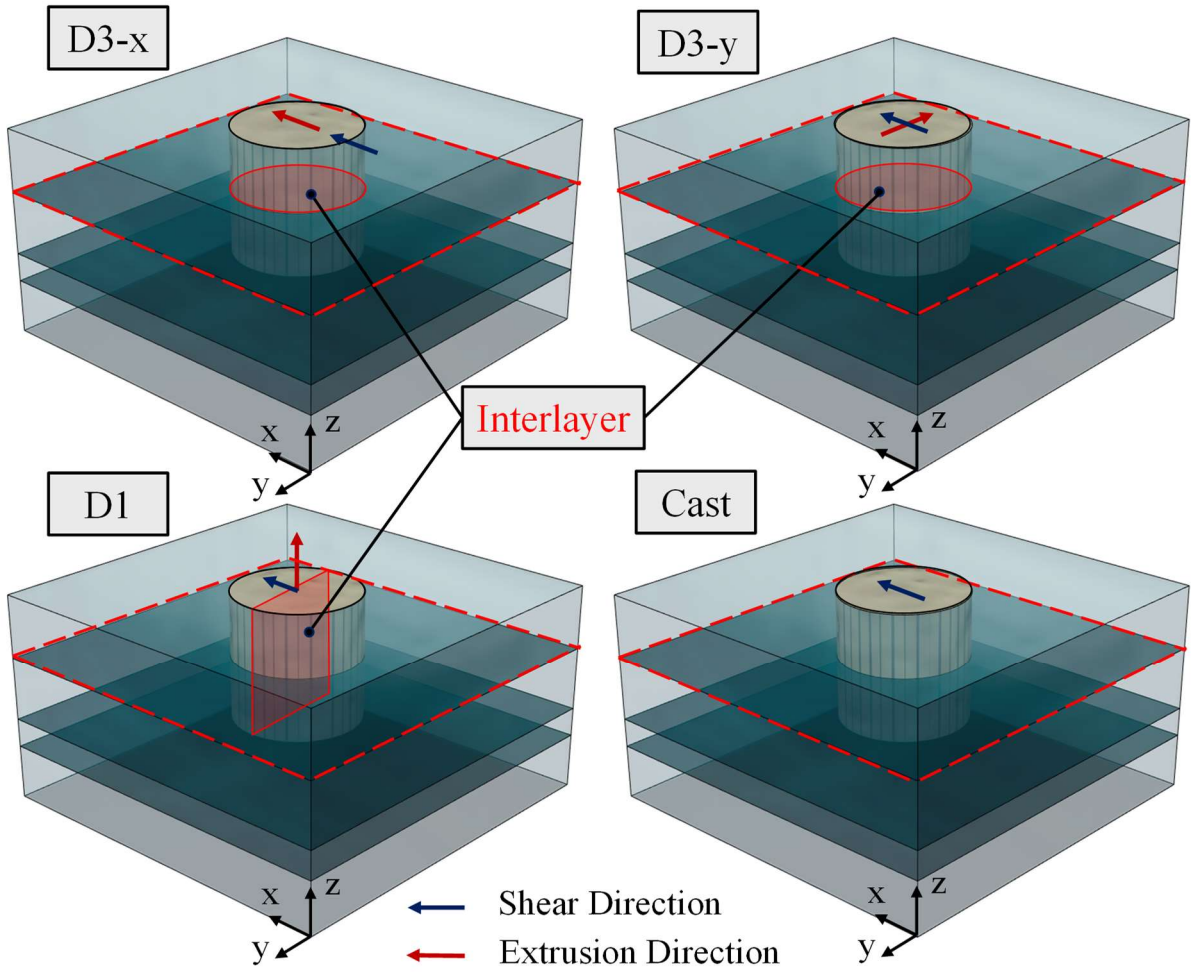

Fig. 6.2: Sample configurations assessed in the DST. For each configuration the blue arrow indicates the shearing direction, while the red arrow indicates the original extrusion direction from when the sample object was fabricated. The broken red line indicates the shear plane.

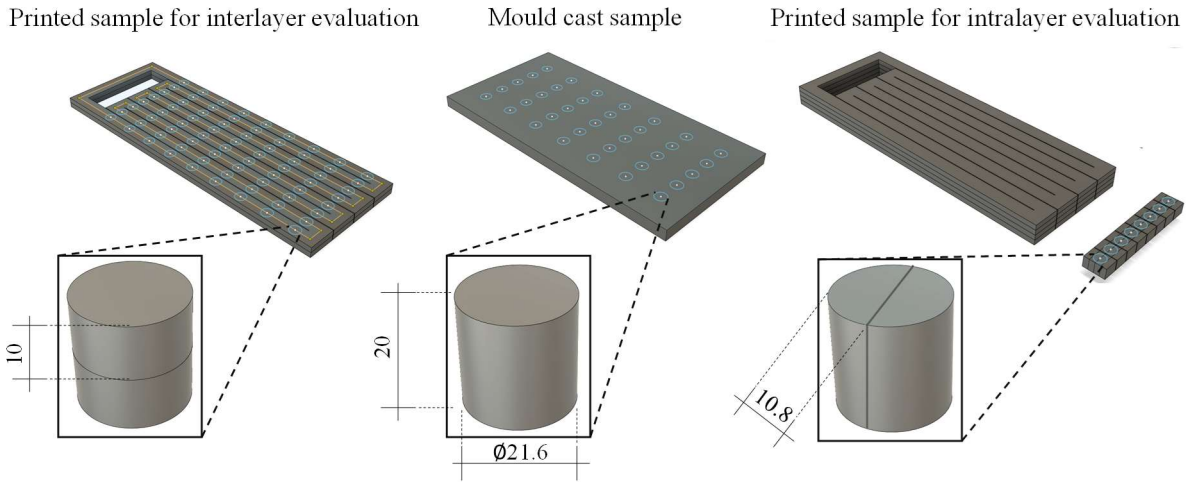

Fig. 6.3: Sample objects, illustrating from left to right the two-layer printed item for interlayer evaluation (directions D3-x and D3-y), the mould cast sample (Cast), and a four-layer printed object for intralayer evaluation (direction D1). Note all dimensions are in mm.

6.2.3 Direct shear test apparatus

The DST apparatus is illustrated in Fig. 6.4. A Digishear 27-WF2060 DST machine is utilised to apply the loading conditions described in Section 6.2.4. The horizontal shearing displacement is applied by a high-resolution stepper motor ($1x10^{-4}$ revolution increments) and a worm reduction unit. The setup is instrumented with an external digital acquisition system for load, dilation and shearing deformation, and speed determination. Two linear variable differential transducers (LVDTs) are used to measure the normal and shear displacements. The LVDTs have acceptable ranges of travel (19 mm) and sensitivities (0.0025 mm). The maximum permissible horizontal load is limited by the preinstalled 5 kN load cell. A static vertical load is imposed directly on the specimen via a load frame carrying the vertical and cantilever hangers, respectively. The vertical load can be amplified by factor 10 utilising the cantilever hanger to a maximum of 5 kN and is applied to a 5 x Ø21.5 mm circular top end cap to ensure uniform normal load application. The inner plan dimensions of the top and bottom boxes of the original shear box assembly are 60 x 60 mm. However, to be commensurate with the layer width and height specification of the sample, a modified assembly is sought. Here we provide machined top and bottom blocks of 59.8 x 59.8 x 10 mm (l x b x h) with a centred Ø21.7 ± 0.1 mm circular void where the concrete samples are inserted. A 4.5 mm spacer block is supplied above the 8.5 mm bottom endplate to ensure that the predefined shear interface aligns with the original shear box assembly at a height of 23 mm.

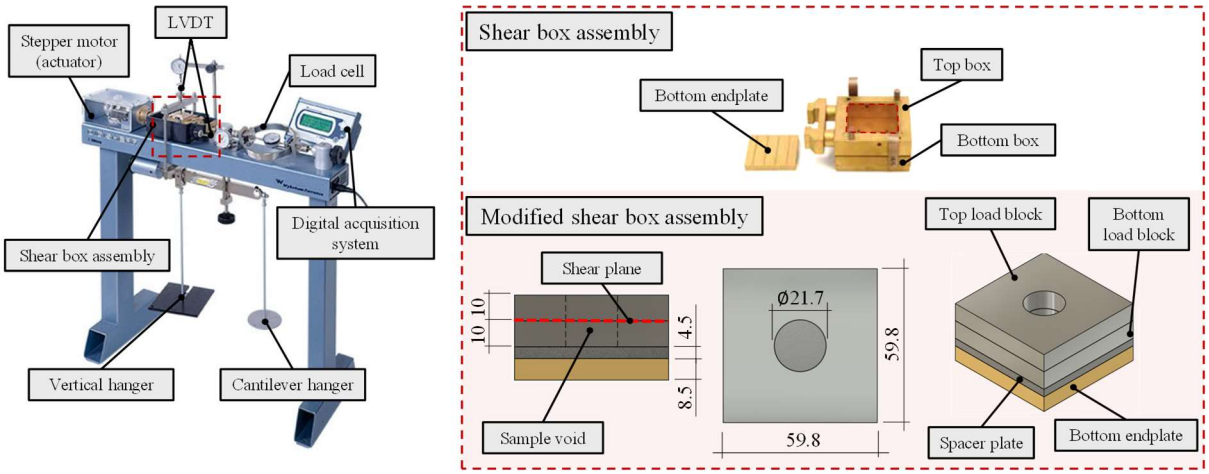

Fig. 6.4: Direct shear test (DST) apparatus, illustrating the Digishear 27-WF2060 testing machine (left), the original shear box assembly (top-right), and the modification made to the original shear box assembly (bottom-right). Note that all dimensions are in mm.

6.2.4 Direct shear test methodology

The proposed DST methodology is founded on ASTM D5607-95 [70] and considers the apparent direct shear strength of concrete specimens under a constant normal force. The ASTM D5607-95 procedure is selected for its compatibility with both intact homogenous specimens and discontinuous specimens with planes of weakness under drained conditions. It is reported that the ASTM D5607 standard can be employed to attain the shear characteristics of fibre-reinforced concrete (FRC) [71] and that it should be employed as opposed to JSCE-SF6, which is traditionally used for FRC assessment. Additionally, Tonon [71] concludes that the increase in the peak shear resistance is attributed to Mode I (tensile) mechanisms and not Mode II (shear) mechanisms in the JSCE-SF6 standard rendering its application obsolete for FRC material characteristic determination endeavours.

The term *'normal force'* is intentionally selected as opposed to *'normal stress'* since the true contact area on the shearing plane is indefinable. Given that the actual contact areas fluctuate during testing and are likely affected by interfacial defects, the nominal area is generally considered for pragmatic exposition at peak shear load points and termed the *'apparent shear strength'* [70]. However, such an assumption is rather crude since the shear stress distribution is non-uniform over the cross-sectional area. Therefore, the representative shearing area options presented in Section 6.2.5 are considered.

Table 6.1 presents the respective constant hanger mass increments considered to attain the normal to shear strength ratios of the 3DCP composite and mould cast specimens. Note that only one discontinuity can be evaluated per specimen. Therefore, four individual configurations are assessed per normal load increment. Five samples per hanger mass increment are tested; thus, 20-25 samples are extracted for each of the four configurations (95 samples in total) to ensure the reliability of the experimentally obtained DST data.

Table 6.1: Summary of constant hanger mass increments and sample configurations.

Hanger Mass Increment	Constant Normal Force	Samples per Category			
(kg)	(N)	3DCP-D1	3DCP-D3-x	3DCP-D3-y	CAST
0	0	5	5	5	5
5	491	5	5	5	5
10	981	5	5	5	5
15	1472	5	-	-	-
20	1962	-	5	5	5
30	2943	-	5	5	5
Total		20	25	25	25

Maintaining a constant normal force with respect to the predefined shear plane within the specimen, an increasing shear displacement is applied. The horizontal displacement is applied at a rate of 0.25 mm/min, and the experimental load and deformation data is continuously acquired at 10 Hz sampling rate. The dimension of each specimen is measured prior to testing to determine the nominal shear area. The test is terminated once the sample has fractured, and the peak shear and constant normal loads are recorded. The apparent shear and normal stresses can then be computed according to Eqs. (6.4) and (6.5), respectively. Additionally, the fracture surface of selected specimens from the 0 N hanger mass increment is investigated via X-ray computed tomography (CT) to ascertain quantitative evidence of the encountered asperities for surface roughness determination and interpretation. The fracture surfaces of all specimens are measured with a digital calliper to determine the fracture inclination angle (θ) for subsequent apparent nominal area adjustment as per Eq. (6.6).

$$\tau = {}^{P_s}/_{A'} \tag{6.4}$$

$$\sigma = {}^{P_n}/_{A'} \tag{6.5}$$

$$A' = \frac{A}{\cos(\theta)} \tag{6.6}$$

Parameters P_s and P_n are the peak shear and normal loads, and parameters A and A' are the nominal initial and adjusted cross-sectional areas of the circular shear plane.

6.2.5 Direct shear test stress distribution

It is appreciated that the shear stress distribution over the predefined shear plane is non-uniform and in an elastic continuum follows a trend similar to that presented by the solid black line in Fig. 6.5. Here the maximum shear stress is expressed by Eq. (6.7). Eq. (6.8) gives a parabolic function for the shear stress as a function of position over the shear plane.

$$\tau_{max} = \frac{4P_s}{3\pi R^2} \tag{7}$$

$$\tau(x) = \left[\frac{-4P_s}{3\pi R^4}\right] x^2 + \frac{4P_s}{3\pi R^2} \tag{8}$$

Here parameter R represents the radius of the shear plane, and parameter x represents the position on the shear plane.

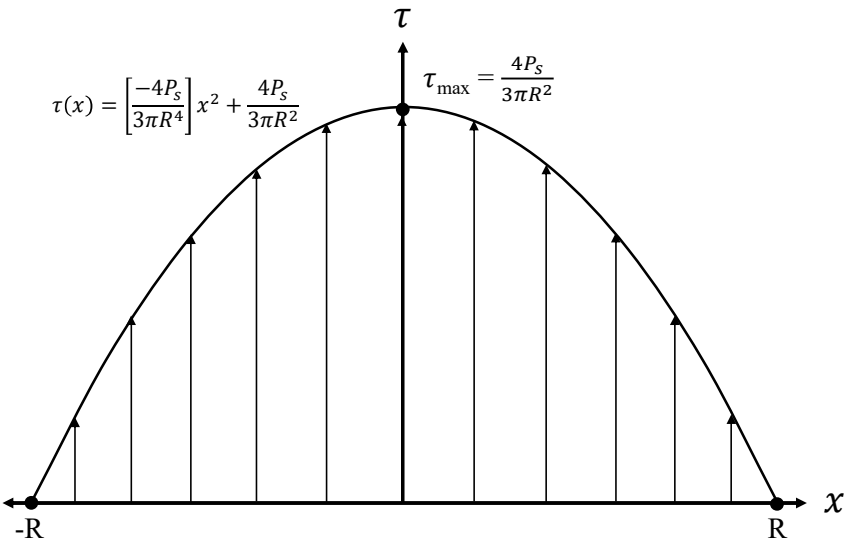

Fig. 6.5: Shear stress distribution over circular cross-sections in an elastic continuum.

Knowing that quasi-brittle materials such as the FRPC mixture utilised in this research are subject to a non-linear hardening brought by the formation and coalescence of micro-cracks before the global cross-sectional peak strength is reached, the assumption in Fig. 6.5 is technically also inaccurate.

6.2.5.1 Numerical study of DST stress distribution and evolution

A 3D non-linear FE analysis is conducted on the 3DCP D3-x loading scheme in the DIANA FEA software package to elucidate the resulting stress states encountered in the particular DST utilised in this research. Displacement based analyses are conducted at 0 N and 5000 N constant normal force increments, respectively. The FE analysis employs the geometric configuration and boundary conditions presented in Fig. 6.6. An interfaced-based micro-modelling approach is adopted, which comprises an interface elastoplastic constitutive model for the interlayer interface material and isotropic elastic continuum elements for the intralayer material with Young's modulus (E) and Poisson's ratio (ν) equal to 21.9 GPa and 0.2, respectively. Detailed elaborations on the prescription of model parameters can be found in [67]. The material properties utilised in the FE analyses are given in Table 6.2 and are attained from [42,69] and implemented in [67] with good agreement to the experimental results.

The 3D continuum elastic elements comprise linear 8-node brick (HX24L) and 6-node wedge (TP18L) isoparametric solid elements, whilst the 3D interface elements include a 4-by-4 node plane quadrilateral (Q24IF) and 3-by-3 node plane triangular (T18IF) elements. An elastic sliding zero tension interface connection is prescribed between the steel plate and the concrete specimen to permit rotation of the specimen within the sample void and not induce nonphysical stress fields over the sample boundaries. The prescribed displacement of 0.3 mm is applied in the negative x-direction in 200 increments. A non-linear structural analysis, which considers material nonlinearity in combination with an incremental-iterative secant (quasi-newton) BFGS solution procedure, is utilised. Energy and force convergence norms are set to 0.001 and 0.01, and a line search algorithm is employed to increase the convergence rate of the numerical analysis.

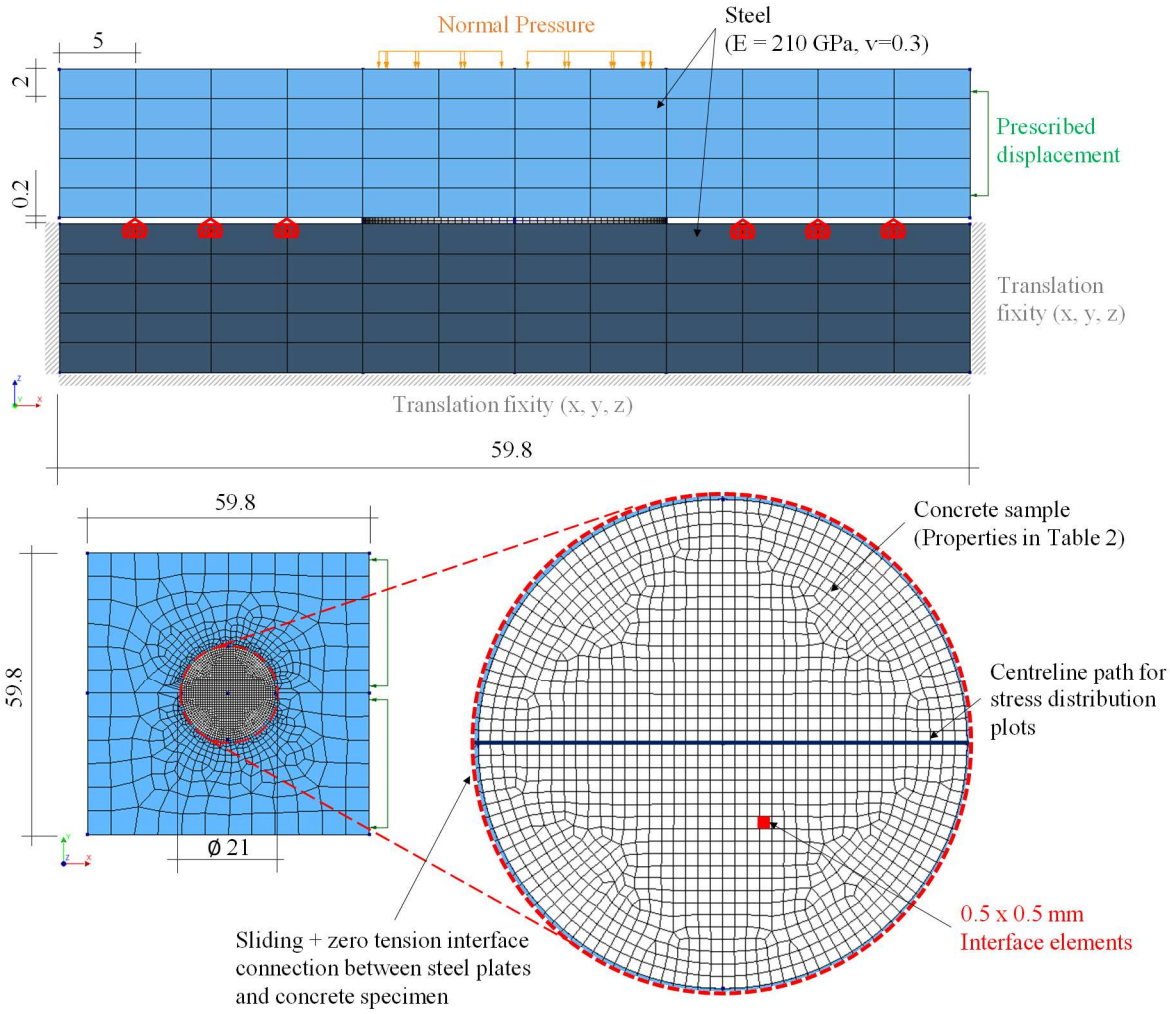

Fig. 6.6: Finite element analysis model discretisation.

Table 6.2: Input parameters for the interface-based model.

Parameter	Value	Units
Linear material parameters		
Normal stiffness modulus-z	1×10^6	N/mm^3
Shear stiffness modulus-x	4.17×10^5	N/mm^3
Shear stiffness modulus-y	4.17×10^5	N/mm^3
Combined cracking-shear-crushing parameters		
Tensile strength ($f_{t,j}$)	1.25	N/mm^2
Tensile fracture energy ($G^I_{f,j}$)	0.063	N/mm
Cohesion (c_c)	2.96	N/mm^2
Friction angle (φ)	36.87	degree
Dilatancy angle (ψ)	0	degree
Residual friction angle (φ_r)	36.87	degree
Confining normal stress	-1	N/mm^2
Exponential degradation coefficient	1	-
Shear fracture energy (G^{II}_{fc})	0.296	N/mm
a	0	mm
b	0.296	N/mm
Compressive fracture energy (G_{cc})	26.17	N/mm
Shear stress contribution to compressive failure ($c_{ss,j}$)	3.5	-
Compressive strength ($f_{c,j}$)	38.2	N/mm^2
Equivalent relative displacement (κ_p)	0.0096	N/mm^2

The total interface shear traction evolution in the x-direction with increasing shear displacement increments is presented in Figs. 6.7 and 6.8. In Fig. 6.7, step 4 corresponds to the maximum shear capacity of the section and a non-uniform shear traction distribution is observed. A quasi-uniform shear traction distribution is observed when the entire section has yielded (≈ steps 100 – 200). In contrast, Fig. 6.8 depicts a non-uniform shear traction distribution when a constant normal load of 5000 N is applied throughout the loading regime. Step 76 corresponds to the maximum shear capacity in this case.

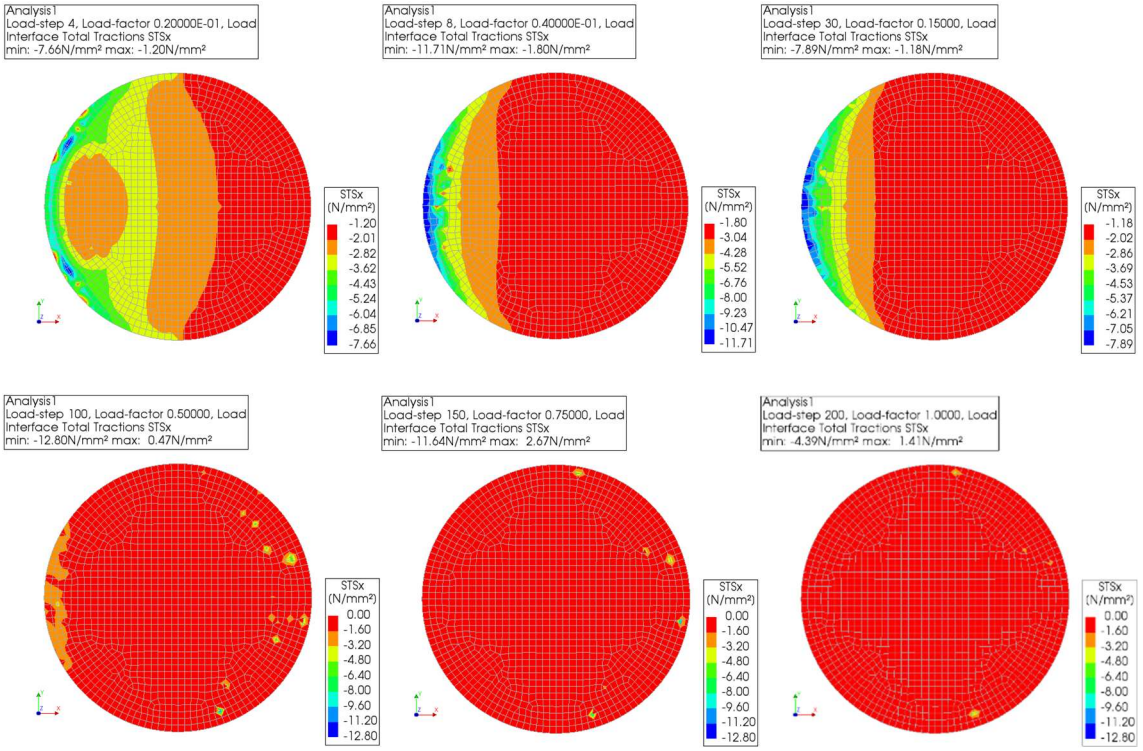

Fig. 6.7: Total shear traction (STS_x) at a 0 N constantly applied normal load.

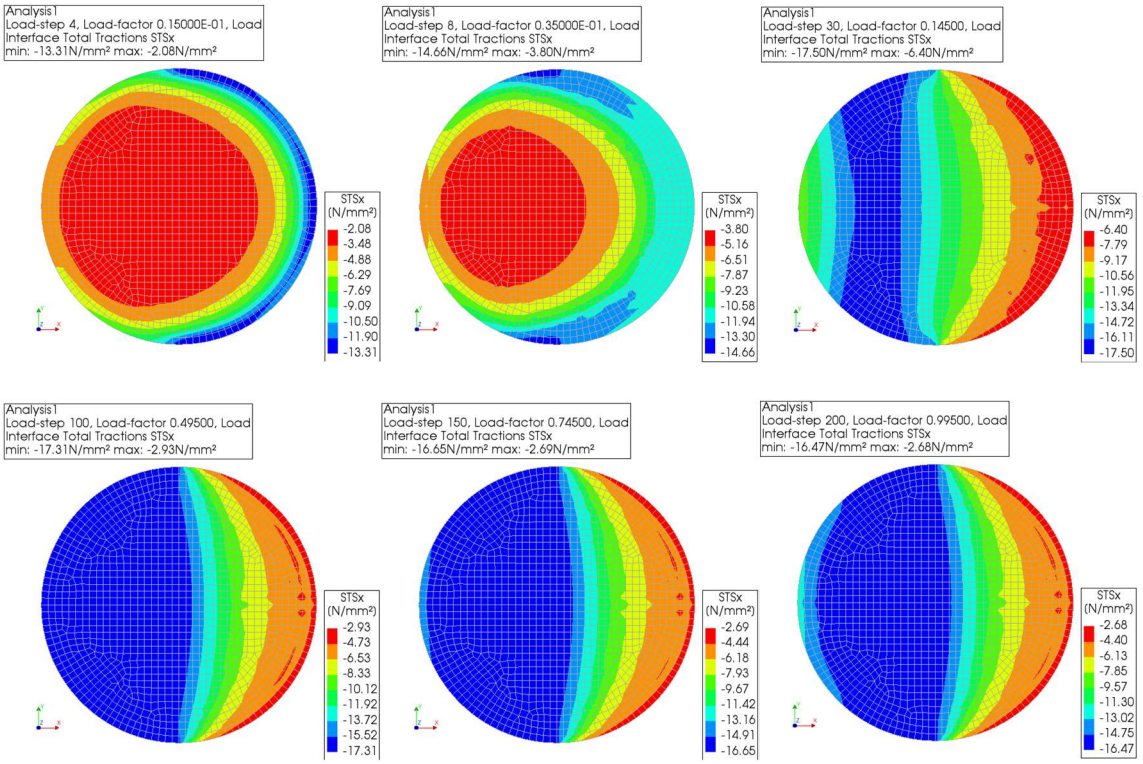

Fig. 6.8: Total shear traction (STS_x) at a 5000 N constantly applied normal load.

The normal and shear traction distributions along the centreline path (shown by the dark blue line in Fig. 6.6) are presented in Figs. 6.9 and 6.10, for a more detailed representation of the traction distributions. Here the influence of the induced bending moment is highlighted by the normal traction (STS_z) distributions, which result in greater shear tractions within the compression zone following the Coulomb friction specification.

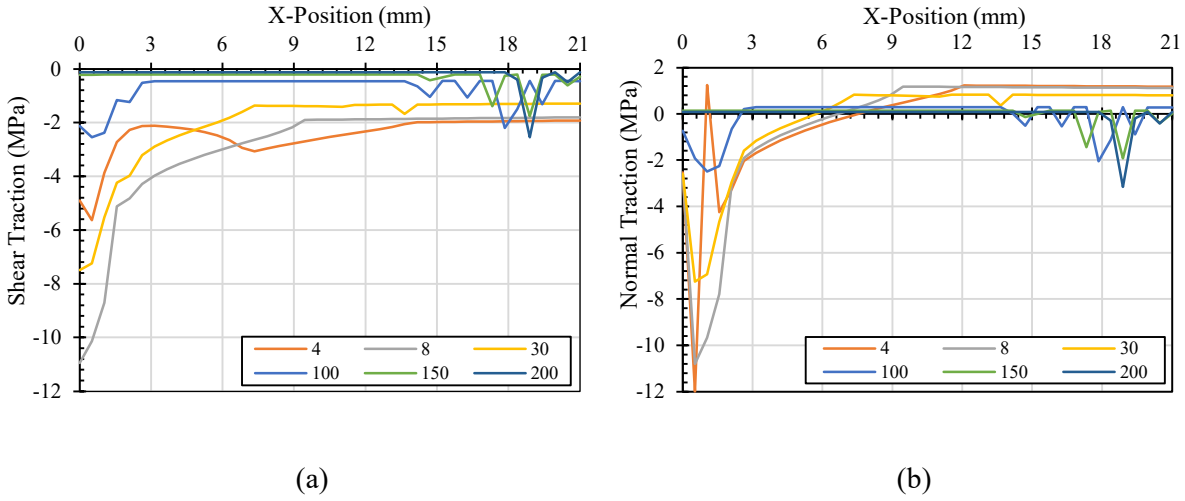

Fig. 6.9: 0 N applied constant normal load (a) Shear traction distribution and (b) Normal traction distribution as a function of position.

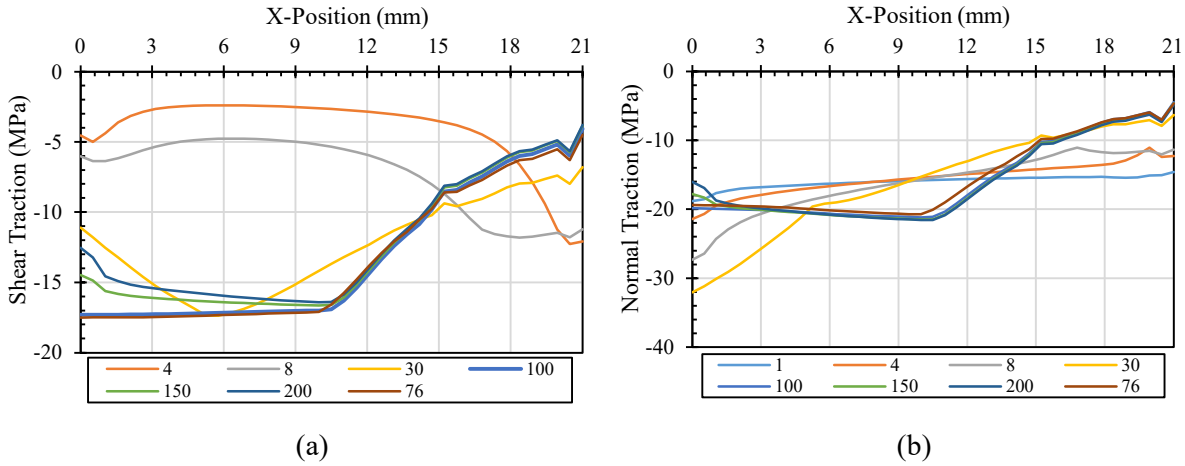

Fig. 6.10: 5000 N applied constant normal load (a) Shear traction distribution and (b) Normal traction distribution as a function of position.

However, considering the comparison between the actual and apparent shear stress distributions presented in Fig. 6.11 it is deduced that the assumption of a uniform apparent shear stress distribution (i.e., the total reaction force divided by the initial cross-sectional area) yields satisfactory agreement with the average actual shear stress distribution obtained by summing and averaging the shear tractions at individual material points (nodes) on the shear plane. From such observation, it is contended that for the macroscopic interpretation of the far-field stress state in the employed DST methodology, an

apparent shear capacity is a suitable assumption to evaluate the capacity of the shear plane. This conclusion aligns with those made by Tonon [71].

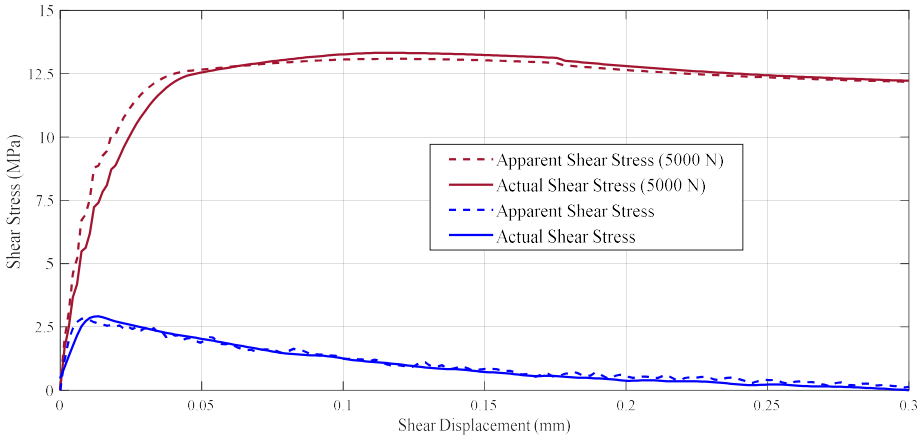

Fig. 6.11: Numerical comparison of average actual vs. apparent shear stress as a function of horizontal shear displacement.

It should be noted that the microstructural morphology of the shearing plane is porous and contains macro pores produced by the casting and embodied extrusion-based 3DCP process, which alters the effective cross-sectional area, as illustrated in Fig. 6.19. Considering the above notion, it is set forth that the cross-sectional area of the shear plane could be eliminated from the expression of shear to normal strength. Instead, only the shear and normal forces could be considered when evaluating the compression-shear performance via a DST. This is substantiated by the fact that both compressive and shear force components act on an identical cross-sectional area irrespective of the geometric or microstructural defects that could occur.

6.2.6 X-Ray CT scanning methodology

X-ray computed tomography [72,73] is performed with a Nanotom S system using 120 kV and 130 µA for X-ray generation, at a voxel size of 20 µm. A total of 2400 images are recorded in a full rotation of the sample, which is used to reconstruct a volumetric dataset using Datos reconstruction software. Visualization and quantitative analysis are performed in Volume Graphics VGSTUDIO MAX 3.5, providing information on pores in the sample larger than 8 voxels (2 x 2 x 2 in three orthogonal axes), with methods described below.

An initial adaptive Gauss filter was applied to remove noise, followed by a manual registration of the sample in the XYZ coordinate axes (samples are scanned at an angle to minimize image artefacts). A surface determination function was used with a regular automatic threshold, based on the grey values of the background and the concrete (midpoint was used as the threshold). This allowed a simplified porosity evaluation using the custom defect mask method, including only internal pores (no porosity connected to the surface). Statistical information on pore sizes and shapes are recorded in a CSV file.

It should be noted that the method used for regular thresholding segmentation combined with the relatively large voxel size of 20 µm allows minimum pore sizes of 40 µm to be quantified. Therefore, the porosity values would be lower than expected for concretes scanned at a higher resolution but directly comparable with each other in this study due to identical settings and methodology within this set of results.

For angle measurements of the fracture surface, best-fit planes were used on the top (flat surface) and the fracture surface. Several points were randomly selected to define a mean plane, from which an angle is measured between the two planes, as shown in Fig. 6.18.

The fracture surface itself was selected by using a circular region of interest covering the entire height of the fracture surface and using a combination of morphological tools to allow measurement of only the fracture surface area, removing a small area near the cylindrical surface. This surface area is determined using the properties tab of VGSTUDIO after appropriate surface determination of the fracture surface alone (without cylindrical surfaces or pore spaces), as shown in Fig 6.19.

6.3 Results & Discussions

This section presents the DST results of the experimental campaign for the respective sample configurations. Initially, the peak shear resistance relative to the applied constant normal load increments is offered, which serves as a quantitative means for evaluating the proportional mechanical resistance and evolution with increasing constant normal loading. Note that a force-based comparison is permitted by the negligible sample geometric variation, where diameter variances are within 0.1 mm (0.46 %) following the meticulous sample preparation procedure presented in Section 6.2.2. X-ray CT scanning results provide quantitative information pertaining to the hardened-state microstructural morphology of the FRPC mixture, as well as the resulting fracture surface angle and the tortuosity of the fracture surface area. Thereafter, the force-based results are transformed to representative apparent stress conditions and the pure tensile capacities are superimposed to the experimental dataset. The pure tensile capacities are attained from a previous study [42]. Subsequently, the microscopic pore structure is related to the observed mechanical response and appropriate constitutive relations are evaluated. Finally, this section elucidates the physical implications of the attained non-linear constant compression-shear response and proposes potential remedies.

6.3.1 Shear resistance at increasing constant normal load

6.3.1.1 3DCP-D1

The 3DCP-D1 DST results are presented in Fig. 6.12 and summarised in Table 6.3. The results portray a maximum coefficient of variation (CoV) of 13.49 % under pure shear, reducing to a minimum CoV of 9.28 % at hanger mass increment 15. The results are best described by a second-order

polynomial regression (green, $R^2 = 0.983$) but are followed closely by a linear regression (red, $R^2 = 0.979$). An internal friction angle of 42.6 ° is observed.

Table 6.3: Summary of 3DCP-D1 DST results.

Hanger Mass Increment (kg)	0	5	10	15
Average Normal Force (N)	0	491	981	1472
Average Shear Force (N)	2701	3334	3604	4115
CoV (%)	13.49	12.89	11.89	9.28

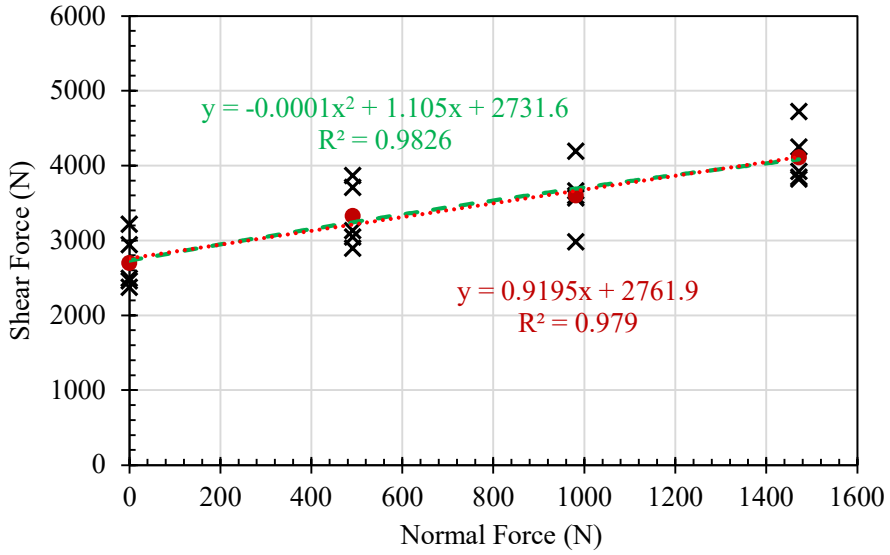

Fig. 6.12: 3DCP-D1 shear force vs. increasing normal force increments.

6.3.1.2 3DCP-D3-x

The 3DCP-D3-x DST results are presented in Fig. 6.13 and summarised in Table 6.4. The results portray a maximum coefficient of variation (CoV) of 19.34% at hanger mass increment 5 and a minimum CoV of 6.53% at hanger mass increment 10. It is inferred that this sample configuration is generally more susceptible to variation at lower hanger mass increments. The shear-normal force results are best described by a second-order polynomial regression (green, $R^2 = 0.979$) and are substantially less suitably resembled by a linear regression (red, $R^2 = 0.850$). An internal friction angle of 44.9 ° is observed. The portrayed dissimilarity in regression analyses indicates that the shear resistance of the interlayer region subject to shear fracture along the extrusion direction deviates from the commonly assumed linear increase with increasing normal load following the Mohr-Coulomb failure criterion. Such observation affirms the hypothesis of this investigation and aligns with the conclusions presented in [67], where the shear capacity in reinforced 3DCP elements is overestimated employing the material properties attained in [42] as presented in Fig. 6.25.

Table 6.4: Summary of 3DCP-D3-x DST results.

Hanger Mass Increment (kg)	0	5	10	20	30
Average Normal Force (N)	0	491	981	1962	2943
Average Shear Force (N)	1569	2441	3094	3563	4235
CoV (%)	10.56	19.34	6.53	8.93	8.16

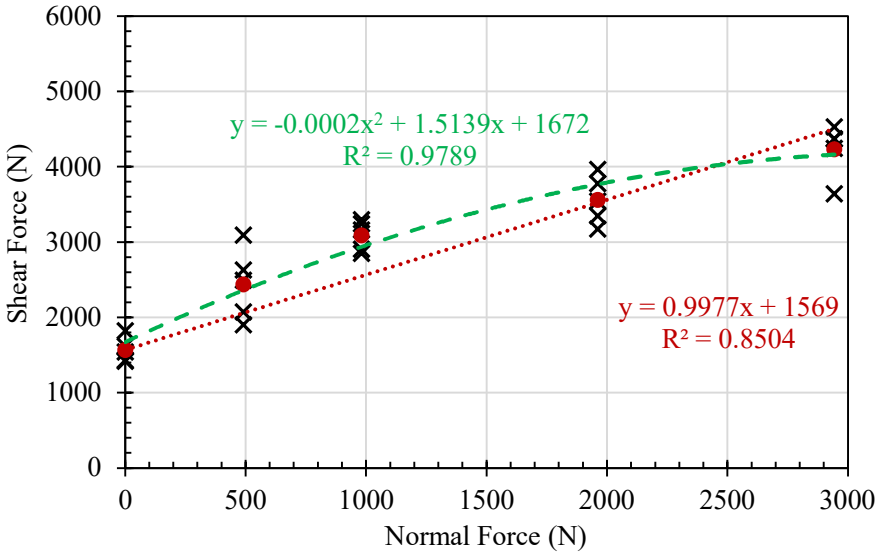

Fig. 6.13: 3DCP-D3-x shear force vs. increasing normal force increments.

6.3.1.3 3DCP-D3-y

The 3DCP-D3-y DST results are presented in Fig. 6.14 and summarised in Table 6.5. The results portray a maximum coefficient of variation (CoV) of 17.8 % in pure shear and a minimum CoV of 3.74 % at hanger mass increment 30. This sample configuration is also more susceptible to variation at lower hanger mass increments. The shear-normal force results are again as in 3DCP-D3-x and 3DCP-D1 best described by a second-order polynomial regression (green, $R^2 = 0.993$) and are less suitably resembled by a linear regression (red, $R^2 = 0.917$). A relatively high internal friction angle of 45.9° is observed. Deviance from the conventionally assumed Mohr-Coulomb failure criterion is evident but to a lesser degree than exhibited in 3DCP-D3-x. Such observations are contended to be correlated to the microstructural morphology, specifically the 3D void topological attributes and orientation concerning the loading direction since the average porosity content at the interlayer location is consistent for both 3DCP-D3-x and 3DCP-D3-y [43,57].

Table 6.5: Summary of 3DCP-D3-y DST results.

Hanger Mass Increment (kg)	0	5	10	20	30
Average Normal Force (N)	0	491	981	1962	2943
Average Shear Force (N)	1929	2796	3126	4221	5124
CoV (%)	17.80	14.19	14.50	7.20	3.74

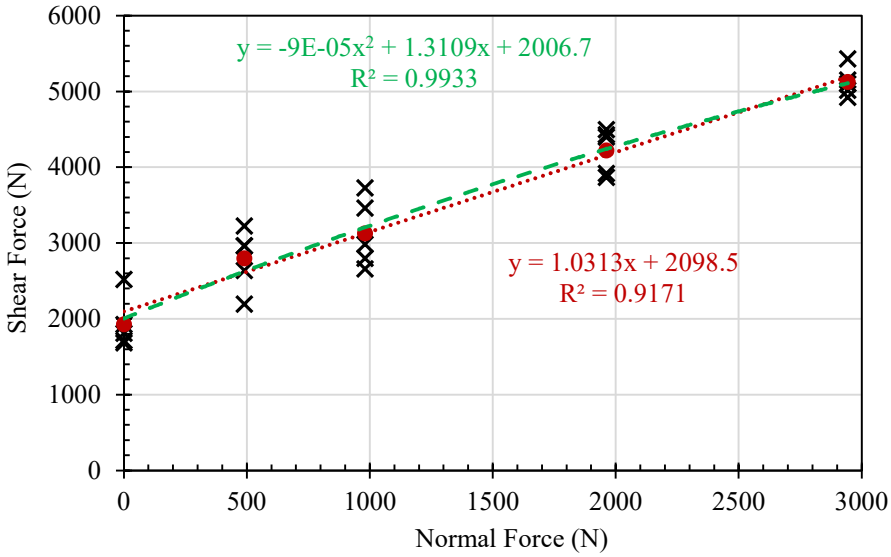

Fig. 6.14: 3DCP-D3-y shear force vs. increasing normal force increments.

6.3.1.4 Cast

The cast DST results are presented in Fig. 6.15 and summarised in Table 6.6. The results portray a maximum coefficient of variation (CoV) of 12.99 % in pure shear, reducing to a minimum CoV of 5.09 % at hanger mass increment 30. Clearly, the cast sample configuration is likewise more susceptible to variation at lower hanger mass increments. The shear-normal force results are more aptly described by a second-order polynomial regression (green, $R^2 = 0.985$) and are marginally less duly resembled by a linear regression (red, $R^2 = 0.945$). The similarity in the regression analyses is contended to stem from the more rounded (compact) void topological configuration observed in cast specimens that have not undergone pumping and extrusion processes. An internal friction angle of 44.7 ° is observed. In the current investigation, the shear strength performance of cast specimens is lower than expected due to the increased porosity, as presented in Table 6.9.

Table 6.6: Summary of Cast DST results.

Hanger Mass Increment (kg)	0	5	10	20	30
Average Normal Force	0	491	981	1962	2943
Average Shear Force	1509	2209	2867	3472	4584
CoV (%)	12.99	10.70	9.51	6.28	5.09

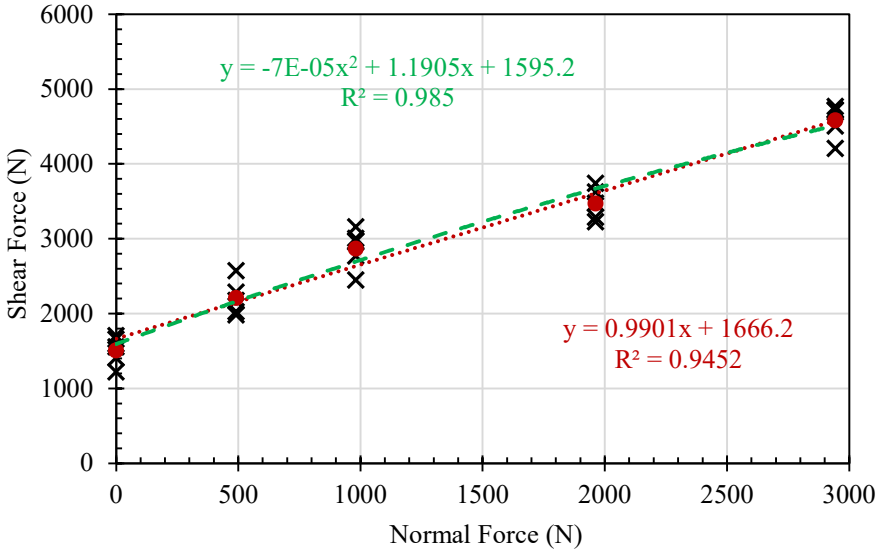

Fig. 6.15: Cast specimens shear force vs. increasing normal force increments.

The reduced shear strength variance observed at larger hanger mass increments for all samples configurations is postulated to originate from the dilatancy constraints imposed by the increased normal loading. Increased confinement of dilatant uplift stabilises the shear fracture plane and results in the mechanical shearing of surface asperities resulting in a less tortuous fracture path and thus reduced variation in resistance. The relatively high internal friction angles are ascribed to the tortuosity of the fracture surface, where crack propagation is intermittently halted and redirected at the interface between microstructural features, such as aggregate grains and critically size and orientated encapsulated pores.

6.3.2 X-ray CT scanning results

The X-ray CT scanning results obtained employing the methods presented in Section 6.2.6 are presented for three arbitrarily selected specimens per sample configuration in Section 6.2.2 at the 0 N normal force increment. Table 6.7 provides a summary of the porosity content, measured fracture surface angle, and fracture surface area results, respectively. Porosity measurements exclude capillary and colloidal porosity because of the CT scanning resolution. Additionally, the two samples that omit fracture surface angle and area quantities where not fully fractured (i.e., still bound by the PP microfibres) rendering image processing impossible according to the procedure employed for the remainder of the samples.

Cast samples portrayed the highest average porosity equal to 6.6 %, while all printed samples exhibited average porosities equal to 0.87 %. Following the works presented by Castro et al. [74], the observed 5.73 % increase in average porosity affirms the reduced shear capacity shown by cast samples in Sections 6.3.1 and 6.3.3. In a prior study, cast samples comprised reduced average porosity and increased mechanical resistance compared to 3DCP samples [43]. The observed increase in porosity is

contended to originate from the high viscosity of the FRPC mixture, which more readily entraps air voids. Printed samples displayed significantly less porosity compared to the 10.8 % observed in [43]. However, although both studies employ a voxel size of 20 μm, different instrumentation was used in the respective studies, rendering only qualitative comparisons feasible. Nevertheless, the porosity content in the samples in this study is significantly lower and pores are smaller, leading to the lower porosity values quantified here. Fig. 6.16 provides a visual illustration of the observed changes in the microstructural porosity characteristics between these two studies and elucidates the increased strength witnessed in the DST experiments. Additionally, the consistent average porosity measurements for 3DCP samples substantiates that, in addition to porosity content, the pore size, shape, and orientation relative to the induced stress state also dictates the mechanical capacity of 3DCP specimens in the presented experimental campaign. Elaborate discussion of the underlying theories pertaining to this assertion is presented in Section 6.3.3.2.

Table 6.7: Summary of X-Ray CT scanning results.

Sample	Porosity (%)	Fracture surface angle (degrees)	Fracture surface area (mm^2)
Cast-0-1	6.0	8.9	551
Cast-0-6	6.9	2.9	515
Cast-0-3	6.9	-	-
3DCP-D1-0-1	0.8	4.4	437
3DCP-D1-0-5	1.0	2.6	458
3DCP-D1-0-6	0.8	7.0	503
3DCP-D3-x-0-1	1.4	8.0	426
3DCP-D3-x-0-3	0.8	8.4	468
3DCP-D3-x-0-4	0.4	9.4	420
3DCP-D3-y-0-2	0.9	-	-
3DCP-D3-y-0-3	1.0	4.1	477
3DCP-D3-y-0-4	0.7	0.6	489

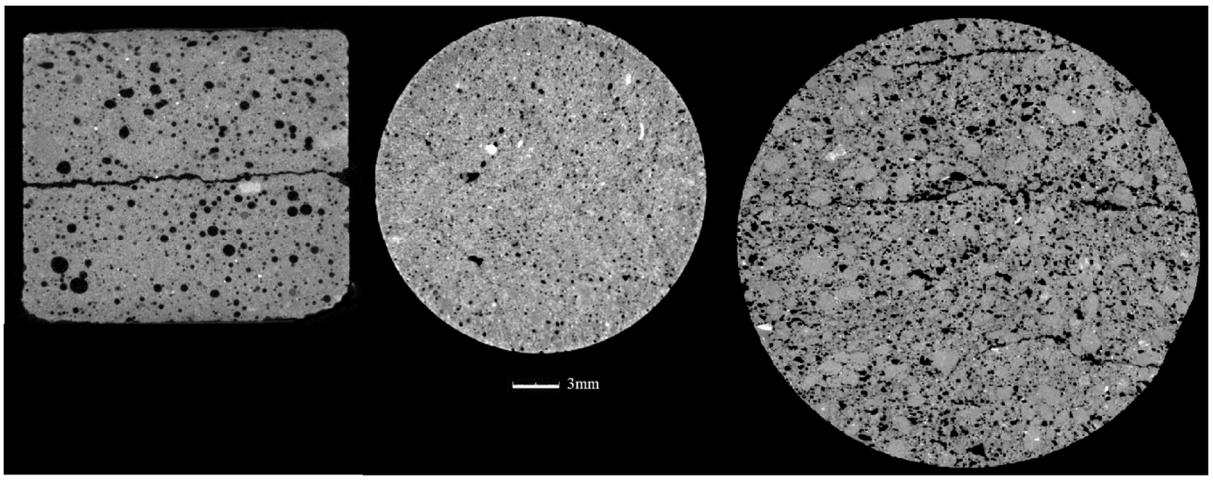

Fig. 6.16: Visual comparison of microscopic pore structure attained via X-ray CT scanning, illustrating (left) a cast specimen, (centre) a 3DCP-D1 specimen from the current investigation and (right) a 3DCP-D1 specimen from [43]. *The illustration scale is according to the sample geometric dimensions, making the scale bar applicable to all images and the observed sizes of pores comparable.*

6.3.2.1 Pore size distribution

The pore size distributions obtained via X-ray CT scanning are presented in Fig. 6.17. It is shown that cast specimens comprise an increased number of pores with equivalent diameters larger than 0.2 mm. The maximum noteworthy pore size bin is 1.25 mm. 3DCP samples display a smaller number of pores with equivalent diameters greater than 0.2 mm and portray maximum noteworthy pore size bins of 0.7 mm (3DCP-D1), 0.725 mm (3DCP-D3-x), and 0.8 mm (3DCP-D3-y), respectively. These observations align with the porosity measurements reported in Table 6.7 and provide critical insights pertaining to the size of pores in the respective sample configurations.

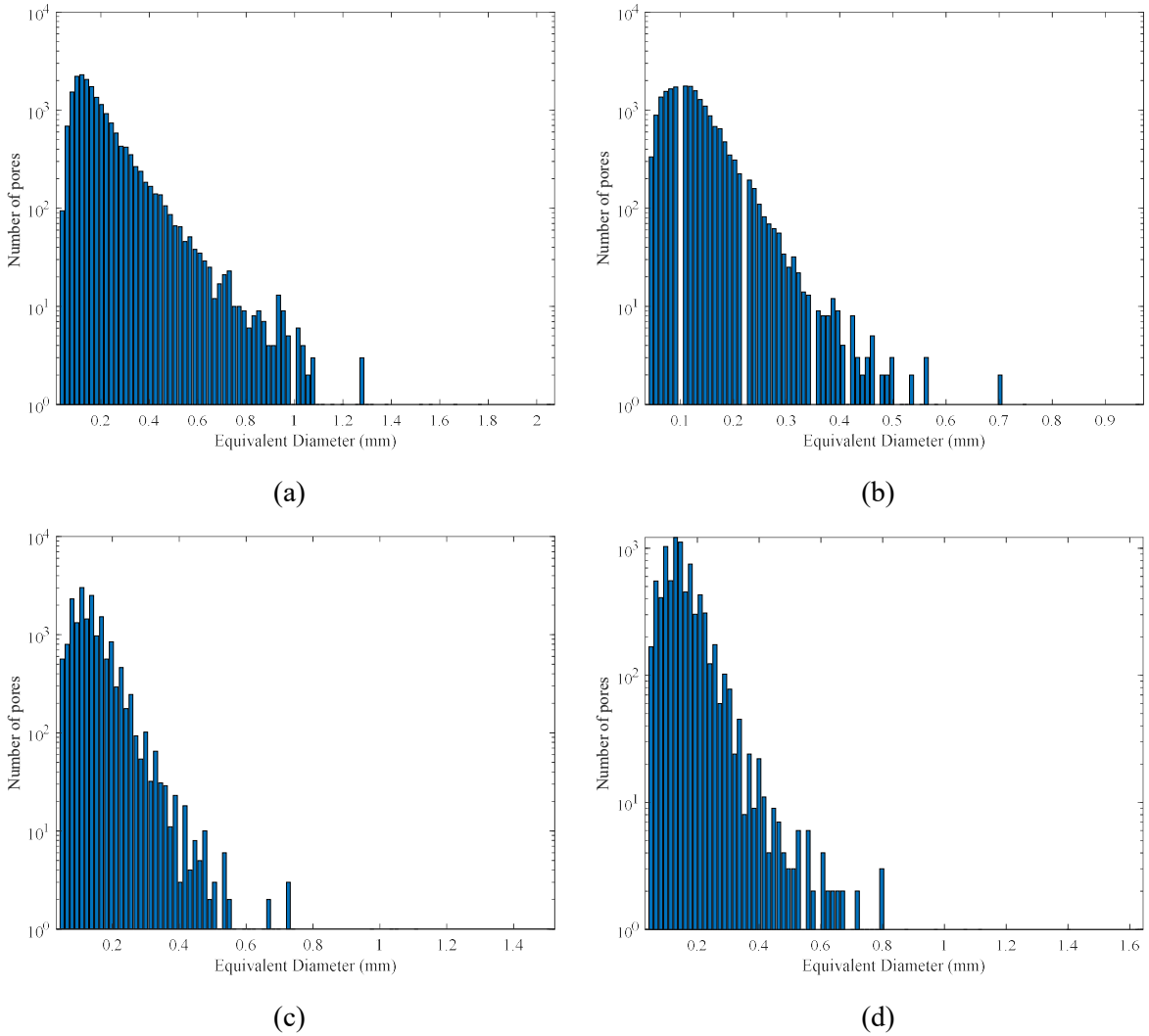

Fig. 6.17: Pore size distribution providing the number of pores versus the equivalent diameter of pores, for (a) Cast, (b) 3DCP-D1, (c) 3DCP-D3-x, and (d) 3DCP-D3-y, respectively.

6.3.2.2 Fracture surface angle

Mean fracture surface angles are provided, as determined in Fig. 6.18, and illustrate the effects of the non-uniform stress distributions presented in Section 6.2.5.1. The perceived acuity of the fracture

surface angles imposes marginal effects on the apparent fracture surface area, showcasing a maximal increase of 1.36 % for 3DCP-D3-x-0-4.

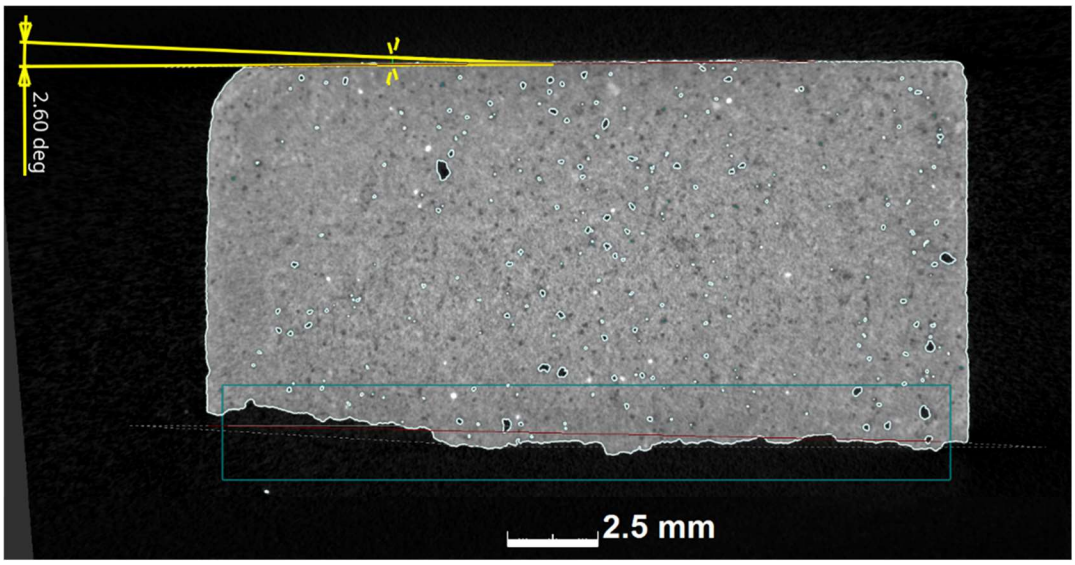

Fig. 6.18: Fracture surface angle determination. Best fit plane indicated by the red line in the cyan box. The illustration depicts sample 3DCP-D1-0-5.

6.3.2.3 Fracture surface area

Visual illustrations of the fracture surfaces are presented in Fig. 6.19. The tortuous nature of the fracture surface is graphically illustrated and corroborated by the large fracture surface area measurements presented in Table 6.7 compared to the apparent area equal to 366 ± 3 mm^2. The spatial undulation is a result of the microstructural morphology of the fracture surface. The increase in the fracture surface area is contended to affect the experimentally attained shear strength and friction angle. However, the local stress state at pore boundaries is subject to the stress contours shown in Figs. 6.7 and 6.8, resulting in localised yielding, load attenuation, and subsequent stress redistribution characteristic to quasi-brittle materials.

Moreover, the fractional volume of critically sized pores within the pore size distribution on the fracture plane is known to influence the effective area and thus the resistance and mechanisms of fracture propagation [75]. However, such information is arduous to ascertain for non-planar surfaces and extends the scope of the current investigation. Therefore, no strength adjustment is made to the experimentally attained results, but these results should be considered an upper bound representation of the actual shear strength.

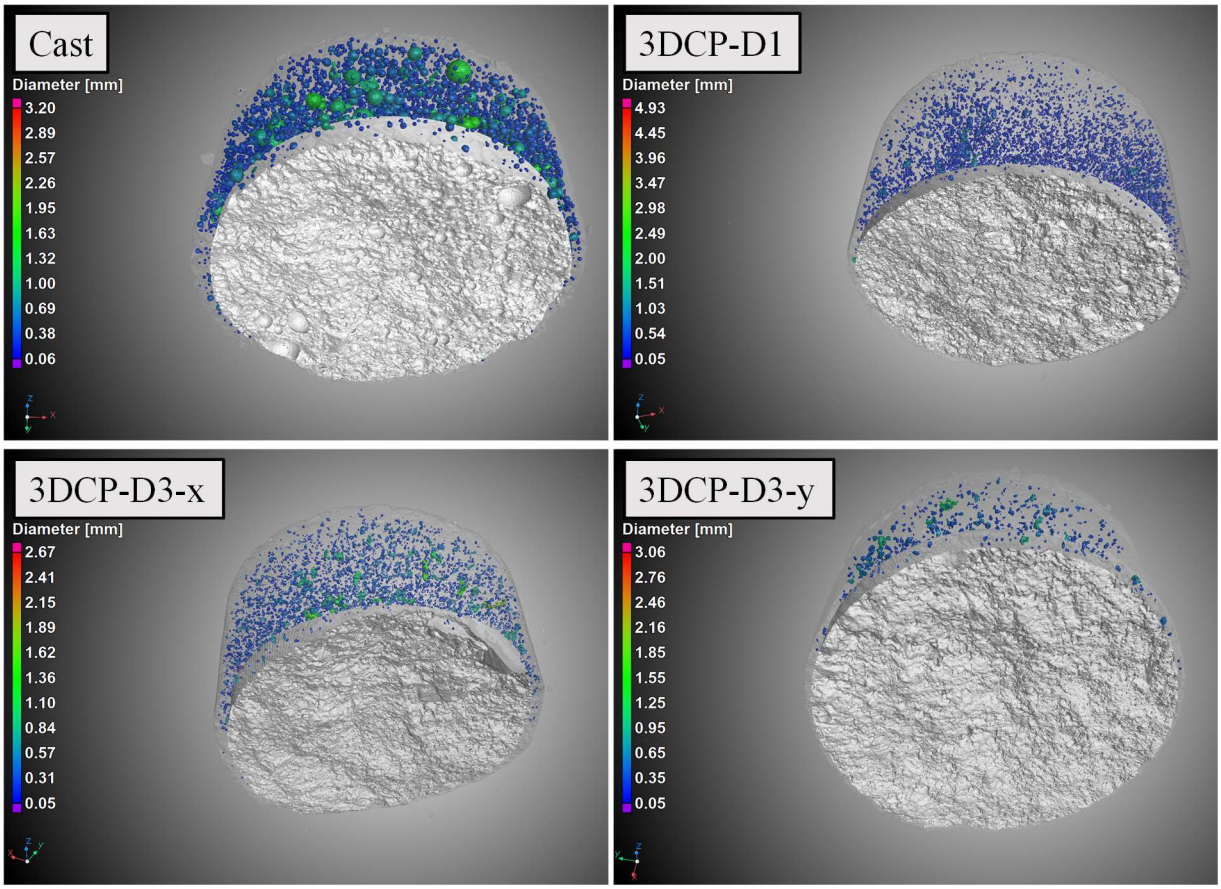

Fig. 6.19: Visual illustration of fracture surfaces.

6.3.3 Apparent shear stress transformation results

The apparent shear strength results at various normal stress increments are collectively presented in Fig. 6.20 and summarised in Table 6.8. Average shear strength values are illustrated by the coloured markers, while the solid lines depict the respective regression analyses of the modified Mohr-Griffith failure criterion. The presented results show that 3DCP elements display anisotropic mechanical capacity when subject to the induced shear loading conditions at all normal force increments investigated. The inclusion of the anisotropic uniaxial tensile capacities ascertained from previous investigations permits the holistic representation of the apparent shear-normal stress capacity. This delineation represents the upper symmetric half of Mohr's failure envelope. Note in this section compressive normal forces are considered positive for practical exposition, and tensile normal forces should be inserted in subsequent expressions using a negative sign to accord to the employed sign convention.

Table 6.8: Summary of apparent stress transformation results.

Hanger Mass Increment	f_t	0	5	10	15	20	30
D1							
Average Normal Stress (MPa)	-2.45	0	1.33	2.66	3.99	-	-
Average Shear Stress (MPa)	0	7.32	9.04	9.77	11.16	-	-
Average Shear Stress Std Dev. (MPa)	-	0.99	1.17	1.16	1.04	-	-
CoV (%)		13.49	12.89	11.89	9.28	-	-
D3x							
Average Normal Stress (MPa)	-1.25	0	1.33	2.66	-	5.33	7.99
Average Shear Stress (MPa)	0	4.26	6.63	8.40	-	9.68	11.50
Average Shear Stress Std Dev. (MPa)	-	0.45	1.28	0.55	-	0.86	0.94
CoV (%)	-	10.56	19.34	6.53	-	8.93	8.16
D3y							
Average Normal Stress (MPa)	-1.25	0	1.33	2.66	-	5.32	7.98
Average Shear Stress (MPa)	0	5.23	7.58	8.48	-	11.44	13.89
Average Shear Stress Std Dev. (MPa)	-	0.93	1.08	1.23	-	0.82	0.52
CoV (%)	-	17.80	14.19	14.50	-	7.20	3.74
Cast							
Average Normal Stress (MPa)	-1.44	0	1.35	2.70	-	5.40	8.11
Average Shear Stress (MPa)	0	4.16	6.08	7.90	-	9.56	12.63
Average Shear Stress Std Dev. (MPa)	-	0.54	0.65	0.75	-	0.60	0.64
CoV (%)	-	12.99	10.70	9.51	-	6.28	5.09

Consideration of the apparent pure shear strength at zero normal load (cohesion) depicts that the shear strength in 3DCP-D1 is highest, followed by 3DCP-D3-y, then 3DCP-D3-x, and lowest for cast specimens. This trend is followed by all 3DCP sample configurations over all the normal force increments investigated. However, the cast specimens exhibit a steeper incline in shear strength and subsequently surpasses the shear strength of 3DCP-D3-x beyond hanger mass increment 20. In addition, it is noted that the regression to an expression of the modified Mohr-Griffith failure criterion deviates more significantly at larger normal force increments and is better represented by a linear expression and thus the Mohr-Coulomb failure criterion. Former contributions investigating the shear capacity of the same FRPC mixture suggest that the shear LOA considering 3DCP-D1 and 3DCP-D3-x is 2.43, but these experiments exhibit a LOA of 1.72, due to the 44 % increase in the shear capacity of 3DCP-D3-x. Evidently, constituent batch variability significantly influences the total porosity content and thus the shear capacity of 3DCP components and should be considered in future experimental campaigns.

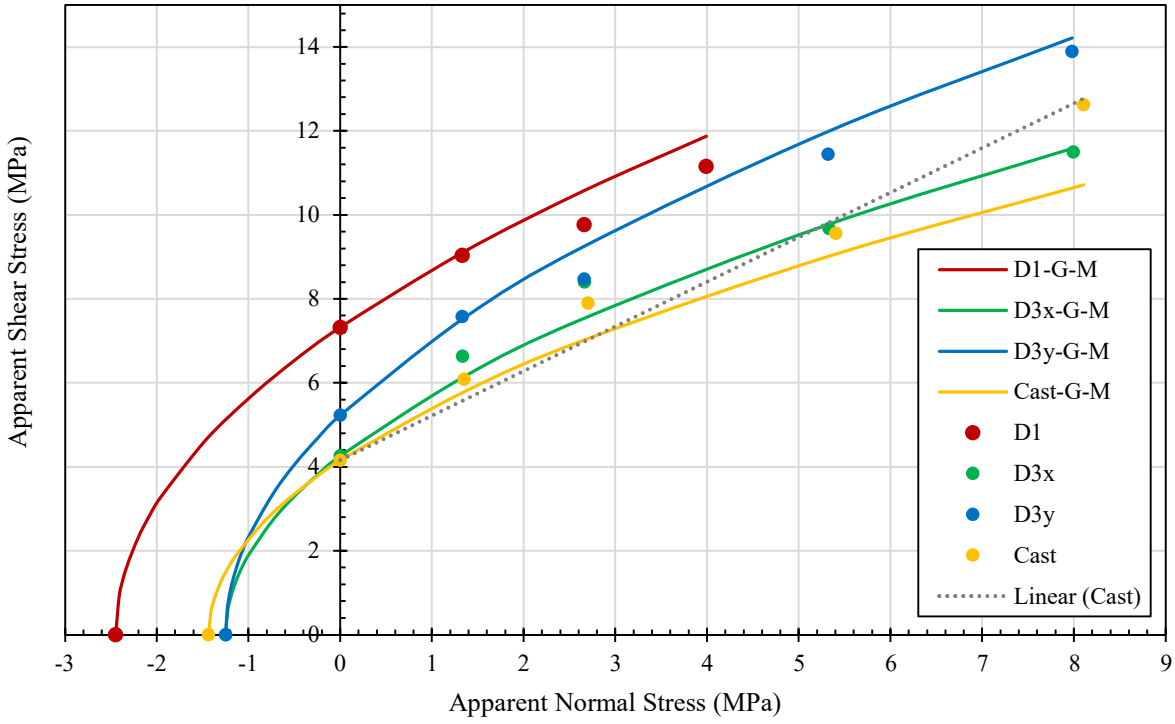

Fig. 6.20: Apparent shear stress versus apparent normal stress results and regressed modified Mohr-Griffith expressions.

6.3.3.1 Modified Mohr-Griffith failure criterion

In this section, a modified Mohr-Griffith failure criterion is proposed, Eq. (6.9), which includes an additional empirical material scaling factor (M). M is intrinsically related to the ratio between the respective anisotropic cohesive and uniaxial tensile capacities of the sample configurations and can be expressed via Eq. (6.10).

$$\tau^2 = M(4f_t^2 + 4f_t\sigma_n) \tag{6.9}$$

$$M = \left(\frac{c_i}{2f_{t,i}}\right)^2 \tag{6.10}$$

The rationale behind the introduction of the empirical material scaling factor resides in the fact that the experimental data portrays cohesion to tensile capacity ratios over the factor two proposed by Griffith (reference Fig. 6.1). Hence, M presents a practical means to empirically calibrate the proposed failure criterion to the experimentally obtained results without augmenting the physical mechanisms of the mechanical energy (i.e., elastic strain and external work or surface energy) balance as derived by Griffith [60]. Indeed, a suitable correlation between the experimental results and the proposed criterion is obtained for all 3DCP samples. The specific M and R^2 values are presented in Table 6.9.

Table 6.9: Summary of the employed material scaling factors and regression results to the modified Mohr-Griffith failure criterion for 3DCP elements. Note cast elements are excluded due to their visual dissimilarity to the employed failure criterion.

Sample loading configuration	3DCP-D1	3DCP-D3-x	3DCP-D3-y
M	2.235	2.908	4.379
R^2	0.995	0.991	0.997

6.3.3.2 Effect of microstructural morphology on shear strength

This section provides a mechanistic evaluation of the microstructural features responsible for the shear strength hierarchy presented in Fig. 6.20. An explanation is postulated to stem from five origins, (i) pore size, (ii) pore shape, (iii) local porosity content, (iv) pore spacing and interconnectivity, and (v) pore orientation with respect to the induced stress state [43]. Pores are reportedly larger and concentrate at interlayer interfaces [43,57–59,76], locally increasing porosity and interconnectivity in these regions. Additionally, microstructural pores can be approximated as ellipsoidal voids (Fig. 6.21) that are elongated in the extrusion direction, pressed in the vertical building direction, and slightly broader in the transverse direction as opposed to the building direction [43,57,77]. Such observations are graphically illustrated in Fig. 6.22.

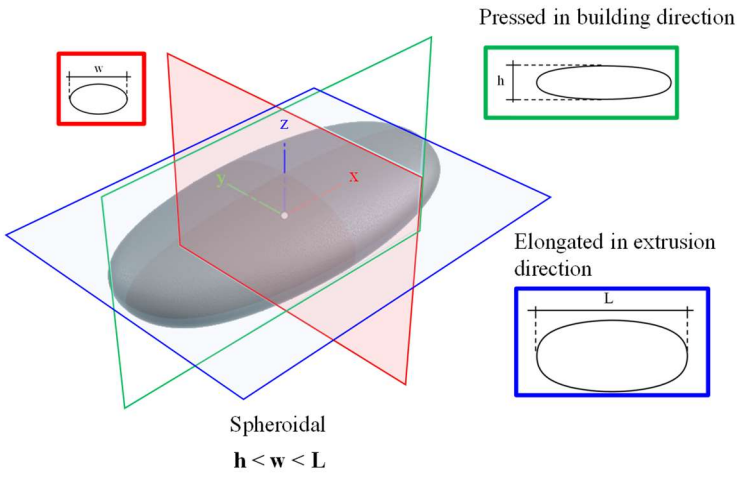

Fig. 6.21: Generalised pore shape encountered in concrete printed filaments. Here the x-direction corresponds to the extrusion direction, the y-direction parallels the transverse direction, and the z-direction represents the vertical building direction, which is normal to the deposition plane. Reproduced from [43].

As shown in Section 6.3.2.1, increased porosity is the consequence of either larger pores with increased volume or an increased number of smaller pores aggregating to a higher volumetric quantity. Given the increased porosity witnessed in cast samples, we note both an increased number of pores and pores with larger equivalent diameters compared to the 3DCP sample configurations. This supports the

reduction in shear strength, stemming from an increase in the critical crack length and a decrease in the distance between neighbouring pores. This is visually quite clear in Figs. 6.19 and 6.22.

Consequently, cast samples exhibit the weakest pure shear strength but subsequently surpasses the shear strength of 3DCP-D3-x at load increment 20. As shown in Figs. 6.22 and 6.23, this response is attributed to the more spherical voids encountered in cast samples, which experience lower stress concentration factors at void boundaries as opposed to the higher stress concentration factors found in the oblate ellipsoidal voids in 3DCP-D3-x samples [78]. Lower stress concentration permits increased shear capacity at larger normal stress increments. In contrast, higher stress concentration at void boundaries ensues reduced shear strength and explains why the compression-shear response of 3DCP samples is non-linear and better described by the proposed modified Mohr-Griffith criterion.

Fig. 6.23 illustrates the location of the critically stressed sub-domain (Γ) within the DST sample domain (ζ) and provides a generalised representation, derived from Fig. 6.22, of the resulting pore morphology exhibited in the respective DST sample configurations. The matrix area (A_m) is illustrated by the darker red plane in Γ and represents a simplified planar exposition of the potential fracture plane within Γ. Luping [75] provides theories linking strength to the pore size distribution in a porous medium. It is argued that for a porous medium comprising the same cementitious matrix and pore size distribution, increased porosity effectively reduces A_m, which increases the induced stress under a certain load, which then reduces the load the porous body can bear (i.e., lower strength) [75]. On the other hand, it is also shown that for a porous medium comprising the same cementitious matrix and porosity, the number of larger pores within the pore size distribution in Γ results in a more rapid reduction in A_m, resulting in complete fracture at a lower load, even for a less porous material. This clarifies why 3DCP samples with similar porosity display anisotropic shear-strength characteristics.

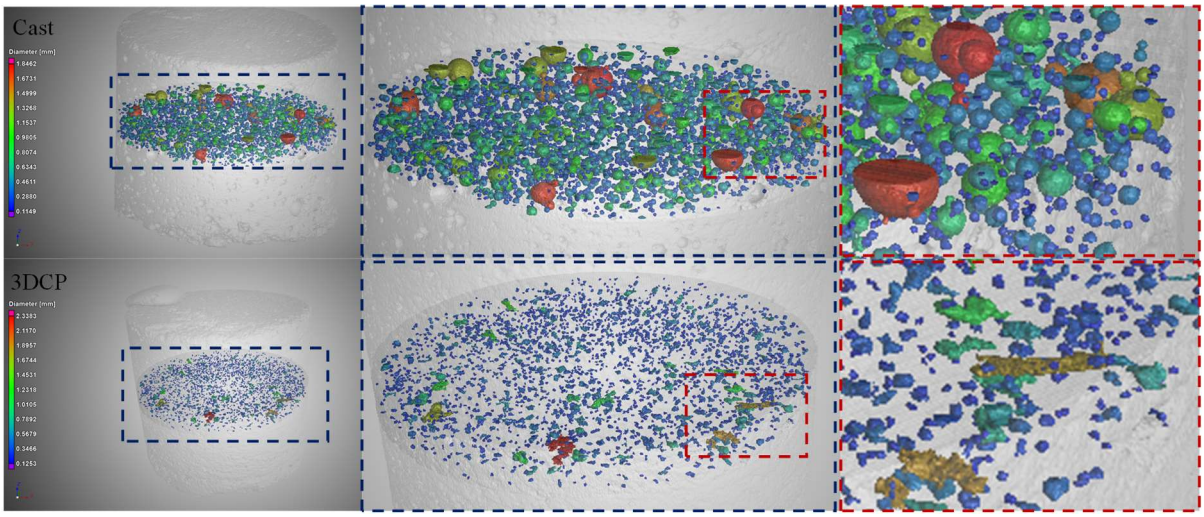

Fig. 6.22: Visual exhibition of pore morphology in cast and 3DCP specimens, respectively. Pores in 3DCP specimens are shown to preferentially align and elongate in the extrusion direction (x-direction in this case), where the pores in cast specimens are spherical.

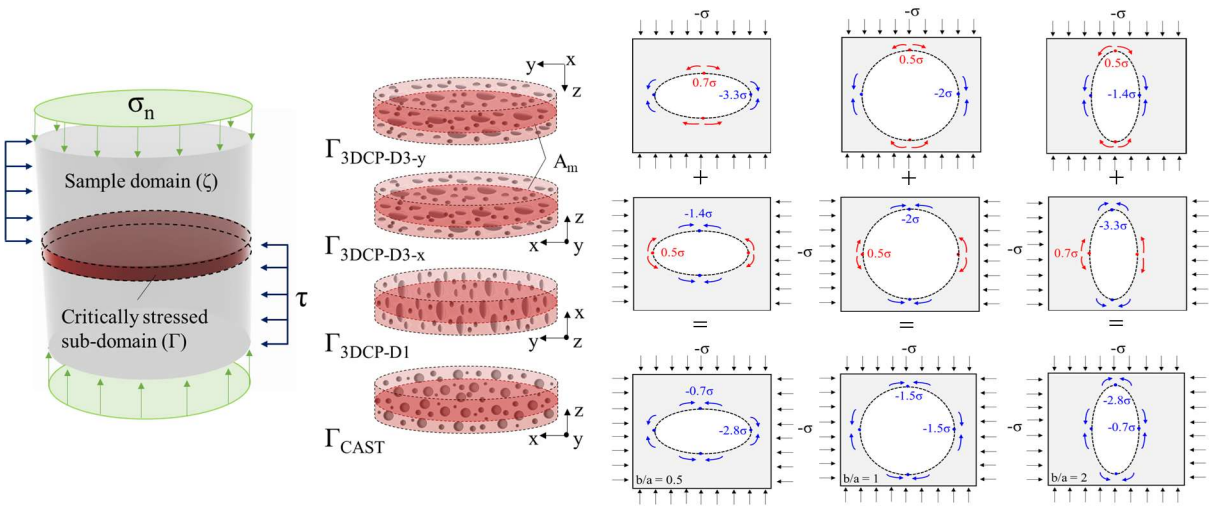

Fig. 6.23: Generalised illustration of pore morphology in the critically stressed subdomain within the DST sample domain. The effect of void topology and orientation with respect to the loading direction is derived from [78] and *presented for three generalised pore shapes, subject to equal normal and transverse stress states.*

The above assertions by Luping [75] are corroborated by Castro et al. [74] who report that the ratio between half the critical crack length (a_c) and the critical length of the fracture process zone (L_{FPZ}) influences the shear capacity at respective normal stress states, as illustrated in Fig. 6.24. L_{FPZ} is a system parameter related to the local plasticity or fracture energy, microstructural features, sample geometry, material stiffness, and loading conditions of the matrix [79]. Particularly, crack propagation in heterogeneous, multi-phase, materials like concrete and mortar are influenced by factors such as the size of grains and micro inclusions and therefore, proportionality between these features and L_{FPZ} are expected [74]. Again, considering that the cementitious matrix surrounding the macro pores encountered in 3DPC comprises the same material constituents and proportions, it is reasonable to assume that the L_{FPZ} remains somewhat consistent in a continuum of the cementitious matrix. Therefore, the ratio a_c/L_{FPZ} is by and large affected by the critical crack length (i.e., the size of the macro voids on A_m) and the distance to neighbouring pores [78] in the respective directions on the fracture plane.

Reviewing the orientation of the ellipsoidal pores encountered in Γ in the respective sample configurations, it is perceptible that $a_{c,3DCP\text{-}D1}$, sheared on the YZ-plane in Fig. 6.23, is smaller than $a_{c,3DCP\text{-}D3\text{-}y}$ sheared on the XY-plane in the Y-direction in Fig. 6.23, which is less than $a_{c,3DCP\text{-}D3\text{-}x}$ sheared on the XY-plane in the X-direction in Fig. 6.23. Noting that the ratio a_c/L_{FPZ} is inversely proportional to the shear strength, it is deduced that $\tau(\sigma_n)_{3DCP\text{-}D1} > \tau(\sigma_n)_{3DCP\text{-}D3\text{-}y} > \tau(\sigma_n)_{3DCP\text{-}D3\text{-}x}$ as exhibited by the experimental results.

It is certainly worth pointing out that these notions align with Griffith's initial formulation, $f_{tc} = (2EG_f/\pi a_c)^{1/2}$, where the critical attainable far-field stress is inversely proportional to the square of half the critical crack length of an enclosed discontinuity [60]. It is maintained that the above assertions

validate the applicability of the proposed modified Mohr-Griffith failure criterion presented in this contribution.

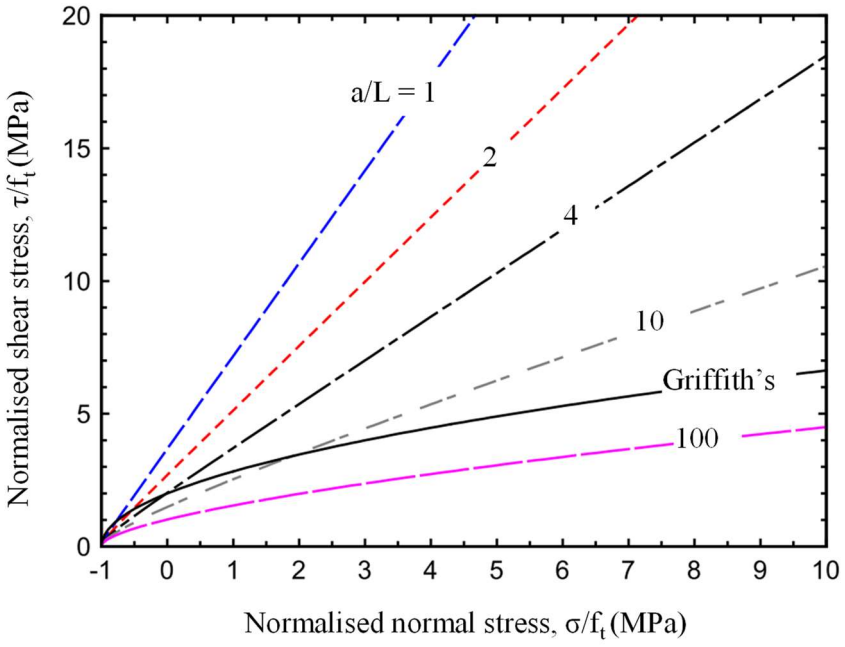

Fig. 6.24: Modified Griffith failure criterion in Mohr's diagram. Adapted from [74].

6.3.4 Physical implication of observed response

The physical implication of the experimentally observed shear-normal response is illustrated in Fig. 6.25. Here it is shown that the assumption of Mohr-Coulomb's failure criterion initially underestimates the shear strength prior to a normal stress equal to 18.6 MPa and subsequently increasingly overestimates the shear strength thereafter. Note that the initial underestimation in shear strength is ascribed to the comparatively higher shear strength obtained in this investigation as opposed to the material properties given in Table 6.2, which is utilised to prescribe the presented Mohr-Coulomb response. Suppose the capacity is equated to those obtained from previous experiments (broken grey line), it is shown that the shear strength is effectively subject to consistent underestimation at increasing normal stresses.

From a computational perspective, the accuracy of FE analyses could be substantially increased by the advent and implementation of the proposed modified Mohr-Griffith failure criterion for 3DCP elements. This criterion can readily be incorporated into existing FE simulation packages via user material subroutines since a single expression is provided, which provides unique shear strengths at any normal stress increment until the cap mode is reached where shear strength reduces due to compressive crushing [80].

From a material performance perspective, the effects of pore topology on the shear strength of the FRPC matrix are highlighted and correlated to the observed anisotropy. It is shown that a spherical

(more compact) pore topology adheres to the Mohr-Coulomb failure criterion and provides increased shear capacity at increased normal stress increments, despite higher average porosity. In the pursuit of isotropic material characteristics for 3DCP composites, future investigations should consider methods to reduce local increases in porosity at interlayer locations, resulting in a lack of fusion [10], but should also endeavour to stabilise the remaining inclusions in the cementitious matrix, i.e. improve sphericity of pores. This assertion is supported by the experimental results which portray that improved mechanical performance and reduced anisotropy is permitted by the stabilisation of the microstructural morphology in 3DPC. Which is contended to reduce computational complexity and thus uncertainty from a material design perspective.

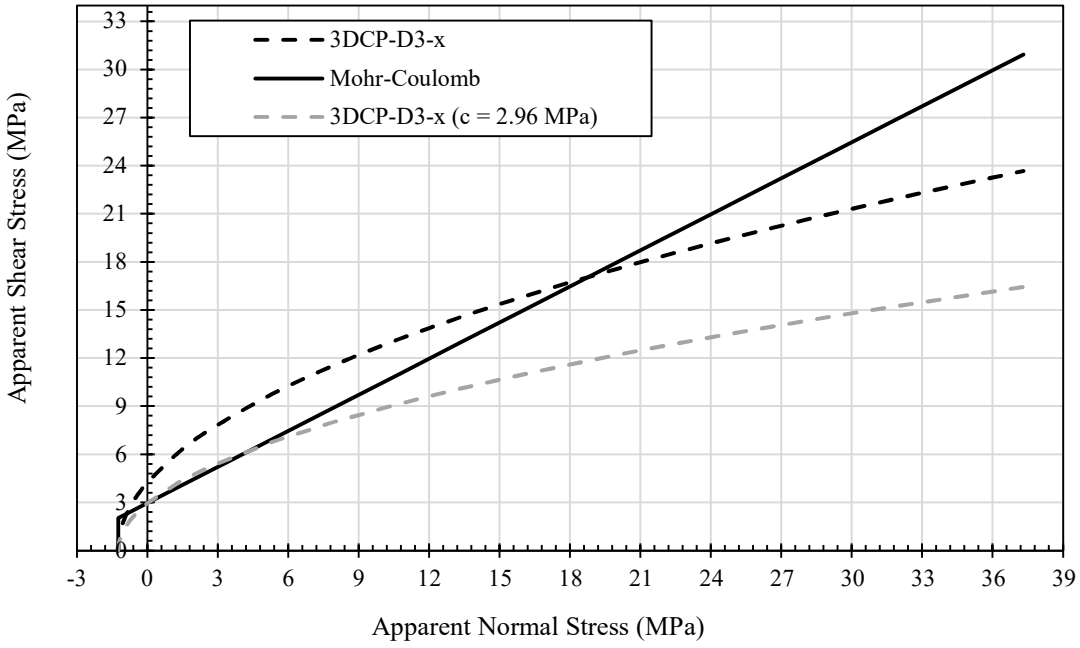

Fig. 6.25: Physical implication of respective failure criteria with respect to shear strength estimation at increasing normal load increments.

It is purported that the porosity in 3DCP components can be controlled by the specification of a proper mix design, selection of appropriate process parameters (particularly nozzle velocity, nozzle standoff distance, and extrusion rate), and by reducing the moisture evaporation rate through sufficient moisture curing [77,81]. Pore stabilisation can be attained by incorporating air-entraining agents with surface-active molecules [82], as illustrated in Fig. 6.26. However, further experimental investigation is required to determine the optimum dosage, and at which point in the manufacturing process the air-entraining agents should be incorporated to stabilise the air voids but not incorporate excessive amounts of unwanted porosity, which will diminish the mechanical capacity of the hardened-state matrix [83].

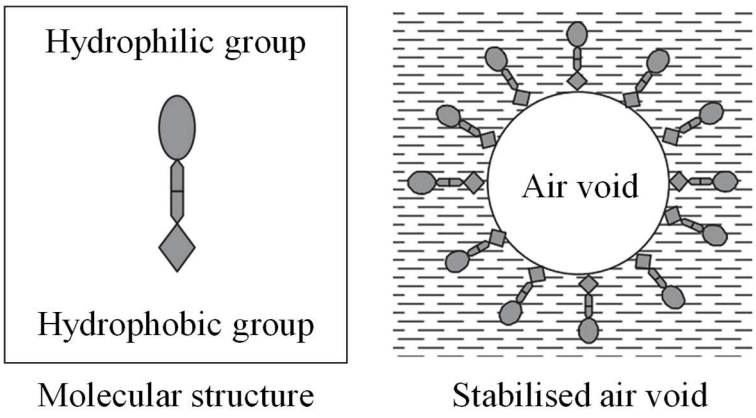

Fig. 6.26: Schematic of air entrainment by surface-active molecules. Adapted from [84].

Noting the pore topology presented in Fig. 6.27 and the deductions made in this investigation, it is set forth that those activities directed at reducing the anisotropy of 3DCP components should not exclusively focus on the performance and microstructure of interlayer regions (although much resolution is required [10]), but should also consider the anisotropy within intralayer filaments containing entrained ellipsoidal pores as these inclusions will undoubtedly impose a source of anisotropy due to their preferential alignment and elongation in the extrusion direction [57]. Clearly, both inter and intralayers are sources of anisotropy in 3DCP elements.

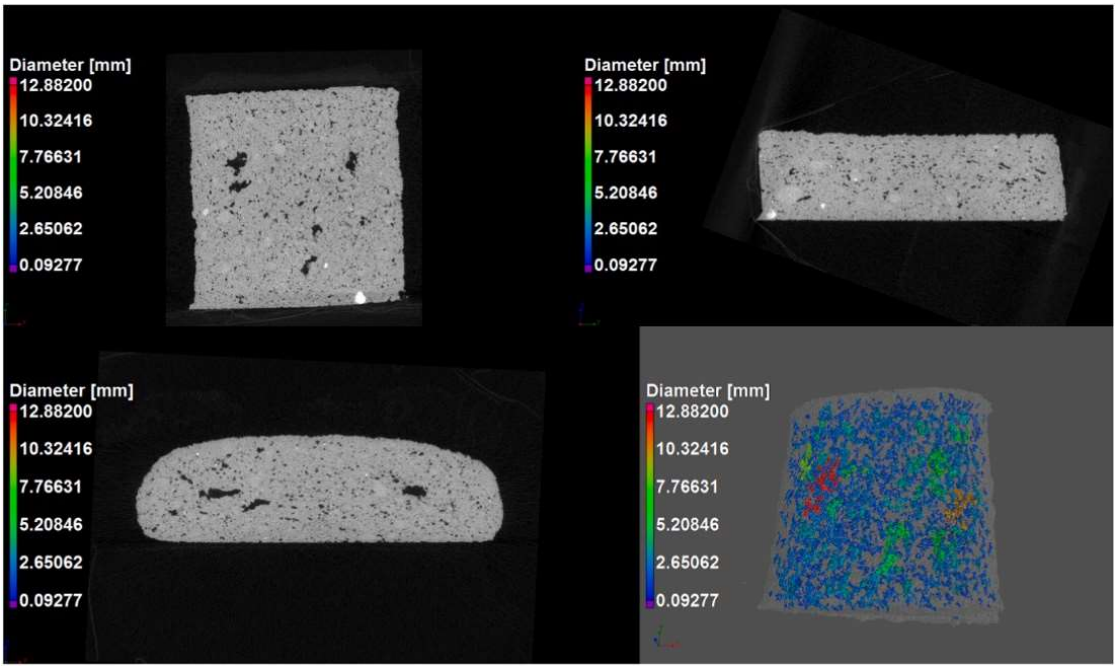

Fig. 6.27: Pore topology in intralayer filaments of a 3DCP specimen, reproduced from [57].

6.4 Conclusions

A comprehensive investigation of the constant compression-shear performance of a FRPC mixture is conducted via a DST methodology for concrete samples additively manufactured by extrusion-based 3DCP. The anisotropic material strength is investigated in the three orthogonal material planes, suitable failure criteria are examined, and a novel modified Mohr-Griffith criterion proposed. X-ray CT is employed to explore the microstructural morphology (size, shape, orientation, and total porosity content), fracture surface angle, and fracture surface area of 3DCP inter and intralayers compared to specimens cast from the same FRPC mixture. A mechanistic evaluation of the constant compression-shear performances relates the ensuing shear strength to the porosity and pore morphology observed in the experimentally assessed samples. From the presented results, the following main conclusions are drawn:

- 3DCP elements display anisotropic mechanical capacities when subject to the induced shear loading conditions at all hanger mass increments investigated. 3DCP-D1 specimens are the strongest, followed by 3DCP-D3-y, and then 3DCP-D3-x over the entire loading spectrum.
- Cast samples containing higher porosity and larger pore sizes initially display the lowest shear strength but exhibit a linear increase in shear strength with increasing normal stress as described by the Mohr-Coulomb criterion surpassing 3DCP-D3-x a normal stress of 5.5 MPa.
- For 3DCP samples, a non-linear compression-shear resistance evolution is observed at increasing normal load increments.
- A modified Mohr-Griffith failure criterion is proposed for 3DCP elements, which includes an additional empirical material scaling factor (M) related to the ratio between the anisotropic cohesive and uniaxial tensile capacities in the respective material axes. Solid agreement between the experimentally attained results and the modified Mohr-Griffith criterion is found for all 3DCP samples.
- A mechanistic evaluation relates the exhibited anisotropy and non-linear shear strength evolution to the microscopic pore morphology concerning the stress state in the evaluated samples. The constant compression-shear behaviour of both 3DCP and cast samples comprising the same FRPC mixture can aptly be described by the theories presented in this contribution.
- The accuracy of hardened-state FE analyses could be substantially increased by the advent and implementation of the proposed modified Mohr-Griffith failure criterion for 3DCP elements. This criterion can readily be incorporated into existing FE simulation packages via user material subroutines since a single expression is provided, which provides unique shear strengths at any normal stress increment up until the cap mode is reached. Effectively, the three-surface limit function is reduced to a two-surface limit function.
- In the pursuit of isotropic material characteristics for 3DCP composites, future investigations should consider methods to reduce local increases in porosity but should also endeavour to

stabilise the remaining inclusions in the cementitious matrix. It is postulated that improved mechanical performance and reduced anisotropy, evoking less computational complexity and uncertainty, is permitted by improving the sphericity (stabilising) of the microstructural morphology in 3DPC.

- Activities aimed at reducing the anisotropy of 3DCP components should not exclusively focus on the performance and microstructure of interlayer regions but should also consider the anisotropy within intralayer filaments containing entrained ellipsoidal pores. As these inclusions impose a source of anisotropy due to their preferential alignment and elongation in the extrusion direction.

In essence, this contribution provides the basis for a fundamentally deeper understanding of the hardened-state mechanical capacity of 3DCP components, which is supported by a novel failure criterion and solid theoretical explanations of the influential microstructural features affecting the mechanical response. It is recommended that experimental methods employed in this contribution be utilised for various printable materials over a vaster loading spectrum to increase the available dataset. Finally, computational procedures should be updated to include the novel modified Mohr-Griffith failure criterion to enable more detailed discrete interface-based analyses to be conducted.

CRediT authorship contribution statement

Marchant van den Heever: Conceptualisation, Methodology, Validation, Investigation, Data curation, Writing - original draft, Writing - review & editing, Visualisation, Project administration.

Anton du Plessis: Investigation, Methodology, Software, Resources, Writing - review & editing.

Frederick Bester: Investigation, Writing - review & editing.

Jacques Kruger: Resources, Writing - review & editing, Supervision.

Gideon van Zijl: Resources, Writing - review & editing, Supervision, Funding acquisition.

Declaration of Competing Interest

The authors declare no financial interests/personal relationships which may be considered as potential competing interests.

Acknowledgements

The support by The Concrete Society of South Africa is gratefully acknowledged. Funding of Anton du Plessis through the South African Collaborative Programme in Additive Manufacturing (CPAM) is thankfully acknowledged.

6.5 References

[1] F.P. Bos, P.J. Kruger, S.S. Lucas, G.P.A.G. van Zijl, Juxtaposing fresh material characterisation methods for buildability assessment of 3D printable cementitious mortars, Cement and Concrete Composites. 120 (2021) 104024. https://doi.org/10.1016/j.cemconcomp.2021.104024.

[2] H. Kloft, H.W. Krauss, N. Hack, E. Herrmann, S. Neudecker, P.A. Varady, D. Lowke, Influence of process parameters on the interlayer bond strength of concrete elements additive manufactured by Shotcrete 3D Printing (SC3DP), Cement and Concrete Research. 134 (2020) 106078. https://doi.org/10.1016/j.cemconres.2020.106078.

[3] S.C. Paul, G.P.A.G. van Zijl, M.J. Tan, I. Gibson, A review of 3D concrete printing systems and materials properties: current status and future research prospects, Rapid Prototyping Journal. (2018) 0. https://doi.org/10.1108/RPJ-09-2016-0154.

[4] Y. Weng, M. Li, D. Zhang, M. Jen, S. Qian, Investigation of interlayer adhesion of 3D printable cementitious material from the aspect of printing process, Cement and Concrete Research. 143 (2021) 106386. https://doi.org/10.1016/j.cemconres.2021.106386.

[5] J. Xiao, S. Zou, Y. Yu, Y. Wang, T. Ding, Y. Zhu, J. Yu, S. Li, Z. Duan, Y. Wu, L. Li, 3D recycled mortar printing: System development, process design, material properties and on-site printing, Journal of Building Engineering. 32 (2020) 101779. https://doi.org/10.1016/j.jobe.2020.101779.

[6] R.J.M. Wolfs, F.P. Bos, T.A.M. Salet, Hardened properties of 3D printed concrete: The influence of process parameters on interlayer adhesion, Cement and Concrete Research. 119 (2019) 132–140. https://doi.org/10.1016/j.cemconres.2019.02.017.

[7] V. Mechtcherine, F.P. Bos, A. Perrot, W.R.L. da Silva, V.N. Nerella, S. Fataei, R.J.M. Wolfs, M. Sonebi, N. Roussel, Extrusion-based additive manufacturing with cement-based materials – Production steps, processes, and their underlying physics: A review, Cement and Concrete Research. 132 (2020) 106037. https://doi.org/10.1016/j.cemconres.2020.106037.

[8] N. Roussel, Rheological requirements for printable concretes, Cement and Concrete Research. (2018) 1–10. https://doi.org/10.1016/j.cemconres.2018.04.005.

[9] M.T. Souza, I.M. Ferreira, E. Guzi de Moraes, L. Senff, A.P. Novaes de Oliveira, 3D printed concrete for large-scale buildings: An overview of rheology, printing parameters, chemical admixtures, reinforcements, and economic and environmental prospects, Journal of Building Engineering. 32 (2020). https://doi.org/10.1016/j.jobe.2020.101833.

[10] J. Kruger, G. van Zijl, A compendious review on lack-of-fusion in digital concrete fabrication, Additive Manufacturing. 37 (2021) 101654. https://doi.org/10.1016/j.addma.2020.101654.

[11] J.G. Sanjayan, B. Nematollahi, M. Xia, T. Marchment, Effect of surface moisture on inter-layer strength of 3D printed concrete, Construction and Building Materials. (2018). https://doi.org/10.1016/j.conbuildmat.2018.03.232.

[12] J. van der Putten, M. Azima, P. van den Heede, T. van Mullem, D. Snoeck, C. Carminati, J. Hovind, P. Trtik, G. de Schutter, K. van Tittelboom, Neutron radiography to study the water

ingress via the interlayer of 3D printed cementitious materials for continuous layering, Construction and Building Materials. 258 (2020) 119587. https://doi.org/10.1016/j.conbuildmat.2020.119587.

[13] L. Wang, H. Jiang, Z. Li, G. Ma, Mechanical behaviors of 3D printed lightweight concrete structure with hollow section, Archives of Civil and Mechanical Engineering. 20 (2020) 1–17. https://doi.org/10.1007/s43452-020-00017-1.

[14] A. du Plessis, A.J. Babafemi, S.C. Paul, B. Panda, J.P. Tran, C. Broeckhoven, Biomimicry for 3D concrete printing: a review and perspective, Additive Manufacturing. (2020) 101823. https://doi.org/10.1016/j.addma.2020.101823.

[15] J. Yu, C.K.Y. Leung, Impact of 3D Printing Direction on Mechanical Performance of Strain-Hardening Cementitious Composite (SHCC) Jing, Springer International Publishing, 2019. https://doi.org/10.1007/978-3-319-99519-9.

[16] G. Ma, Z. Li, L. Wang, F. Wang, J. Sanjayan, Mechanical anisotropy of aligned fiber reinforced composite for extrusion-based 3D printing, Construction and Building Materials. (2019). https://doi.org/10.1016/j.conbuildmat.2019.01.008.

[17] D. Asprone, C. Menna, F.P. Bos, T.A.M. Salet, J. Mata-Falcón, W. Kaufmann, Rethinking reinforcement for digital fabrication with concrete, Cement and Concrete Research. 112 (2018) 111–121. https://doi.org/10.1016/j.cemconres.2018.05.020.

[18] F.P. Bos, Z.Y. Ahmed, E.R. Jutinov, T.A.M. Salet, Experimental exploration of metal cable as reinforcement in 3D printed concrete, Materials. 10 (2017). https://doi.org/10.3390/ma10111314.

[19] V. Mechtcherine, J. Grafe, V.N. Nerella, E. Spaniol, M. Hertel, U. Füssel, 3D-printed steel reinforcement for digital concrete construction – Manufacture, mechanical properties and bond behaviour, Construction and Building Materials. 179 (2018) 125–137. https://doi.org/10.1016/j.conbuildmat.2018.05.202.

[20] F.P. Bos, E. Bosco, T.A.M. Salet, Ductility of 3D printed concrete reinforced with short straight steel fibers, Virtual and Physical Prototyping. 14 (2019) 160–174. https://doi.org/10.1080/17452759.2018.1548069.

[21] F.A. Bester, M. van den Heever, P.J. Kruger, G.P.A.G. van Zijl, Reinforcing digitally fabricated concrete: A systems approach review, Additive Manufacturing. (2020).

[22] T. Marchment, J. Sanjayan, Mesh reinforcing method for 3D Concrete Printing, Automation in Construction. 109 (2020) 102992. https://doi.org/10.1016/j.autcon.2019.102992.

[23] T. Marchment, J. Sanjayan, Bond properties of reinforcing bar penetrations in 3D concrete printing, Automation in Construction. 120 (2020) 103394. https://doi.org/10.1016/j.autcon.2020.103394.

[24] J. Kruger, S. Cho, S. Zeranka, C. Viljoen, G. van Zijl, 3D concrete printer parameter optimisation for high rate digital construction avoiding plastic collapse, Composites Part B: Engineering. 183 (2020) 107660. https://doi.org/10.1016/j.compositesb.2019.107660.

[25] B. Baz, G. Aouad, S. Remond, Effect of the printing method and mortar's workability on pull-out strength of 3D printed elements, Construction and Building Materials. 230 (2020) 117002. https://doi.org/10.1016/j.conbuildmat.2019.117002.

[26] Y. Chen, K. Jansen, H. Zhang, C. Romero Rodriguez, Y. Gan, O. Çopuroğlu, E. Schlangen, Effect of printing parameters on interlayer bond strength of 3D printed limestone-calcined clay-based cementitious materials: An experimental and numerical study, Construction and Building Materials. 262 (2020). https://doi.org/10.1016/j.conbuildmat.2020.120094.

[27] S. Lim, R. Buswell, T. Le, R. Wackrow, S. Austin, A. Gibb, T. Thorpe, Development of a viable concrete printing process, Proceedings of the 28th International Symposium on Automation and Robotics in Construction, ISARC 2011. (2011) 665–670. https://doi.org/10.22260/isarc2011/0124.

[28] R. Duballet, O. Baverel, J. Dirrenberger, Classification of building systems for concrete 3D printing, Automation in Construction. 83 (2017) 247–258. https://doi.org/10.1016/j.autcon.2017.08.018.

[29] R.J.M. Wolfs, F.P. Bos, T.A.M. Salet, Hardened properties of 3D printed concrete: The influence of process parameters on interlayer adhesion, Cement and Concrete Research. 119 (2019) 132–140. https://doi.org/10.1016/j.cemconres.2019.02.017.

[30] T. Marchment, J. Sanjayan, M. Xia, Method of enhancing interlayer bond strength in construction scale 3D printing with mortar by effective bond area amplification, Materials and Design. 169 (2019) 107684. https://doi.org/10.1016/j.matdes.2019.107684.

[31] V.N. Nerella, S. Hempel, V. Mechtcherine, Effects of layer-interface properties on mechanical performance of concrete elements produced by extrusion-based 3D-printing, Construction and Building Materials. 205 (2019). https://doi.org/10.1016/j.conbuildmat.2019.01.235.

[32] G.M. Moelich, J. Kruger, R. Combrinck, Plastic shrinkage cracking in 3D printed concrete, Composites Part B: Engineering. 200 (2020) 108313. https://doi.org/10.1016/j.compositesb.2020.108313.

[33] M. Sonebi, S. Amziane, A. Perrot, Mechanical Behavior of 3D Printed Cement Materials, 3D Printing of Concrete. (2019) 101–124. https://doi.org/10.1002/9781119610755.ch4.

[34] S.C. Figueiredo, C.R. Rodrıguez, Z.Y. Ahmed, D.H. Bos, Y. Xu, T.M. Salet, O.C. Opurog˘lu, E. Schlangen, F.P. Bos, Mechanical behaviour of printed strain hardening cementitious composites, Materials. 13 (2020).

[35] P. Feng, X. Meng, J. Chen, L. Ye, Mechanical properties of structures 3D printed with cementitious powders, CONSTRUCTION & BUILDING MATERIALS. 93 (2015) 486–497. https://doi.org/10.1016/j.conbuildmat.2015.05.132.

[36] B. Panda, S. Chandra Paul, M. Jen Tan, Anisotropic mechanical performance of 3D printed fiber reinforced sustainable construction material, Materials Letters. (2017). https://doi.org/10.1016/j.matlet.2017.07.123.

[37] S.C. Paul, Y.W.D. Tay, B. Panda, M.J. Tan, Fresh and hardened properties of 3D printable cementitious materials for building and construction, Archives of Civil and Mechanical Engineering. (2018). https://doi.org/10.1016/j.acme.2017.02.008.

[38] A. Vespalec, J. Novák, A. Kohoutková, P. Vosynek, J. Podroužek, D. Škaroupka, T. Zikmund, J. Kaiser, D. Paloušek, Interface behavior and interface tensile strength of a hardened concrete mixture with a coarse aggregate for additive manufacturing, Materials. 13 (2020) 1–20. https://doi.org/10.3390/ma13225147.

[39] B. Nematollahi, P. Vijay, J. Sanjayan, A. Nazari, M. Xia, V.N. Nerella, V. Mechtcherine, Effect of polypropylene fibre addition on properties of geopolymers made by 3D printing for digital construction, Materials. 11 (2018). https://doi.org/10.3390/ma11122352.

[40] S. Hou, Z. Duan, J. Xiao, J. Ye, A review of 3D printed concrete: Performance requirements, testing measurements and mix design, Construction and Building Materials. 273 (2021) 121745. https://doi.org/10.1016/j.conbuildmat.2020.121745.

[41] H. Lee, J.H.J. Kim, J.H. Moon, W.W. Kim, E.A. Seo, Correlation between pore characteristics and tensile bond strength of additive manufactured mortar using X-ray computed tomography, Construction and Building Materials. 226 (2019) 712–720. https://doi.org/10.1016/j.conbuildmat.2019.07.161.

[42] M. van den Heever, F.A. Bester, P.J. Kruger, G.P.A.G. van Zijl, Mechanical Characterisation for Numerical Simulation of Extrusion-based 3D Concrete Printing, Journal of Building Engineering. Submitted (2021) 102944. https://doi.org/10.1016/j.jobe.2021.102944.

[43] M. van den Heever, A. du Plessis, J. Kruger, G. van Zijl, Evaluating the Effects of Porosity on the Mechanical Properties of Extrusion-based Fibre-reinforced 3D Printed Concrete, Additive Manufacturing. (Submitted (2021).

[44] A. Roberts, Failure Criteria for Solids and Rocks, in: A. Roberts (Ed.), Geotechnology, Elsevier, 1977: pp. 41–53. https://doi.org/https://doi.org/10.1016/B978-0-08-019602-2.50008-3.

[45] C. Menna, J. Mata-Falcón, F.P. Bos, G. Vantyghem, L. Ferrara, D. Asprone, T. Salet, W. Kaufmann, Opportunities and challenges for structural engineering of digitally fabricated concrete, Cement and Concrete Research. 133 (2020) 106079. https://doi.org/10.1016/j.cemconres.2020.106079.

[46] T. Wangler, E. Lloret, L. Reiter, N. Hack, F. Gramazio, M. Kohler, M. Bernhard, B. Dillenburger, J. Buchli, N. Roussel, R. Flatt, Digital Concrete: Opportunities and Challenges, RILEM Technical Letters. 1 (2016) 67. https://doi.org/10.21809/rilemtechlett.2016.16.

[47] F. Bos, R. Wolfs, Z. Ahmed, T. Salet, Additive manufacturing of concrete in construction: potentials and challenges of 3D concrete printing, Virtual and Physical Prototyping. 11 (2016) 209–225. https://doi.org/10.1080/17452759.2016.1209867.

[48] T.A.M. Salet, F.P. Bos, R.J.M. Wolfs, Z.Y. Ahmed, 3D concrete printing – a structural engineering perspective, in: High Tech Concrete: Where Technology and Engineering Meet - Proceedings of the 2017 Fib Symposium, 2017. https://doi.org/10.1007/978-3-319-59471-2.

[49] T.A.M. Salet, Z.Y. Ahmed, F.P. Bos, H.L.M. Laagland, Design of a 3D printed concrete bridge by testing, Virtual and Physical Prototyping. 0 (2018) 1–15. https://doi.org/10.1080/17452759.2018.1476064.

[50] A. Nadai, Theory of flow and fracture of solids, 2nd ed., McGraw-Hill (Engineering societies monographs), New York, 1950.

[51] J.J. Royer, Hydraulic fracturing in transverse isotropic media - A theoretical framework, 14th European Conference on the Mathematics of Oil Recovery 2014, ECMOR 2014. (2014). https://doi.org/10.3997/2214-4609.20141885.

[52] R.J.M. Wolfs, F.P. Bos, T.A.M. Salet, Early age mechanical behaviour of 3D printed concrete: Numerical modelling and experimental testing, Cement and Concrete Research. 106 (2018) 103–116. https://doi.org/10.1016/j.cemconres.2018.02.001.

[53] F.A. Bester, M. van den Heever, P.J. Kruger, S. Zeranka, G.P.A.G. van Zijl, Benchmark structures for 3D concrete printing, Proceedings of the Fib Symposium 2019: Concrete - Innovations in Materials, Design and Structures. (2019) 305–312.

[54] R. Jayathilakage, J. Sanjayan, P. Rajeev, Direct shear test for the assessment of rheological parameters of concrete for 3D printing applications, Materials and Structures/Materiaux et Constructions. 52 (2019) 1–13. https://doi.org/10.1617/s11527-019-1322-4.

[55] J.F. Labuz, A. Zang, Mohr-Coulomb failure criterion, Rock Mechanics and Rock Engineering. 45 (2012) 975–979. https://doi.org/10.1007/s00603-012-0281-7.

[56] J.C. Jaeger, N.G.W. Cook, Fundamentals of Rock Mechanics, 3rd ed., Chapman and Hall, London, 1979.

[57] J. Kruger, A. du Plessis, G. van Zijl, An investigation into the porosity of extrusion-based 3D printed concrete, Additive Manufacturing. 37 (2021) 101740. https://doi.org/10.1016/j.addma.2020.101740.

[58] J. van der Putten, M. Deprez, V. Cnudde, G. de Schutter, K. van Tittelboom, Microstructural characterization of 3D printed cementitious materials, Materials. 12 (2019). https://doi.org/10.3390/ma12182993.

[59] Y. Chen, O. Çopuroğlu, C. Romero Rodriguez, F.F. de Mendonca Filho, E. Schlangen, Characterization of air-void systems in 3D printed cementitious materials using optical image scanning and X-ray computed tomography, Materials Characterization. 173 (2021) 110948. https://doi.org/10.1016/j.matchar.2021.110948.

[60] A.A. Griffith, The phenomena of rupture and flow in solids, Royal Society. 221 (1920). https://doi.org/https://doi.org/10.1098/rsta.1921.0006.

[61] S.A.F. Murrell, The theory of the propagation of elliptical Griffith cracks under various conditions of plane strain or plane stress: Part I, British Journal of Applied Physics. 15 (1964) 1195–1210. https://doi.org/10.1088/0508-3443/15/10/308.

[62] F.A. McClintock, J.B. Walsh, Friction on Griffith cracks under pressure, Proc. 4th U.S. Natl. Congr. Appl. Mech. (1962) 1015–1021.

[63] P.B. Lourenço, J.G. Rots, J. Blaauwendraad, Continuum model for masonry: Parameter estimation and validation, Journal of Structural Engineering. 124 (1998) 642–652. https://doi.org/10.1061/(ASCE)0733-9445(1998)124:6(642).

[64] P. Menetrey, K.J. Willam, Triaxial Failure Criterion for Concrete and its Generalization, ACI Structural Journal. (1996) 311–318.

[65] S.W. Tsai, E.M. wu, A General Theory of Strength for Anisotropic Materials, Journal of Composite Materials. 5 (1971) 58–80. https://doi.org/10.1177/002199837100500106.

[66] L. Liu, D. Tang, X. Zhai, Failure criteria for grouted concrete block masonry under biaxial compression, Advances in Structural Engineering. 9 (2006) 229–239. https://doi.org/10.1260/136943306776987001.

[67] M. van den Heever, F. Bester, J. Kruger, G. van Zijl, Numerical Modelling Strategies for Reinforced 3D Concrete Printed Elements, Additive Manufacturing. Submitted (2021).

[68] P. Valle-Pello, F.P. Álvarez-Rabanal, M. Alonso-Martínez, J.J. del Coz Díaz, Numerical study of the interfaces of 3D-printed concrete using discrete element method, Materialwissenschaft Und Werkstofftechnik. 50 (2019) 629–634. https://doi.org/10.1002/mawe.201800188.

[69] M. van den Heever, F. Bester, M. Pourbehi, J. Kruger, S. Cho, G. van Zijl, Characterizing the Fissility of 3D Concrete Printed Elements via the Cohesive Zone Method, 2nd RILEM International Conference on Concrete and Digital Fabrication. 3 (2020) 1–10.

[70] ASTM, ASTM D5607-95: Standard Test Method for Performing Laboratory Direct Shear Strength Tests of Rock Specimens Under Constant Normal Force, (1996).

[71] F. Tonon, JSCE-SF6 Limitations for Shear Tests and ASTM D5607 Shear Tests on Fiber-Reinforced Concrete, ACI Materials Journal. 118 (2021). https://doi.org/10.14359/51732599.

[72] P.J. Withers, D. Grimaldi, C.K. Hagen, E. Maire, M. Manley, A. du Plessis, X-ray computed tomography, Nature Reviews Methods Primers. (2021). https://doi.org/10.1038/s43586-021-00015-4.

[73] A. du Plessis, S.G. le Roux, M. Tshibalanganda, Advancing X-ray micro computed tomography in Africa: going far, together, Scientific African. 3 (2019) p.e00061.

[74] J. Castro, S. Cicero, C. Sagaseta, A Criterion for Brittle Failure of Rocks Using the Theory of Critical Distances, Rock Mechanics and Rock Engineering. 49 (2016) 63–77. https://doi.org/10.1007/s00603-015-0728-8.

[75] T. Luping, A study of the quantitative relationship between strength and pore-size distribution of porous materials, Cement and Concrete Research. 16 (1986) 87–96. https://doi.org/10.1016/0008-8846(86)90072-4.

[76] J. Xiao, N. Han, L. Zhang, S. Zou, Mechanical and microstructural evolution of 3D printed concrete with polyethylene fiber and recycled sand at elevated temperatures, Construction and Building Materials. 293 (2021) 123524. https://doi.org/10.1016/j.conbuildmat.2021.123524.

[77] S. Yu, M. Xia, J. Sanjayan, L. Yang, J. Xiao, H. Du, Microstructural characterization of 3D printed concrete, Journal of Building Engineering. 44 (2021). https://doi.org/10.1016/j.jobe.2021.102948.

[78] T. Davis, D. Healy, A. Bubeck, R. Walker, Stress concentrations around voids in three dimensions: The roots of failure, Journal of Structural Geology. 102 (2017) 193–207. https://doi.org/10.1016/j.jsg.2017.07.013.

[79] J. Xie, A.M. Waas, M. Rassaian, Estimating the process zone length of fracture tests used in characterizing composites, International Journal of Solids and Structures. 100–101 (2016) 111–126. https://doi.org/10.1016/j.ijsolstr.2016.07.018.

[80] P.B. Lourenço, J.G. Rots, Multisurface interface model for analysis of masonry structures, Journal of Engineering Mechanics. 123 (1997) 660–668. https://doi.org/10.1061/(ASCE)0733-9399(1997)123:7(660).

[81] T.T. Le, S.A. Austin, S. Lim, R.A. Buswell, R. Law, A.G.F. Gibb, T. Thorpe, Hardened properties of high-performance printing concrete, Cement and Concrete Research. 42 (2012) 558–566. https://doi.org/10.1016/j.cemconres.2011.12.003.

[82] F. Al-Neshawy, J. Punkki, Securing the stable protective pore system of concrete, Helsinki, Finland, 2017. http://urn.fi/URN:ISBN :978-952-60-7640- 9.

[83] T.C. Powers, Structure and Physical Properties of Hardened Portland Cement Paste, Journal of the American Ceramic Society. 41 (1958) 1–6. https://doi.org/doi:10.1111/j.1151-2916.1958.tb13494.x.

[84] P. Domone, J. Illston, eds., Construction Materials: Their Nature and Behaviour, 4th ed., Spon Press, New York, 2010. https://doi.org/10.1016/B978-0-444-88887-7.50012-X.

CHAPTER 7 : Conclusions

7.1 Summary of Research Contributions

This research seeks to develop hardened-state mechanical characterisation procedures that appropriate the proposal of suitable finite element (FE) computational modelling strategies and facilitate the establishment of rational design guidelines for extrusion-based 3D concrete printing. To achieve the primary aim of this research four main objectives are set, comprehensively investigated, and addressed as sequentially presented in Chapters 3 to 6.

Chapter 3 elucidates the hardened-state mechanical characterisation procedures required to ascertain the unique material properties for the correct prescription of FE model parameters needed to numerically simulate the anisotropic non-linear material response of a fibre-reinforced printable concrete (FRPC) mixture. These procedures comprise direct tensile, uniaxial compression, Young's modulus, and four-point bending (FPB) crack mouth opening displacement (CMOD) tests. The results portrayed anisotropic non-linear and similar elastic behaviour (in terms of Young's modulus) in all experimental tests conducted. Two elastic parameters, seven strength parameters and five inelastic parameters are derived from the experimental campaign and validated via supplementary numerical evaluation, which permits the selection of suitable constitutive relations. The mechanical parameters are implemented in an anisotropic Rankine-Hill continuum multi-surface plasticity FE model, and the FPB-CMOD fracture response of 3DCP specimens is simulated with acceptable agreement, validating the accuracy of the proposed mechanical characterisation procedures.

Chapter 4 proposes two respective FE modelling strategies for the computational analysis of 3DCP building elements, of which both applications are novel in 3DCP. The anisotropic material behaviour exhibited in Chapter 3 is accounted for by either an anisotropic continuum constitutive relation or via the superposition of discrete interface-based and isotropic continuum-based constitutive relations. The first FE modelling strategy comprises an anisotropic Rankine-Hill plasticity continuum crack model, with separate softening in tension (Rankine) and compressive hardening-softening (Hill) behaviour. In comparison, the second comprises a multi-surface interface elastoplastic micro-modelling strategy for interlayer regions and a hypo-elastic isotropic total strain-based rotating crack model for intralayer continuum elements. The objective of these models is to predict the hardened-state structural capacity and failure mechanisms of singularly and dually reinforced concrete deep beams under various loading configurations. An analogy between masonry and 3DCP structures provides a premise to the presented FE modelling strategies. Succinct descriptions of the respective modelling strategies are given, allowing adaptions to the 3DCP design space to be made and material model prescriptions to be provided. Strikingly, the recommended input parameters provide sound agreement with the experimentally evaluated configurations, with all simulations exhibiting a load carry capacity within 14 % of the

experimental observations. Not only is the load-displacement response deemed appropriate, but also the numerically produced cracking patterns, placing confidence in the proposed numerical simulation strategies.

Chapter 5 investigates the effects of porosity on the mechanical characteristics of 3DCP components. It is established that the 3DCP process influences the ensuing microstructural morphology both in and in-between filaments. Higher porosity, on average and at interlayer locations, as well as alterations in the spatial and topological attributes of pores in 3DCP samples compared to mould-cast samples, are observed. The effects of porosity metrics such as total porosity content; 3D void topology (shape, size, and orientation); pore spatial, size and compactness distributions; and interconnectivity are quantitatively investigated via X-ray computed tomography (X-CT) and related to the elasticity, compressive strength and observed fracture patterns of mould-cast and 3DCP specimens consisting of the same FRPC matrix. It is shown that both reductions in the elastic modulus and compressive capacity can be physically linked to the porosity metrics detected in 3DCP elements. From the consideration and interpretation of these aspects, the anisotropic mechanical response of 3DCP samples is elucidated. It is established that elasticity is dominated by porosity content. In comparison, compressive capacity is far more complex and subject to the interrelation between four key morphological features. These include porosity content, loading direction relative to the interlayer orientation, void topological features (effecting the stress concentration magnitudes at pore boundaries), and the increased deformability of the composite configuration.

Chapter 6 amalgamates the findings presented in Chapters 3 to 5 and extends the fundamental knowledge basis pertaining to the anisotropic mechanical characteristics found in 3DPC. Chapter 6 offers a comprehensive investigation of the compression-shear performance of a FRPC mixture via a direct shear test (DST) methodology. Analysing the anisotropic material strength in the three orthogonal material planes reveals that a linear Coulomb friction assumption misrepresents the compression-shear constitutive behaviour exhibited in 3DPC. A novel non-linear modified Mohr-Griffith failure criterion, including an empirical material scaling factor (M), is proposed and validated by a mechanistic evaluation of the observed microstructural morphology. Again, X-CT is employed to explore the microstructural morphology, fracture surface angle, and fracture surface area of inter and intralayer regions compared to cast specimens. It is shown that the exhibited degree of anisotropy and the non-linear shear strength evolution in 3DPC is related to the pore morphological features and spatial distribution of porosity with regard to the induced stress state. It is shown that both 3DPC inter and intralayer present a source of anisotropy. Finally, it is suggested that improving the sphericity of pores and reducing local porosity permits reduced anisotropy in 3DPC.

Essentially, this research elucidates the experimental mechanics for the proper material characterisation of 3DCP elements and proposes computational simulation strategies that can accurately

represent the non-linear anisotropic response of 3DCP structural components. The computational mechanics of the proposed simulation strategies are studied and found to overestimate the shear capacity of interfacial regions. The microstructural morphology is comprehensively characterised and deemed a definite contributor to the reduced strength and stiffness attributes portrayed by 3DCP specimens. Additionally, it is demonstrated how the microstructure influences the direction of crack propagation. It is then revealed why anisotropy is so prevalent in 3DCP and why the shear strength of interfacial regions is overestimated. Finally, it is divulged how to better predict the non-linear compression-shear constitutive behaviour computationally through a simplified limit function and potential remedies to alleviate the anisotropic response are proposed.

7.2 Significant Findings

Specific conclusions are presented in Chapters 3 to 6. Here, conclusions pertinent to the experimental and computational mechanics for the constitutive modelling of extrusion-based 3DCP are drawn.

Chapter 3: Mechanical characterisation procedures

- In the absence of standardised testing protocols, the proposed experimental methodology captures the similar elastic and anisotropic tensile, compressive, and flexural material strength and deformation characteristics of 3DCP specimens. As opposed to tensile tests, flexural tests impose strain and stress gradients, whereby material model parameters cannot directly and uniquely be derived. Therefore, it is recommended that flexural tests be excluded as a method to attain tensile material parameters for 3DPC mixtures, and used exclusively for comparative purposes.
- The mechanical characterisation procedures appropriately describe the unique material properties required for the computational analysis of 3DCP elements. However, meticulous sample preparation procedures and a comprehensive understanding of the experimental mechanics are necessary for successful hardened-state material testing.
- It is envisaged that standardised hardened-state material testing protocols can be established if these experimental techniques are utilised in future studies and extensive data sets are generated for various 3DCP mixtures from multiple institutions.

Chapter 4: Numerical simulation strategies

- The proposed multi-surface anisotropic continuum and interface-based FE simulation strategies show immense potential for implementation in the non-linear design and analysis of 3DCP components. The similarities between the experimental and numerical results in the force-displacement response and crack patterns validate the applicability of the FE modelling strategies to 3DCP and steel reinforced 3DPC.

- Tension dominated bending failure is accurately modelled by both strategies with a minimal peak resistance variation and identical cracking patterns. However, model parameter calibration yields better agreement with the experimental results for mixed compression-shear and shear-bending failure modes and provides critical insights to material and model uncertainty. The implementation of a viscous energy regularisation technique and multi-linear softening constitutive relation to describe the tensile softening regime is contended to yield additional FE modelling accuracy for fibre-reinforce printable composites.
- The model parameter calibration procedures emphasise that the shear strength is overestimated by the recommended relationships presented in the literature.
- The advent of a 2D plane stress simplification of the hollow beam geometry yields acceptable agreement while significantly reducing the computational expense of simulations. Note, the effective contact area between filaments should be considered for structural design activities and not the nominal layer width.
- Appropriate computational modelling strategies are shown to take an incremental step towards the detailed design and analysis of load-bearing 3DCP components and structures.

Chapter 5: Effects of porosity on the compressive strength, elasticity, and fracture patterns

- The embodied extrusion-based 3DCP process both spatially and geometrically alters the microstructural morphology of the 3DCP composite. It is shown that the pores encountered in cast samples are generally more spherical (compact) compared to the irregular, approximately ellipsoidal shaped pores observed in 3DCP samples. As a consequence of shear-induced particle migration, 3DCP specimens exhibit higher porosity and an increase in the concentration and interconnectivity of pores at interlayer locations.
- The pores in 3DCP samples are consistently elongated in the extrusion direction and flattened in the vertical building direction. This indicates that the hydraulic pressure gradient induced by the extrusion process preferentially aligns and elongates voids in the extrusion direction while pressing/squeezing in the vertical building direction occurs due to overlay compaction. Additionally, more significant variations in semi-axis lengths are noticed in 3DCP samples, validating their reduced compactness.
- The altered microstructural morphology at interlayer locations affirms the reduced capacity at interlayer locations and affects the orientation of crack propagation. Additionally, such observation accords with Griffith's fracture theory for tensile fracture around enclosed defects.
- It is imperative to assess the mechanical characteristics of samples extracted from actual 3DCP objects since cast samples neglect the interrelated effects induced by the fabrication process.

Chapter 6: Mechanistic evaluation relating microstructural morphology to a modified Mohr-Griffith compression-shear constitutive model for 3D printed concrete

- 3DCP samples display anisotropic mechanical capacities and a non-linear shear strength increase, whereas cast samples exhibit an isotropic linear shear strength increase when subject to increasing compression-shear loading conditions.
- A mechanistic evaluation relates the exhibited anisotropy and non-linear shear strength evolution in 3DPC to the microscopic pore morphology concerning the stress state, and a modified Mohr-Griffith failure criterion is introduced. Solid agreement between the experimentally attained results and the modified Mohr-Griffith criterion is found for all 3DCP samples. Additionally, the presented theories can aptly describe the observed response in both 3DPC and cast specimens.
- The accuracy of hardened-state FE analyses can be considerably increased by implementing the recommended modified Mohr-Griffith failure criterion for 3DCP elements.
- In the pursuit of isotropic material characteristics for 3DCP composites, future investigations should consider methods to reduce local increases in porosity but should also endeavour to stabilise the remaining inclusions in the cementitious matrix.
- It is postulated that improved mechanical performance and reduced anisotropy, evoking less computational complexity and uncertainty, is permitted by improving the sphericity of pores within 3DPC elements.

7.3 Recommendations

The mechanical characterisation procedures can be extended to include post-peak compression characterisation and methods to experimentally examine Poisson's ratio in 3DPC, as compression dominated structural members will be heavily reliant on these parameters. Additionally, biaxial testing of 3DCP wallets is advised to further calibrate the model parameters of the anisotropic Rankine-Hill continuum macro-modelling approach to 3DPC. The 2.5D curved shell approach permitted by the computational strategies should be employed for more complex 3DCP geometric configurations and experimentally assessed to validate its applicability. The interface-based micro-modelling method should be extended to include the novel modified Mohr-Griffith failure criterion to enable more detailed FE analyses to be conducted accurately.

The analogy between 3DCP and masonry material characterisation and computational analysis techniques is apparent and should therefore be considered to prescribe structural design guidelines for components or structures additively manufactured by extrusion-based 3DCP. Moreover, to catch up and

keep pace with the rapid developments in this exciting field, it is recommended that structural design guidelines take on the form of amendments or specific annexes to existing standards, such as EN 1996-1-2 for reinforced and unreinforced masonry, EN 1996-1-1 for load-bearing walls, or even a chapter in EN 1992-1-1 for structural concrete. The proposed computational modelling strategies should be employed along with Annex D of EN-1990's standard procedure to support design by testing to verify the conformity of a component or structure to the above-listed standards. Note, it is of utmost importance that holistic design prescriptions be set that considers the interrelated material, process, fresh and hardened-state design requirements and their ensuing effects on the performance, quality, and integrity of the additively manufactured product.

Finally, forthcoming studies should not exclusively focus on interlayer regions but should also consider the anisotropy within intralayer filaments containing entrapped ellipsoidal pores since these inclusions impose a source of anisotropy due to their preferential alignment and elongation in the extrusion direction. Additionally, it is recommended that material design methods be investigated that aim at (1) reducing the overall and localised porosity and (2) improving the sphericity of microstructural pores in and in-between 3DCP filaments. The successful execution of such methods is contended to significantly reduce both computational complexity and material uncertainty, providing a more directed path towards the mass adoption and implementation of this promising automated construction technology.

Addendum A – Article Declarations

Declaration by the candidate:

With regard to **Chapter 3**, the nature and scope of my contributions were as follows:

Nature of contribution	**Extent of contribution (%)**
Conceptualisation, Methodology, Validation, Experimental work, Formal analysis, Investigation, Data curation, Writing - original draft, Writing - review & editing, Visualisation, Project administration.	85

The following co-authors have contributed to Chapter 3:

Name	**E-mail address**	**Nature of contribution**	**Extent of contribution (%)**
Mr Frederick Bester	fabester@sun.ac.za	Assisted with experiments, review of manuscript.	5
Dr Jacques Kruger	pjkruger@sun.ac.za	Review of manuscript, proposed insightful amendments, Supervision.	5
Prof Gideon van Zijl	gvanzijl@sun.ac.za	Review of manuscript, proposed insightful amendments, Supervision.	5

Candidate signature: 

Date: 26/07/2021

Declaration by co-authors:

The undersigned hereby confirm that

1. the declaration above accurately reflects the nature and extent of the contributions of the candidate and the co-authors to Chapter 3,
2. no other authors contributed to Chapter 3 besides those specified above, and
3. potential conflicts of interest have been revealed to all interested parties and that the necessary arrangements have been made to use the material in Chapter 3 of this dissertation.

Signature	**Institutional affiliation**	**Date**
	Stellenbosch University	26/07/2021
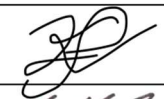	Stellenbosch University	26/07/2021
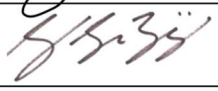	Stellenbosch University	27 July 2021

Declaration by the candidate:

With regard to **Chapter 4**, the nature and scope of my contributions were as follows:

Nature of contribution	**Extent of contribution (%)**
Conceptualisation, Methodology, Validation, Experimental work, Formal analysis, Investigation, Data curation, Writing - original draft, Writing - review & editing, Visualisation, Project administration.	85

The following co-authors have contributed to Chapter 4:

Name	**E-mail address**	**Nature of contribution**	**Extent of contribution (%)**
Mr Frederick Bester	fabester@sun.ac.za	Assisted with experiments, review of manuscript.	5
Dr Jacques Kruger	pjkruger@sun.ac.za	Review of manuscript, proposed insightful amendments, Supervision.	5
Prof Gideon van Zijl	gvanzijl@sun.ac.za	Review of manuscript, proposed insightful amendments, Supervision.	5

Candidate signature: 

Date: 26/07/2021

Declaration by co-authors:

The undersigned hereby confirm that

1. the declaration above accurately reflects the nature and extent of the contributions of the candidate and the co-authors to Chapter 4,
2. no other authors contributed to Chapter 4 besides those specified above, and
3. potential conflicts of interest have been revealed to all interested parties and that the necessary arrangements have been made to use the material in Chapter 4 of this dissertation.

Signature	**Institutional affiliation**	**Date**
	Stellenbosch University	26/07/2021
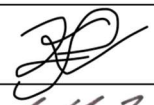	Stellenbosch University	26/07/2021
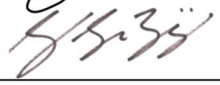	Stellenbosch University	27 July 2021

Declaration by the candidate:

With regard to **Chapter 5**, the nature and scope of my contributions were as follows:

Nature of contribution	**Extent of contribution (%)**
Conceptualisation, Methodology, Validation, Experimental work, Formal analysis, Investigation, Data curation, Writing - original draft, Writing - review & editing, Visualisation, Project administration.	85

The following co-authors have contributed to Chapter 5:

Name	**E-mail address**	**Nature of contribution**	**Extent of contribution (%)**
Prof Anton du Plessis	anton2@sun.ac.za	X-ray CT scanning and processing, review of manuscript, proposed insightful amendments.	5
Dr Jacques Kruger	pjkruger@sun.ac.za	Review of manuscript, proposed insightful amendments, Supervision.	5
Prof Gideon van Zijl	gvanzijl@sun.ac.za	Review of manuscript, proposed insightful amendments, Supervision.	5

Candidate signature: 

Date: 26/07/2021

Declaration by co-authors:

The undersigned hereby confirm that

1. the declaration above accurately reflects the nature and extent of the contributions of the candidate and the co-authors to Chapter 5,
2. no other authors contributed to Chapter 5 besides those specified above, and
3. potential conflicts of interest have been revealed to all interested parties and that the necessary arrangements have been made to use the material in Chapter 5 of this dissertation.

Signature	**Institutional affiliation**	**Date**
	Stellenbosch University	26/07/2021
	Stellenbosch University	26/07/2021
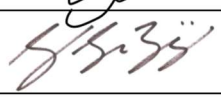	Stellenbosch University	27 July 2021

Declaration by the candidate:

With regard to **Chapter 6**, the nature and scope of my contributions were as follows:

Nature of contribution	**Extent of contribution (%)**
Conceptualisation, Methodology, Validation, Experimental work, Formal analysis, Investigation, Data curation, Writing - original draft, Writing - review & editing, Visualisation, Project administration.	80

The following co-authors have contributed to Chapter 6:

Name	**E-mail address**	**Nature of contribution**	**Extent of contribution (%)**
Mr Frederick Bester	fabester@sun.ac.za	Assisted with experiments, review of manuscript.	5
Prof Anton du Plessis	anton2@sun.ac.za	X-ray CT scanning and processing, review of manuscript, proposed insightful amendments.	5
Dr Jacques Kruger	pjkruger@sun.ac.za	Concept, Review of manuscript, proposed insightful amendments, Supervision.	5
Prof Gideon van Zijl	gvanzijl@sun.ac.za	Review of manuscript, proposed insightful amendments, Supervision.	5

Candidate signature: 

Date: 26/07/2021

Declaration by co-authors:

The undersigned hereby confirm that

1. the declaration above accurately reflects the nature and extent of the contributions of the candidate and the co-authors to Chapter 6,
2. no other authors contributed to Chapter 6 besides those specified above, and
3. potential conflicts of interest have been revealed to all interested parties and that the necessary arrangements have been made to use the material in Chapter 6 of this dissertation.

Signature	**Institutional affiliation**	**Date**
	Stellenbosch University	26/07/2021
	Stellenbosch University	26/07/2021
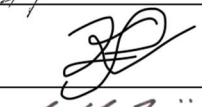	Stellenbosch University	26/07/2021
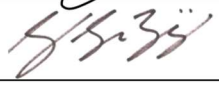	Stellenbosch University	27 July 2021

Addendum B – Copyright Permission

Elsevier:

Table of Author's Rights

	Preprint version (with a few exceptions- see below *)	Accepted Author Manuscript	Published Journal Articles
Use for classroom teaching by author or author's institution and presentation at a meeting or conference and distributing copies to attendees	Yes	Yes	Yes
Use for internal training by author's company	Yes	Yes	Yes
Distribution to colleagues for their research use	Yes	Yes	Yes
Use in a subsequent compilation of the author's works	Yes	Yes	Yes
Inclusion in a thesis or dissertation	Yes	Yes	Yes
Reuse of portions or extracts from the article in other works	Yes	Yes with full acknowledgement of final article	Yes with full acknowledgement of final article
Preparation of derivative works (other than for commercial purposes)	Yes	Yes with full acknowledgement of final article	Yes with full acknowledgement of final article
Preprint servers	Yes	Yes with the specific written permission of Elsevier	No
Voluntary posting on open web sites operated by author or author's institution for scholarly purposes	Yes (author may later add an appropriate bibliographic citation, indicating subsequent publication by Elsevier and journal title)	Yes, with appropriate bibliographic citation and a link to the article once published	Only with the specific written permission of Elsevier
Mandated deposit or deposit in or posting to subject-oriented or centralized repositories	Yes under specific agreement between Elsevier and the repository	Yes under specific agreement between Elsevier and the repository**	Yes under specific agreement between Elsevier and the repository
Use or posting for commercial gain or to substitute for services provided directly by journal	Only with the specific written permission of Elsevier	Only with the specific written permission of Elsevier	Only with the specific written permission of Elsevier

** Voluntary posting of Accepted Author Manuscripts in the arXiv subject repository is permitted.